



Application of synchrotron-based x-ray diagnostics for the investigation of pressurised metered-dose inhaler sprays

Nicholas J. Mason-Smith
Bachelor of Aerospace Engineering (Honours)
Bachelor of Commerce (Sustainability)

A thesis submitted for the degree of Doctor of Philosophy at
Monash University in 2018
Department of Mechanical & Aerospace Engineering

© Nicholas J. Mason-Smith (2018).

Abstract

An experimental and theoretical investigation of transient spray properties of pressurised metered-dose inhalers (pMDI) has been conducted. Synchrotron x-ray diagnostics were applied to these sprays for the first time, and provided measurements in regions previously inaccessible to experiment. Quantitative measurements of spray projected mass and drug concentration, and visualisations of the internal flow structure, were obtained.

Synchrotron x-ray radiography was used to measure profiles of the ensemble-mean time-variant projected mass of sprays from a pMDI and a pMDI analogue. Transverse integration of these profiles demonstrated that the spray in the near-nozzle region is low density, consistent with a highly vaporised spray. Dominant sources of uncertainty were identified.

Phase contrast imaging was used to visualise the vapour-liquid structure of the internal flows of drug-free pMDIs with and without ethanol. The inclusion of ethanol was found to affect these structures; increased ethanol concentration is associated with a decrease of the scale at which vapour is distributed within the liquid. Visualisations also showed that large droplets, which likely contribute to oropharyngeal deposition in suspension pMDIs, are produced internally.

Visible light diagnostics were used for the measurement of downstream properties of pressurised metered-dose inhalers. The measurements showed an improved spray steadiness with ethanol addition. This finding was consistent with the flow-structural effect of ethanol observed with phase contrast imaging.

The experimental results were used to advance thermodynamic modelling of pMDIs. A comparison of x-ray radiography data of propellant-only pMDI sprays with thermodynamic model predictions indicated that metastability effects are significant in the nozzle flows of pMDIs. A thermodynamic model was also developed for the modelling of multicomponent liquids that more realistically represent formulations used in drug-containing pMDIs.

The combination of high-fidelity near-nozzle measurements and phenomenological modelling provides a way forward for the performance prediction of pressurised metered-dose inhalers.

List of Publications

Mason-Smith, Nicholas, Daniel J. Duke, Alan L. Kastengren, Daniela Traini, Paul M. Young, Yang Chen, David A. Lewis, Daniel Edgington-Mitchell, and Damon Honnery. 2017. "Revealing pMDI spray initial conditions: flashing, atomisation and the effect of ethanol." *Pharmaceutical Research* 34 (4): 718-729.

Mason-Smith, Nicholas, Daniel J. Duke, David A. Lewis, Daniel Edgington-Mitchell, and Damon Honnery. 2017. "High-speed X-ray Imaging of Pressurized Metered-dose Inhaler Sprays with Variable Ethanol Content". In *Proceedings of the 19th Annual Conference on Atomization and Spray Systems - Asia*.

Duke, Daniel J., Alan L. Kastengren, Nicholas Mason-Smith, Yang Chen, Paul M. Young, Daniela Traini, David Lewis, Daniel Edgington-Mitchell, and Damon Honnery. 2016. "Temporally and spatially resolved x-ray fluorescence measurements of in-situ drug concentration in metered-dose inhaler sprays." *Pharmaceutical Research* 33 (4): 816-825.

Mason-Smith, Nicholas, Daniel J. Duke, Alan L. Kastengren, Peter J. Stewart, Daniela Traini, Paul M. Young, Yang Chen, David A. Lewis, Julio Soria, and Damon Honnery. 2016. "Insights into spray development from metered-dose inhalers through quantitative X-ray radiography." *Pharmaceutical Research* 33 (5): 1249-1258.

Mason-Smith, Nicholas, Daniel J. Duke, Marcus Fedrizzi, Julio Soria, Daniel Edgington-Mitchell, and Damon R. Honnery. 2015. "Back-Illumination Imaging of Pressurised Metered-Dose Inhaler Sprays". In *Proceedings of the 7th Australian Conference on Laser Diagnostics in Fluid Mechanics and Combustion*.

Mason-Smith, Nicholas, Daniel J. Duke, James S. Harkess, Daniel Edgington-Mitchell, and Damon R. Honnery. 2016. "Acoustic unsteadiness of sprays from pressurised metered-dose inhalers". In *20th Australasian Fluid Mechanics Conference*.

Mason-Smith, Nicholas, Daniel Edginton-Mitchell, Damon Honnery, Daniel Duke, and Julio Soria. 2015. "Pressurised metered-dose inhaler spray structure". In *Proceedings of Turbulence and Shear Flow Phenomena 9*.

Declaration

I hereby declare that this thesis contains no material which has been accepted for the award of any other degree or diploma at any university or equivalent institution and that, to the best of my knowledge and belief, this thesis contains no material previously published or written by another person, except where due reference is made in the text of the thesis.

This thesis includes three original papers published in peer-reviewed journals and four original papers published in peer-reviewed conferences. The core theme of the thesis is the investigation of transient sprays from pressurised metered-dose inhalers with experimental synchrotron-based x-ray techniques. The ideas, development and writing up of all the papers in the thesis, with the exception of the paper presented in Appendix D, were the principal responsibility of myself, the student, working within the Department of Mechanical & Aerospace Engineering under the supervision of Professor Damon Honnery and Dr. Daniel Edgington-Mitchell.

The inclusion of co-authors reflects the fact that the work came from active collaboration between researchers and acknowledges input into team-based research.

In the case of Chapters 2, 3, 4, 5 and Appendices B, C and D, my contribution to the work involved the following:

Thesis chapter	Publication title	Status	Nature and % of student's contribution	Co-author name(s); Nature and % of co-author's contribution	Co-author(s), Monash student Y/N
2	Pressurised metered-dose inhaler spray structure	Published	60%; Development of ideas, data collection, data analysis, figure preparation, writing	Edgington-Mitchell, D., Honnery, D.R.H, Duke, D., Soria, J.	N
3	Insights into Spray Development from Metered-Dose Inhalers Through Quantitative X-ray Radiography	Published	50%; Development of ideas, data collection, data analysis, figure preparation, writing	Duke, D., Kastengren, A.L., Stewart, P.J., Traini, D., Young, P.M., Chen, Y., Lewis, D.A., Soria, J., Edgington-Mitchell, D., Honnery, D.R.H	N
4	Revealing pMDI Spray Initial Conditions: Flashing, Atomisation and the Effect of Ethanol	Published	50%; Development of ideas, data collection, data analysis, figure preparation, writing	Duke, D., Kastengren, A.L., Traini, D., Young, P.M., Chem, Y., Lewis, D.A., Edgington-Mitchell, D., Honnery, D.R.H	N
5	High-speed X-ray Imaging of Pressurized Metered-dose Inhaler Sprays with Variable Ethanol Content	Published	60%; Development of ideas, data collection, data analysis, figure preparation, writing	Duke, D., Kastengren, A.L., Edgington-Mitchell, D., Honnery, D.R.H	N

Appendix B	Back-Illumination Imaging of Pressurised Metered-Dose Inhaler Sprays	Published ideas, data collection, data analysis, figure preparation, writing	60%; Development of ideas, data collection, data analysis, figure preparation, writing	Duke, D., Fedrizzi, M. (data collection), Soria, J., Edgington-Mitchell, D., Honnery, D.R.H	N/Y/N/N/N
Appendix C	Acoustic unsteadiness of sprays from pressurised metered-dose inhalers	Published ideas, data collection, data analysis, figure preparation, writing	60%; Development of ideas, data collection, data analysis, figure preparation, writing	Duke, D., Harkess, J. (data collection), Edgington-Mitchell, D., Honnery, D.R.H	N/Y/N/N
Appendix D	Temporally and Spatially Resolved x-ray Fluorescence Measurements of in-situ Drug Concentration in Metered-Dose Inhaler Sprays	Published ideas, Data collection	25%; Development of ideas, Data collection	Duke, D., Kastengren, A.L., Chen, Y., Young, P.M., Traini, D., Lewis, D.A., Edgington-Mitchell, D., Honnery, D.R.H	N

I have not renumbered sections of submitted or published papers in order to generate a consistent presentation within the thesis.

Student signature:

Date: 29 August 2018

The undersigned hereby certify that the above declaration correctly reflects the nature and extent of the student's and co-authors' contributions to this work. In instances where I am not the responsible author I have consulted with the responsible author to agree on the respective contributions of the authors.

Main Supervisor signature:

Date: 29 August 2018

Acknowledgements

“Digressions, incontestably, are the sunshine;—they are the life, the soul...”

— Sterne ([1759] 1950, 73–74)

Beyond the research training that is the primary purpose of a PhD, I leave this program with a number of close relationships, and a trove of memories. Though many of the classes, events, projects and conversations I was involved in during my candidature did not directly progress my research (and at times directly hindered its progress), the interactions so afforded were no less valuable than the research training itself. It is a privilege to acknowledge those who made my candidature such a fulfilling experience, and those whose support was instrumental in its successful completion.

I wish to begin by thanking my supervisors, Professor Damon Honnery and Dr Daniel Edgington-Mitchell. They have shown me models of how to conduct quality research, and the human connection that can exist in the research process. The breadth of their knowledge and interests made our meetings particularly enjoyable; Sterne knew what he was talking about. Damon’s style of teaching has had a significant influence on my own. His knowledge, Socratic questioning and informed hunches, not to mention his collection of ageing technical books, contributed much to my intellectual development. Daniel’s support and encouragement of me, and his willingness to engage in both professional and personal discourse, have been unwavering ever since he first inspired me as an undergraduate.

I would like to thank Dr Daniel Duke of Monash University, and Drs Alan Kasten-gren and Christopher Powell of the Advanced Photon Source at Argonne National Laboratory. Working alongside them at the synchrotron was one of the distinct pleasures of my life, and showed me how a first-rate laboratory can be run.

I am fortunate to have been welcomed into the Laboratory for Turbulence Research in Aerospace and Combustion, not only for the research opportunities but for the company. In particular, I would like to acknowledge Dominic Tan, Joel Weightman, Graham Bell, Tom Knast, Marcus Wong, Bhavraj Thethy and Michael Eisfelder, and thank them for their friendship, collaboration and humour. The talent and character in this group gives me great hope for the future. I would also

like to acknowledge the assistance of Professor Julio Soria, who was most helpful at various stages in my analyses.

I would like to thank my fellow residents of ‘The Northcote Manor’, both past–Tom, Ginny, Robyn and Kajute–and present–Amaya, Sam, Sarah, Jon, Rita and Belinda. Communal living has greatly enriched my life, and I am fortunate to have done so with such generous and creative people.

Central to any of my achievements is the work of my parents, Jenny and Del. It is a testament to their skill as parents that I had the confidence to do a PhD. My close friends have been supportive and loyal during a process that has, at times, turned me into a fair-weather friend. In particular, I would like to thank Tom, Talal, Bella, Nathan, Lauren, Phoebe and James. I would also like to thank my beloved Jennifer. Having experienced her support while I completed my thesis, I look forward to returning the favour while she completes hers.

This thesis is dedicated to my brother Sam. Despite my growth as a writer, I still cannot put into words my feelings of love for and solidarity with him.

This research was supported by an Australian Government Research Training Program (RTP) Scholarship.

Contents

List of Figures	xiii
List of Tables	xix
1 Introduction & Background	1
1.1 The pressurised metered-dose inhaler	1
1.2 Development of pMDIs	5
1.3 Experimental measurement of pMDI sprays	8
1.4 Phenomenological modelling of pMDIs	16
1.5 Summary	18
2 Pressurised metered-dose inhaler spray structure	19
2.1 Introductory statement	19
2.2 Concluding statement	28
3 Insights into Spray Development from Metered-Dose Inhalers Through Quantitative X-ray Radiography	31
3.1 Introductory statement	31
3.2 Concluding statement	43
4 Revealing pMDI Spray Initial Conditions: Flashing, Atomisation and the Effect of Ethanol	45
4.1 Introductory statement	45
4.2 Concluding statement	59
5 High-speed X-ray Imaging of Pressurized Metered-dose Inhaler Sprays with Variable Ethanol Content	61
5.1 Introductory statement	61
5.2 Concluding statement	67

6 A comparison of quantitative radiography and a propellant-only phenomenological model	69
6.1 Motivation	69
6.2 Nomenclature	70
6.3 Analysis methodology	71
6.4 Results	86
6.5 Discussion	92
7 A non-equilibrium thermodynamic model of multicomponent pMDIs	97
7.1 Motivation	97
7.2 Nomenclature	98
7.3 Analysis methodology	99
7.4 Results	109
7.5 Discussion	115
8 Conclusions	119
Bibliography	123
Appendix A Governing equations of pMDI thermodynamic models	135
A.1 Two-phase speeds of sound	135
A.2 Differential equations of thermodynamic models	141
Appendix B Back-illumination imaging of pressurised metered-dose inhaler sprays	147
B.1 Introductory statement	147
Appendix C Acoustic unsteadiness of sprays from pressurised metered-dose inhalers	155
C.1 Introductory statement	155
Appendix D Temporally and Spatially Resolved x-ray Fluorescence Measurements of in-situ Drug Concentration in Metered-Dose Inhaler Sprays	161
D.1 Introductory statement	161
D.2 Concluding statement	173

List of Figures

1.1 Schematic of typical pressurised metered-dose inhaler (reprinted from Newman (2005)).	7
2.1 Schematical of the experimental apparatus for Mie scattering, consisting of PILS laser, 45 degree mirror, automated pMDI device and PCO 4000 camera. Coordinate system shown is used for the PIV and laser extinction measurements.	23
2.2 Maximum mean axial velocity against axial distance for the HFA 134a spray, 50 ms after actuation.	24
2.3 Ensemble average velocity magnitude field 50 ms after actuation for HFA 134a (top) and HFA 134a with ethanol (bottom) sprays. Mean fields are generated from 121 velocity fields. Masking is applied in regions where the spray is inconsistent (shown in gray).	25
2.4 Axial and vertical turbulence intensities for HFA 134a & ethanol spray, downstream of the mouthpiece at 50 ms after actuation.	25
2.5 Non-dimensional velocity profiles for sprays from HFA 134a canisters with and without ethanol (left and right, respectively). The collapse of velocity profiles onto a single curve demonstrates self-similarity of the mean axial velocity for the region of interest studied.	26
2.6 Ensemble average and individual $x - t$ spray images from the electronic metering inhaler with HFA 134a & ethanol (left), HFA 227 (center) and HFA 227 & ethanol (right). The start and end of spray actuation from the electronic metering inhaler are indicated by horizontal dash-dot lines, and the line used for the mean and single shot is indicated by a vertical dotted line. All plots are normalised by \bar{M}_{max} for the formulation.	27
2.7 Instantaneous Mie scatter images from a pure HFA 134a canister spray from the pMDI, 5 mm downstream of mouthpiece 50 ms after actuation. Images are background subtracted, and the mouthpiece is illuminated by scattering from the spray.	27

3.1	Side cutaway view of spray chamber and apparatus	35
3.2	Detail view of volume between solenoid valve and nozzle orifice.	36
3.3	$x-t$ evolution of (a) argon jet, (b) 134a-E-I spray and (c) 227-E-I spray at $y =$ (top) -15 mm, (middle) 5 mm and (bottom) 25 mm from mouthpiece. Black vertical lines indicate end of injection.	37
3.4	Time traces of (left) 134a-E-I and (right) 227-E-I sprays at $y = 25$ mm, $x = 0$ mm with different absorption coefficients based on propellant and ethanol state. Lower bound corresponds to liquid state, upper bound to vaporous state, and white line to vaporous propellant and liquid ethanol. Vertical dashed lines indicate end of injection.	38
3.5	Time traces of (left) 134a-E-I and (right) 227-E-I sprays at $y = 25$ mm, $x = 0$ mm with variable injection duration (indicated). Vertical dashed lines indicate end of injection for each injection duration.	39
3.6	Time traces of spray projected mass at $y = 25$ mm, $x = 0$ mm with different formulations (indicated). Vertical dashed lines indicate end of injection.	40
3.7	Transverse integrated mass M' as a function of distance from the nozzle y' for argon jet, 134a-E-I spray and 227-E-I spray. A separate axis is used for argon M'	40
4.1	Schematic of pMDI metering chamber, valve stem and atomising nozzle cross-section.	48
4.2	Temporal trace of nozzle and valve stem surface temperatures with HFA134a 100% sprays at 20 s dwell time. Gray region indicates ambient temperature ± 5 K.	50
4.3	Experimental layouts for (left) phase contrast imaging and (right) quantitative radiography (not to scale).	51
4.4	Phase contrast images of HFA134a flow in (left) valve stem and (right) sump and nozzle (top) 5 ms, (middle) 30 ms and (bottom) 90 ms after start of injection. Regions are shown schematically at the bottom of each column. A mounting bracket obscures the top-left corner of the valve stem images.	52
4.5	Phase contrast images of HFA134a/Ethanol flow in (left) valve stem and (right) sump and nozzle (top) 5 ms, (middle) 30 ms and (bottom) 90 ms after start of injection.	53
4.6	Phase contrast images of (left) HFA134a and (right) HFA134a/Ethanol flow from nozzle exit orifice.	54

4.7	$y - t$ plots of spray projected mass M for (top) HFA134a and (bottom) HFA134a/Ethanol sprays at $x = 0.3$ mm.	54
4.8	Nozzle orifice flow mixture density ρ_m against time.	54
4.9	Absorption coefficients μ_l and μ_v of liquid and vapour phases of HFA134a/ethanol equilibrium saturated mixtures against liquid phase ethanol mass fraction $w_{l,eth}$. Data presented at 298.15 K.	56
4.10	Mass flowrate \dot{m} and discharged mass m against time.	56
5.1	Schematic of pMDI metering chamber and nozzle geometry.	63
5.2	Instantaneous images of internal flows of (top) HFA134a propellant-only, (middle) HFA134a/ethanol (5% by weight) and (bottom) HFA134a/ethanol (15% by weight) formulations. All images are 45 ms after start of injection. Flow enters at top of frame and exits to the right as indicated by arrows.	64
5.3	Instantaneous images of internal flows of (top) HFA134a propellant-only, (middle) HFA134a/ethanol (5% by weight) and (bottom) HFA134a/ethanol (15% by weight) formulations. All images are 90 ms after start of injection. Flow enters at top of frame and exits to the right as indicated by arrows.	64
5.4	Instantaneous images of HFA134a propellant-only internal flow at the nozzle inlet 71 ms after start of injection. Flow travels from left to right.	65
5.5	Instantaneous image of internal flow of HFA134a propellant-only 76 ms after start of injection.	65
5.6	Instantaneous image of nozzle and near-nozzle flow of HFA134a/Ethanol (15% by weight) 45 ms after start of injection.	66
6.1	Schematic of pMDI geometry used in the thermodynamic model.	72
6.2	Control volume used for analysis of near-nozzle flow.	78
6.3	Basic flow patterns for square-edged cylindrical nozzles as the choked condition is reached: (left) marginally reattached flow, (middle) fully reattached flow with vena contracta choking, and (right) fully reattached flow with outlet (Fanno) choking (adapted from Ward-Smith (1979)). . .	82
6.4	Time series of TIM_e/A_t for experiment ($z = 0.3$ mm) and thermodynamic models.	87
6.5	$y - t$ plots of projected mass from (left, top) experiment ($z = 0.3$ mm), (right, top) HDE ($\eta = 0.95$), (bottom, left) HEM and (bottom, right) HFM. Dynamic range is reduced by clipping to the colour range of the HDE.	88

6.6	Experimental ($z = 0.3$ mm) and modelled projected mass M (top) centre line ($y = 0$ mm) time series and (bottom) transverse profiles at peak TIM.	89
6.7	TIM_e/A_t for (top) $y > 0$ and (bottom) $y < 0$.	90
6.8	Experimental ($z = 0.3$ mm) and modelled projected mass M profiles with $\sigma_0/D_{\text{no}} = 0.75$.	91
6.9	$y - t$ plots of M ($y > 0$) for (top, left) experiment ($z = 0.3$ mm), (top, right) HDE ($\eta = 0.8$), (bottom, left) HEM and (bottom, right) HFM. For all modelled profiles, $\sigma_0/D_{\text{no}} = 0.75$. Dynamic range is reduced by clipping to the range of the experimental data.	92
6.10	Experimental ($z = 0.3$ mm) and modelled projected mass M profiles with $\sigma_0/D_{\text{no}} = 1.25$.	93
6.11	$y - t$ plots of M ($y < 0$) for (top, left) experiment ($z = 0.3$ mm), (top, right) HDE ($\eta = 0.95$), (bottom, left) HEM and (bottom, right) HFM. For all modelled profiles, $\sigma_0/D_{\text{no}} = 1.25$.	93
7.1	Visual representation of dynamic vapour-liquid equilibrium (adapted from Feynman, Leighton, and Sands (2011)).	103
7.2	Estimated bubble diameter distribution as function of time after start of injection.	106
7.3	Time series of TIM_e/A_t for experiment ($z = 0.3$ mm) and thermodynamic model.	110
7.4	$y - t$ plots of M for (left column) experiment and (right column) HFM. Formulations are (top) HFA134a, (middle) HFA134a w/ 5% ethanol and (bottom) HFA134a w/ 15% ethanol. For all modelled profiles, $\sigma_0/d_{\text{no}} = 1.25$.	111
7.5	TIM_e/A_t for (top) $y > 0$ and (bottom) $y < 0$.	113
7.6	Time series of the conditions at the nozzle exit ($z = 0$). Lines are coloured by formulation as indicated in the fourth subfigure. Subfigures are, from top to bottom: expansion chamber (solid lines) and throat (dotted lines) pressures P ; expansion chamber (solid lines) and throat (dotted lines) temperatures T ; void fraction α (solid lines) and throat density ρ (dashed lines); throat velocity U_t ; and ethanol mass fraction w_e for (solid lines) liquid phase and (dashed lines) total mass.	114
B.1	Schematic of (a) Bespak inhaler body with mouthpiece removed, allowing visualisation of the near-nozzle region; and (b) nozzle internal geometry.	150

B.2 Temporal evolution of ensemble average transverse profile at $x = 2$ mm. Spray axes (black dashed lines) and spray half-widths (black solid lines) are overlaid.	150
B.3 Ensemble-average spray half-widths at $x = 2$ mm, above and below the spray axis.	151
B.4 Temporal evolution of transverse profile RMS at $x = 2$ mm.	151
B.5 Instantaneous back-illumination spray images of near-nozzle region for independent 134a spray events, both imaged 50 ms after start of injection.	152
B.6 Instantaneous back-illumination spray images of near-nozzle region for independent 227 spray events, both imaged 50 ms after start of injection.	152
B.7 Instantaneous back-illumination spray images of near-nozzle region for (top) 134a-E and (bottom) 227-E sprays, both imaged 50 ms after start of injection.	153
C.1 Phase contrast images for sump and nozzle flow 50 ms after start of injection of (top) HFA134a and (bottom) HFA134a/Ethanol.	158
C.2 Acoustic signals from sprays of (top) HFA134a and (bottom) HFA134a/Ethanol.	158
C.3 Short time segment of HFA134a spray acoustic signal and signal envelope $\pm a(t)$ (shown in gray).	159
C.4 Ensemble (top) mean, (middle) RMS and (bottom) unsteadiness of E with (solid line) HFA134a and (dashed line) HFA134a/Ethanol formula- tions.	159
C.5 Effect of filter width on U averaged over the interval 25-75 ms.	160
D.1 Side cutaway view of spray chamber, showing the MDI nozzle inside the mouthpiece, the airflow passage, and the connection of the unmetered canister to the nozzle. The red line represents the x-ray beam, and the blue lines represent omnidirectional x-ray fluorescence emitted from a line source where the beam intersects the spray.	165
D.2 Plan view of experiment. The red line represents the x-ray beam, the green line represents the 532 nm laser beam, and the blue lines represent omnidirectional x-ray fluorescence emitted from a line source where the beam intersects the spray.	166

D.3 30 ms injection at $x = 0, y = 5$ mm for HFA 134a propellant. The optical density (blue line, left vertical axis) is compared to the drug concentration (red markers, right vertical axis).	167
D.4 Several samples of optical density measurements (from photodiode) for 30 ms injection at $x = 0, y = 5$ mm for HFA 134a propellant.	167
D.5 30 ms injection at $x = 0, y = 5$ mm for two propellants. The markers represent the XFS data, and the lines represent the optical density. . . .	168
D.6 Axial scans along centreline ($x = 0$).	168
D.7 Radial scans across the spray for HFA 134a propellant.	169
D.8 Radial scan across the spray for HFA 227 propellant.	169
D.9 Transverse line-of-sight integrated profiles of time-integrated drug concentration (red) compared to time-average optical density (blue) for a HFA 227 spray at $y = 25$ mm from the nozzle. The error bars represent two standard deviations about the time-averaged value.	170
D.10 Examples of several typical projected density profiles (solid lines), and their corresponding radial density distributions computed by the inverse Abel transform (dashed lines).	170

List of Tables

1.1	Device and formulation variables that influence drug delivery from pressurised metered-dose inhalers (adapted from Newman (2005))	6
2.1	Imaging and processing parameters for particle image velocimetry measurements	23
2.2	Imaging parameters for laser extinction measurements	24
2.3	Placebo formulations used in the study	24
3.1	Absorption coefficients at 6 keV, liquid and vaporous densities and latent heats of vaporisation for constituents of pressurised metered dose inhaler canisters	35
3.2	Canister formulations, percentage by weight of HFA propellant (HFA), ethanol (EtOH) and Ipratropium Bromide (IPBr), and injection pressures .	36
3.3	Estimated nozzle densities for sprays and argon jet from M' measurements.	40
4.1	Canister and nozzle dimensions	49
4.2	Radiography dwell times, thermophysical and optical properties of formulations studied. Data presented at saturation conditions at 298.15 K .	50
4.3	Measured and predicted spray mass m	57
6.1	Initial conditions and modelling parameters	86
7.1	Diffusion parameters for HFA propellants, ethanol and air	107
7.2	Initial conditions and modelling parameters	108
B.1	Canister and nozzle dimensions	150
B.2	Canister formulations, composition by weight of propellant (HFA134a and HFA227) and ethanol (EtOH)	150
B.3	Back-illumination imaging parameters	150
C.1	Vapour pressures p_v and saturated liquid densities ρ_l of formulations studied	157

D.1 Several candidate drugs for x-ray fluorescence spectroscopy without a tracer, in order of increasing x-ray emission energy (decreasing wavelength, and increasing ease of detection).	165
D.2 Experimental parameters and calibration values.	166

Chapter 1

Introduction & Background

1.1 The pressurised metered-dose inhaler

Since its invention in 1956, the pressurised metered-dose inhaler (pMDI) has been medically and commercially successful in treating respiratory illnesses. The aerosol formed from the device is inhaled by the user, and deposits in the respiratory system predominantly by inertial impaction and sedimentation. For these deposition mechanisms, the particle and droplet size is a governing parameter (Carvalho, Peters, and Williams III 2011). Flash atomisation, which is the operative principle of the pMDI, is an effective way to produce fine sprays at low injection pressures (Sher, Bar-Kohany, and Rashkovan 2008).

The pMDI is the most widely used medical inhaler for the treatment of asthma and chronic obstructive pulmonary disease (COPD). These conditions are widespread and debilitating; depending on how it is defined, an estimated 65 million people suffer from moderate to severe COPD (World Health Organisation 2018). Both prevalence of and morbidity due to COPD are higher in poorer populations (Mannino and Buist 2007), where poverty is a significant barrier to accessing treatment.

The success of the pMDI has been achieved despite a comparatively low delivery efficiency (De Backer et al. 2010). Significant oropharyngeal deposition occurs with

many inhalers (Bell and Newman 2007). This results in not only wasted drug, but can also result in side effects (Roland, Bhalla, and Earis 2004), including oral candidiasis (Salzman and Pyszczynski 1988). The hoarseness and discomfort resulting from oropharyngeal deposition of inhaled corticosteroids, beyond being problems in their own right, can impact patient adherence to their treatment plans (Roland, Bhalla, and Earis 2004).

Improvements to pMDI design could reduce oropharyngeal deposition, and increase their efficiency and ease of use. These benefits could lead to the use of pMDIs in dose-critical applications, where oropharyngeal deposition and dose variability currently prohibit their use. Increasing the efficiency of pMDIs would reduce their cost, which is a significant factor driving their continued use over alternative inhaled drug delivery devices, such as dry powder inhalers and soft mist inhalers (Stein et al. 2014).

Propellants

Chlorofluorocarbon (CFC) refrigerants were used as propellants in pMDIs from 1956 until the 1980s. This state of affairs was disrupted by the regulatory response to ozone depletion caused by CFCs (Thiel 1996):

A big bombshell struck in 1987. CFC propellants were going to be banned! The Montreal Protocol was signed in September of 1987. Propellant, or rather refrigerant manufacturers, said that they would cease production before the turn of the century. Of course, they moved that date up to January 1996.

Although exemptions were included in the Montreal Protocol for pMDIs to continue using CFCs, it became apparent that their continued use would be impossible while other industries transitioned away from them (Thiel 1996):

[M]ajor CFC manufacturers said that they could not supply propellants

to us because it would be un-economic to do so. Their production plants were so large that one or two day's production would supply all of the needs for MDI's for a year.

For the refrigeration industry, replacement refrigerants were sought that had similar thermophysical properties to CFCs, such as their pressure-temperature relationships, and chemical compatibility with existing componentry (Cavallini 1996). Hydrofluoroalkanes (HFAs) quickly became the front runners for these applications. For pMDIs, the additional requirements of drug dispersion and/or solution meant that reformulation to use HFA propellants would not be straightforward. As described by Thiel (1996, emphasis mine):

After much cajoling of propellant manufacturers, we were able to obtain a sample bottle of HFA 134a in late spring of 1988. It was then that we discovered that our faithful old dispersing agents, that had served us so well for more than 30 years, would not work in HFA 134a. [...] Conversion would not be a simple matter. After some stumbling around, it became apparent that a patient-focused systems engineering approach—a new paradigm—for MDI development would be required to develop suitable MDI's with the new propellants. *It was just like starting over—almost as if MDI's had never been invented.* Iterations through drug specific formulation, valve and actuator design are now required in order to develop an MDI that truly meets the needs of the patient.

In this way, the Montreal Protocol acted as a catalyst for substantial research into pMDI development. This ‘new paradigm’ is perhaps best exemplified by the work of Clark (1991), who was the first to investigate the thermodynamics of the metered discharge process that occurs in pMDIs. The result of this investigation was a thermodynamic model of the metered discharge process. Clark (1991) also developed a correlation for the droplet size of pMDI sprays, as a function of the

pressure and quality in the expansion chamber. These combined to form the first phenomenological model of spray formation from pressurised metered-dose inhalers.

This history holds important lessons for pMDI developers today (Santayana 1905). Amendments have recently been made to the Montreal Protocol to include HFAs as banned substances, due to their high global warming potentials (GWP) (Sharadin 2018). Some automotive manufacturers have replaced HFAs with hydrofluoroolefins (HFOs); HFO1234yf is a straightforward replacement for HFA134a in refrigeration and air conditioning (Lee and Jung 2012). Its flammability (Minor and Spatz 2008) raises doubts about its suitability for pMDIs. If history is any guide, it is unlikely that pMDI manufacturers will be unaffected by the global shift away from HFAs.

Motivation

The tools available to pMDI designers today are largely unchanged from those of the past, and empirical approaches remain widespread. A lack of high-fidelity experimental data regarding the spray formation process is a contributing factor in the difficulty of adopting a phenomenological approach to pMDI development. Typical measurements are conducted far downstream of the atomising nozzle, often after particle formation has occurred. Considering the limited experimental data available for its development, it is not surprising that Clark's correlation is insufficient to account for the diversity of formulations and geometries currently in use.

This thesis concerns the application of synchrotron x-ray diagnostics to sprays from pressurised metered-dose inhalers. These techniques have the capacity to measure spray properties in regions previously inaccessible to the investigator. These new measurements, and insights gained from their application, are used to advance the phenomenological approach to pMDI development.

1.2 Development of pMDIs

The development of metered-dose inhalers has largely been achieved through the use of empirical correlations developed from experimental particle size data (Finlay 2001). These correlations take a parametric approach to particle size prediction, and determine a ‘best-fit’ relationship between device and formulation variables and the final particle size (Ivey et al. 2014). This approach treats the inhaler as a ‘black box’. Many of the functional relationships between inhaler and formulation variables and drug particle sizes for HFA-propelled pMDIs have been empirically determined, and the resulting correlations enable design within a limited window of operation (Finlay 2001). Much of this data is not in the public domain.

The parameter space associated with metered-dose inhalers makes the empirical approach difficult. The range of formulation and geometric variables available to the designer is enormous; some of these are outlined in Table 1.1 (adapted from Newman (2005)). A schematic of a typical pMDI is also shown in Figure 1.1. Parametric studies have shown that spray properties, including droplet sizes and spreading angles, are sensitive to even small changes in device variables, and that there are strong interactions between device variables (Smyth et al. 2006). This empirical approach may be insufficient to further increase the efficiency of pMDIs. Should pMDIs need to be reformulated to use low GWP propellants, reformulation will require the development of new correlations, likely at great expense.

Phenomenological models have greater flexibility than empirical correlations, and use a limited set of sub-models for phenomena to predict the atomisation process. Since the pioneering work of Clark (1991), thermodynamic modelling has been used by a number of researchers to predict spray dispersion (Dunbar, Watkins, and Miller 1997), spray velocities (Ju, Shrimpton, and Hearn 2010; Gavtash et al. 2017b) and droplet sizes (Gavtash et al. 2017a) of pMDI sprays. These models treat the pMDI as a series of connected control volumes, across which the conservation of mass and energy are applied. Some of the assumptions used to complete these mod-

Table 1.1: Device and formulation variables that influence drug delivery from pressurised metered-dose inhalers (adapted from Newman (2005)).

Component	Details
Container	Internal coating
Propellants	Type and mixture Vapour pressure Ambient temperature
Formulation	Suspension versus solution Presence of surfactants Presence of ethanol and other excipients Drug concentration Drug particle size in suspension formulations
Metering valve	Volume of metering valve Valve design Elastomers Time since last actuation Orientation during storage
Actuator	Expansion chamber size and shape Nozzle diameter Nozzle path length Mouthpiece length and shape Breath-actuation/breath coordination Spray velocity modification Spacer attachments

els are uninformed by experiment. These models are computationally inexpensive, permitting exploration of wide parameter spaces. Thermodynamic models can be combined with empirical correlations (Clark 1991) or atomisation models (Gavtash et al. 2017a) to form a phenomenological model that predicts droplet, and ultimately particle (Stein and Myrdal 2004), sizes. As the model output depends upon the assumptions used, experimental data plays an important role in both model development and assessment.

At the other extreme of complexity, computational fluid dynamics (CFD) can be used to simulate pMDI sprays. The real flows of pMDI sprays are inhomogeneous, three-dimensional and unsteady; unlike one-dimensional thermodynamic models, CFD may be able to account for some of these effects. The computational costs of CFD simulations have prevented their widespread adoption as tools for pMDI

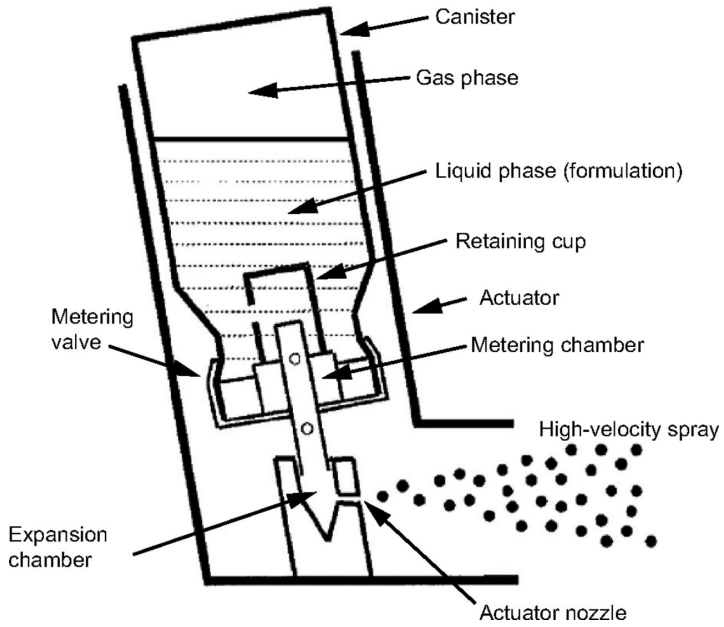


Figure 1.1: Schematic of typical pressurised metered-dose inhaler (reprinted from Newman (2005)).

development (Ruzycki, Javaheri, and Finlay 2013). CFD has been used to simulate the ex-nozzle spray and dispersion of CFC and HFA pMDIs with and without spacers (Kleinstreuer, Shi, and Zhang 2007), and showed that HFA pMDIs have lower oropharyngeal deposition than CFC pMDIs. Accurate specification of the boundary conditions for ex-nozzle pMDI spray simulations is challenging; Dunbar and Miller (1997) used a thermodynamic model to predict the nozzle exit conditions, and used CFD to model the ex-nozzle spray dispersion. No 3D CFD modeling of pMDI internal flows has yet been published. Methods have recently been developed for the simulation of internal nozzle flows of flashing cryogenic liquids (Lytras et al. 2018). Large-eddy simulations (LES) have also been performed for cavitating multicomponent flows (Duke et al. 2013). Although 3D CFD is not explored in this thesis, it will undoubtedly play an increasing role in pMDI development as computational power continues to increase.

Though the basic processes are well understood, much is unknown about the operative mechanisms of pressurised metered-dose inhalers. The performance prediction of flash atomisers, even with geometries and boundary conditions far sim-

pler than the pMDI, is difficult. This is especially true when the formulation to be atomised comprises multiple components (Bar-Kohany and Levy 2016), as it does in pMDIs. A solid theoretical foundation for the processes that lead from metered formulation to drug particle formation and deposition in the body is lacking, in large part due to the difficulties of obtaining experimental data associated with the spray. The flow has micrometre length scales, microsecond time scales, and is transient, turbulent, multiphase and multicomponent, with heat and mass transfer between phases. The absence of a detailed mechanistic understanding prevents a first-principles engineering approach to pMDI design.

1.3 Experimental measurement of pMDI sprays

Particle sizing measurements

Cascade impactor particle size measurements are widely used for the characterisation of pMDI sprays, and are a standardised procedure for *in vitro* testing of pMDIs (U.S. Pharmacopoeia 2018). Cascade impactor measurements partition the delivered dose into stages that are indicative of different regions of the respiratory system. The technique provides no temporal or spatial resolution; the entire spray is averaged into a single measurement. Other issues include particle ‘bounce’, regional segregation on impactor plates, and calibration (Mitchell and Nagel 2003). Cascade impactor testing is also time-consuming (De Boer et al. 2002). Although cascade impactor measurements provide a measure of the particle size distribution, arguably the spray property most relevant to deposition in the respiratory system, alternative measurement techniques are sought that provide spatial and temporal resolution, for informing and validating models.

Visible-light diagnostics

Visible-light diagnostics have been established as useful tools for the measurement of sprays from pMDIs (Dunbar, Watkins, and Miller 1997). Optical imaging (Chigier 1991) has been used (Dunbar, Watkins, and Miller 1997; Versteeg, Hargrave, and Kirby 2006) to visualise dynamic features of the spray boundary in the near-nozzle region, and the spray in the dilute region downstream. Laser diagnostics, such as laser diffraction and phase-doppler anemometry (PDA) (Myatt et al. 2015; Dunbar, Watkins, and Miller 1997), have also been used to measure droplet velocities and sizes in sprays from metered-dose inhalers.

These diagnostics are restricted in their application to dilute spray regions. The spray is optically dense in the near-nozzle region (Finlay 2001), and becomes dilute only after a large number of nozzle diameters. For laser diagnostics, this high optical density creates measurement issues due to beam steering and multiple scatter (Kastengren and Powell 2014). Dunbar, Watkins, and Miller (1997) found that PDA measurements of propellant-only sprays closer than 10 mm from the nozzle exit ($x/D = 20$) had exceedingly high concentrations, which led to data rejection. Similarly, Myatt et al. (2015) performed PDA measurements of propellant/ethanol mixtures 15 mm from the nozzle ($x/D = 30$) for this reason, and to avoid multiple scatter. For optical imaging, the near-nozzle spray cannot be observed in detail; the observable spray feature is the spray boundary. Imaging systems enable the effects of device and environment variables (such as the nozzle diameter and the ambient pressure) on this spray boundary to be measured.

Further downstream, where the spray is dilute, optical imaging and laser extinction can be used to measure the optical density, and to obtain instantaneous snapshots of the spray structure. Planar Mie scattering can also be used to perform particle image velocimetry (PIV) (Crosland, Johnson, and Matida 2009). Although the near-nozzle region of the pMDI is challenging to probe, optical diagnostics remain powerful tools for the measurement of spray properties. In the present work,

visible-light diagnostics are used to probe dilute spray regions, allowing the investigation of dynamic spray features that are unattainable with point measurements. These investigations are reported in Chapter 2 and Appendix B.

Synchrotron x-ray diagnostics

To overcome the problems associated with visible-light diagnostics in dense spray regions, fuel spray researchers developed synchrotron x-ray diagnostics (Kastengren and Powell 2014). There is established precedent of x-rays in multiphase flow measurement, notably by Reocreux (1976) who non-intrusively measured the void fraction in a flashing pipe flow. The low fluxes of laboratory x-ray sources prohibit their use in applications where short exposure times are required. For applications where a monochromatic beam is advantageous, monochromators further reduce the x-ray flux, meaning that a very high flux light source is required (Halls et al. 2017). Synchrotron x-ray sources have photonic fluxes orders of magnitude greater than laboratory sources (Kastengren et al. 2012), allowing instantaneous measurements of transient phenomena in fuel injection (MacPhee et al. 2002).

X-rays have high penetrating power, low refraction and scatter, making them well-suited for sprays, which are characterised by steep refractive index gradients and high optical depths. These diagnostics provide spray measurements in regions where optical diagnostics fail (MacPhee et al. 2002), including inside the nozzle (Duke et al. 2014). Importantly, these measurements paint an entirely different picture of the spray structure to that which may be interpreted from schlieren and back-illumination imaging; quantitative mass measurements show that fuel sprays, which appear uniformly dark in conventional spray imaging (Naber and Siebers 1996), comprise a narrow spray core surrounded by a low density droplet cloud (MacPhee et al. 2002; Pickett et al. 2014).

Synchrotron x-ray diagnostics have matured into an established range of techniques for spray measurement (Lefebvre and McDonell 2017). A number of different

techniques are available, and each provides a distinct piece of information regarding the spray under investigation. For pMDIs, in which much remains unknown about the operative mechanisms and the spray's initial formation, synchrotron x-ray techniques are a promising tool that may be used to investigate these devices. Data from x-ray diagnostics are capable of providing experimental validation of model outputs, and of guiding the assumptions used in the development of spray models. The combination of high-fidelity experimental data and new phenomenological modelling approaches may assist in the development of more efficient, more consistent and easier-to-use inhalers, as will be required for the pMDI to remain a preferred treatment option. These synchrotron x-ray techniques are outlined below.

Quantitative x-ray radiography

Quantitative x-ray radiography uses the attenuation of an x-ray beam to probe dense sprays. Scattering, which occurs with visible light and small droplets, is negligible at typical x-ray wavelengths (Kastengren and Powell 2014), meaning that the attenuation of the beam is almost entirely due to absorption. This allows the spray's projected mass, or path-integrated spray density, to be measured.

The reduction in intensity of an x-ray beam as it passes through a spray is a function of the spray's composition, and the length of spray along the beam path. This relationship is described by the Beer-Lambert law, which is a solution to the differential equation of light absorption (Kastengren and Powell 2014). The projected mass M ($\mu\text{g mm}^{-2}$) is obtained from the transmission $\frac{I}{I_0}$:

$$M = -\frac{1}{\mu} \log_e \left(\frac{I}{I_0} \right) \quad (1.1)$$

where μ is the absorption coefficient ($\text{mm}^2 \mu\text{g}^{-1}$), I is the photonic flux (photons/s) and I_0 is the photonic flux in the absence of spray. The projected mass is equivalent to a path-integrated density along the beam. If a monochromatic beam is used, the absorption coefficient is a function only of the compound being sprayed, the photon energy of the x-ray beam, and the mass of ambient gas displaced by the spray. In

non-vaporising sprays, these properties are easily obtained; additional uncertainty arises for vaporising sprays.

Radiography can be performed in several ways for sprays. When a monochromatic beam is used, it is typically focused to a small spot, allowing a spatially-resolved measurement of the projected mass, which is determined from the intensity drop as measured by a single photodiode. The beam and detector are then raster-scanned through the spray, with several repeat sprays at each point (Kastengren et al. 2012). The resulting time series can be combined to provide an ensemble-averaged time-resolved representation of the spray projected mass.

Quantitative x-ray radiography allows dense sprays to be compared in terms of physically meaningful parameters. For the near-nozzle region, this is in contrast to visible light imaging, in which the spray is defined by an image boundary that is a function of both the imaging system and image processing used (Arai 2017). In an investigation by Pickett et al. (2014), the near-nozzle region ($x/D = 0.5$) of fuel sprays was probed with radiography and back-illumination imaging. While little information could be obtained from optical imaging in this region, radiography was capable of quantifying the projected mass with high spatial and temporal resolutions. Radiography was then performed tomographically to obtain the time-variant liquid volume fraction across the spray cross-section.

The nozzle exit sets the boundary condition for the downstream spray development. For pMDI sprays, this plays a large role in the deposition within the respiratory system. The ability to probe dense spray regions is of great value in understanding how the spray forms, and it is for this reason that radiography is used in the present study. The work resulting from this is presented in Chapters 3 and 4.

The ensemble averaging used and the point measurement approach mean that the projected mass field is determined from a large number of separate, uncorrelated sprays. The instantaneous spray structure, which is not apparent in a time-variant

ensemble mean, may have important effects on the spray development. These instantaneous spray structures can be revealed with phase contrast imaging.

X-ray phase contrast imaging

X-ray phase contrast imaging is a powerful visualisation technique that has been extensively used in a range of fields (Snigirev et al. 1995). For sprays, phase contrast allows full-field images of the structure of the gas-liquid interface to be obtained. The high penetration power of x-rays means that, for some injectors, images can be obtained inside the nozzle, which is inaccessible to optical diagnostics. Transparent inhaler analogues permit the outer layer of the gas-liquid interface to be visualised with visible light; the high penetration power of x-rays allows additional details in the interior to be observed.

Phase contrast arises from diffraction occurring at refractive index gradients (Willmott 2011). When the imaging sensor is placed downstream of the object under investigation, diffraction effects propagate and give rise to fringes. The fringe pattern obtained is a function of the energy of incident radiation, the spot-size of the x-ray source and the sample-to-image plane distance (Kastengren and Powell 2014). The images obtained combine phase contrast and absorption contrast (radiography) in a single image; at higher beam energies, phase contrast dominates, while at lower beam energies absorption dominates. For multiphase flows, in which liquid-vapour (and liquid-gas) interfaces give rise to refractive index gradients, phase contrast is a technique capable of imaging the flow structure.

Advantages of synchrotron x-ray phase contrast imaging include the short time resolution obtainable. Motion blur is a common problem in visualising high-speed fluid flows. A simple criterion (Chigier 1991) for the permissible exposure time to image a feature of characteristic length L moving at a velocity U with a permissible motion blur, expressed as a relative displacement k ($k = \frac{\Delta L}{L}$) is:

$$t_{\text{exp}} = \frac{kL}{U} \quad (1.2)$$

If a k value of 0.1 is used, a $10\text{ }\mu\text{m}$ feature travelling at 10 m s^{-1} would require an exposure time of 100 ns or less to be imaged without motion blur. Synchrotron sources operating in ‘hybrid singlet’ mode enable exposure times of 150 ps full-width at half-maximum (FWHM) (Moon et al. 2016). Using this light source, a feature with $L = 12\text{ }\mu\text{m}$ moving at the re-entry speed of a space shuttle ($U \approx 7500\text{ m s}^{-1}$) will pass this motion blur criterion.

The technique is limited in its ability to provide information in regions of very high feature density along the beam axis, due to the interaction of diffraction patterns produced (Linne 2012). However, this shortcoming is shared by all current line-of-sight optical techniques (Kastengren and Powell 2014), and images are capable of being interpreted with ease when the interfaces occurring along the beam path are relatively few. Phase contrast has been used as a method for the visualisation of internal and near-nozzle flows in cavitating (Duke et al. 2014) and flashing (Jeon et al. 2018) sprays.

For pressurised metered-dose inhalers, x-ray phase contrast imaging is capable of providing visualisations of liquid/vapour structure in regions where imaging with visible light is not possible. The internal flows of pMDIs, which are known to comprise a complex multiphase structure (Versteeg, Hargrave, and Kirby 2006), can be imaged at high-speed inside real pMDIs, without the need for transparent analogues. Furthermore, the high penetration power of x-rays permits visualisation of the entire flow structure along the beam path, rather than the outermost surface.

Phase contrast imaging complements quantitative radiography well, as it provides snapshots of the instantaneous flow structure rather than the ensemble-average. For this reason, phase contrast imaging is used in the present investigation. Images of the internal flows of propellant-only and ethanol-containing pMDIs are provided in Chapters 4 and 5.

X-ray fluorescence spectroscopy

X-ray fluorescence spectroscopy provides a method for direct concentration measurement (Kastengren and Powell 2014). For pMDI sprays containing drugs that have elements with suitable emission edges in the soft x-ray range, x-ray fluorescence allows the drug concentration to be measured with high temporal and spatial resolution.

The basic working principles of x-ray fluorescence spectroscopy are described here. Sufficiently energetic photons from an x-ray source can remove electrons from a sample. As higher shell electrons transition to fill the hole, a process on the order of 100 fs (Willmott 2011), a fluorescence photon may be released. The characteristic energies of these photons depend on the levels of the transition; the energy differences between electron shells in a particular element are distinct, giving rise to narrowband fluorescence emission (Willmott 2011). In this way, peaks in the fluorescence emission spectrum can be measured to determine the concentration of a target species in the sample. For sufficiently energetic electron relaxations, the fluorescence photon is itself an x-ray, meaning it can penetrate the sample. These high energy x-rays can be detected with photon counters, allowing the wavelength to be determined on a per-photon basis without filters (Lechner et al. 2001). With either a calibration or a first-principles approach, the fluorescence signal can be used to determine the concentration within the sample.

Fluorescence and spectroscopy both have established precedent in fluid mechanics research. Laser-induced fluorescence is used for the investigation of scalar transport in single-phase turbulent flows (Tokumaru and Dimotakis 1995), where fluorescent dye is used to track mixing. X-ray fluorescence has similarly been used to quantitatively measure mixing in impinging jet atomisers (Halls, Meyer, and Kastengren 2015), a complex multiphase flow field.

Typical measurements of the drug distribution in pMDI sprays with cascade impactors use particle filtration devices far downstream of the atomising nozzle,

and lack spatial and temporal resolution. Laser diagnostics provide both spatial and temporal resolution of the spray, however the information provided is typically limited to the geometry of droplets, and no information on composition is obtained. X-ray fluorescence provides a method for detecting the drug concentration in the spray directly, irrespective of its state. In this thesis, x-ray fluorescence spectroscopy is used to directly detect the concentration of a bromine-containing drug in sprays from a pMDI analogue. This work is reported in Appendix D.

1.4 Phenomenological modelling of pMDIs

Phenomenological modelling can be used for the prediction of pMDI performance. These models typically incorporate a thermodynamic model for the internal flow, mass flow rate models, and atomisation models. Until very recently (Gavtash et al. 2017a), Clark's correlation (Clark 1991) was the main method by which the droplet size in pMDI sprays could be predicted; this correlation was developed with aerodynamic particle size data taken far downstream, and extrapolated to the nozzle. Ideal measurements for model validation would be obtained in those regions where the thermodynamic model predicts: inside or at the atomising nozzle exit. This eliminates the need to extrapolate the experimental data to the model, which introduces a source of uncertainty. The measurements obtained with synchrotron x-ray diagnostics reported here are used in two ways to advance thermodynamic modelling of pMDIs. These are described below.

Mass flow rate modelling

pMDI thermodynamic models incorporate multiphase mass flow rate models. These models predict different conditions at the nozzle exit depending upon the flow phenomenology between the reservoir and the nozzle (Gavtash et al. 2017b). For flashing flows, these effects include slip and thermal non-equilibrium between phases

(Brennen 2005). Different spray properties are predicted depending on the extent of thermal non-equilibrium between liquid and vapour phases (Downar-Zapolski et al. 1996). Restricting our attention to homogeneous flow models, in which the liquid and vapour phases are treated as sufficiently mixed so as to preclude any relative motion, this non-equilibrium is represented at its extremes by the homogeneous equilibrium model (HEM), where both liquid and vapour are in thermal equilibrium, and the homogeneous frozen model (HFM), in which the liquid is metastable and does not undergo phase change during depressurisation. Misty or dense bubbly flows can approach homogeneity; dispersed phase relaxation times become extremely small for small dispersed phase elements (Brennen 2005). Comparison with experimental data is necessary if these mass flow rate models are to be assessed in terms of their predictive power for pMDIs. Gavtash et al. (2017b) used turbulent jet theory to extrapolate PDA droplet velocity measurements taken in the dilute spray region (Myatt et al. 2015) to the near-nozzle region, allowing them to be compared with predictions of pMDI thermodynamic models. In this comparison, the HFM was found to more closely agree with experiment than the HEM. Gavtash et al. (2017b) also used PDA measurements of droplet velocity in the near-nozzle region (Wigley, Versteeg, and Hodson 2002); potential issues with beam steering and multiple scatter raise doubts as to the validity of the data. The extent of vaporisation prior to the nozzle exit affects the atomisation and dispersion of formulation in pMDI sprays (Gavtash et al. 2017a), and determining the influence of formulation and geometric parameters on these properties is of practical importance.

X-ray radiography measurements taken in the near-nozzle region are a high fidelity observable which can be compared with model predictions, providing additional assessment of the predictive power of homogeneous flow models for pMDI sprays. For this reason, a thermodynamic model of propellant-only internal flows was developed in this research program, and was compared with the radiography measurements reported in Chapter 4. This model and comparison are the subjects

of Chapter 6.

Non-equilibrium internal flow

Previous thermodynamic modelling approaches permit the prediction of nozzle exit conditions of pressurised metered-dose inhalers. However, the internal flow structure is assumed to be homogeneous, contrary to experimental observations in real pMDIs (Chapters 4 & 5). To investigate the role of the internal structure on the flow rates from pMDIs, the prior art in thermodynamic modelling of pMDIs is insufficient. Prior models (Dunbar and Miller 1997; Ju, Shrimpton, and Hearn 2010; Gavtash et al. 2017b) assumed equilibrium states in the expansion chamber, as determined from a pair of enthalpy-mass state variables. This assumes that conditions are at all times saturated for both liquid and vapour, meaning that vaporisation and interphase heat transfer instantaneously restore the system to thermodynamic equilibrium after removal of mass. Non-equilibrium effects in the expansion chamber were considered for the propellant-only case by Clark (1991). No attention has yet been given to non-equilibrium conditions with multicomponent formulations. To incorporate these effects, a non-equilibrium thermodynamic model was developed and compared with the estimated near-nozzle density from experiment. This model and comparison are presented in Chapter 7.

1.5 Summary

This thesis concerns the application of synchrotron-based x-ray diagnostics to the investigation of sprays from pressurised metered-dose inhalers. These techniques provide insights and quantitative measurements that have the potential to improve our capacity to develop treatments that are affordable and effective. With these x-ray techniques, we may be able to get away from the empirical approach and take a mechanistic, phenomenological approach to pMDI development.

Chapter 2

Pressurised metered-dose inhaler spray structure

2.1 Introductory statement

As will be demonstrated in later chapters, the internal flow structure of metered-dose inhalers is a strong determinant of the external spray characteristics. Without x-ray diagnostics or a suitable transparent analogue, the experimentalist is restricted to investigating the external spray structure, and must infer what they can regarding the upstream flow state.

This chapter is concerned with the application of visible-light techniques to the spray formation in pMDIs. A number of visualisation experiments (Dunbar, Watkins, and Miller 1997; Versteeg, Hargrave, and Kirby 2006; Ju et al. 2012) noted that the structure of pMDI sprays is variable, and argue that the spray is highly unsteady. This variability had not been quantitatively investigated, nor had it been investigated with ethanol-containing formulations. Spray unsteadiness is associated with intermittent coarse atomisation (Jedelsky and Jicha 2008) which, in the case of the pMDI, may contribute to oropharyngeal deposition.

In this work, laser extinction was used to measure spray optical depth (here

termed ‘effective mass’). Due to multiple scatter effects, the produced data is not proportional to the spray projected mass, accordingly a distinction is drawn between mass and optical depth. The technique was applied to sprays from an unmetered ‘electronic metering inhaler’, a device developed for application to x-ray spray measurements (Chapter 3 and Appendix D). This provided a spray that was free from metering chamber transients, and was nominally steady-state after a start-of-injection transient.

In addition, particle image velocimetry had been applied by Crosland, Johnson, and Matida (2009) to sprays from pMDIs. Previous PIV investigations of pMDI sprays (Crosland, Johnson, and Matida 2009) reported their results in terms of empirical spray profiles for different inhalers. In the present work, PIV was performed on several formulations sprayed from identical inhaler bodies. This was intended to assess whether spray profiles are functions of formulation variables. The spray velocity field was then examined through the lens of turbulent jet theory (Abramovich 1963). Key to this understanding is that, after sufficient distance from the nozzle outlet, turbulent jets spread in a manner that allows their velocity profiles to be collapsed in terms of local parameters. The application of turbulent jet theory to sprays was thought to have some relevance, as a substantial mass of vapour is discharged in pMDI sprays.

Particle image velocimetry is typically applied to flows of a single continuous phase. A dispersed phase is introduced to track the motion of the continuous phase (Raffel et al. 2013). A key distinction between these tracer-embedded flows and sprays is the relationship between the velocity of the continuous phase and the dispersed phase, nominally considered in terms of the Stokes number (Mitchell, Honnery, and Soria 2011). Sprays are polydisperse, with droplets of different sizes travelling at different velocities. This raises questions about the applicability of particle image velocimetry, where windowed cross-correlation of Mie scatter images is used to determine the velocity of a continuous phase, for spray measurement.

Vapour is discharged in sprays from pMDIs (Buchmann et al. 2014), and the small droplets are expected to have minimal slip with this continuous vapour phase. As such, it is likely that droplet size and velocity are correlated in pMDI sprays. If the droplet size and velocity are uncorrelated, the velocity estimated by PIV will be the mean droplet velocity. If not, the velocity estimated by PIV will be biased towards large droplets, due to their greater contribution to the cross-correlation function. In spite of these limitations to its application, PIV provides a velocity estimate of sprays that have some relevance (Ikeda, Yamada, and Nakajima 2000), due to the role of inertial impaction in unrespirable mass in pMDIs (Gabrio, Stein, and Velasquez 1999).

The work is presented in the form of a conference paper presented at the *Ninth International Symposium on Turbulence and Shear Flow Phenomena*¹.

¹ “The series of biennial TSFP Symposia is the principal venue for reporting and disseminating recent and ongoing research on turbulence and shear flow phenomena.”

PRESSURISED METERED-DOSE INHALER SPRAY STRUCTURE

Nicholas Mason-Smith, Daniel Edgington-Mitchell & Damon Honnery

Laboratory for Turbulence Research in Aerospace and Combustion

Department of Mechanical and Aerospace Engineering

Monash University

Wellington Road, Clayton 3800 VIC Australia

Nicholas.Mason-Smith@Monash.edu

Daniel Duke

Energy Systems Division

Argonne National Laboratory

Lemont IL USA 60439

Julio Soria

Laboratory For Turbulence Research in Aerospace and Combustion,

Department of Mechanical and Aerospace Engineering, Monash University, Clayton 3800, AUSTRALIA

Department of Aeronautical Engineering, King Abdulaziz University,

Jeddah 21589, Kingdom of Saudi Arabia

ABSTRACT

Sprays with and without ethanol issuing from a pressurised metered-dose inhalers (pMDI) are studied with Mie scattering, particle image velocimetry and laser extinction. Preliminary PIV measurements in the sagittal plane show that axial velocities are lower immediately downstream of the mouthpiece for ethanol-containing sprays at 50 ms after the start of actuation; further downstream, the velocity appears equal for both formulations. Vertical profiles of axial velocity collapse to a single curve when non-dimensionalised by peak velocity and distance from the atomising nozzle, suggesting that outside the mouthpiece the mean spray behaves like a self-similar turbulent jet. High turbulence intensities for the axial and vertical velocity fluctuations are measured, and found to decay with increasing axial distance from the nozzle. Laser extinction measurements downstream of the mouthpiece reveal an intermittent high amplitude fluctuation in spray density, an observation consistent with conjectures from prior studies of pMDIs with less temporal resolution. Propellant-only sprays are found to have higher fluctuations in absorption, indicative of a higher amplitude pulsation taking place in the nozzle.

BACKGROUND

The pressurised metered-dose inhaler is an extensively used drug delivery device and is predominantly used for the treatment and management of respiratory diseases. In a pMDI canister, a drug is kept in solution or suspension in a propellant liquid, often with a cosolvent to aid stability.

When the canister is depressed, the liquid suspension or solution is forced out of the canister by the vapour pressure of the propellant and is expelled from an atomising nozzle, forming a spray that is inspired by the user. Evaporation of liquid propellant and cosolvent as the droplets convect downstream results in the formation of an aerosol of drug particles, which are intended to deposit in the lung. Efficiency of pMDIs is typically low, with the majority of the delivered drug depositing in the mouth of the user. This is the result of droplets with large aerodynamic diameters and high initial velocities, which cannot trace the inspired flow into the lung of the user. Ivey *et al.* (2014b) reviews research into the effects of device and formulation parameters on pMDI performance. Ethanol is a cosolvent typically used to improve drug solubility in hydrofluoralkane propellants, however its effect on atomisation and deposition can be significant and detrimental to efficient delivery (Stein & Myrdal, 2006).

Sprays from pMDIs have been observed to have a pulsatile behaviour, with large variation of ejected spray density and cone angle at a frequency of around 1000 Hz. This frequency has been estimated in prior studies by observing the distance between large pulsatile bursts in the spray (Ju *et al.*, 2012) or from high-speed visualisations (Dunbar *et al.*, 1997; Versteeg *et al.*, 2006). Visualisations of a transparent expansion chamber showed the formation of large bubbles, with the pulsation attributed to their formation and collapse (Versteeg *et al.*, 2006). However, only a single formulation was tested, and the expansion chamber and nozzle used were scaled up from typical pMDI geometries.

Prior studies have attempted to characterise the ve-

locity field of the spray with particle image velocimetry (Crosland *et al.*, 2009; Harang, 2013) amongst other techniques, including phase doppler anemometry (Dunbar *et al.*, 1997). These studies noted the high value of turbulent fluctuations, with estimates of peak turbulence intensity greater than 50% (Harang, 2013).

We present measurements using particle image velocimetry to characterise the velocity field for ethanol-containing and ethanol-free formulations. Time-resolved laser extinction measurements are used to explore pulsatile spray behaviour.

EXPERIMENTAL METHODOLOGY

Particle image velocimetry measurements were performed with a double shutter camera, dual cavity pulsed laser and a simple Mie scattering arrangement, as shown in Figure 1. Velocity measurements were performed by cross correlating images of the droplets issued from the pMDI, with no additional tracer particles added. This introduces a difficulty in estimating velocity in regions where turbulent fluctuations give rise to intermittent spray presence. For this reason, velocity measurements are only shown for regions where the spray is consistently present. Experimental and processing parameters are summarised in Table 1. For the cross-correlation, errant vectors were determined using a maximum displacement difference of 5 pixels between windows, and were replaced by interpolation. Images were preprocessed with a dynamic histogram clipping technique, removing the highest 2.5% of pixels.

Table 1. Imaging and processing parameters for particle image velocimetry measurements.

Parameter	Value
Camera	PCO 4000
Laser	PILS Nd:YAG
Interframe time (μs)	10
Magnification ($\frac{\text{px}}{\text{mm}}$)	52
Field of view (mm x mm)	77 x 51
Aperture	f2.8, f4
Focal length (mm)	105
Window size (px x px)	48 x 48
Window overlap (px)	16

Laser extinction was used to obtain time-resolved information about fluctuations in spray density. Where multiple species are present, the intensity drop is the product of the contributions from each component. An estimation of the absorption coefficient is made difficult by the change in concentration of the propellant and ethanol as evaporation occurs at different rates. The laser extinction results are presented as an ‘effective mass’ M , the non-dimensional ratio of mass per unit area $\frac{d^2m}{dx dy} \left(\frac{\text{kg}}{\text{m}^2} \right)$ normalised by the absorp-

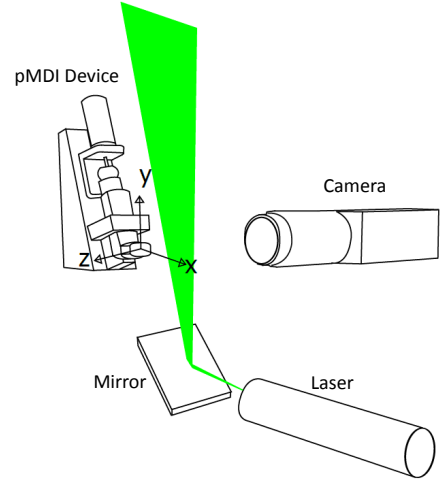


Figure 1. Schematic of the experimental apparatus for Mie scattering, consisting of PILS laser, 45 degree mirror, automated pMDI device and PCO 4000 camera. Coordinate system shown is used for the PIV and laser extinction measurements.

tion coefficient $\mu \left(\frac{\text{m}^2}{\text{kg}} \right)$:

$$M = \frac{1}{\mu} \cdot \left(\frac{d^2m}{dx dy} \right) = -\log_e \left(\frac{I}{I_0} \right) \quad (1)$$

Details of the data acquisition parameters are summarised in Table 2. The laser sheet was aligned with the centreline of the spray axis. A region of interest of 360 by 12 pixels in the axial and vertical directions was used. A reference intensity I_0 image was obtained by ensemble averaging 100 images in which no spray was present. After normalising the obtained image sequence by the reference intensity image, the sequence was binned in the vertical direction to provide a line measurement of extinction. Uncertainty on absorption measurements in optically dense sprays is considered to be comparatively high, as much of the attenuation of the incident light is a result of scatter and refraction from phase boundaries rather than direct absorption (Kastengren & Powell, 2014). For the present results, laser extinction is used as a visualisation technique and not as a tool for measuring spray mass.

Four placebo formulations were used for the measurements, two of which contained only propellant and two of which contained a mixture of propellant and ethanol (EtOH), which is a common cosolvent used in commercial pMDIs. Propellant-only canisters consisted of either 100% HFA134a or HFA227. Effects due to the presence of the drug are considered negligible for this study. Table 3 details the formulations used, their vapour pressures p_v and liquid densities ρ_l in the canisters. The vapour pressures presented for the ethanol-containing formulations are molar-weighted averages of the constituent vapour pressures (Ivey *et al.*, 2014a).

Two spray devices were used for measurements. A linear solenoid-driven pMDI actuator was used for PIV

Table 2. Imaging parameters for laser extinction measurements.

Parameter	Value
Camera	MotionPro X3
Exposure time (μs)	10
Frame rate (FPS)	40,000
Magnification ($\frac{\text{px}}{\text{mm}}$)	28.9
Field of view (mm x mm)	12.5 x 0.4
Aperture	f2.8
Focal length (mm)	105
Radiometric resolution	8-bit

Table 3. Placebo formulations used in the study.

Formulation (w/w)	p_v ($\text{Pa} \times 10^5$)	ρ_l ($\frac{\text{kg}}{\text{m}^3}$)
HFA 134a	5.76	1206
HFA 227	3.90	1408
HFA 134a 85% EtOH 15%	4.16	1116
HFA 227 85% EtOH 15%	2.39	1258

measurements, and has previously been used to study the spray plume from a pMDI using schlieren (Buchmann *et al.*, 2014). Canisters were installed in a Bespak inhaler body, which had a nozzle diameter of 0.3 mm and a distance of 20 mm from the nozzle to the end of the mouthpiece. The inhaler was actuated by an externally triggered linear solenoid, and was held at a 15 degree angle to the vertical to orient the mouthpiece in the horizontal plane. An electronic metering inhaler (EMI) (Lewis, 2013) with expansion chamber attachment was used for laser extinction measurements. The EMI uses an unmetered canister capable of continuous operation and an electric solenoid capable of dispensing microlitre liquid quantities. The expansion chamber attachment was used with a Bespak 0.3 mm diameter nozzle. No coflow was used for the presented measurements.

VELOCITY MEASUREMENTS

Particle image velocimetry measurements were obtained for each of the canisters, however for brevity we present results for canisters with and without ethanol, for a single propellant. The ensemble average velocity magnitude fields for HFA134a canisters at 50 ms after actuation are shown in Figure 2.

Several features are observable for the mean velocity magnitude field. The spray is inclined to the horizontal axis. Prior studies (Buchmann *et al.*, 2014) have shown that a coflow directs the spray downward; in the absence of a coflow, we find the spray from the Bespak inhaler to be directed upward at an angle of 5 degrees. The velocity magnitudes are higher for the propellant-only canisters, which is

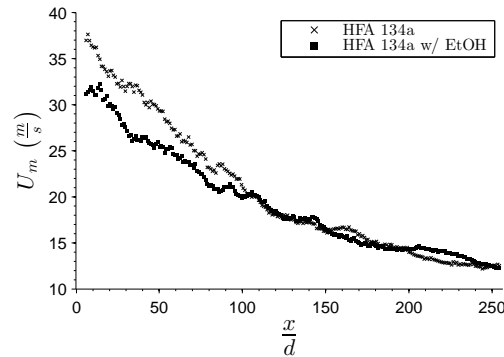


Figure 3. Maximum mean axial velocity against axial distance for the HFA 134a spray, 50 ms after actuation.

expected to be a result of the higher vapour pressure.

For the presented velocity fields, the maximum mean axial velocity is obtained for each axial location of the velocity field, and is shown in Figure 3. U_m appears to follow a relation $U_m \propto \frac{c}{x+a}$ for some constants c and a , which is consistent with the self-similar turbulent jet described by Abramovich (1963). Notably, these values are approximately a factor of three higher than those obtained at 50 ms after actuation with propellant-only HFA 134a sprays by Harang (2013), however this may be the result of different apparatus delays, resulting in measurements being taken at different times in the spray.

To test whether the velocity field outside the mouthpiece is self-similar, vertical profiles of axial velocity U are normalised by the maximum axial velocity U_m for each x . Self-similar velocity profiles collapse with a characteristic width of the spray, typically the half-width or full-width half-maximum (Rajaratnam, 1976), which is proportional to the axial distance from the nozzle if a constant cone angle θ is assumed. Figure 4 shows the velocity profiles for the two formulations, normalised by U_m and the axial distance $(x+a)$ where $a = 20\text{mm}$ which is the distance from the atomising nozzle to the mouthpiece exit. The horizontal axis for the velocity profiles is $(y-b)$, where b is the vertical location of U_m .

The vertical profiles of velocity, when appropriately non-dimensionalised, collapse onto each other, suggesting that the spray behaves like a self-similar turbulent jet in the region studied. Non-dimensional profiles are similar for the ethanol-containing and ethanol-free cases, suggesting that mean spreading rates are comparable with and without ethanol.

A further property of a self-similar turbulent jets is a constant turbulence intensity along the line of U_m , such as that found over the range $(x/d) = 50-97.5$ for a Reynolds number on the order of 10^5 by Wygnanski & Fiedler (1968). Axial and transverse turbulence intensities for the spray from the ethanol-containing canister are shown in Figure 5. As x/d increases, u'_{rms}/U_m has a gradual decaying trend while v'_{rms}/U_m increases, suggesting that the spray does not satisfy this criterion. This trend towards lower turbulence intensity may be an artifact of the measurement technique. Larger droplets have a disproportionate influence on the cross-correlation used in PIV, and it is possible that further from the mouthpiece where the finely atomised droplets have evaporated, comparatively large droplets remain and the velocity measurement is biased towards droplets with

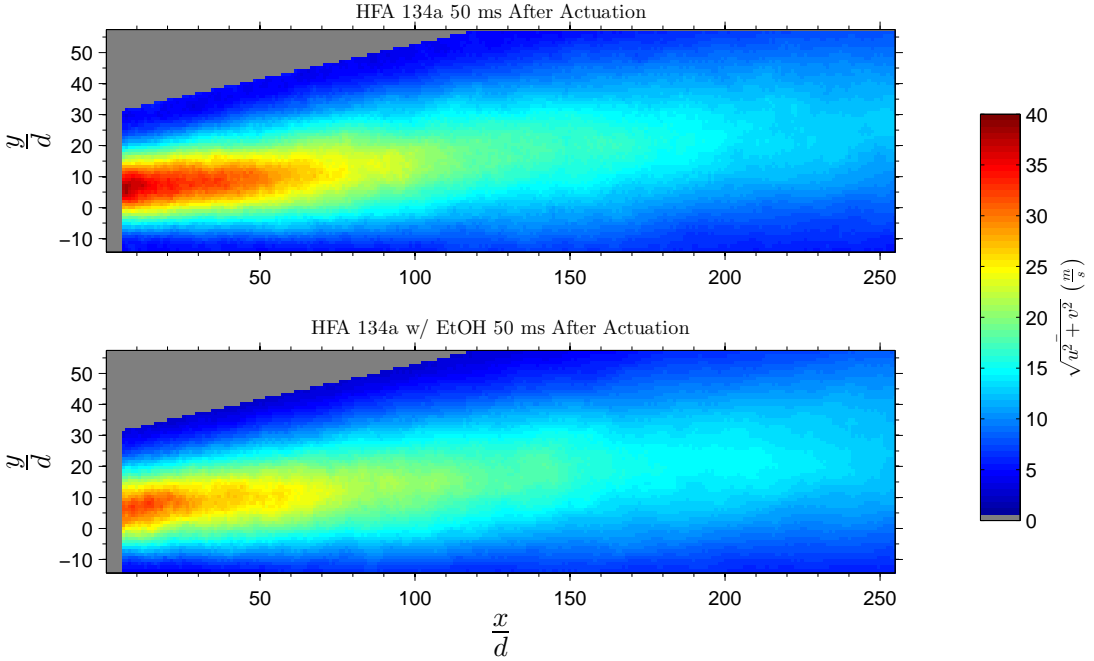


Figure 2. Ensemble average velocity magnitude field 50 ms after actuation for HFA 134a (top) and HFA 134a with ethanol (bottom) sprays. Mean fields are generated from 121 velocity fields. Masking is applied in regions where the spray is inconsistent (shown in gray).

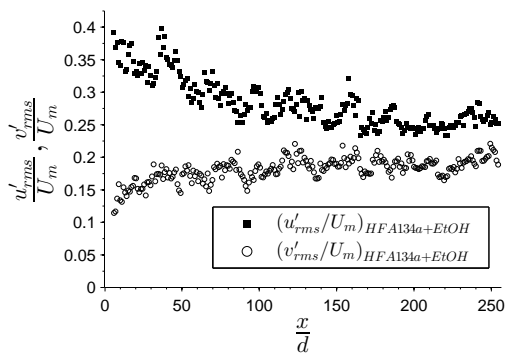


Figure 5. Axial and vertical turbulence intensities for HFA 134a & ethanol spray, downstream of the mouthpiece at 50 ms after actuation.

high inertia and poor flow tracing ability.

ABSORPTION MEASUREMENTS

Mean absorption $x - t$ plots were generated from 20 separate spray events for each formulation presented. As there appeared to be high frequency fluctuations, a centreline mean absorption $\bar{M}(t)$ was generated by applying a simple moving average with a kernel width of 2.5 ms, or 100 samples, to the mean effective mass at the centre of the region depicted. For each formulation, effective masses M are normalised by the maximum value of the centreline mean absorption \bar{M}_{max} .

Figure 6 shows plots of the mean effective mass $\bar{M}(x,t)$, the centreline mean effective mass $\bar{M}(t)$, the effec-

tive mass for an individual spray event $M_i(x,t)$ and its centreline residual $(M_i(t) - \bar{M}(t))$, all normalised by the maximum centreline mean effective mass \bar{M}_{max} . The normalised residual is only plotted for regions where $(\bar{M}(t)/\bar{M}) > 0.25$.

Prior studies have treated the spray as consisting of three main phases: a start-up transient, a steady state spray, and a decay for the end of the spray. Our results with unmetered canisters show that a steady state case is reached rapidly, relative to typical metered dose discharge times. The propellant-only case does not reach its steady state as rapidly as those with ethanol. The effective mass is seen to peak for the ethanol-containing formulations around 50-60 ms, and maintains at a quite constant value. For the ethanol-containing formulations a steady state spray is achieved by approximately 40 ms; the propellant only spray develops more slowly, reaching a steady state around 70 ms.

The measurements for individual spray events exhibit very large fluctuations in absorption, and the convection of these structures is observed in the (x,t) plots as diagonal lines. The normalised residuals are much larger for the propellant-only case, indicating that ethanol serves to reduce the magnitude of density fluctuations in the spray. The measurement is integrated across the width of the spray in the z -direction, consequently large fluctuations in the measurement are likely to be coherent across the cross-section of the spray.

To observe whether the variation is laser extinction is related to pulsatile ejection from the nozzle or a turbulent fluctuation about the centreline of the spray, crossplanar Mie scattering images of sprays from the pMDI are shown in Figure 7. At 50 ms after actuation and 5 mm downstream of the nozzle mouthpiece, the Mie scattering images vary greatly in their intensity, indicating the large differences in spray density that occur in the spray. Reductions in inten-

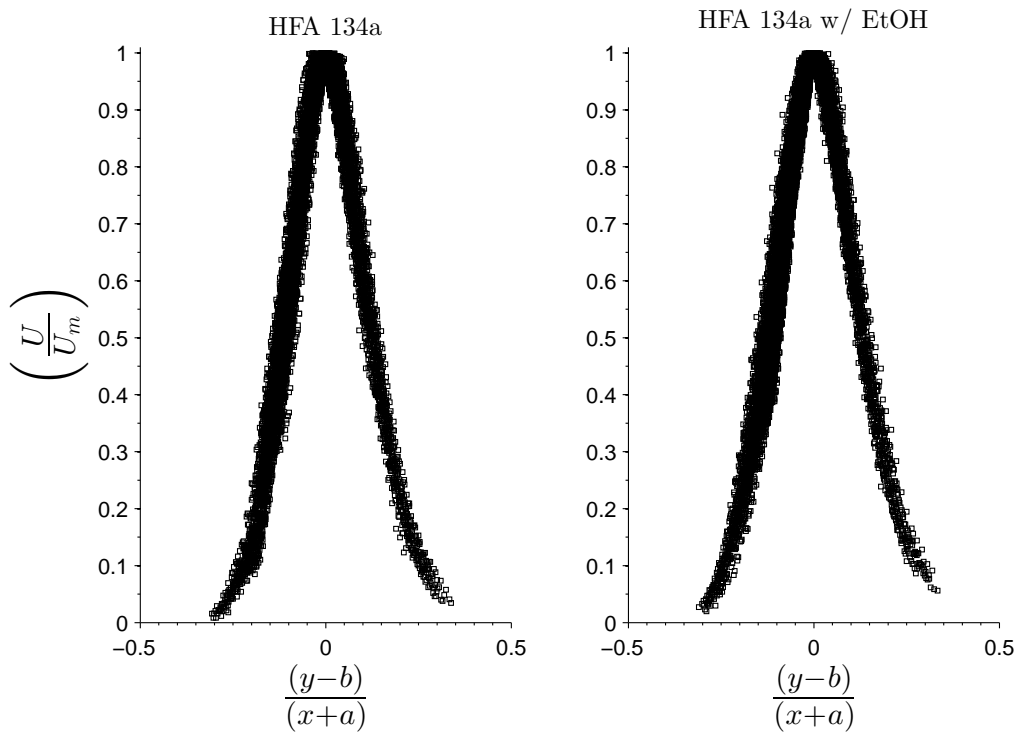


Figure 4. Non-dimensional velocity profiles for sprays from HFA 134a canisters with and without ethanol (left and right, respectively). The collapse of velocity profiles onto a single curve demonstrates self-similarity of the mean axial velocity for the region of interest studied.

sity in the laser extinction measurements are the result of reductions in spray mass across the entire cross-section of the spray, rather than a fluctuation in the spatial distribution about the spray centreline.

CONCLUDING REMARKS

Sprays from pressurised metered-dose inhalers were studied with particle image velocimetry and laser extinction. Propellant droplets are observed many diameters downstream of the nozzle, and can be used to obtain velocity measurements with particle image velocimetry. Large fluctuations in velocity are observed, however mean axial velocity profiles appear to be self-similar. Laser extinction showed that density fluctuations in sprays from a propellant-only formulation are higher than sprays containing ethanol. Mie scattering showed that the absorption fluctuations in the extinction measurements appear to be the result of large axial variations in cross-sectional mass, rather than a turbulent fluctuation about the jet centreline.

Acknowledgements

The authors gratefully acknowledge the support given to the project by the Australian Research Council.

REFERENCES

- Abramovich, GN 1963 The theory of turbulent jets,(1963). R411 p. 541.
- Buchmann, Nicolas A, Duke, Daniel J, Shakiba, Sayed A, Mitchell, Daniel M, Stewart, Peter J, Traini, Daniela,
- Young, Paul M, Lewis, David A, Soria, Julio & Honnery, Damon 2014 A novel high-speed imaging technique to predict the macroscopic spray characteristics of solution based pressurised metered dose inhalers. *Pharmaceutical research* pp. 1–12.
- Crosland, Brian Michael, Johnson, Matthew Ronald & Matida, Edgar Akio 2009 Characterization of the spray velocities from a pressurized metered-dose inhaler. *Journal of aerosol medicine and pulmonary drug delivery* **22** (2), 85–98.
- Dunbar, CA, Watkins, AP & Miller, JF 1997 An experimental investigation of the spray issued from a pmdi using laser diagnostic techniques. *Journal of aerosol medicine* **10** (4), 351–368.
- Harang, Marie 2013 Characterisation of aerosols generated by pressurised metered dose inhalers. PhD thesis, King's College London.
- Ivey, James W, Lewis, David, Church, Tanya, Finlay, Warren H & Vehring, Reinhard 2014a A correlation equation for the mass median aerodynamic diameter of the aerosol emitted by solution metered dose inhalers. *International journal of pharmaceutics* **465** (1), 18–24.
- Ivey, James W, Vehring, Reinhard & Finlay, Warren H 2014b Understanding pressurized metered dose inhaler performance. *Expert opinion on drug delivery* (0), 1–16.
- Ju, Dehao, Shrimpton, John, Bowdrey, Moira & Hearn, Alex 2012 Effect of expansion chamber geometry on atomization and spray dispersion characters of a flashing mixture containing inerts. part II: High speed imaging measurements. *International journal of pharmaceutics* **432** (1), 32–41.
- Kastengren, Alan & Powell, Christopher F 2014 Syn-

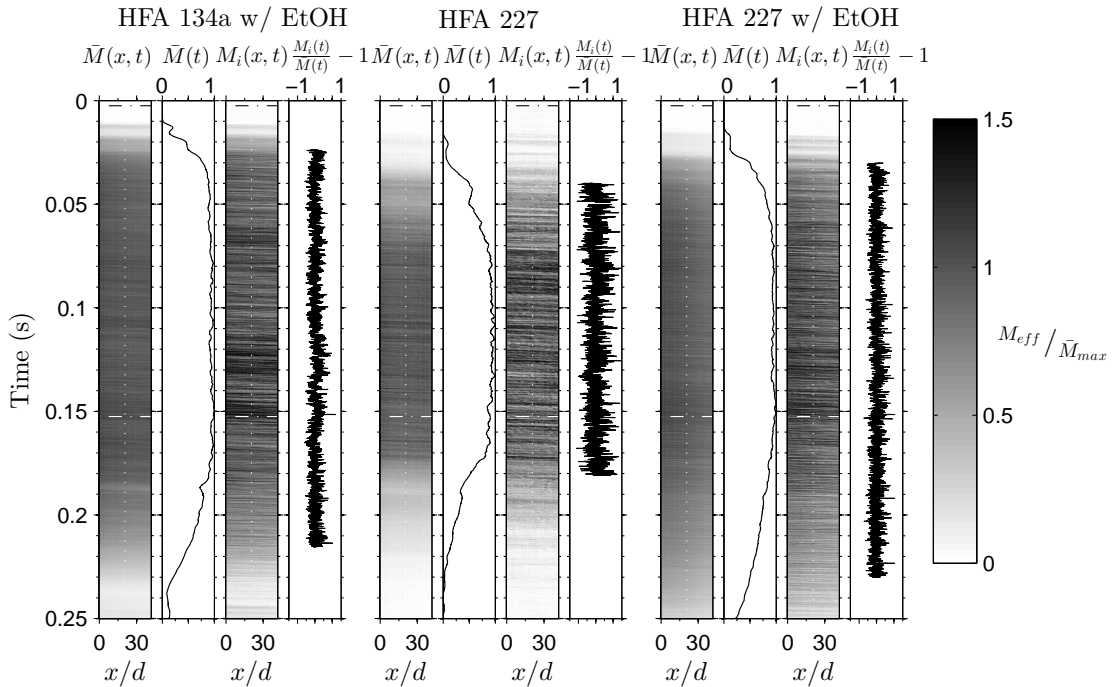


Figure 6. Ensemble average and individual $x-t$ spray images from the electronic metering inhaler with HFA 134a & ethanol (left), HFA 227 (center) and HFA 227 & ethanol (right). The start and end of spray actuation from the electronic metering inhaler are indicated by horizontal dash-dot lines, and the line used for the mean and single shot is indicated by a vertical dotted. All plots are normalised by \bar{M}_{max} for the formulation.

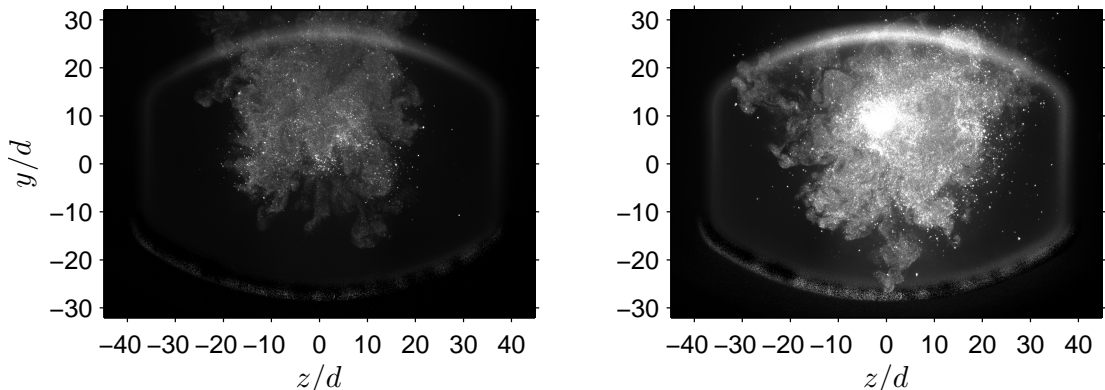


Figure 7. Instantaneous Mie scatter images from a pure HFA 134a canister sprayed from the pMDI, 5 mm downstream of mouthpiece 50 ms after actuation. Images are background subtracted, and the mouthpiece is illuminated by scattering from the spray.

- chrotron X-ray techniques for fluid dynamics. *Experiments in Fluids* **55** (3), 1–15.
 Lewis, D.A. 2013 Method and system for electronic MDI model. WO Patent App. PCT/EP2012/074,278.
 Rajaratnam, Nallamuthu 1976 *Turbulent jets*. Elsevier.
 Stein, Stephen W & Myrdal, Paul B 2006 The relative influence of atomization and evaporation on metered dose inhaler drug delivery efficiency. *Aerosol Science and Tech-*

- nology* **40** (5), 335–347.
 Versteeg, HK, Hargrave, GK & Kirby, M 2006 Internal flow and near-orifice spray visualisations of a model pharmaceutical pressurised metered dose inhaler. In *Journal of Physics: Conference Series*, , vol. 45, p. 207. IOP Publishing.
 Wygnanski, I & Fiedler, Ho 1968 *Some measurements in the self preserving jet*. Cambridge Univ Press.

2.2 Concluding statement

A number of findings emerged from the visible light experiments conducted.

Laser extinction measurements showed that high magnitude optical depth fluctuations occurred in unmetered sprays from the electronic metering inhaler. Propellant-only sprays of HFA227ea had optical depth fluctuations with a high coefficient of variation, relative to sprays of both HFA134a and HFA227ea with 15% ethanol by weight. This indicated that ethanol reduces the amplitude of these fluctuations. This observation is consistent with optical depth variations of metered pMDI sprays under back-illumination imaging (Appendix B). This was also examined with an acoustic method, described in Appendix C.

The different variances of optical depth suggest that the upstream conditions of ethanol-containing and propellant-only pMDI sprays are distinct. The internal flow structure is investigated with x-ray phase contrast imaging in Chapter 4.

Particle image velocimetry measurements showed that mean velocity profiles collapsed with relatively good agreement when scaled by local jet half-width and centreline velocity. Second-order statistics did not collapse in the manner expected of turbulent jets—nor should they, given the flow under study is not a jet. It has since been shown that the scaling approach shown here causes both HFA134a and HFA227ea profiles to collapse onto each other (Versteeg et al. 2017).

Performing PIV measurements of pMDI sprays revealed a number of issues related to its applicability in these sprays. As noted in the introductory statement, particle image velocimetry is a technique for measurement of the velocity of a continuum fluid by introducing flow tracers. The suitability of these tracers is largely governed by their Stokes numbers, which relate particle relaxation times to the time scales of the flow (Mitchell, Honnery, and Soria 2011). In a spray, which comprises droplets of varying diameters, a large range of Stokes numbers are encountered. Furthermore, the velocities of these droplets are governed by their initial velocities, and their interaction with the surrounding gas and vapour. For this reason, in each

interrogation window there may be a range of droplets with distinct velocities; this was observed during analysis. Assigning a single velocity per interrogation region is a simplistic way of representing the correlated droplet size-velocity distribution of pMDI sprays.

Furthermore, the measurement of the spatio-temporal velocity distributions of pMDI sprays was found to be a significant experimental challenge. This was due to the enormous amount of data required. In sprays with constant reservoir conditions during injection, such as the temperature, pressure and vapour quality, the transient spray process may be approximated as a nominally statistically-stationary process, bounded by start-of-injection and end-of-injection transients (Bendat and Piersol 2010). For a nominally statistically-stationary process, it is possible to obtain an accurate statistical description from either a sufficiently long single record (Piersol 1965) or an ensemble of records taken at arbitrary time during the stationary process (Bendat and Piersol 1993). For the pMDI, in which the injection pressure, temperature and void fraction vary throughout the injection (Ju, Shrimpton, and Hearn 2010), a statistical description of the velocity field requires an ensemble of measurements at a sufficient number of times to characterise the transient process. If these various samples cannot be obtained in the one spray event, the number of sprays required rapidly grows. Furthermore, the non-axisymmetric geometry of the inhaler upstream of the atomising nozzle (Figure 1.1) further increases the data requirements, due to the need for measurement from multiple directions if the spray is not axisymmetric.

Although experimental challenges represent the opportunity for new insights, the conceptual problems with PIV application to pMDI sprays meant that it was not examined further during this research program.

Chapter 3

Insights into Spray Development from Metered-Dose Inhalers Through Quantitative X-ray Radiography

3.1 Introductory statement

Quantitative x-ray radiography permits the measurement of the projected mass of samples with known absorption coefficients. This technique has been applied to diesel sprays under non-evaporating conditions. The technique provides a quantitative mass measurement which can be performed tomographically to obtain a quantitative measure of entrainment (Kastengren and Powell 2014).

In this chapter, quantitative radiography is applied to an analogue pMDI for the first time. Due to interspray variability and the low signal-to-noise ratio of radiography measurements, a number of repeats were obtained at each point and ensemble-averaged to produce an ensemble-mean time-variant projected mass distribution. This ensemble-averaging required all sprays to be set against a common

time base, meritng a spray device with low jitter. An electric solenoid valve-driven pMDI analogue was used for the experiments reported in this chapter. This achieved high precision in timing and eliminated this possible source of error.

Measurements were made at a number of axial locations, and transverse integration of these profiles was used to find the total mass in the cross-section at these axial locations. The transverse integrated mass increases with downstream distance, which is consistent with spatial accumulation in the cross-section due to deceleration. Extrapolation of this trend toward the nozzle, which is predicated on a linear entrainment assumption, predicts that the nozzle exit density is substantially below that of pure liquid and shows that a substantial fraction of the nozzle exit is occupied by vapour.

Radiography measurements are most straightforward when the liquid density and absorption coefficient are known. A correction must be made for the ambient gas displaced by the spray; this is straightforward at non-evaporating conditions. The uncertainty of the absorption coefficient under vaporising conditions, such as those in pMDI sprays, had not been established. This source of uncertainty is explored in this chapter, and informs the application of quantitative radiography to a real pMDI in Chapter 4.

The work is presented in the form of a journal article published in *Pharmaceutical Research*¹. This article is reprinted by permission from Springer: *Pharmaceutical Research*, “Insights into Spray Development from Metered-Dose Inhalers Through Quantitative X-ray Radiography”, Mason-Smith, Nicholas, Daniel J. Duke *et al.* © 2016.

¹*Pharmaceutical Research* ranked at 87/252 in JCR Impact Factor rankings in Pharmacology & Pharmacy in 2016, placing it in Q2.

Insights into Spray Development from Metered-Dose Inhalers Through Quantitative X-ray Radiography

Nicholas Mason-Smith¹ • Daniel J. Duke² • Alan L. Kastengren³ • Peter J. Stewart⁴ • Daniela Traini⁵ • Paul M. Young⁵ • Yang Chen⁵ • David A. Lewis⁶ • Julio Soria^{1,7} • Daniel Edgington-Mitchell¹ • Damon Honnery¹

Received: 13 August 2015 / Accepted: 1 February 2016

© Springer Science+Business Media New York 2016

ABSTRACT

Purpose Typical methods to study pMDI sprays employ particle sizing or visible light diagnostics, which suffer in regions of high spray density. X-ray techniques can be applied to pharmaceutical sprays to obtain information unattainable by conventional particle sizing and light-based techniques.

Methods We present a technique for obtaining quantitative measurements of spray density in pMDI sprays. A monochromatic focused X-ray beam was used to perform quantitative radiography measurements in the near-nozzle region and plume of HFA-propelled sprays.

Results Measurements were obtained with a temporal resolution of 0.184 ms and spatial resolution of 5 μm . Steady flow conditions were reached after around 30 ms for the formulations examined with the spray device used. Spray evolution was affected by the inclusion of ethanol in the formulation and unaffected by the inclusion of 0.1% drug by weight. Estimation of the nozzle exit density showed that vapour is

likely to dominate the flow leaving the inhaler nozzle during steady flow.

Conclusions Quantitative measurements in pMDI sprays allow the determination of nozzle exit conditions that are difficult to obtain experimentally by other means. Measurements of these nozzle exit conditions can improve understanding of the atomization mechanisms responsible for pMDI spray droplet and particle formation.

KEY WORDS pressurised metered dose inhaler · radiography · synchrotron radiation · X-ray

ABBREVIATIONS

EMI	Electronic metering inhaler
EtOH	Ethanol
HFA	Hydrofluoroalkane
IPBr	Ipratropium bromide
PDA	Phase doppler anemometry
pMDI	Pressurised metered-dose inhaler
SLPM	Standard litres per minute

INTRODUCTION

Pressurised metered-dose inhalers are widely used for the treatment of asthma and other pulmonary diseases. These devices rely on the vapour pressure of a propellant, typically a hydrofluoroalkane (HFA), to drive liquid containing a drug in suspension or solution through an atomising nozzle to form an aerosol. The solubility of many drugs in HFA propellants is poor, and cosolvents such as ethanol are often used to ameliorate this problem (1).

The devices suffer from a well-documented low delivery efficiency, with the majority of drug deposition in the oropharynx (2). This is the result of inertial impaction and turbulent deposition, with many droplets unable to trace the bulk flow

✉ Nicholas Mason-Smith
nick.masonsmith@gmail.com

¹ Laboratory for Turbulence Research in Aerospace and Combustion, Department of Mechanical and Aerospace Engineering, Monash University, Melbourne, Australia

² Energy Systems Division, Argonne National Laboratory, Lemont, Illinois USA

³ X-ray Science Division, Argonne National Laboratory, Lemont, Illinois USA

⁴ Faculty of Pharmacy and Pharmaceutical Sciences, Monash University, Melbourne, Australia

⁵ Respiratory Technology, Woolcock Institute of Medical Research and the Discipline of Pharmacology, Sydney Medical School, Sydney, Australia

⁶ Chiesi Ltd, Chippenham, UK

⁷ Department of Aeronautical Engineering, King Abdulaziz University, Jeddah, Kingdom of Saudi Arabia

through the oropharynx and trachea into the lung. Attempts to improve deposition efficiency have been stymied by a lack of understanding of the underlying spray physics and droplet formation processes. Both experimental and numerical fluid mechanics techniques have been utilized in attempts to address this knowledge deficit. The influence of device and formulation variables on the spray structure has been studied by several authors (3,4).

Metered-dose inhaler sprays have historically been characterised using intrusive particle sizing measurements, such as cascade impaction (5) or aerodynamic particle sizing (6). The final particle size is then used as an indicator of initial droplet size, assuming that the formulation is well-mixed. These studies are limited in that spatial or temporal effects are not considered. The flow is multiphase, turbulent and transient, with evaporation of multiple constituents at different rates (7). Because droplet sizes change as the cosolvent and propellant evaporate, formulations with equivalent final particle size distributions may have significantly different deposition characteristics *in vivo* due to different evaporation rates (8).

Due to the limitations of intrusive techniques, investigations of pMDI spray structure have been conducted with a variety of visible light diagnostics. Phase doppler anemometry (9) permits investigation of droplet size and velocity characteristics in interrogation regions well downstream of the nozzle. Wigley (10) obtained measurements in the near-orifice region from an ensemble of spray events and characterised some of the rapid transient events in metered-dose inhalers, and these measurements were used to validate numerical spray simulations. A scaling model for spray penetration and tip velocity (11) was validated against experimental data obtained using an optical technique.

Despite the success of these studies, visible light diagnostics suffer severe drawbacks when probing multiphase flows such as those issuing from pMDIs. Refractive index gradients are very high between the droplets, vapour components and inspired airflow. These refractive index gradients arise from differences in phase at droplet surfaces, differences in gaseous refractive index where the propellant mixes with the surrounding air, and from thermal gradients that result from propellant and cosolvent evaporation. Refraction of incident light adds uncertainty on the measurement domain in PDA (9) and can add significant uncertainty for absorption-based measurements with visible light.

These same challenges also occur in the study of other dense sprays, such as in automotive fuel injection. For these other applications, novel solutions have been developed which can be equally applied to the study of pMDI sprays. X-rays from a high-flux synchrotron source have been used for some time to measure dense sprays. They can penetrate high-density materials and scatter very weakly, allowing them to overcome many of the limitations of conventional diagnostics (12). Of most interest here is X-ray radiography, as it provides

a direct measurement of mass in the spray. Importantly, the small X-ray beam cross-section and high flux enable highly resolved, transient measurement of the mass distribution in the spray (12,13).

In this paper, we make use of X-ray radiography to measure the time resolved mass distribution in sprays issuing from a purpose designed pressurised metered-dose inhaler. Two propellants (HFA134a and HFA227) containing ipratropium bromide and ethanol, as well as test cases of propellant only and argon gas are examined. In addition to providing insight into spray dynamics, we demonstrate how these measurements can yield important detail on the liquid-vapour state of the fluid leaving the inhaler nozzle. This work demonstrates the capacity of the X-ray radiography technique to pierce into the core of the dense spray leaving the pMDI, providing the first quantitative insight into the spray characteristics there. These insights can lead to the development of models better capable of predicting the downstream drug particle distribution, and thus to the design of devices that can yield a higher deposition efficiency.

EXPERIMENTAL METHODOLOGY

Experimental Facility

The 7-BM beamline at the Advanced Photon Source at Argonne National Laboratory was used for spray measurements presented in this paper. A brief summary of this facility is given below; further details can be found in Kastengren *et al.* (14).

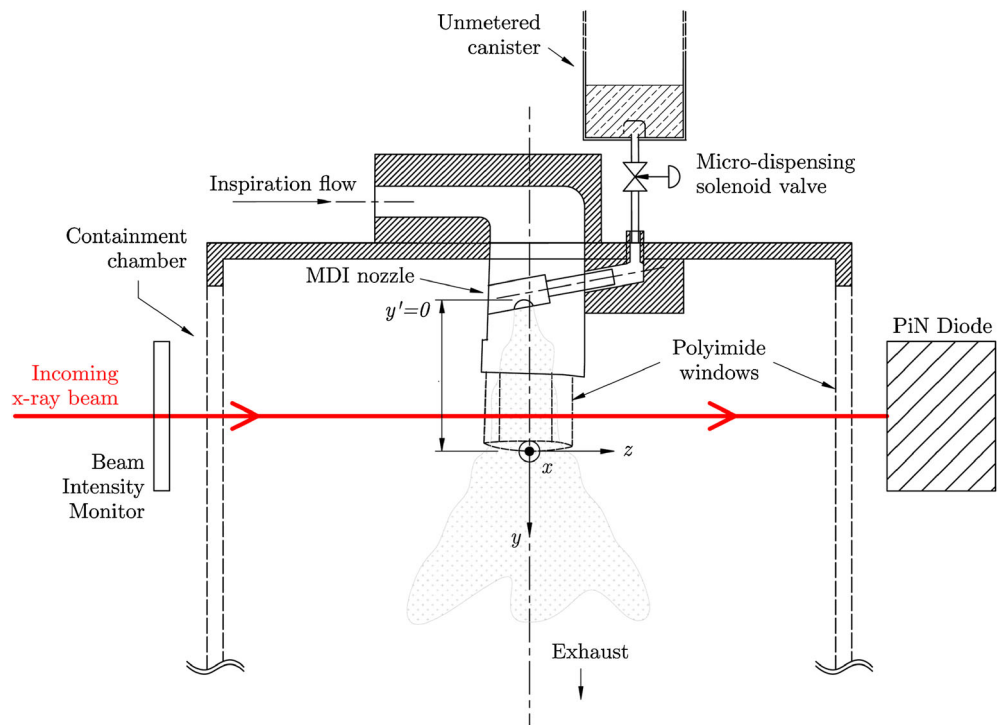
A monochromatic beam with mean energy of 6 keV, 4% $\frac{dE}{E}$ was focused to approximately 6 μm by 5 μm . The beam passed through the spray chamber (Fig. 1) and illuminated a photodiode, the measured current of which is a function of the incident light. The recorded signal gave a point measurement for each spray injection, and the beam was raster scanned to generate transverse profiles at five axial locations.

When light interacts with matter, it can be absorbed, reflected, scattered or transmitted (15). In the X-ray regime, absorption and transmission dominate. The transmission τ of light that passes through an absorptive medium is given by the Beer-Lambert law:

$$\tau = \frac{I}{I_0} = e^{-\mu M} \quad (1)$$

where I is the detected radiant flux (photons/s), I_0 is the incident flux (photons/s), μ is the absorption coefficient of the material ($\text{mm}^2/\mu\text{g}$) and M is the projected mass of absorbing material ($\mu\text{g}/\text{mm}^2$). The projected mass is obtained by rearranging Eq. 1:

$$M = -\frac{1}{\mu} \ln\left(\frac{I}{I_0}\right) \quad (2)$$

Fig. 1 Side cutaway view of spray chamber and apparatus.

The projected mass can alternatively be expressed as the path-integrated spray density along the length of the beam from the source to the detector:

$$M = \int \rho_s \, dz \quad (3)$$

where y is the spray axis, x is the transverse direction and z is the beam propagation direction (Fig. 1).

A high sampling rate and small beam size were used because the projected mass is nonlinearly related to the transmission, and spatial or temporal averaging during a sampling period can bias the measurement (16). Data acquisition was performed at 1 MHz with a digital oscilloscope, giving many independent samples. The recorded signal was binned in the time domain to reduce noise while retaining adequate temporal resolution of 0.184 ms. Fifteen sprays were recorded at each point and ensemble averaged to eliminate the effect of shot-to-shot variation.

Projected mass uncertainty arises from transmission measurement error and absorption coefficient uncertainty. Measurement error of the technique as applied to monocomponent non-vaporising sprays is discussed in detail elsewhere (16). Shot noise introduced an error on the transmission measurement, and the uncertainty from this source was estimated at approximately $0.06 \mu\text{g}/\text{mm}^2$. This is only a minor contribution to overall measurement uncertainty. Absorption coefficient uncertainty is large in vaporising multicomponent sprays such as these, and is explored in more detail in “Experimental Methodology” section.

Absorption coefficients, densities and latent heats of the compounds used are shown in Table I. Absorption coefficients

are obtained from Saloman (17), and are weighted averages of elemental absorption coefficients for the molecules used. Formulation absorption coefficients are mass-weighted averages of constituent absorption coefficients. Densities, vapour pressures and latent heats of propellants, nitrogen and argon are obtained from various sources (18–22); for ethanol, the vapour pressure is obtained from Ambrose (23), the liquid density is obtained from Khattab (24) and the gaseous density is approximated from the gas law. Densities and latent heats are calculated at the facility ambient temperature of 298 K.

Spray Apparatus

The apparatus developed for the presented experiments (Fig. 1) is intended to be analogous to a pressurised metered-dose inhaler, and was used in place of an actual pMDI due to the need for repeatability of timing for the raster-scan

Table I Absorption Coefficients at 6 keV, Liquid and Vaporous Densities and Latent Heats of Vaporisation for Constituents of Pressurised Metered Dose Inhaler Canisters

Canister constituent	$\mu \left(\frac{\text{cm}^2}{\text{g}} \right)$	$\rho_v \left(\frac{\text{kg}}{\text{m}^3} \right)$	$\rho_l \left(\frac{\text{kg}}{\text{m}^3} \right)$	$h_{fg} \left(\frac{\text{kJ}}{\text{kg}} \right)$
HFA134a	30.30	5.2593	1376.7	177.93
HFA227	31.44	8.4936	1542.7	111.44
Ethanol	15.05	2.06	785.8	920.6
Nitrogen	17.70	1.145	–	–
Argon	258.2	1.634	–	–
Ipratropium bromide	47.57	–	–	–

radiography technique. Electro-mechanical actuation of pMDIs suffers from non-negligible variation of the start of injection timing. The Chiesi electronic metering inhaler (EMI) (25) uses unmetered canisters and an electronic solenoid valve to form sprays with accurate and precise timing, and was used as the basis of the current experimental rig.

Modifications were made to the Chiesi device so that a Bespak pMDI inhaler nozzle could be used (Fig. 1). Similar to a pMDI, the nozzle, with orifice diameter 0.3 mm, was attached to a purpose built valve stem, connected in turn to the solenoid via a 0.8 mm diameter, 16.5 mm long connecting pipe (Fig. 2). The total volume making up the space between the nozzle and solenoid valve exit was 38 μL , comparable to typical commercial expansion chamber volumes of around 10–30 μL . The nozzle was aligned with the chamber axis to ensure symmetry about the sagittal plane.

The expansion chamber attachment was coupled with a pMDI mouthpiece analogue. A nitrogen coflow of 30 SLPM was used. The mouthpiece was fitted with polyimide film windows, which allowed spray measurements to be obtained close to the nozzle (the film is highly transparent to X-rays). The pMDI analogue assembly was mounted to a spray chamber with polyimide windows. The spray and coflow were ducted through a particle filter and exhausted. The spray was oriented downward, in order to take advantage of the polarisation of the incident X-ray beam; this allowed placement of detectors in the x - z plane where elastic scattering is minimised. Measurements were made with the major axis of the mouthpiece parallel to the z axis.

Canisters

Several formulations were studied, as per Table II. For drug-containing formulations, a batch solution of drug and ethanol was made then dispensed by pipette to individual canisters. Canisters were then crimped and filled with propellant to a target weight. The estimated uncertainty on the ethanol/propellant ratio was 3.4%. Injection pressures are specified

Table II Canister Formulations, Percentage by Weight of HFA Propellant (HFA), Ethanol (EtOH) and Ipratropium Bromide (IPBr), and Injection Pressures

Formulation	% HFA	% EtOH	% IPBr	$p_{\text{inj}}(\text{Pa} \times 10^5)$
I34a-E-I	85	15	0.1	4.78
I34a-E	85	15	0	4.78
I34a	100	0	0	6.62
227-E-I	85	15	0.1	3.28
227-E	85	15	0	3.28
227	100	0	0	4.53
Argon jet	0	0	0	6.62

in Table II; for sprays, injection pressure corresponds to the formulation vapour pressure at the facility ambient temperature as calculated with Raoult's law.

Large scale variability in line-of-sight mass necessitated a large number of samples to obtain a measurement with low uncertainty. Sprays were generated at a repetition rate of 0.2 Hz. Phase change of the propellant during discharge cools the nozzle, and a high repetition rate may alter nozzle flow processes if the nozzle does not maintain a constant temperature. Canister temperature was monitored during data acquisition; little variation was found during operation. The temperature of the nozzle and expansion chamber were not monitored during injection. Any reduction in temperature at the nozzle is expected to be mitigated by the thermal mass and conductivity of the aluminium expansion chamber attachment, the use of small injections and the flow of nitrogen through the system.

RESULTS

Comparison of Sprays and Jet

Due to the aforementioned complexity of multiphase sprays, the technique is first demonstrated on a simpler canonical jet flow. Argon was discharged through the pMDI nozzle to generate a gaseous jet with the same nozzle geometry as the pMDI spray. Figure 3 contrasts the temporal evolution of the argon jet with pMDI sprays at several distances relative to the mouthpiece lip.

Though sprays from metered dose inhalers exhibit some similarities to turbulent gaseous jets, following scaling laws to good agreement (11), certain important differences exist between liquid sprays and gaseous jets. As the gaseous argon jet and liquid sprays are initiated by the opening of the solenoid valve, they will have a transient before steady flow is established. The argon jet rapidly reaches a steady state, with constant projected mass and jet width from approximately 10 ms onward for all axial positions shown. The startup

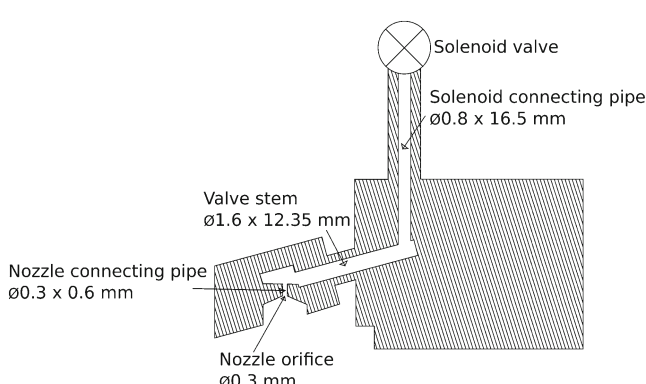
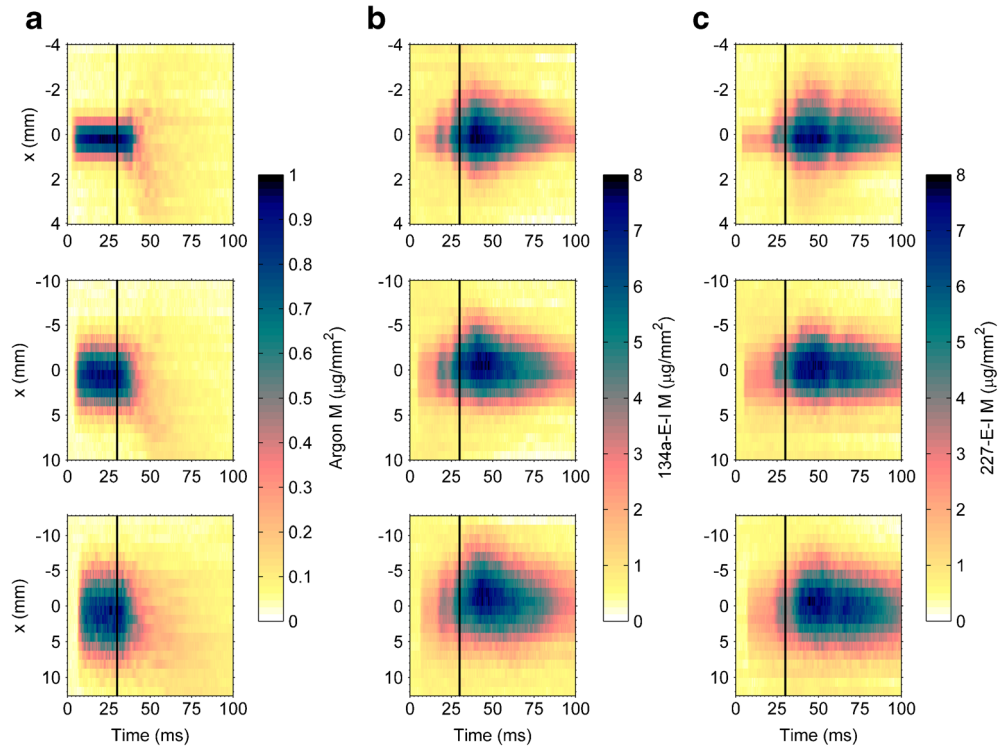


Fig. 2 Detail view of volume between solenoid valve and nozzle orifice.

Fig. 3 x - t evolution of (a) argon jet, (b) 134a-E-I spray and (c) 227-E-I spray at $y =$ (top) -15 mm, (middle) 5 mm and (bottom) 25 mm from mouthpiece. Black vertical lines indicate end of injection.



transients for the 134a-E-I and 227-E-I sprays have much longer durations, with a low mass region preceding the peak spray mass around 40 ms. Once the flow from the solenoid valve ceases, the mass of the gaseous argon jet drops off rapidly, whereas the spray projected masses continue to rise, reach a peak value some time later, and slowly decay back to zero.

This difference in behaviour between the gaseous jet and the propellant sprays is a result of the type of fluid filling the volume between the solenoid valve and nozzle. As the density of the liquid forming the spray is significantly higher than that of the pressurised argon, there is the possibility of greater mass filling the volume in the case of the spray. Factors which control the rate at which the fluid mass leaves the volume through the nozzle are pressure, the phase of the fluid (liquid or gaseous), and the ratio of specific heats in the case of the flow being choked (3,4,26).

For the argon jet, the pressure is such that critical conditions will occur at the nozzle exit; the flow is choked, and the exit velocity will correspond to the speed of sound for argon. For the spray, if the flow is dominated by liquid leaving the nozzle, the nozzle exit conditions will be directly determined by the square root of the pressure in the valve stem. If dominated by vapour, critical conditions will occur giving rise to choked flow in the nozzle. An additional factor for the spray is that nozzle conditions could vary as the flow transitions from the starting transient to being steady as the balance between liquid and vapour changes in the valve stem volume (4).

Absorption Coefficient Uncertainty

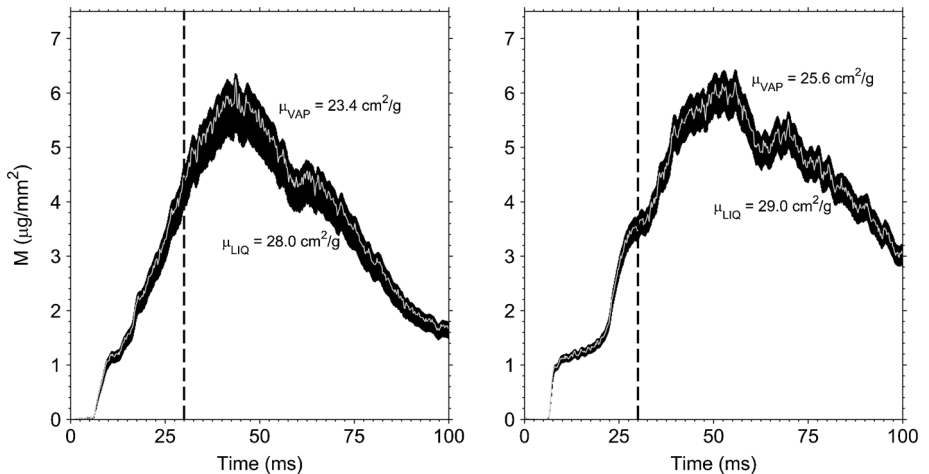
The measured transmission is converted to a projected mass using the Beer-Lambert law in Eq. 1, however a correction is required. The I_0 measurement is the flux transmitted through the air between the source and detector, polyimide windows and the nitrogen in the spray chamber. Though the air and windows remain constant, the nitrogen in the beampath is reduced when the spray is present.

The correction can be made by use of a spray absorption coefficient $\mu_{s,c}$ that accounts for the displaced nitrogen. The corrected absorption coefficient is a function of the spray and nitrogen absorption coefficients (μ_s and μ_{N_2} respectively) and their densities (ρ_s and ρ_{N_2}):

$$\mu_{s,c} = \mu_s - \mu_{N_2} \left(\frac{\rho_{N_2}}{\rho_s} \right) \quad (4)$$

For evaporating sprays such as those from a pMDI, the spray density ρ_s depends on the extent of evaporation in the spray, which varies temporally and spatially ($\rho_s = f(\mathbf{x}, t)$). The flow is multiphase, and could consist of both liquid and vapour, and this introduces an uncertainty in the corrected absorption coefficient. The disparity in evaporation rates between the propellant and the ethanol co-solvent offer further complication. By way of an example, the temporal evolution of 30 ms ethanol and drug-containing sprays propelled by HFA134a and HFA227, 25 mm downstream of the mouthpiece lip, are shown in Fig. 4, with different assumptions about

Fig. 4 Time traces of (left) 134a-E-I and (right) 227-E-I sprays at $y = 25$ mm, $x = 0$ mm with different absorption coefficients based on propellant and ethanol state. Lower bound corresponds to liquid state, upper bound to vaporous state, and white line to vaporous propellant and liquid ethanol. Vertical dashed lines indicate end of injection.



the phase of the propellant and ethanol. The presented lines represent the projected mass, with the corrected absorption coefficient assuming three different cases: liquid propellant and ethanol; vaporous propellant and ethanol; and vaporous propellant and liquid ethanol.

There is an uncertainty in the measurement which cannot be eliminated without additional information on the proportion of each phase of each constituent at the measurement point. Furthermore, the temporal dependence of ρ_s means that the true projected mass may follow a trace that is not a simple interpolation between these upper and lower bounds. The temperature of the gaseous phase affects its density, and the densities chosen correspond to typical pMDI plume temperatures (27). Heat transfer between the spray and entrained air will warm the plume and reduce the vapour density, however this has a small (<5%) effect on the uncertainty associated with the absorption coefficient correction over the relevant temperature range.

In addition, the uncorrected absorption coefficient μ_s is uncertain because the spray has multiple constituents. The approach used assumes that at the measurement point, the relative concentration of ethanol to propellant along the beam path and in the formulation are equivalent, meaning that the spray is well-mixed. For the well-mixed case, μ_s is simply the mass-weighted average of the constituent absorption coefficients. Complementing these measurements with a spectroscopic technique based on laser-induced fluorescence (28) or X-ray fluorescence (29,30) could indicate whether systematic spatial or temporal variations in relative concentration exist and eliminate this uncertainty. If the spray is well-mixed, Fig. 4 demonstrates that spray phase variation may dominate the measurement uncertainty.

Injection Duration

The radiography experiments required a very large number of spray events. To minimize canister consumption, a reduced

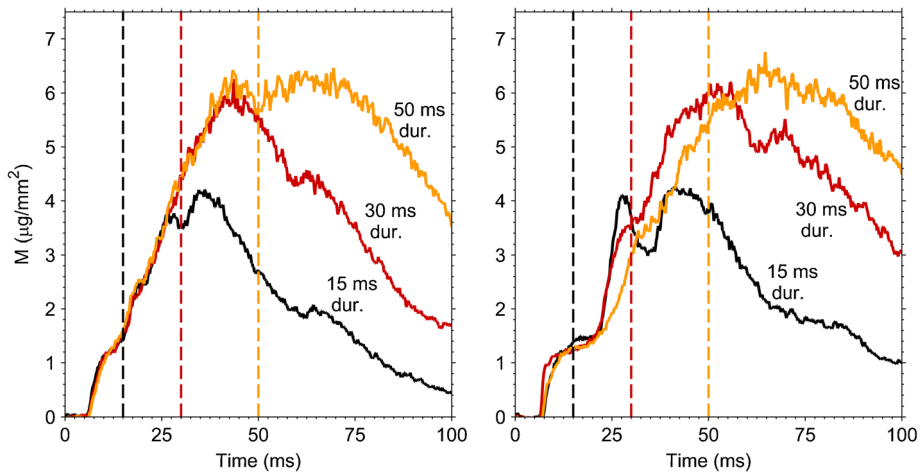
injection duration compared to a standard pMDI device was used. To allow for this optimization of canister use, the effect of varying spray duration was investigated. This established the length of the transient start-up spray phenomena, as well as the nature of the discharge after the solenoid is no longer actuated. Figure 5 shows time traces of M for both HFA 134a and HFA 227 with ethanol and ipratropium bromide, using sprays of varying injection duration.

Three dominant stages are apparent in the projected mass traces shown in the figure. For the 50 ms injection, the start and end transients bracket a steady state period indicated by almost constant projected mass. The relatively long steady period is only evident for the 50 ms injection; the 30 ms injection reaches a maximum value similar to that of the 50 ms injection, although it does so only for a very short period. The maximum projected mass of the 15 ms injection is much lower, and never reaches a steady flow condition.

The time traces for ethanol- and drug-containing HFA227 sprays do not show such strong agreement as the HFA134a sprays during the time of spray injection. In addition to this, an interesting feature of the starting transient for all cases is a period of near constant projected mass commencing at around 7.5 ms. For HFA134a, this lasts for only around 2.5 ms, while for HFA227, it lasts for almost 15 ms. It is possible that this results from the evacuation of the gas in the valve stem volume as this volume fills with fluid on actuation of the solenoid valve. The vapour pressure of the HFA227 and ethanol solution is considerably lower than that of HFA134a and ethanol. Sprays were generated at a rate of 0.2 Hz, which may not be adequate to entirely rid the valve stem volume of the prior solution.

There is a considerable delay between the end of actuation for the 15 ms spray and its divergence from the time traces for the 30 and 50 ms sprays. Similarly, the projected mass time series for the 30 ms spray follows the trend of that for the 50 ms spray until approximately 45 ms. Comparison with measurements made further upstream (Fig. 3, $y = -15$ mm)

Fig. 5 Time traces of (left) 134a-E-I and (right) 227-E-I sprays at $y = 25$ mm, $x = 0$ mm with variable injection duration (indicated). Vertical dashed lines indicate end of injection for each injection duration.



show a similar time delay between the end of injection and the turning point in projected mass, suggesting it is likely the continued discharge of mass from the valve stem volume is responsible for this effect.

Critically, Fig. 5 demonstrates that 30 ms injection is sufficient to achieve the same steady peak mass as observed in the 50 ms spray event, suggesting that this peak in the 30 ms injection is equivalent to a steady flow event. On this basis, the data presented in the remainder of the paper is for 30 ms spray durations.

The temporal evolutions of projected mass for the 30 ms sprays for three different measurement positions are shown in Fig. 3. The starting transient, near steady middle section and end transient are clearly evident, as are minor differences between the formulations.

Formulation

The inclusion of ethanol in the formulation is necessary to achieve dissolution of the drug. It is well established that the presence of ethanol significantly affects the behaviour of the spray (1). The radiography technique can offer further insight into these effects. Figure 6 compares time traces for six spray formulations: two propellants, propellants with ethanol and propellants with ethanol and drug. The addition of the drug to the propellant and ethanol mix is seen to make no difference within the uncertainty bounds of the experiment; given the very low drug concentrations, no fluid mechanical effect would be expected. The addition of ethanol to the propellant has a more noticeable influence on the dynamics of the spray; the vapour pressure driving the spray is reduced so the initial reduction in mass is expected, if ethanol inclusion does not introduce other effects. Well after the end of injection, the effect of ethanol varies significantly between the two propellants: an increase in the mass trace is observed for HFA134a, while a reduction is observed for HFA227. The mechanism behind this variation

is not yet clear; this behaviour serves to highlight the complexity of the metered dose spray process.

Nozzle Exit Conditions

One of the long-standing questions regarding pMDI spray mechanisms concerns the nature of the flow at exit from the nozzle. Competing theories about the manner in which the spray atomizes have been developed, generally based on limited experimental evidence. A consideration of the mass at the nozzle exit has the potential to offer some further insight into the flow regime in the region where atomization occurs, which strongly influences the droplet size and is a significant determinant of drug deposition.

Mass profiles can be integrated across the spray (31), yielding the ‘transverse integrated mass’ M' ($\mu\text{g}/\text{mm}$):

$$M'(y, t) = \int M \, dx \quad (5)$$

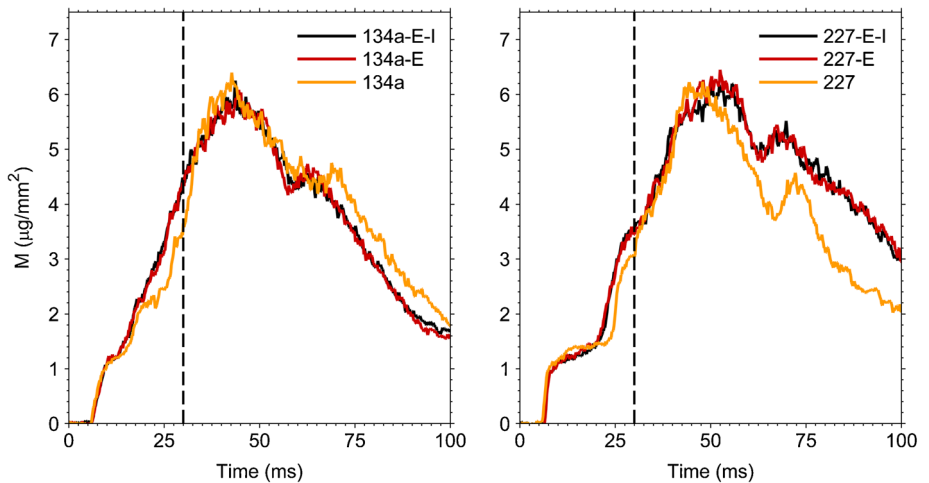
This is equivalent to the axial gradient of spray mass m :

$$M' = \frac{dm}{dy} \quad (6)$$

Figure 7 depicts the transverse integrated mass as a function of distance from the nozzle y' , which is the distance from the mouthpiece y plus the distance from the end of the mouthpiece to the nozzle exit orifice (Fig. 1). The graphed M' values are the maxima obtained with 30 ms 134a-E-I and 227-E-I sprays and are at or near the steady flow condition. For the argon jet, the M' values in Fig. 7 are 10 ms after spray penetration and are shown with a secondary axis (Fig. 7, right).

M' increases as a function of downstream distance due to aerodynamic drag between liquid droplets and the surrounding air, and the consequent deceleration of the spray. Accompanying this is an entrainment of the surrounding nitrogen into the spray. The mass flux \dot{m} through a cross-section

Fig. 6 Time traces of spray projected mass at $y = 25$ mm, $x = 0$ mm with different formulations (indicated). Vertical dashed lines indicate end of injection.



is equal to the product of the transverse integrated mass and the mass-averaged axial spray velocity:

$$M'(y) = \dot{m}(y)/\bar{u}(y) \quad (7)$$

The growth in M' with increasing distance from the nozzle is indicative of the drop in mass-averaged spray velocity \bar{u} . Upstream extrapolation of the plots of M' provides indicative values of M' at the nozzle exit orifice. As M' is related to the mean spray density by the area occupied by the spray mass:

$$M' = \bar{\rho}_s A \quad (8)$$

it is possible to estimate the mean density $\bar{\rho}_s(0)$ of the mass of formulation discharged from the nozzle, using the known area of the nozzle exit of diameter d_o :

$$\bar{\rho}_s(0) = \frac{4M'(0)}{\pi d_o^2} \quad (9)$$

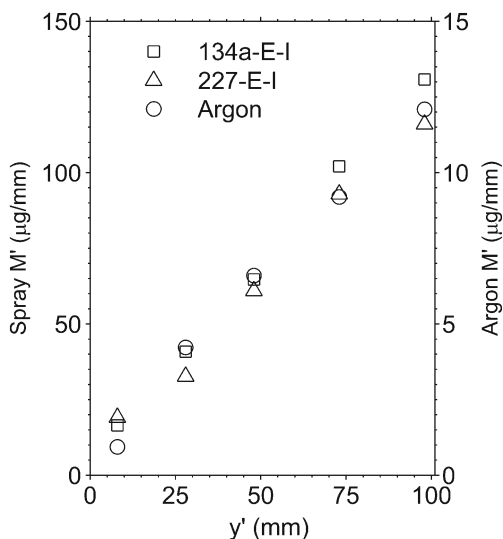


Fig. 7 Transverse integrated mass M' as a function of distance from the nozzle y' for argon jet, 134a-E-I spray and 227-E-I spray. A separate axis is used for argon M'

It is important to note that entrainment and atomisation behave nonlinearly in the near nozzle region (32); even for sprays as complex as these, a potential core region near the nozzle could be expected to exist. Higher near nozzle spatial resolution would resolve these effects and improve the estimation of the extrapolated value. Although present, this nonlinearity is not expected to greatly alter the value of M' extrapolated from the downstream values.

Estimated $M'(0)$ and $\bar{\rho}_s(0)$ values for the sprays and argon jet are tabulated in Table III. The argon case has an estimated density at the nozzle of 6.4 kg/m^3 , which corresponds approximately to the density of argon at the injection pressure. For the sprays, the indicated densities are very low relative to the liquid density of the propellant and ethanol mixture. For each of these cases, the results correspond to a gas/liquid ratio by mass of 94% for 134a-E-I and 93% for 227-E-I. This suggests the flow leaving the nozzle under steady flow conditions is dominated by vapour.

An important additional observation is that as the nozzle exit diameter is the same as that of the pipe connecting the nozzle to the valve stem volume, vapour is also likely to dominate the flow in this small connecting pipe. As the area of the solenoid valve is around 7 times larger than the nozzle exit area, the valve stem volume is expected to fill with fluid as the nozzle is the controlling orifice. Based on our estimates, a 30 ms injection would provide sufficient liquid to fill around 60% of the valve stem volume for the 134a-E-I formulation, and around 50% for 227-E-I formulation, assuming no flow

Table III Estimated Nozzle Densities for Sprays and Argon Jet from M' Measurements

Spray/jet	$M'(0) (\mu\text{g}/\text{mm})$	$\bar{\rho}_s(0) (\text{kg}/\text{m}^3)$
134a-E-I	5.27	75
227-E-I	6.70	95
Argon	0.452	6.4

from the nozzle during injection. Vapour is therefore likely to make up a large fraction of the fluid in the valve stem volume.

We have previously noted that the device used here is not identical to a pMDI; a pMDI device could give rise to nozzle exit conditions that are different from those found here. While injection times for typical pMDI metered doses are longer than the injection period used here, the mass discharged from a pMDI, although metered to a set dose, is also higher. If the vapour state dominates the flow from the nozzle during much of the pMDI injection period, it is interesting to speculate on the consequences for the formation of droplets and ultimately precipitation of the drug particle in the spray. Under these circumstances, ethanol is likely to form a large fraction of the liquid flowing from the nozzle. If this is the case, droplet formation could be an aerodynamic process driven by the high speed vapour stripping droplets from the liquid flow before, in and external to the nozzle. Other X-ray techniques have the capacity to reveal flow structures inside the nozzle (33) and canister, and could resolve the atomization mechanism in pMDIs.

CONCLUSIONS

Through this preliminary set of experiments, we have shown that it is possible to yield time resolved measurement of the mass in the spray issuing from an inhaler nozzle. For the electronic metering inhaler used here, we find that steady flow conditions are reached after around 30 ms for the two formulations examined (HFA134a and HFA227). HFA134a was found to produce a spray with greater repeatability than HFA227, although it is as yet uncertain as to whether this is a product of the experimental system used or a property of the propellant. Analysis of the spray mass revealed that vapour is likely to dominate the flow leaving the nozzle of the inhaler used during steady flow rather than liquid. If similar conditions are confirmed for pMDIs, this could yield insight into the mechanism controlling droplet formation and ultimately precipitation of the drug particle in these sprays.

X-ray radiography offers many benefits to the study and development of pharmaceutical sprays. The quantitative measurements allow for the development and validation of far more accurate numerical models than have previously been possible. These models, with sufficient validation, can be used to predict nozzle discharge conditions that are very difficult to measure experimentally. The nozzle exit conditions can be used to predict the particle size distribution as a function of formulation and geometry. The technique can also be used in a more direct diagnostic manner; the operation of new pMDI designs can be clearly elucidated by measurement. The power of the technique is most clearly demonstrated in its ability to reveal the state of the flow in the near nozzle region. Understanding the atomization processes in this region is of

critical importance to the design of new, more efficient pMDI devices. The radiography technique for the first time allows the mechanics of this near-nozzle region to be studied directly. By understanding the inception of the spray and the primary/secondary atomization processes involved in droplet formation, more accurate prediction and control of final drug-particle size will be possible.

ACKNOWLEDGMENTS AND DISCLOSURES

The authors gratefully acknowledge the support given to the project by the Australian Research Council. The authors wish to thank Dr. Chris Powell and Dr. Andrew Swantek, Energy Systems Division, Argonne National Laboratory. This research was performed at the 7-BM beamline of the Advanced Photon Source at Argonne National Laboratory. Use of the APS is supported by the U.S. Department of Energy (DOE) under Contract No. DE-AC02-06CH11357. The submitted manuscript has been created by UChicago Argonne, LLC, Operator of Argonne National Laboratory (“Argonne”). Argonne, a U.S. Department of Energy Office of Science laboratory, is operated under Contract No. DEAC02-06CH11357. The U.S. Government retains for itself, and others acting on its behalf, a paid-up nonexclusive, irrevocable worldwide license in said article to reproduce, prepare derivative works, distribute copies to the public, and perform publicly and display publicly, by or on behalf of the Government.

REFERENCES

- Gupta A, Stein SW, Myrdal PB. Balancing ethanol cosolvent concentration with product performance in 134a-based pressurized metered dose inhalers. *J Aerosol Med.* 2003;16(2):167–74.
- Dhand R. Aerosol plumes: slow and steady wins the race. *J Aerosol Med.* 2005;18(3):261–3.
- Dunbar C. An experimental and theoretical investigation of the spray issued from a pressurised metered-dose inhaler. Manchester: University of Manchester; 1996.
- Ju D, Shrimpton J, Hearn A. The effect of reduction of propellant mass fraction on the injection profile of metered dose inhalers. *Int J Pharm.* 2010;391(1):221–9.
- Stein SW. Size distribution measurements of metered dose inhalers using Andersen Mark II cascade impactors. *Int J Pharm.* 1999;186(1):43–52.
- Stein SW, Myrdal PB. A theoretical and experimental analysis of formulation and device parameters affecting solution MDI size distributions. *J Pharm Sci.* 2004;93(8):2158–75.
- Stein SW, Myrdal PB. The relative influence of atomization and evaporation on metered dose inhaler drug delivery efficiency. *Aerosol Sci Technol.* 2006;40(5):335–47.
- Stein SW. Aiming for a moving target: challenges with impactor measurements of MDI aerosols. *Int J Pharm.* 2008;355(1):53–61.
- Dunbar C, Watkins A, Miller J. An experimental investigation of the spray issued from a pMDI using laser diagnostic techniques. *J Aerosol Med.* 1997;10(4):351–68.

10. Wigley G, Versteeg H, Hodson D. Near-orifice PDA measurements and atomisation mechanism of a pharmaceutical pressurised metered dose inhaler. In: 18th Annual Conference on Liquid Atomization & Spray Systems. Zaragoza, Spain: Institute for Liquid Atomization & Spray Systems. 2002. .
11. Buchmann NA, Duke DJ, Shakiba SA, Mitchell DM, Stewart PJ, Traini D, et al. A novel high-speed imaging technique to predict the macroscopic spray characteristics of solution based pressurised metered dose inhalers. *Pharm Res*. 2014;31(11):2963–74.
12. Kastengren AL, Tilocco FZ, Duke DJ, Powell CF, Zhang X, Moon S. Time-resolved X-ray radiography of sprays from engine combustion network spray A diesel injectors. *Atomization Sprays*. 2014;24(3):251–72.
13. Duke DJ, Kastengren AL, Tilocco FZ, Swantek AB, Powell CF. X-ray radiography measurements of cavitating nozzle flow. *Atomization Sprays*. 2013;23(9).
14. Kastengren A, Powell CF, Arms D, Dufresne EM, Gibson H, Wang J. The 7BM beamline at the APS: a facility for time-resolved fluid dynamics measurements. *J Synchrotron Radiat*. 2012;19(4):654–7.
15. Als-Nielsen J, McMorrow D. Elements of modern X-ray physics. Chichester: John Wiley & Sons; 2011.
16. Kastengren A, Powell CF. Synchrotron X-ray techniques for fluid dynamics. *Exp Fluids*. 2014;55(3):1–15.
17. Saloman E, Hubbell J, Scofield J. X-ray attenuation cross sections for energies 100 eV to 100 keV and elements Z= 1 to Z= 92. At Data Nucl Data Tables. 1988;38(1):1–196.
18. Tillner-Roth R, Baehr HD. An international standard formulation for the thermodynamic properties of 1, 1, 1, 2-Tetrafluoroethane (HFC-134a) for temperatures from 170 K to 455 K and pressures up to 70 MPa. *J Phys Chem Ref Data*. 1994;23(5):657–729.
19. Huber ML, Laesec A, Perkins RA. Model for the viscosity and thermal conductivity of refrigerants, including a new correlation for the viscosity of R134a. *Ind Eng Chem Res*. 2003;42(13):3163–78.
20. Span R, Lemmon EW, Jacobsen RT, Wagner W, Yokozeki A. A reference equation of state for the thermodynamic properties of nitrogen for temperatures from 63.151 to 1000 K and pressures to 2200 MPa. *J Phys Chem Ref Data*. 2000;29(6):1361–433.
21. Tegeler C, Span R, Wagner W. A new equation of state for argon covering the fluid region for temperatures from the melting line to 700 K at pressures up to 1000 MPa. *J Phys Chem Ref Data*. 1999;28(3):779–850.
22. Majer V, Svoboda V, Kehiaian HV. Enthalpies of vaporization of organic compounds: a critical review and data compilation. vol. 32. Oxford: Blackwell Scientific; 1985.
23. Ambrose D, Sprake C. Thermodynamic properties of organic oxygen compounds XXV. Vapour pressures and normal boiling temperatures of aliphatic alcohols. *J Chem Thermodyn*. 1970;2(5): 631–45.
24. Khattab IS, Bandarkar F, Fakhree MAA, Jouyban A. Density, viscosity, and surface tension of water+ ethanol mixtures from 293 to 323 K. *Korean J Chem Eng*. 2012;29(6):812–7.
25. Lewis DA. Method and system for electronic MDI model. Google Patents; 2013. WO Patent App. PCT/EP2012/074,278. Available from: <http://www.google.com/patents/WO2013083530A2?cl=en>.
26. Clark AR. Metered atomisation for respiratory drug delivery. Loughborough University of Technology. 1991.
27. Gabrio BJ, Stein SW, Velasquez DJ. A new method to evaluate plume characteristics of hydrofluoroalkane and chlorofluorocarbon metered dose inhalers. *Int J Pharm*. 1999;186(1):3–12.
28. Van Cruyningen I, Lozano A, Hanson R. Quantitative imaging of concentration by planar laser-induced fluorescence. *Exp Fluids*. 1990;10(1):41–9.
29. Kastengren A, Powell CF, Dufresne EM, Walko DA. Application of X-ray fluorescence to turbulent mixing. *J Synchrotron Radiat*. 2011;18(5):811–5.
30. Duke DJ, Kastengren AL, Mason-Smith N, Chen Y, Young PM, Traini D, et al. Temporally and spatially resolved x-ray fluorescence measurements of in-situ drug concentration in metered-dose inhaler sprays. *Pharm Res*. 2015.
31. Kastengren AL, Powell CF, Cheong SK, Wang Y, Im KS, Liu X, et al. Determination of diesel spray axial velocity using X-ray radiography. *SAE Trans*. 2007-01-0666. 2007.
32. Cossali G. An integral model for gas entrainment into full cone sprays. *J Fluid Mech*. 2001;439:353–66.
33. Duke D, Swantek A, Tilocco Z, Kastengren A, Fezzaa K, Neroorkar K, et al. X-ray imaging of cavitation in diesel injectors. *SAE Trans*. 2014.

3.2 Concluding statement

This paper is the first to explore the use of radiography for the quantitative measurement of properties of pressurised metered-dose inhaler sprays.

Reviewer comments led to the expansion of the manuscript into the form that appears here. The original manuscript contained a less detailed discussion of the sources of uncertainty that exist in applying quantitative radiography to pMDI sprays. It was considered appropriate to expand the discussion of uncertainty to benchmark the technique and acknowledge its limitations, particularly as it represented the first application of the technique to a pMDI.

Reviewers also noted that the high repetition rate used could result in significant cooling of the pMDI nozzle over a number of sprays. This cooled condition represents a departure from the true conditions encountered in pMDI sprays. Due to limited beamtime and the need for many samples, high repetition rates were required, and a compromise between repetition rate and nozzle cooling was encountered. This was investigated for pMDIs using thermal imaging (Chapter 4) and was mitigated in later experiments with a heat exchanger (Chapter 4).

This work showed that the transverse integrated mass of sprays from metered-dose inhalers grows almost linearly with increasing downstream distance. When this linear trend is extrapolated to the nozzle exit, a vapour concentration fraction of more than 90% is predicted for both HFA134a and HFA227ea formulations at all times during the 30 ms sprays from the spray device used, indicating that the spray is highly vaporised. Having established the capacities of radiography for pMDI spray investigation, radiography experiments performed on a pMDI (Chapter 4) were conducted as close as possible to the nozzle exit.

Chapter 4

Revealing pMDI Spray Initial Conditions: Flashing, Atomisation and the Effect of Ethanol

4.1 Introductory statement

“The greatest value of a picture is when it forces us to notice what we never expected to see.”

— Tukey (1977, vi)

Previous work in this thesis (Chapter 3) established the capacity of x-ray radiography as a technique for the quantification of spray mass in metered-dose inhalers. Laser extinction additionally showed that ethanol-containing HFA sprays have lower optical depth fluctuations than propellant-only sprays (Chapter 2), suggesting a difference in their upstream conditions.

The initial conditions of sprays from metered-dose inhalers are not well understood. Internal flow visualisations of transparent inhaler analogues (Fletcher 1975; Versteeg, Hargrave, and Kirby 2006) demonstrated the presence of vapour at large

scales in propellant-only flows. The low penetration power of visible light, due to refraction and reflection at liquid-vapour phase boundaries, meant that the internal structure of this two-phase flow could not be studied in detail. As this transient internal flow is not well understood (Finlay 2001), flow visualisations were expected to assist in developing the collective understanding of these flows.

Furthermore, radiography measurements of a pMDI analogue indicated that it had a nozzle exit that was dominantly occupied by vapour (Chapter 3). These measurements had not been performed with a real metered-dose inhaler. Consequently, the nozzle exit conditions of real pMDIs are not known. It had been known for some time that substantial vaporisation occurred upstream of and inside the atomising nozzles of pMDIs (Finlay 2001); radiography is a way to quantitatively investigate this vaporisation and these nozzle exit conditions.

In this chapter, quantitative radiography and phase contrast imaging are used to investigate spray formation in pMDIs, and how it is affected by the inclusion of ethanol. The work is presented as a journal paper published in *Pharmaceutical Research*¹. This article is reprinted by permission from Springer: *Pharmaceutical Research*, “Revealing pMDI Spray Initial Conditions: Flashing, Atomisation and the Effect of Ethanol”, Mason-Smith, N., Daniel J. Duke *et al.* © 2017.

¹*Pharmaceutical Research* rankings for 2017 are unavailable; it ranked at 87/252 in JCR Impact Factor rankings in Pharmacology & Pharmacy in 2016, placing it in Q2.

Revealing pMDI Spray Initial Conditions: Flashing, Atomisation and the Effect of Ethanol

Nicholas Mason-Smith¹ • Daniel J. Duke² • Alan L. Kastengren³ • Daniela Traini⁴ • Paul M. Young⁴ • Yang Chen⁴ • David A. Lewis⁵ • Daniel Edginton-Mitchell¹ • Damon Honnery¹

Received: 23 September 2016 / Accepted: 4 January 2017
© Springer Science+Business Media New York 2017

ABSTRACT

Purpose Sprays from pressurised metered-dose inhalers are produced by a transient discharge of a multiphase mixture. Small length and short time scales have made the investigation of the governing processes difficult. Consequently, a deep understanding of the physical processes that govern atomisation and drug particle formation has been elusive.

Methods X-ray phase contrast imaging and quantitative radiography were used to reveal the internal flow structure and measure the time-variant nozzle exit mass density of 50 µL metered sprays of HFA134a, with and without ethanol cosolvent. Internal flow patterns were imaged at a magnification of 194 pixels/mm and 7759 frames per second with 150 ps temporal resolution. Spray projected mass was measured with temporal resolution of 1 ms and spatial resolution 6 µm × 5 µm.

Results The flow upstream of the nozzle comprised large volumes of vapour at all times throughout the injection. The inclusion of ethanol prevented bubble coalescence, altering

the internal flow structure and discharge. Radiography measurements confirmed that the nozzle exit area is dominantly occupied by vapour, with a peak liquid volume fraction of 13%.

Conclusion Vapour generation in pMDIs occurs upstream of the sump, and the dominant volume component in the nozzle exit orifice is vapour at all times in the injection. The flow in ethanol-containing pMDIs has a bubbly structure resulting in a comparatively stable discharge, whereas the binary structure of propellant-only flows results in unsteady discharge and the production of unrespirable liquid masses.

KEY WORDS phase contrast imaging · pressurised metered-dose inhaler · radiography · synchrotron radiation

ABBREVIATIONS

APS	Advanced Photon Source
FWHM	Full-width at half-maximum
HFA	Hydrofluoroalkane
HFM	Homogeneous frozen model
pMDI	Pressurised metered-dose inhaler
TIM	Transverse integrated mass

INTRODUCTION

Despite a long period of use, much remains unknown about the physical mechanisms driving atomisation in pressurised metered-dose inhalers (pMDI). The general understanding of the device is thoroughly reviewed by Ivey et al. (20), who note that much of the existing knowledge base used for pMDI development is empirical. Understanding of the mechanisms that determine droplet size and velocity, which are the dominant parameters governing deposition *in vivo*, is necessary for development of improved devices. The internal flow in

¹ Laboratory for Turbulence Research in Aerospace and Combustion, Department of Mechanical and Aerospace Engineering, Monash University, Clayton, Australia

² Energy Systems Division, Argonne National Laboratory, Lemont, Illinois, USA

³ X-ray Science Division, Argonne National Laboratory, Lemont, Illinois, USA

⁴ Respiratory Technology, Woolcock Institute of Medical Research and the Discipline of Pharmacology, Sydney Medical School, Sydney, Australia

⁵ Chiesi Ltd, Chippenham, UK

pMDIs is transient, turbulent, multiphase and multicomponent, with both heat and mass transfer between phases.

The atomisation mechanism of propellant-only pMDI sprays was the subject of experimental and numerical investigations by Clark (9) and Dunbar (13). Summaries of these works often state that Clark (9) suggested an airblast atomisation mechanism was responsible for droplet formation, whereas Dunbar (13) attributed atomisation to flash evaporation upstream of the nozzle. A close reading suggests that the distinction between the two is commonly overstated. The source of vapour in the pMDI nozzle flow is from flash boiling, and one nozzle flow pattern of flash boiling sprays is an annular liquid film with a vaporous core (38) which is functionally identical to the flow pattern in some twin-fluid airblast atomisers (35). Furthermore, these mechanistic investigations of propellant-only sprays are applicable to suspension pMDIs that do not contain excipients, but are of limited applicability to current marketed solution pMDIs, in which cosolvents are added to the propellant to aid drug solubility (50). Flows of such multicomponent mixtures can differ considerably from propellant-only flows (36,43), which may alter the atomisation mechanism. For these reasons, it is pertinent to investigate where atomisation occurs in the pMDI, and how the atomisation is affected by inclusion of cosolvent.

Visible light techniques are poorly suited to near-nozzle measurements of many spray systems. The difficulty of studying the near-nozzle region in these systems arises from strong refraction at gas–liquid interfaces, beam steering due to temperature gradients and multiple scattering in dense droplet fields (23,25,39). X-ray spray techniques have been developed that overcome these difficulties. These techniques include phase contrast imaging for visualisation of the internal flow and quantitative radiography for spray mass measurement. A review of synchrotron radiation techniques for fluid mechanics is given in Kastengren and Powell (24). The spray density of a pMDI analogue was measured at a number of stations downstream of the nozzle with quantitative radiography (33). Analysis of the spatial distribution of peak mass indicated that the nozzle exit orifice was predominantly occupied by vapour. Direct drug concentration measurements in sprays from this metered-dose inhaler analogue were performed with x-ray fluorescence by Duke et al. (12). The density of the nozzle exit mixture in pMDIs has not been measured experimentally, and knowledge of the internal two-phase flow structure has to date been limited by the need for transparent analogues and by poor light penetration into the mixture (32). X-ray phase contrast imaging provides full-field time-resolved visualisations of dense flowfields through both absorption and weak refraction of x-rays at gas–liquid interfaces (16,40), and also enables visualisation of multiphase flows inside opaque materials (11).

In this paper we present x-ray phase contrast imaging of the internal and near-nozzle flows of a pressurised metered-dose

inhaler. We show that the volume directly upstream of the nozzle is dominantly occupied by vapour. Nucleation occurs well upstream of the nozzle orifice and the structure in all regions visualised is a mixture of liquid and vapour. The internal flow is sensitive to the inclusion of ethanol, with a substantial change in the flow structure and dynamics resulting from this addition. The findings from the phase contrast visualisations are quantified with radiography measurements directly downstream of the nozzle exit orifice, which are used to estimate the mixture density at the nozzle exit. The density measurements enable determination of volume fractions of vapour and liquid, and reveal that the dominant component in the nozzle by volume is vapour. Commentary is provided on atomisation in pMDIs, and the differences between propellant-only sprays and those containing cosolvents. These findings indicate a new way forward for understanding the atomisation mechanisms of suspension and solution pMDIs.

EXPERIMENTAL METHODOLOGY

Spray Apparatus

The spray apparatus used for these measurements was an inhouse rig to simulate pMDI use during a normal dosage event. A linear solenoid was used to insert metered canisters into a Bespak pMDI nozzle. The geometry of the pMDI is shown schematically in Fig. 1. The solenoid was actuated for 350 ms to inject 50 μL of metered formulation. Measurements of canister weights demonstrated that this injection duration was sufficient to discharge more than 95% of the mass

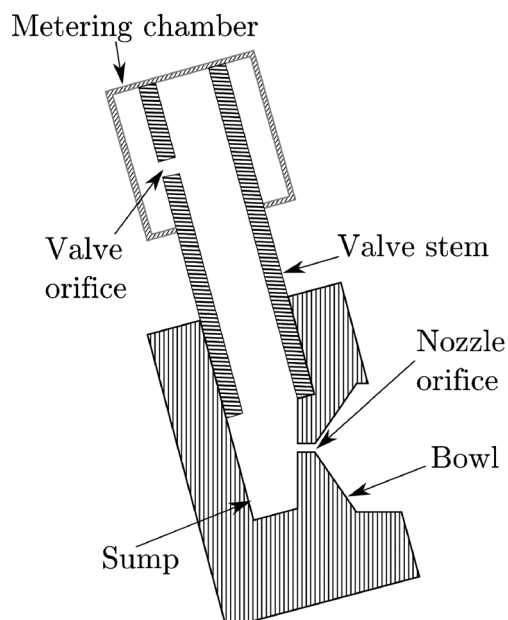


Fig. 1 Schematic of pMDI metering chamber, valve stem and atomising nozzle cross-section.

contained in the metering chamber. No coflow was used. Propellant and ethanol were evacuated from the test section with a suction exhaust duct located approximately 300 mm downstream of the nozzle exit.

A modified Bespak nozzle with its bowl removed was used for radiography. This allowed measurements to be obtained one nozzle diameter downstream of the nozzle exit orifice. To estimate the density of the nozzle exit flow, Mason-Smith et al. (33) measured the transverse integrated mass at several axial positions and extrapolated to the nozzle. For the present experiments, the approach used was to measure the transverse integrated mass as close as possible to the nozzle exit orifice. Comparison of phase contrast images for the flow in the modified and unmodified nozzles showed that bowl removal had no discernible effect on nozzle discharge, but was expected to affect downstream spray spreading (6). Canister and nozzle dimensions are given in Table I.

A heat exchanger was used to warm the nozzle between injections during the radiography measurements. The radiography technique required sprays to be generated at high repetition rates. Both depressurisation and phase change of the formulation removed heat from the inhaler nozzle and if uncorrected had the potential to substantially cool the nozzle. The desire to replicate typical operation by a patient merited maintaining the nozzle temperature at standard room conditions. Water at 37.5°C in a temperature-controlled bath was circulated through an aluminium heat exchanger block. The pMDI nozzle was held in place in this heat exchanger block with conductive paste on its rear and side surfaces, across which heat was transferred. As the amount of cooling induced by each formulation used was different, different dwell times were used, as shown in Table II. Dwell times were determined from thermal imaging of the valve stem and nozzle, and were chosen to allow the nozzle front surface and external surface of the valve stem to reach the ambient temperature with a tolerance of $\pm 5\text{K}$ (Fig. 2). A level of thermal inhomogeneity in the nozzle was expected to exist with the water bath temperature and repetition rates used, and could have been reduced at the expense of repetition rate. A number of priming shots were

rapidly fired before data acquisition to cool the nozzle to the operational condition.

For phase contrast imaging, an unobstructed path was required between the x-ray source, nozzle and detector. Accordingly, the heat exchanger was not used and a comparatively long dwell time of 1 min was used.

Formulations

Formulations used for this study are given in Table II. Both formulations used propellant HFA134a, and one formulation contained 15% ethanol by weight. Neither formulation contained any drug; Mason-Smith et al. (33) found that inclusion of 0.1% dissolved drug by weight had no significant effect on spray projected mass for HFA134a sprays with 15% ethanol by weight. The propellant-only formulation was representative of an excipient-free suspension pMDI and the ethanol-containing formulation was representative of a solution pMDI.

Aluminium canisters (Prespart, UK) were manufactured with 50 μL metering valves (Bespak, UK) and contained approximately 10 g of propellant. Ethanol was pipetted to individual canisters, which were then crimped and filled with propellant to a target weight. Uncertainty of the ethanol/propellant ratio was 3.4%. Solution vapour pressures p_v were estimated using the correlations developed in Gavtash et al. (15), which account for non-ideality of the solution (45). Specific heats of liquid were obtained using Lemmon et al. (29) and Andreoli-Ball et al. (1). The experiment hutch pressure and temperature were maintained at 1 atm and 25°C respectively.

Advanced Photon Source

The 7-ID and 7-BM beamlines of the Advanced Photon Source (APS) at Argonne National Laboratory were used for phase contrast imaging and radiography experiments respectively. Experimental layouts for phase contrast and radiography measurements are shown in Fig. 3.

Phase Contrast Imaging

X-ray phase contrast imaging was used to obtain time-resolved visualisations of the internal flow structure of the pMDI. Phase contrast imaging exploits refraction at phase boundaries and uses free space propagation to enhance these features, making it a viable candidate to image the internal flow structure of pMDIs. The resulting images are path-integrated representations of the combined beam absorption and refraction through the sample. Imaging results are presented for the sump, nozzle and valve stem. Further details of the ID beamline and phase contrast imaging can be found in Moon et al. (34). The experimental layout is depicted in Fig. 3 (left).

Table I Canister and Nozzle Dimensions

Dimension	Size (mm)
Nozzle orifice diameter (d_{no})	0.3
Nozzle orifice length (l_{no})	0.6
Valve stem diameter, inner ($d_{vs,i}$)	2.0
Valve stem diameter, outer ($d_{vs,o}$)	3.2
Valve stem length (l_{vs})	12
Valve orifice diameter (d_{vo})	0.6
Metering chamber diameter (d_{mc})	5.0
Metering chamber length (l_{mc})	4.2

Table II Radiography Dwell Times, Thermophysical and Optical Properties of Formulations Studied. Data Presented at Saturation Conditions at 298.15 K

Formulation	Dwell time (s)	ρ_l (kg/m ³)	p_v (bar)	$c_{p,l}$ (kJ/kg.K)	μ (mm ² /μg)
HFA134a	20	1207	6.65	1.42	3.00×10^{-3}
HFA134a 85% Ethanol 15% w/w	11	1118	5.95	1.57	2.77×10^{-3}

The beamline used an undulator to produce a high intensity ‘white’ (polychromatic) beam. The white beam was passed through the test section and was incident on a fast response scintillator plate. The scintillator converted some of the x-ray radiation into visible light which was imaged with a Photron FASTCAM SA4 at 7759 frames per second. Use of microscope objective optics enabled a magnification of 194 pixels/mm, and the imaged area corresponded to the full size of the x-ray beam, approximately 5 mm × 3 mm. Two-point calibration (21) was used to correct for inhomogeneous spatial illumination. Short exposure times, on the order of nanoseconds, were necessary to prevent motion blur of small dynamic features (8). Experiments were performed during the ‘hybrid-singlet’ mode of the APS, in which a single bright pulse of x-rays containing four times the flux of a normal bunch lasting 150 ps is generated every 3.68 μs. The camera was time gated to capture the singlet light pulse, resulting in an effective exposure time of 150 ps (48).

X-Ray Radiography

Extensive details of the 7-BM beamline can be found in Kastengren et al. (26). A polychromatic beam was passed through a multilayer monochromator, generating a monochromatic x-ray beam with a mean energy of 6 keV and a

bandwidth of 4% $\frac{\Delta E}{E}$ full-width at half-maximum (FWHM). This monochromatic beam was focused and shaped to a 5 × 6 μm (FWHM) spot using a pair of x-ray focusing mirrors and slits. The beam was passed through the spray in the horizontal plane orthogonal to the spray axis and was incident on a high speed PiN diode detector (Fig. 3, right). The detector was connected to an analog antialiasing filter with a cutoff frequency of 1 MHz. The filtered output was then recorded by a Yokogawa oscilloscope at a sample rate of 2.5 MS/s. Fifteen spray records were obtained at each of 37 points spaced 83 μm apart across the nozzle exit. Spray mass traces were synchronised by monitoring start of injection timing with a freefield microphone, and were then ensemble averaged and decimated to 1 kS/s.

The spray projected mass M (μg/mm²) along the path of the x-ray beam is obtained from the detector output with the Beer-Lambert law:

$$M(x,y,t) = -\frac{1}{\mu} \ln\left(\frac{I(x,y,t)}{I_0}\right) \quad (1)$$

where μ is the absorption coefficient (mm²/μg), I is the incident intensity (photons/s) and I_0 is the incident intensity in the absence of spray (photons/s). The projected mass can be expressed as an equivalent liquid length l_{eq} by dividing by the formulation liquid density:

$$l_{eq}(x,y,t) = \frac{M(x,y,t)}{\rho_l} \quad (2)$$

Integration of the projected mass profiles gives the transverse integrated mass TIM (μg/mm):

$$\text{TIM}(x,t) = \int_{-\infty}^{\infty} M(x,y,t) dy \quad (3)$$

Division of the transverse integrated mass by a cross-sectional area gives a spray mixture density. This mixture density takes on meaning at the nozzle exit orifice where the cross-sectional area is known:

$$\rho_m(0,t) = \frac{4 \text{ TIM}(0,t)}{\pi d_{no}^2} \quad (4)$$

where d_{no} is the nozzle orifice diameter. The average exit density can be expressed as volume fractions of vapour and

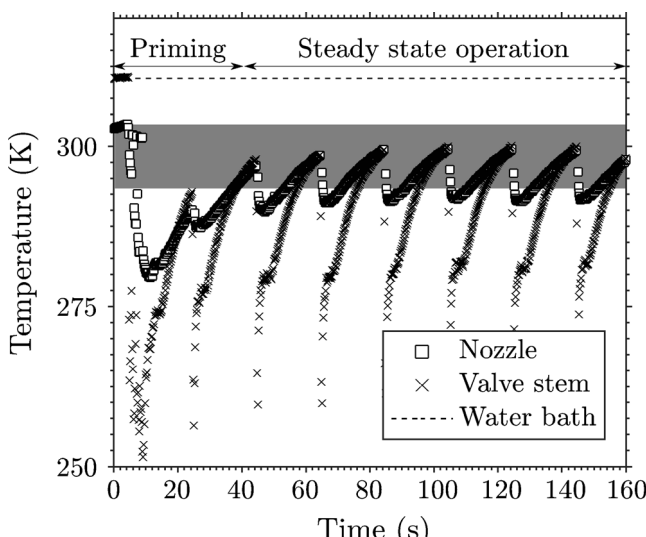
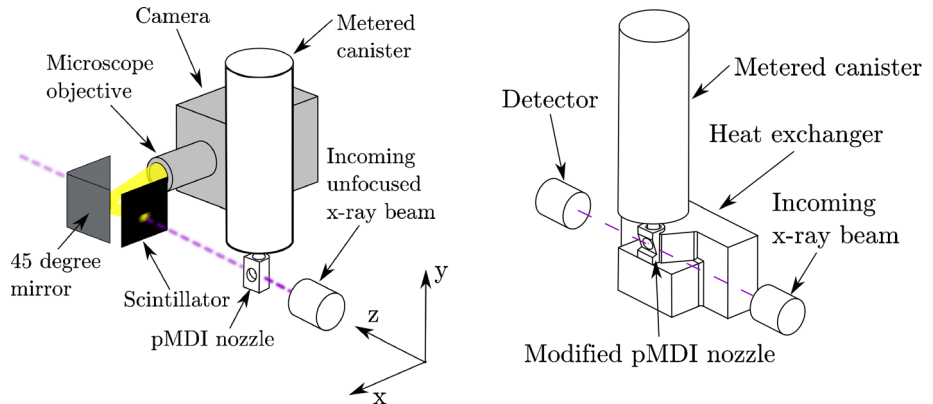


Fig. 2 Temporal trace of nozzle and valve stem surface temperatures with HFA134a 100% sprays at 20 s dwell time. Gray region indicates ambient temperature ± 5 K.

Fig. 3 Experimental layouts for (left) phase contrast imaging and (right) quantitative radiography (not to scale).



liquid. The volume fraction of vapour α_v is obtained by the following equation:

$$\alpha_v = \frac{\rho_l - \rho_m}{\rho_l - \rho_v} \quad (5)$$

and the liquid volume fraction α_l is $(1 - \alpha_v)$. These volume fractions are meaningful where $\rho_m > \rho_v$, as the nozzle is filled with air at the start and end of injection.

Absorption coefficients for the formulations were obtained using data from Berger et al. (5) and are given in Table II. The absorption coefficient is a function of the composition of the spray along the beam path, as well as a correction for the ambient gas displaced by the spray (33). Due to the small spray width in the near-nozzle region, the uncertainty associated with absorption coefficient correction for ambient gas displacement was less than 1%.

Electromagnetic interference created by the solenoid affected the radiography results. Although small in amplitude, the interference could not be eradicated by ensemble averaging as it was not uncorrelated noise (4). This introduced an uncertainty of approximately $0.5 \mu\text{g}/\text{mm}^2$ for M . The mixture density ρ_m was estimated using an integration over the full 3 mm measured domain, giving an uncertainty for ρ_m of $20 \text{ kg}/\text{m}^3$. When estimating the mixture density, the transverse integrated mass was filtered with the empirical mode decomposition of Huang et al. (19) and reconstructed using the five lowest frequency modes. This removed high-frequency noise associated with the solenoid and retained the spray mixture density variation which occurs on comparatively long time scales (22).

RESULTS

Phase Contrast Visualisations

Phase contrast images of the flow in the valve stem, sump and nozzle are shown in Fig. 1. The images are path-integrated representations, meaning that refraction at all phase

boundaries and absorption through all matter along the beam path contribute to the resulting image. Phase boundaries are sharp edges in the images. Due to differential absorption, liquid features show up as darker, and vapour regions as lighter, enabling bubbles and droplets to be distinguished. Interpretation of phase contrast images can be difficult for highly three-dimensional flows, and for regions where large numbers of phase boundaries may obscure each other (24,30).

Images are presented for the propellant-only formulation in Fig. 4 and the ethanol-containing formulation in Fig. 5. The valve stem is shown in the left column, and the sump and nozzle region in the right column. A mounting bracket obscured part of the valve stem, and appears as a black wedge at the top left of the valve stem images. Images are shown at different times after the start of injection. High-speed movies are also available online (youtu.be/R6Y66F4FlyY).

The propellant-only flow is a mixture of liquid and vapour with a structure that varies throughout the injection. The flow establishes a structure with a large vaporous core that extends from the valve stem into the sump. Liquid propellant is observed to accumulate at the base and rear face of the sump. Polydisperse bubbles exist in the liquid phase and coalesce with each other and the vapour core. Several bubbles and droplets, distinguishable by their different levels of absorption, pass through the valve stem (Fig. 4, middle and bottom, left). Video sequences show that some bubbles nucleate at the walls of the stem and sump and coalesce with the vapour core and larger vapour bubbles.

The ethanol-containing formulation has a very different flow structure. Vapour-liquid interfaces occur on a much smaller scale than for the propellant-only case, and there is no continuous vapour core in the valve stem. Circular phase boundaries at early stages in the spray are indicative of spherical bubbles, and consequently continuous liquid separating the bubbles. Bubble size increases throughout the injection, from much smaller to larger than the nozzle orifice diameter, and ultimately to a foam-like structure (28) as the bubbles interact with each other and distort. Although nucleation of new bubbles plays a role in contributing to the increased

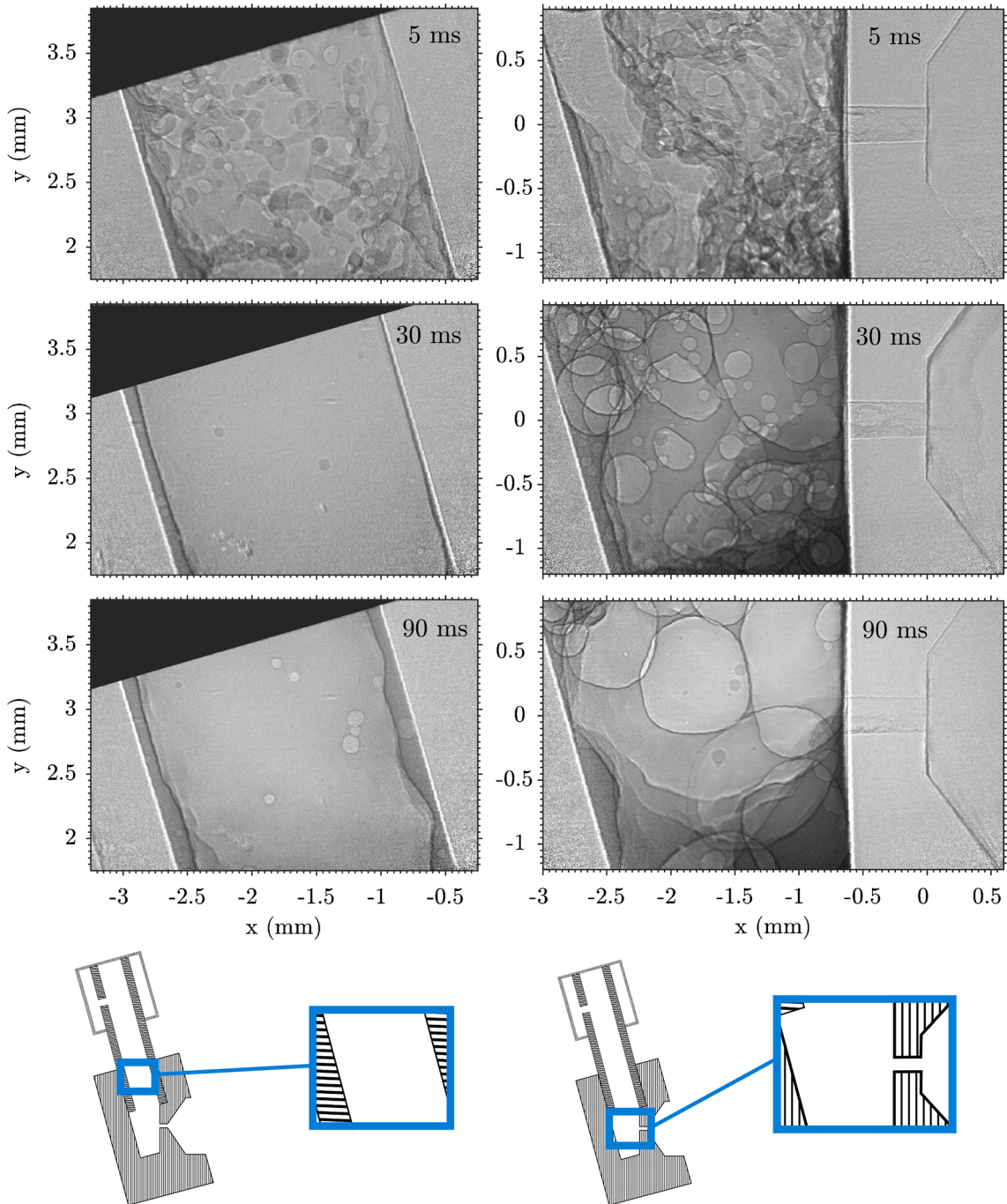


Fig. 4 Phase contrast images of HFAI 34a flow in (left) valve stem and (right) sump and nozzle (top) 5 ms, (middle) 30 ms and (bottom) 90 ms after start of injection. Regions are shown schematically at the bottom of each column. A mounting bracket obscures the top-left corner of the valve stem images.

vapour volume at later stages of the spray, the dominant contribution is from bubble expansion. Bubbles nearest the nozzle are highly distorted as they enter the nozzle orifice. When ethanol is included in the propellant, bubbles do not readily coalesce and the internal flow structure differs from the propellant-only case. Bubble coalescence can be reduced or entirely prevented by raised mixture surface tension (7) and by Marangoni stresses which are driven by surface tension gradients normal to the bubble surface (41,47,49).

For both formulations, much of the volume upstream of the pMDI nozzle orifice is occupied by vapour. The flow structures for each formulation differ considerably from each other. Although occasional droplets are seen in the valve stem and sump, the bulk of the liquid upstream of the nozzle exists as a continuous phase. Atomisation of the liquid, which determines the drug particle sizes, is initiated on entering the nozzle. To highlight some features of the flow inside the nozzle and immediately outside the nozzle orifice exit, images are

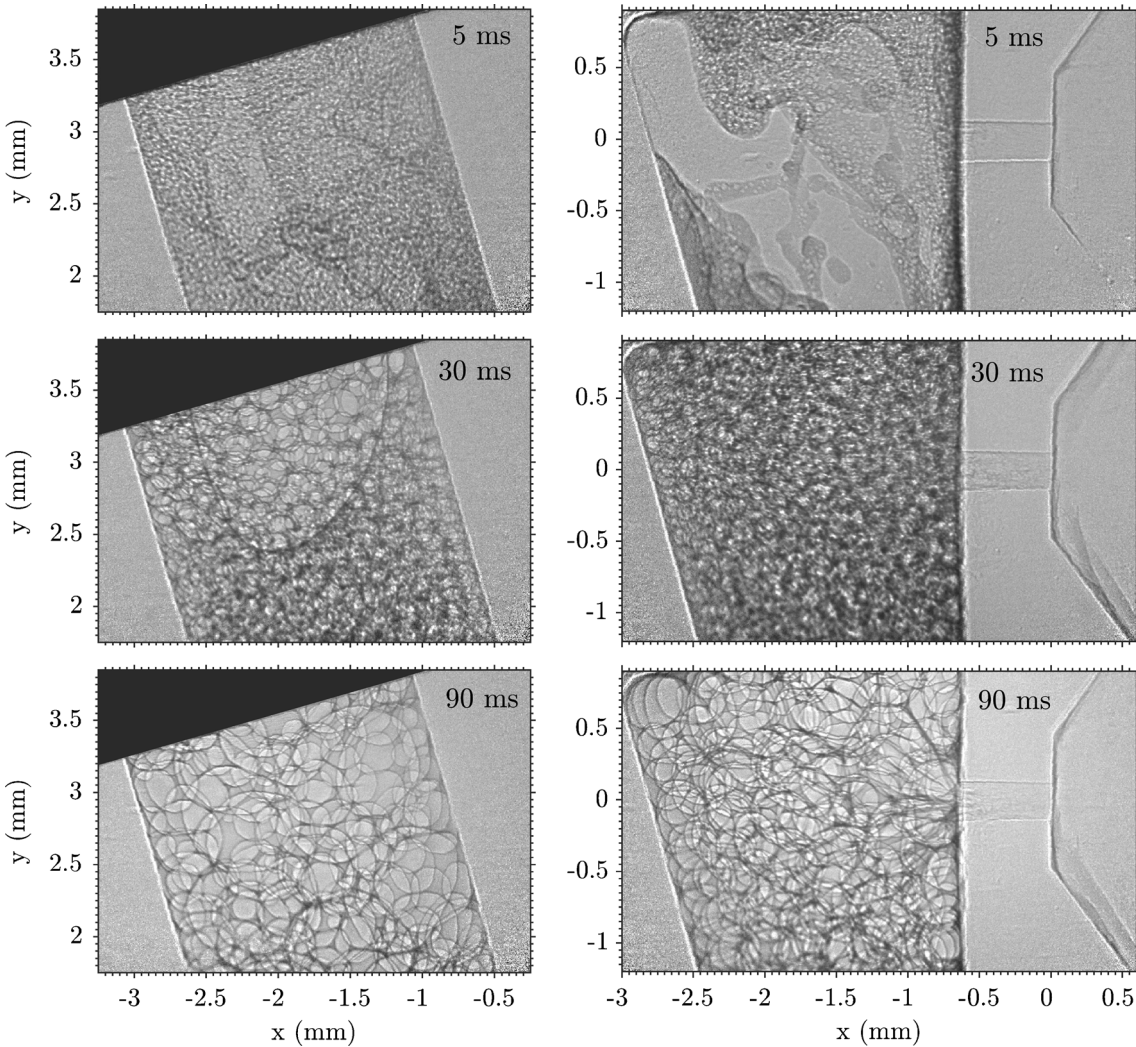


Fig. 5 Phase contrast images of HFA134a/Ethanol flow in (left) valve stem and (right) sump and nozzle (top) 5 ms, (middle) 30 ms and (bottom) 90 ms after start of injection.

shown of flows in the modified nozzle in Fig. 6. This nozzle is selected for these visualisations as the contrast in the near-nozzle region is enhanced with the reduced number of scattering surfaces along the beam path in this region. The dynamic range has been reduced to enhance the liquid-vapour boundaries and absorption through the liquid.

Propellant-only sprays of HFA134a have a Sauter mean diameter that is much larger than its number mean diameter [36], indicating the presence of large droplets. These large droplets have also been observed experimentally [31]. The phase contrast imaging reveals that these droplets are produced when large masses of liquid are discharged through the nozzle. An example is shown in Fig. 6 (left), where a large amount of liquid lines the lower half of the nozzle. At this time, continuous liquid feeds from the lower part of the sump, similar to the continuous liquid from the sump in Fig. 4 (right, bottom). The spray pattern and droplet volume mean diameter of HFA134a sprays from pMDIs are sensitive to the sump

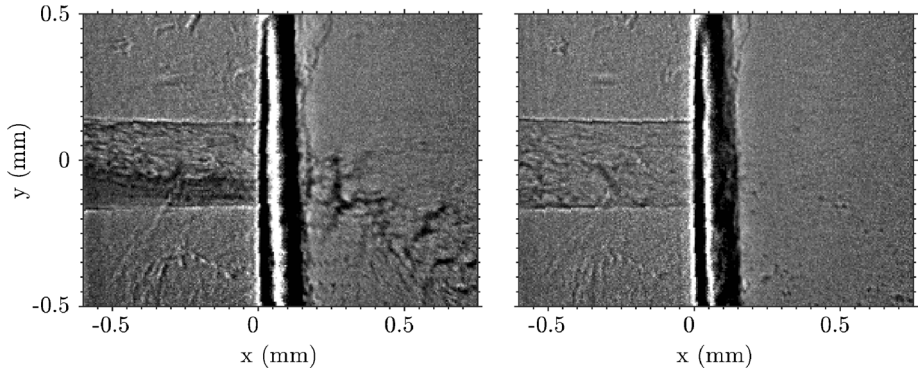
depth [46], suggesting that cyclic accumulation and discharge of liquid propellant in the base of the sump is the source of the large droplets. For the ethanol-containing case, this process is largely suppressed and the discharge is more consistent. This is also reflected in the similarity of the number mean and Sauter mean diameters for ethanol-containing sprays [36].

Phase contrast imaging shows that the flow upstream of and within the nozzle of the pMDI is occupied dominantly by vapour, and suggest that the atomisation mechanism is altered by the inclusion of ethanol. To quantify the extent of vaporisation in the nozzle, quantitative radiography is used and results presented in the next section.

Spray Projected Mass

The radiography technique used provides the ensemble mean time-variant spray properties. Random fluctuations, such as

Fig. 6 Phase contrast images of (left) HFA134a and (right) HFA134a/Ethanol flow from nozzle exit orifice.



those produced by the passage of large droplets through the nozzle, are removed by averaging.

The ensemble mean temporal evolution of the spray projected mass at $x = 0.3$ mm is shown in Fig. 7, with the transverse direction y on the vertical axis and time on the horizontal axis. The peak projected mass occurs for both formulations approximately 30–40 ms after the start of injection. Peak values of projected mass are located on the spray centreline and are approximately $12\text{--}15 \mu\text{g}/\text{mm}^2$. Using the formulation liquid densities, this corresponds to an equivalent liquid length l_{eq} of around $10\text{--}12 \mu\text{m}$, or $l_{eq}/d_{no} = 0.03$. This is much shorter than the liquid lengths for single-phase liquid sprays from plain-orifice nozzles; by way of an example, at $x/d_{no} = 1.1$ for a diesel spray l_{eq}/d_{no} is approximately 0.85 (27). The low values of projected mass for pMDI sprays relative to

fully liquid sprays indicate that at this very short distance downstream of the nozzle orifice exit there are large voids, and only a small segment of the spray cross-section is occupied by liquid. In the near-nozzle region where little entrainment of air has occurred, it is expected that the remaining volume is occupied with vapour discharged from the spray orifice.

The estimated average nozzle exit flow mixture density ρ_m is shown as a function of time in Fig. 8. The results were obtained by applying Eqs. 3 and 4 to the transverse mass profiles in Fig. 7. The nozzle orifice flow density shows several distinct stages for both formulations: a rapid increase in density that is representative of a filling process (0–30 ms), a pseudo-steady state (30–60 ms) and a decrease in density indicative of an emptying stage (60–175 ms). After this emptying stage, the density holds approximately constant at 25 kg/m^3 for the propellant-only case, whereas it continues to zero for the ethanol-containing formulation.

Peak nozzle exit flow mixture densities are 165 kg/m^3 for the propellant-only formulation and 135 kg/m^3 for the ethanol-containing formulation. Volume fractions of vapour and liquid are estimated with Eq. 5, using the saturated liquid density $\rho_{l,sat}$ and an estimated density based on the homogeneous frozen model (HFM) (10). The vapour density depends

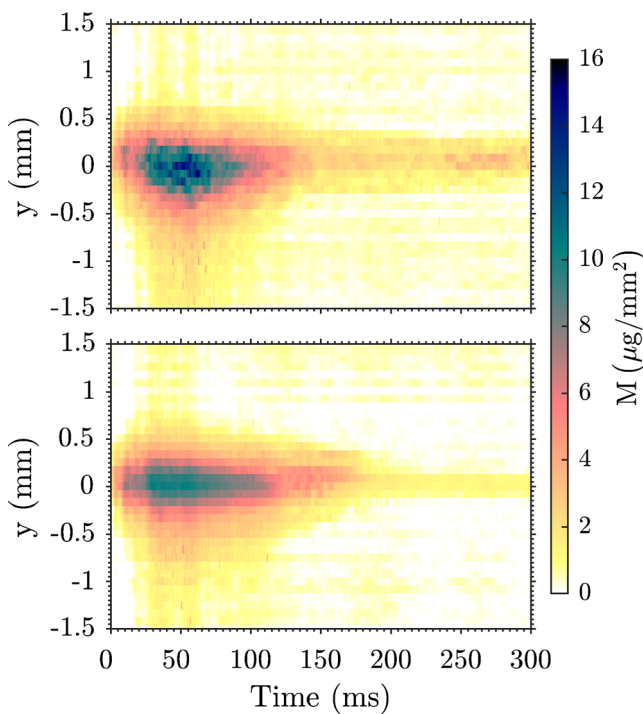


Fig. 7 $y\text{-}t$ plots of spray projected mass M for (top) HFA134a and (bottom) HFA134a/Ethanol sprays at $x = 0.3$ mm.

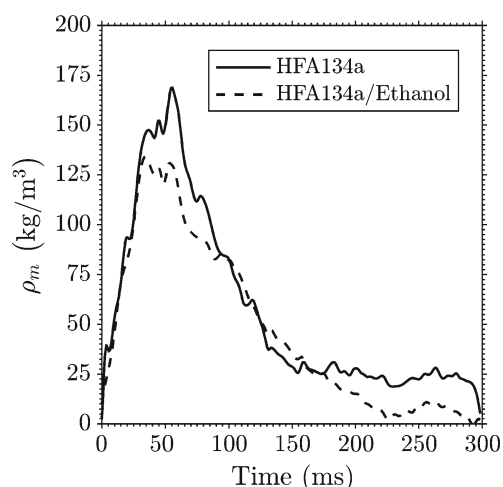


Fig. 8 Nozzle orifice flow mixture density ρ_m against time.

on its degree of expansion at the nozzle. The HFM treats the vapour and liquid as a homogeneous mixture with no relative velocity, no heat or mass transfer between phases and the liquid dispersed as infinitesimal elements in the vapour. Treating the vapour as an ideal gas, the vapour density at the nozzle exit orifice ρ_v is:

$$\rho_v = \rho_{v,sat} \left(1 + Ma^2 \frac{(\gamma_v - 1)}{2} \right)^{\frac{-1}{\gamma_v - 1}} \quad (6)$$

where γ_v is the propellant ratio of specific heats c_p/c_v and Ma is the vapour Mach number:

$$Ma = \frac{U_m}{c_v} \quad (7)$$

The Mach number is the ratio of the mixture velocity U_m to the speed of sound of the vapour, c_v . Assuming the vapour pressure is sufficient to choke the flow, the mixture velocity U_m is the mixture speed of sound c_m :

$$c_m = \sqrt{\left(\rho_v \alpha_v + \rho_l (1 - \alpha_v) \right) \left(\frac{\alpha_v}{\rho_v c_v^2} + \frac{(1 - \alpha_v)}{\rho_l c_l^2} \right)^{-1}} \quad (8)$$

Equations 5, 6, 7 and 8 can be solved iteratively to find ρ_v , Ma , c_m and α . Speeds of sound of the propellant vapour and liquid are obtained from Lemmon et al. (29). Peak values of α_l are 0.12 for HFA134a and 0.10 for HFA134a/ethanol.

At all times during the injection, the dominant volume component in the nozzle of the pMDI is vapour, confirming the findings of previous researchers (9,13,33).

DISCUSSION

Atomisation Mechanisms

Drug particles in pMDI aerosols are formed from droplets that are generated by atomisation of the sump's multiphase flow. Many of the droplets produced by the pMDI, with number mean diameters on the order of 5 µm (36), are at or below the resolution of the phase contrast images. Consequently, direct observation of their formation is not possible. For both formulations, the flow is dominantly atomised prior to the nozzle exit, though contiguous liquid is at times seen to extend outside the nozzle.

Atomisation upstream of the nozzle exit orifice can occur by a number of mechanisms. Shear driven by a velocity difference at liquid-vapour interfaces can produce droplets (2,18). Atomisation can also occur by stretching and rupture of bubbles and liquid as they enter the nozzle. Bubbles in the flow of the ethanol-containing formulation undergo a very large acceleration at the nozzle entry, and this acceleration is

not uniform across the bubble. The liquid films separating them are likely to break under this strain. For those droplets generated on entry to the nozzle, governing parameters would include the bubble size relative to the nozzle diameter and the thickness of the liquid film.

Bubble nucleation and expansion can rupture the liquid phase in flashing sprays, giving rise to atomisation. This mechanism was proposed by Dunbar (13) as the atomisation mechanism in pMDIs. Direct observation of bubble nucleation and liquid phase rupture within the nozzle of the pMDI requires spatial and temporal resolutions higher than those of the presented measurements.

For both formulations, atomisation is initiated upon entry to the nozzle and progresses throughout. The inclusion of ethanol has the added effect of stabilising the spray. The filling and discharge of large volumes of liquid in the propellant-only case is substantially reduced in the ethanol-containing case. As large droplets in pMDI sprays contain large masses of drug and ultimately deposit in the oropharynx, suppression of their formation is of practical interest.

Absorption Coefficient Error

For the radiography measurements published here and in Mason-Smith et al. (33), the absorption coefficient used is a mass-weighted average of the formulation components. It is implicitly assumed in this method that the beam path-integrated mass concentrations of propellant and ethanol are equivalent to those of the formulation. This assumption is not always reasonable; multicomponent mixtures have liquid and vaporous phases with different compositions depending on the relative volatility of each component. This is the principle of distillation (17). For the ethanol-containing discharge, the vapour will be almost entirely propellant and the liquid will have a higher ethanol concentration than the formulation. A change in composition is also associated with a change in absorption coefficient. Here we investigate the potential bias error associated with the absorption coefficient to ensure the finding of high vapour volume fraction in the nozzle is not dependent on the use of the formulation absorption coefficient.

Absorption coefficients of the liquid and vapour phases of equilibrium saturated mixtures of HFA134a and ethanol at 298 K are shown in Fig. 9. The vapour is almost entirely composed of propellant for $w_{l,eth}$ up to 0.95, due to the large difference of relative volatilities for HFA134a and ethanol. Depending on the liquid-vapour mass fractions along the beampath, the projected mass estimated with Eq. 1 using the formulation absorption coefficient may not predict the true mass. The true absorption coefficient is bounded by the absorption coefficient of pure propellant, at most a 10% error for the formulation studied, and the absorption coefficient associated with the liquid, which will deviate from the

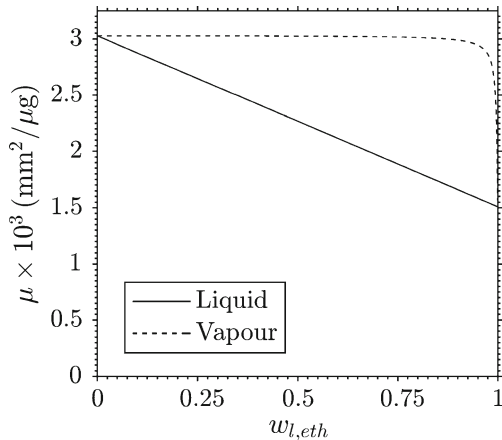


Fig. 9 Absorption coefficients μ_l and μ_v of liquid and vapour phases of HFA134a/ethanol equilibrium saturated mixtures against liquid phase ethanol mass fraction $w_{l,eth}$. Data presented at 298.15 K.

formulation by small amounts near the start of injection and to a greater extent at late stages in the spray when flash boiling of propellant has reduced its concentration in the liquid phase. Within these bounds, the nozzle exit area is always dominantly occupied by vapour.

Mass Flowrates

Radiography provides a quantitative concentration measurement which can be related to the mass flowrate through a multiphase flow model. The mass flowrate is an important spray parameter that is difficult to measure directly.

A number of models exist for discharge of flashing sprays (44). Applying the homogeneous frozen model (HFM), a mixture speed of sound c_m is obtained using Eq. 8. For the results presented here, a constant vapour pressure and saturated liquid density are used. The vapour pressure gradually reduces as propellant flashing cools the mixture, and very late in the injection the pressure is insufficient to choke the flow (9,14,22).

Applying the above assumptions, the mass flow rate m becomes:

$$m(t) = C_D \frac{\pi d_{no}^2}{4} \sqrt{\frac{(\rho_l(1-\alpha_v(t)) + \rho_v(t)\alpha_v(t))}{\left(\frac{\alpha_v(t)}{\rho_v(t)c_v^2} + \frac{(1-\alpha_v(t))t}{\rho_l c_l^2}\right)}} \quad (9)$$

where C_D is the nozzle discharge coefficient:

$$C_D = \frac{\dot{m}}{\dot{m}_{ideal}} \quad (10)$$

Discharge coefficients account for the deviation between the measured flowrate and an idealised flow rate. Deviations from ideality arise from vena contracta effects reducing the effective discharge area, cavitation and/or flashing reducing the nozzle discharge density relative to the upstream chamber

condition, and entropy generation in the flow (42). For sharp-edged orifices such as that for the nozzle entry here, if contraction effects are dominant, the ideal discharge coefficient is $\pi/(\pi + 2)$ (3,37), which is 0.61.

Applying this ideal value of C_D , the mass flowrate can be estimated from the volume fractions and the vapour density. The discharged spray mass can be predicted by time-integration of $m(t)$:

$$m(t) = \int_0^t \dot{m}(t) dt \quad (11)$$

and the total mass discharged is $m(t)$ at end-of-injection, which was chosen to occur when $\alpha_v = 1$. The mass flowrate of the vapour phase is obtained by multiplying the mass flowrate by the quality q , which is equivalent to mass fraction for a homogeneous mixture:

$$q(t) = \frac{\dot{m}_v(t)}{\dot{m}(t)} = \frac{\rho_v(t)\alpha_v(t)}{\rho_m(t)} \quad (12)$$

The estimated mass flowrate and the cumulative mass discharged of each phase as functions of time are shown in Fig. 10. The ratio of vapour-to-liquid discharged during the injection is 0.7 for HFA134a and 0.6 for the HFA134a/Ethanol mixture. For both formulations, 50% of the liquid discharge occurs during the first 60 ms.

The spray mass m was measured experimentally for each formulation by weighing canisters before and after 55 sprays. Table III lists the measured and predicted discharge mass for each formulation, and shows good agreement. If the C_D for sharp-edged orifices is applicable over the time-varying conditions of this flow, the mixture speed of sound predicted with Eq. 8 is a reasonable estimation of the ideal nozzle discharge velocity. This also suggests the radiography measurements can be used to provide a time-variant mass flowrate, a very difficult parameter to measure.

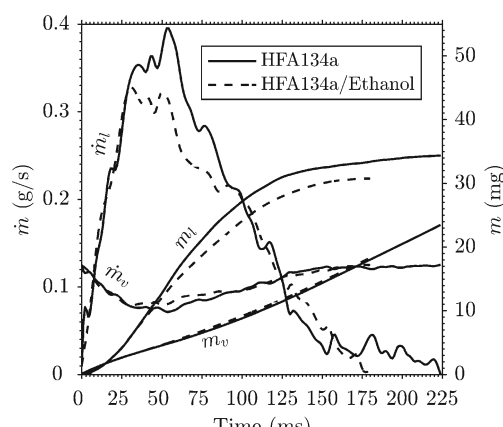


Fig. 10 Mass flowrate m and discharged mass m against time.

Table III Measured and Predicted Spray Mass m

Formulation	Measured (mg)	Predicted (mg)
HFA134a	59.71 ± 0.02	57.7
HFA134a/Ethanol	53.80 ± 0.02	49.0

Experimental validation is necessary to ensure thermodynamic models of pMDI sprays capture the relevant physics. The thermodynamic model of Clark (9) was validated with experimental pressure and temperature measurements inside the expansion chamber, and Dunbar (13) used phase-doppler particle analysis in the dilute spray regions far downstream of the nozzle. More recent efforts at extending thermodynamic modelling to multicomponent pMDI sprays (22) would benefit from experimental validation with measurements of physical spray parameters. The measurements and visualisations presented here have quantified the spray mass and revealed the internal flow structure, enabling the development and validation of a new multicomponent pMDI spray model.

CONCLUSION

The internal flows of pMDIs contain large volumes of vapour that originate upstream of the valve stem and dominate the volume in the expansion chamber. Propellant-only flows are characterised by a continuous vapour core that extends from the valve stem into the sump, and large droplets which are not in the respirable range are produced by liquid discharged from the nozzle when the base of the sump fills with liquid. The inclusion of ethanol substantially alters the internal flow structure by preventing bubble coalescence, additionally stabilising the spray. Quantification of the spray density showed that at all times in the injection the nozzle exit area is dominantly occupied by vapour, with peak liquid volume fractions around 10%. Combining radiography measurements with a multiphase flow model can predict the time-variant mass flowrate and provide experimental validation of thermodynamic models used for pMDI modelling. This research highlights the importance of the internal flow structure on spray formation from suspension and solution pMDIs.

ACKNOWLEDGMENTS AND DISCLOSURES

The authors gratefully acknowledge the support given to the project by the Australian Research Council. The authors wish to thank Dr. Chris Powell and Dr. Katarzyna Matusik, Energy Systems Division, Argonne National Laboratory, Dr. Jin Wang and Dr. Don Walko, X-Ray Science Division, Argonne National Laboratory, and Mr. James Harkess, Monash University. This research was performed at the 7-ID and 7-BM beamlines of the Advanced Photon Source at

Argonne National Laboratory. Use of the APS is supported by the U.S. Department of Energy (DOE) under Contract No. DE-AC02-06CH11357. The U.S. Government retains for itself, and others acting on its behalf, a paid-up nonexclusive, irrevocable worldwide license in said article to reproduce, prepare derivative works, distribute copies to the public, and perform publicly and display publicly, by or on behalf of the Government.

REFERENCES

- Andreoli-Ball L, Patterson D, Costas M, Cáceres-Alonso M. Heat capacity and corresponding states in alkan-1-ol-n-alkane systems. *J Chem Soc, Faraday Trans 1*. 1988;84(11):3991–4012.
- Azzopardi B. Drops in annular two-phase flow. *Int J Multiphase Flow*. 1997;23:1–53.
- Beam H, Buckingham E, Murphy P (1929) Discharge coefficients of square-edged orifices for measuring the flow of air. US National Bureau of Standards Research Paper 49
- Bendat JS, Piersol AG. Random data: analysis and measurement procedures. 2nd ed. New York: Wiley; 1986.
- Berger M, Hubbell J, Seltzer S, Chang J, Coursey J, Sukumar R, et al. Xcom: photon cross sections database. NIST Standard Ref Database. 1998;8:3587–97.
- Chen Y, Young PM, Murphy S, Fletcher DF, Long E, Lewis D, Church T, Traini D. High-speed laser image analysis of plume angles for pressurised metered dose inhalers: The effect of nozzle geometry. *AAPS PharmSciTech* 2016. pp 1–8
- Chesters A, Hofman G. Bubble coalescence in pure liquids. In: Mechanics and Physics of Bubbles in Liquids, Springer, 1982 pp 353–361.
- Chigier N. Optical imaging of sprays. *Prog Energy Combust Sci*. 1991;17(3):211–62.
- Clark AR. Metered atomisation for respiratory drug delivery. PhD thesis, Loughborough University of Technology. 1991.
- Corradini ML (1997) Fundamentals of multiphase flow. URL <http://wins.engr.wisc.edu/teaching/mpBook/main.html>.
- Duke D, Swantek A, Tilocco Z, Kastengren A, Fezzaa K, Neroorkar K, Moulai M, Powell C, Schmidt D. X-ray imaging of cavitation in diesel injectors. Tech. rep., SAE Technical Paper. 2014.
- Duke DJ, Kastengren AL, Mason-Smith N, Chen Y, Young PM, Traini D, Lewis D, Edgington-Mitchell D, Honnery D. Temporally and spatially resolved x-ray fluorescence measurements of in-situ drug concentration in metered-dose inhaler sprays. *Pharm Res*. 2016;33(4):816–25.
- Dunbar C. An experimental and theoretical investigation of the spray issued from a pressurised metered-dose inhaler. PhD thesis, University of Manchester, Manchester, United Kingdom. 1996.
- Dunbar C, Miller J. Theoretical investigation of the spray from a pressurized metered-dose inhaler. *AtomizationSprays*. 1997;7 (4).
- Gavtash B, Myatt B, O'Shea H, Mason F, Church T, Versteeg H, Hargrave G, Brambilla G. Saturated vapour pressure (SVP) measurement of ethanol/HFA binary mixtures. In: Drug Delivery to the Lungs 26. 2015.
- Gureyev T, Mayo S, Myers D, Nesterets Y, Paganin D, Pogany A, et al. Refracting Röntgen's rays: propagation-based x-ray phase contrast for biomedical imaging. *J Appl Phys*. 2009;105(10):102, 005.
- Hengstebeck RJ. Distillation: principles and design procedures. Reinhold Pub. Corp. 1961.

18. Hewitt G, Hall-Taylor N. Annular two-phase flow. Pergamon Press. 1970.
19. Huang NE, Shen Z, Long SR, Wu MC, Shih HH, Zheng Q, *et al.* Liu HH (1998) The empirical mode decomposition and the Hilbert spectrum for nonlinear and non-stationary time series analysis. *Proc R Soc Lond A: Math Phys Eng Sci.* 1971;454:903–95.
20. Ivey JW, Vehring R, Finlay WH. Understanding pressurized metered dose inhaler performance. *Expert Opin Drug Deliv.* 2015;12(6):901–16.
21. Jähne B. Digital image processing, 6th ed. Springer. 2005.
22. Ju D, Shrimpton J, Hearn A. The effect of reduction of propellant mass fraction on the injection profile of metered dose inhalers. *Int J Pharm.* 2010;391(1):221–9.
23. Kastengren A, Powell C. Spray density measurements using x-ray radiography. *Proc Inst Mech Eng, D: Journal of Automob Eng.* 2007;221(6):653–62.
24. Kastengren A, Powell CF. Synchrotron X-ray techniques for fluid dynamics. *Exp Fluids.* 2014;55(3):1–15.
25. Kastengren A, Powell CF, Liu Z, Wang J. Time resolved, three dimensional mass distribution of diesel sprays measured with x-ray radiography. Tech. rep., SAE Technical Paper. 2009.
26. Kastengren A, Powell CF, Arms D, Dufresne EM, Gibson H, Wang J. The 7BM beamline at the APS: a facility for time-resolved fluid dynamics measurements. *J Synchrotron Radiat.* 2012;19(4):654–7.
27. Kastengren AL, Tilocco FZ, Duke DJ, Powell CF, Zhang X, Moon S. Time-resolved X-ray radiography of sprays from engine combustion network spray A diesel injectors. *Atomization Sprays.* 2014;24 (3).
28. Kraynik AM. Foam flows. *Annu Rev Fluid Mech.* 1988;20(1):325–57.
29. Lemmon E, McLinden M, Friend D. Thermophysical properties of fluid systems. NIST Chemistry Webbook, NIST Standard Reference Database 69. 2005.
30. Linne M. Analysis of X-ray phase contrast imaging in atomizing sprays. *Exp Fluids.* 2012;52(5):1201–18.
31. Mason-Smith N, Duke D, Fedrizzi M, Soria J, Edgington-Mitchell D, Honnery D. Back-illumination imaging of pressurised metered-dose inhaler sprays. In: Australian Conference on Laser Diagnostics in Fluid Mechanics and Combustion (Damon Honnery and Daniel Edgington-Mitchell 09 December 2015 to 11 December 2015), Monash University Publishing, 2015. pp 45–50
32. Mason-Smith N, Edgington-Mitchell D, Honnery D, Duke D, Soria J. Pressurised metered-dose inhaler spray structure. In: Proceedings of Turbulence and Shear Flow Phenomena 9, Melbourne, Australia. 2015.
33. Mason-Smith N, Duke DJ, Kastengren AL, Stewart PJ, Traini D, Young PM, *et al.* Insights into spray development from metered-dose inhalers through quantitative x-ray radiography. *Pharm Res.* 2016;33(5):1249–58.
34. Moon S, Gao Y, Park S, Wang J, Kurimoto N, Nishijima Y. Effect of the number and position of nozzle holes on in- and near-nozzle dynamic characteristics of diesel injection. *Fuel.* 2015;150:112–22.
35. Mullinger P, Chigier N. Design and performance of internal mixing multijet twin fluid atomizers. *J Inst Fuel.* 1974;47(393):251–61.
36. Myatt B, Newton R, Lewis D, Church T, Brambilla G, Hargrave G, Versteeg H, Gaytash B, Long E. PDA and high speed image analysis of HFA/ethanol pMDI aerosols: New findings. *Drug Deliv* *Lungs* 2015;26.
37. Nurick W, Ohanian T, Talley D, Strakey P. Impact of orifice length/diameter ratio on 90 deg sharp-edge orifice flow with manifold passage cross flow. *J Fluids Eng.* 2009;131(8):081103.
38. Park BS, Lee SY. An experimental investigation of the flash atomization mechanism. *Atomization Sprays.* 1994;4 (2).
39. Powell CF, Yue Y, Poola R, Wang J. Time-resolved measurements of supersonic fuel sprays using synchrotron x-rays. *J Synchrotron Radiat.* 2000;7(6):356–60.
40. San Lee J, Weon BM, Je JH. X-ray phase-contrast imaging of dynamics of complex fluids. *J Phys D Appl Phys.* 2013;46(49):494, 006.
41. Sanada T, Sato A, Shirota M, Watanabe M. Motion and coalescence of a pair of bubbles rising side by side. *Chem Eng Sci.* 2009;64(11):2659–71.
42. Schmidt DP, Corradini M. The internal flow of diesel fuel injector nozzles: a review. *Int J Engine Res.* 2001;2(1):1–22.
43. Shemirani FM, Church TK, Lewis DA, Finlay WH, Vehring R. Onset of flash atomization in a propellant microjet. *J Fluids Eng.* 2015;137(9):091101.
44. Sher E, Bar-Kohany T, Rashkovan A. Flash-boiling atomization. *Prog Energy Combust Sci.* 2008;34(4):417–39.
45. Smyth H, Mejia-Millan E, Hickey A. The effect of ethanol on solvency, vapor pressure, and emitted droplet size of solution metered dose inhalers containing HFA 134a. *Respir Drug Deliv.* 2002;8:2.
46. Smyth H, Hickey A, Brace G, Barbour T, Gallion J, Grove J. Spray pattern analysis for metered dose inhalers I: orifice size, particle size, and droplet motion correlations. *Drug Dev Ind Pharm.* 2006;32(9):1033–41.
47. Takagi S, Matsumoto Y. Surfactant effects on bubble motion and bubbly flows. *Annu Rev Fluid Mech.* 2011;43:615–36.
48. Wang Y, Liu X, Im KS, Lee WK, Wang J, Fezzaa K, *et al.* Ultrafast x-ray study of dense-liquid-jet flow dynamics using structure-tracking velocimetry. *Nat Phys.* 2008;4(4):305–9.
49. Yang YM, Maa JR. Bubble coalescence in dilute surfactant solutions. *J Colloid Interface Sci.* 1984;98(1):120–5.
50. Zhu B, Traini D, Chan HK, Young PM. The effect of ethanol on the formation and physico-chemical properties of particles generated from budesonide solution-based pressurized metered-dose inhalers. *Drug Dev Ind Pharm.* 2013;39(1):1625–37.

4.2 Concluding statement

In this chapter, phase contrast imaging was used to visualise the internal flow structures of propellant-only and ethanol-containing pMDI sprays. These visualisations revealed the internal flow in detail, and showed that the flow structure was a strong function of the formulation. Vapour is distributed within the liquid, and the scale at which it is distributed differs in the propellant-only and ethanol-containing cases. Many bubbles are present in the ethanol-containing case, whereas they coalesce in the propellant-only formulation and ultimately form a large vapour annulus in the valve stem. Determining whether this vapour annulus runs all the way to the nozzle exit, as has been suggested (Versteeg, Hargrave, and Kirby 2006), is difficult with path-integrated data.

Quantitative x-ray radiography measurements showed that, at all times during the injection, the nozzle exit of pMDIs is dominantly vapour by volume. Experimental uncertainty attributable to the absorption coefficient reduced the confidence in the specific value determined, but did not change the finding of vapour-dominated exit conditions. This behaviour is consistent with that determined from the pMDI analogue used in Chapter 3.

Reviewers highlighted that the original manuscript did not substantially distinguish between suspension and solution pMDIs. This was based on suggestions in the original manuscript that propellant-only sprays were not representative of pMDIs, and could not be used for study of realistic pMDI formulations. Importantly, there is a distinction between solution pMDIs, in which a cosolvent or excipient is added to the propellant, and suspension pMDIs, in which micronised drug particles are kept in suspension. The manuscript was revised to more accurately reflect this distinction, and states that the propellant-only case is representative of a suspension pMDI, while the ethanol-containing case is representative of a solution pMDI. This revision strengthened the paper considerably.

Reviewers also noted that the original manuscript was unclear with regard to the

mechanism by which the observed differences in internal structure may occur. As there are several mechanisms by which bubble coalescence could be prevented in the ethanol-containing formulation, and these are not investigated independently, it was necessary to acknowledge each of these as potential contributors to the phenomenon. These include a greater energy barrier to coalescence, due to a higher mixture surface tension, and Marangoni stresses driven by surface tension gradients normal to the bubble surfaces (Takagi and Matsumoto 2011). The manuscript was revised to acknowledge both of these as possible explanations for the observed behaviour.

The measurements obtained in this work are the first of their kind. The understanding of the internal flow properties of pMDIs that had been obtained from visualisations of transparent analogues (Fletcher 1975; Versteeg, Hargrave, and Kirby 2006; Myatt et al. 2015) is built upon by using both a real pMDI nozzle and a technique with high penetration through the vapour-liquid structure. This high penetration allowed the internal structure to be revealed in detail.

The inhomogeneity of the internal structure, and the substantial differences between propellant-only and ethanol-containing sprays, are of practical importance in understanding the atomisation characteristics of suspension and solution pMDIs. These differences are explored further in Chapter 5.

The radiography measurements obtained suggest a highly vaporised spray at the measurement location, very near to the nozzle exit. The measurements also provide profiles of the spray width, and projected mass distributions. These data can be compared with outputs of thermodynamic modelling. In Chapter 6, a theoretical approach is used to link the nozzle exit conditions to those after expansion to atmospheric pressure for propellant-only sprays. The model outputs are compared with the radiography measurements presented here.

Having established the internal flow behaviour for suspension and solution pMDIs, and having obtained quantitative data in the near-nozzle region, these data are used to develop a model of multicomponent pMDI internal flow in Chapter 7.

Chapter 5

High-speed X-ray Imaging of Pressurized Metered-dose Inhaler Sprays with Variable Ethanol Content

5.1 Introductory statement

In Chapter 4, phase contrast images of propellant-only and ethanol-containing pMDIs were shown. These images detailed the internal flow structure, and highlighted the differences that occur when ethanol is added to the propellant. The highly inhomogeneous internal structure of propellant-only flows was demonstrated.

Backlit spray imaging (Appendix B) and phase doppler anemometry (Versteeg et al. 2017) of pMDIs have shown that these sprays contain large liquid droplets, with diameters of approximately 100 μm . The poor flow tracing ability of these droplets is expected to result in their deposition in the oropharynx. Although small in number, these large droplets likely contain substantial masses of drug, each one the equivalent to thousands of small droplets, based on the third power dependence

of the droplet volume. For this reason, it is important to identify the sources of these large droplets and whether methods for mitigating their formation exist.

Furthermore, determining the trend of vapour/liquid scale with ethanol addition requires more measurements than those presented in Chapter 4. From the two cases previously presented, it is not possible to determine whether the inclusion of ethanol has a highly nonlinear effect on the flow morphology, and specifically whether this modification occurs at low ethanol concentrations. Nonlinear behaviour is exhibited in binary liquids containing surfactants, where even a small concentration of a second liquid can radically alter the flow morphology (Takagi and Matsumoto 2011). To understand the trend of vapour/liquid scale with ethanol concentration, phase contrast images were obtained that covered a broader range of ethanol concentrations. Knowledge of this trend is required to incorporate internal flow inhomogeneity into thermodynamic models of pMDIs.

In this chapter, phase contrast imaging results are presented that extend the work shown in Chapter 4. Images are shown of internal flow structures in the sump at different times, and for an additional ethanol concentration. Higher magnification images of the two-phase flow structures at the atomising nozzle inlet and outlet are also presented. These images permit a discussion of the sources of unrespirable droplets in pressurised metered-dose inhaler sprays.

The work takes the form of a peer-reviewed conference paper presented at *Institution for Liquid Atomization & Spray Systems Asia 2017*¹.

¹ “ILASS-Asia 2017 is the 19th Annual Conference organized by ILASS-Asia that was formed in 1991 as a part of the International Council of Liquid Atomization and Spray Systems (ICLASS). This conference provides a forum to exchange technical information and to promote friendship between the members of each ILASS bodies [*sic*] in the Asia region.”

High-speed X-ray Imaging of Pressurized Metered-dose Inhaler Sprays with Variable Ethanol Content

N. Mason-Smith^{1,*}, D.J. Duke^{1,2}, A.L. Kastengren³, D. Edgington-Mitchell¹, D.R. Honnery¹

¹ Laboratory for Turbulence Research in Aerospace and Combustion, Department of Mechanical and Aerospace Engineering, Monash University, Australia

² Energy Systems Division, Argonne National Laboratory, Illinois, USA

³ X-ray Science Division, Argonne National Laboratory, Illinois, USA

Keywords: x-ray imaging; synchrotron radiation; flash atomization

1. Introduction

There is a need to understand the atomization mechanisms of medical inhalers if we are to improve their low efficiency. Pressurized metered-dose inhalers (pMDI) form a spray of a drug-containing solution or suspension, and are typically driven by hydrofluoroalkane propellants. An obstacle to development of higher efficiency inhalers is a lack of knowledge of the spray's initial conditions. The pressure, temperature and void fraction of the flow entering the atomizing nozzle all vary during the transient injection. There has been a dearth of experimental data regarding the internal flow state, which determines the properties of the aerosol. Hence the need for this work.

We used high-speed x-ray phase contrast imaging to visualize the two-phase flow inside pressurized metered-dose inhalers. These images point toward sources of low efficiency in existing inhalers. We found important differences between propellant-only and ethanol-containing flows, and offer interpretations of the produced data.

2. Research Method and Procedure

2.1 Phase contrast imaging

We performed phase contrast imaging at the 7-ID beamline of the Advanced Photon Source (APS) at Argonne National Laboratory (ANL). The technique is discussed in detail in [1]. Phase contrast images are line-of-sight projections that combine the effects of absorption and diffraction at phase boundaries.

Measurements were performed during 'hybrid singlet' mode at the APS. We were able to set the camera shutter to acquire light from a single bunch, resulting in an effective exposure time of 150 ps [2].

Interpretation of phase contrast images is most

straightforward in the Fresnel diffraction regime, where diffraction patterns associated with phase boundaries are clearly rendered [3]. The regime's lower limit of characteristic size a is determined by the wavelength of light λ and the free-space propagation distance Z_0 [3]:

$$a > \sqrt{Z_0\lambda}$$

Based on a dominant photon energy of 20 keV and the free-space propagation distance used for our experiments, features of interest in our images fall within the Fresnel regime.

A linear solenoid-driven device was used to remotely generate pMDI sprays. The nozzle orifice diameter is 300 μm . A schematic of the pMDI is shown in Figure 1. Drug-free formulations were used and contained either propellant HFA134a or HFA227ea, mixed with ethanol at mass concentrations of up to 30%.

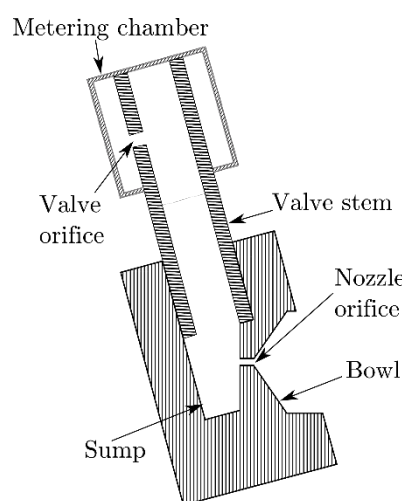


Fig. 1. Schematic of pMDI metering chamber and nozzle geometry (adapted from [2]).

3. Results and Discussion

3.1 Multiphase flow morphologies

Nozzle flow, atomization and the choking condition at the nozzle outlet are affected by the structure of the multiphase flow entering the nozzle inlet [4]. Visualizations of the vapor-liquid structure in the sump of the pMDI, directly upstream of the nozzle orifice, are shown in Figures 2 and 3. Images in Figure 2 were taken 45 ms after start of injection, and Figure 3 shows images taken 90 ms after start of injection. White vertical lines at the nozzle inlet are artefacts associated with two-point calibration background correction [5].

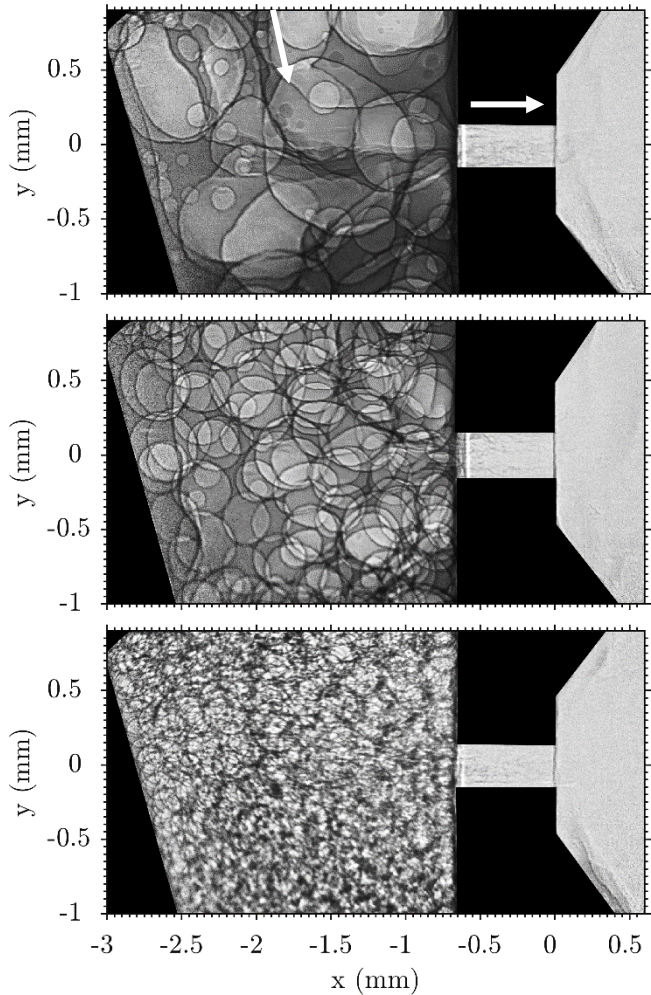


Fig. 2. Instantaneous images of internal flows of (top) HFA134a propellant-only, (middle) HFA134a/ethanol (5% by weight) and (bottom) HFA134a/ethanol (15% by weight) formulations. All images are 45 ms after start of injection. Flow enters at top of frame and exits to the right as indicated by arrows.

Propellant-only flows (Figures 2 & 3, top) consist of a liquid/vapor mixture with a large characteristic size. Individual liquid-vapor boundaries are observable, indicating the presence of bubbles and droplets. The

inclusion of ethanol at the low concentration of 0.5% by weight had no discernible effect in the presented measurements. At an ethanol concentration of 5% by weight, the structure is modified, resulting in a bubbly flow with different characteristic lengths (Figures 2 & 3, middle). At the higher concentration of 15% ethanol by weight, the number density of bubbles is greatly increased, to the point where individual boundaries are almost imperceptible (Figure 2, bottom). At later times in the injection the void fraction is increased and the number density of bubbles is reduced (Figure 3).

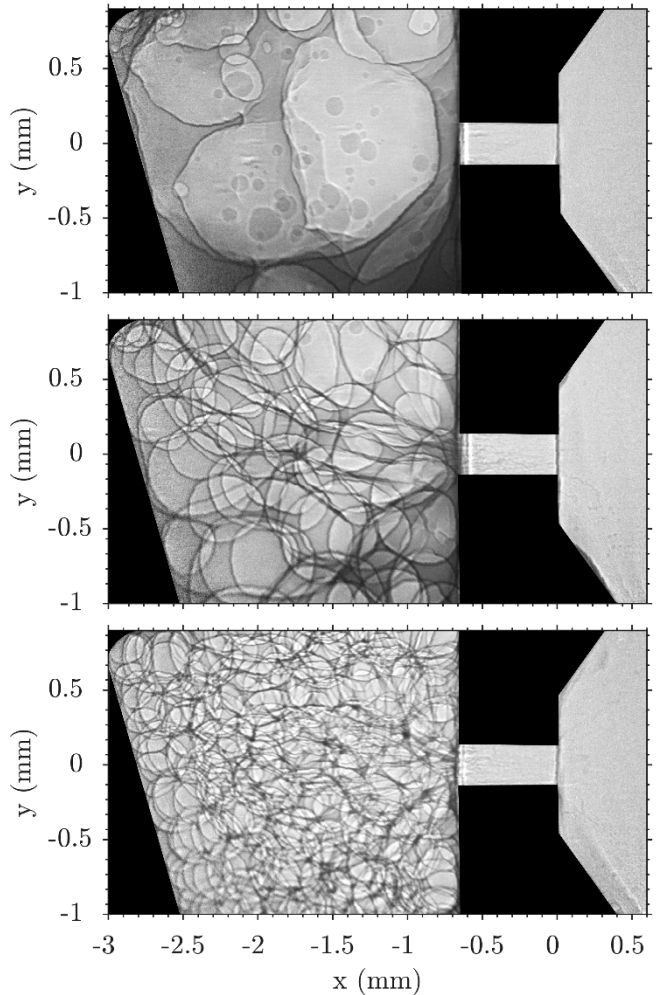


Fig. 3. Instantaneous images of internal flows of (top) HFA134a propellant-only, (middle) HFA134a/ethanol (5% by weight) and (bottom) HFA134a/ethanol (15% by weight) formulations. All images are 90 ms after start of injection. Flow enters at top of frame and exits to the right.

A consideration that arises is whether the change in flow morphology is attributable to the mixture surface tension. Bubble coalescence is expected to be less prevalent in higher surface tension liquid mixtures. In addition, Marangoni stresses, associated with surface tension gradients, may play a role in inhibiting bubble coalescence and contribute to the change in flow

morphology in pMDIs [6]. Predicting the mixture surface tension is not straightforward, particularly for non-ideal mixtures [7]. HFA/ethanol mixtures are non-ideal, as evidenced by a positive deviation from Raoult's law [8]. Experimental measurements of the surface tension of HFA/ethanol mixtures would assist in understanding the mechanisms that give rise to the observed changes in flow morphology.

3.2 Nozzle orifice inlet

A number of atomization mechanisms are expected to be present in metered-dose inhaler sprays. Phase contrast imaging allows us to observe the patterns of features entering and exiting the atomizing nozzle of the inhaler. Flows in these regions are three-dimensional; accordingly, flow behavior implied by these images must be interpreted with caution.

To highlight some of the phenomena associated with the passage of these bubbly flows through the steep pressure gradient at the nozzle inlet, a short image sequence of a propellant-only flow is shown at the nozzle inlet in Figure 4. In the first image, two bubbles are elongated toward the nozzle inlet. These bubbles move into the nozzle, and in the subsequent frame circular fronts are apparent. These appear to be related to rapid expansion of the bubbles in the nozzle, consistent with a steep pressure gradient at the nozzle inlet.

Large droplets and ligaments are also observed in the valve stem and sump. A large liquid mass entering the nozzle inlet is shown in Figure 5. Visible light imaging of the near-nozzle region of pMDIs [9,10] have noted the presence of large droplets, some as large as 100 μm . Phase Doppler anemometry results have also indicated the presence of large isolated droplets in this size range [10]. Phase contrast imaging of the internal flow structure of propellant-only flows shows that discrete masses of continuous liquid with large length scales pass into the atomizing nozzle. The large liquid droplets and ligaments present in the vapor phase inside the sump are expected to be one source of large droplets in the spray, which are of practical importance for pMDIs as they contribute to oropharyngeal deposition. Simultaneous internal and external imaging was not possible at this magnification; determining whether these large liquid masses create unrespirable droplets remains an open question.

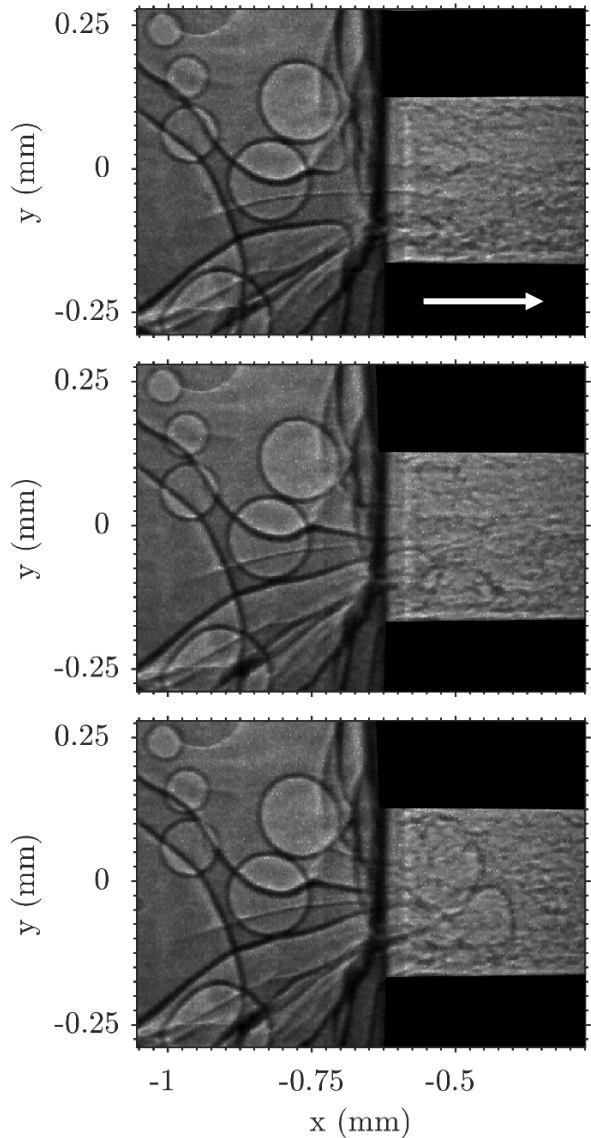


Fig. 4. Instantaneous images of internal flows of HFA134a propellant-only internal flow at the nozzle inlet 71 ms after start of injection. Flow travels from left to right.

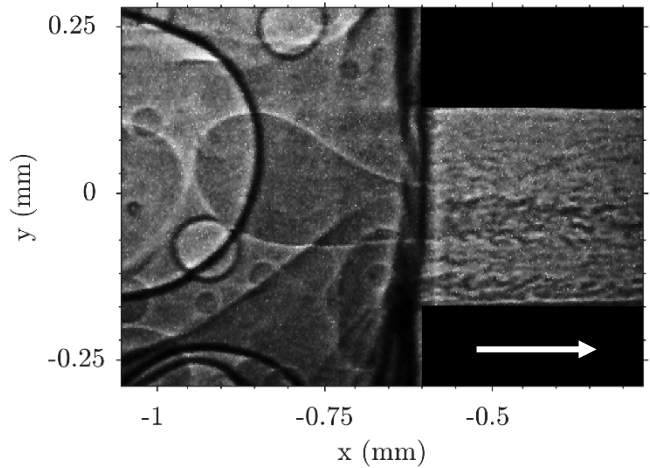


Fig. 5. Instantaneous image of internal flow of HFA134a propellant-only 76 ms after start of injection.

3.3 Nozzle orifice outlet

An instantaneous image of an ethanol-containing spray at the nozzle exit is shown in Figure 6. Several large ligaments are observable, one of which appears to undergo vibrational breakup. These features are similar to ligaments produced by fuel dribble at end-of-injection in diesel injection [11]. The droplets produced by these ligaments are expected to contribute to the unrespirable mass of the spray.

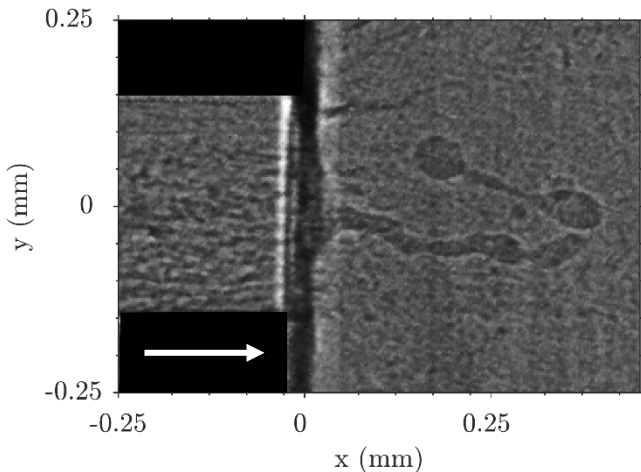


Fig. 6. Instantaneous image of nozzle and near-nozzle flow of HFA134a/Ethanol (15% by weight) 45 ms after start of injection.

4. Conclusion

This paper focused on the imaging of pMDI sprays and internal flows with high speed x-ray phase contrast imaging. Key findings are as follows:

1. The distribution of liquid and vapor is highly inhomogeneous in metered-dose inhaler internal flows.
2. Ethanol-containing cases have their vapor distributed at smaller scales than propellant-only cases. Higher ethanol concentrations have smaller scales of vapor distribution.
3. Large liquid masses are observed in the sump and pass into the atomizing nozzle. Ligaments are also observed at the nozzle exit. Both are expected to be sources of unrespirable droplets in pMDI sprays.

5. Acknowledgments

The authors gratefully acknowledge the support given to the project by the Australian Research Council. The authors wish to thank Dr. Chris Powell and Dr. Katarzyna Matusik, Energy Systems Division, Argonne National Laboratory, and Dr. Jin Wang and Dr. Don Walko, X-Ray Science Division, Argonne National Laboratory. This research was performed at the 7-ID and 7-BM beamlines of the Advanced Photon Source at Argonne National Laboratory. Use of the APS is supported by the U.S. Department of Energy (DOE) under Contract No. DE-AC02-06CH11357.

6. Reference

1. Kastengren, A.L., Powell, C.F., "Synchrotron X-ray techniques for fluid dynamics", *Experiments in Fluids*, 2014.
2. Mason-Smith, N., Duke, D., Kastengren, A., Traini, D., Young, P.M., Chen, Y., Lewis, D.A., Edgington-Mitchell, D., Honnery, D., "Revealing pMDI spray initial conditions: flashing, atomisation and the effect of ethanol", *Pharmaceutical Research*, pp. 718-729, 2017.
3. Willmott, P., "An Introduction to Synchrotron Radiation", Wiley, 2011.
4. Brennen, C.E. "Fundamentals of multiphase flow", Cambridge University Press, 2005.
5. Jähne, B. "Digital image processing", 4th ed., Springer, 2005.
6. Takagi, S., Matsumoto, Y., "Surfactant effects on bubble motion and bubbly flows", *Annual Review of Fluid Mechanics*, pp. 615-636, 2011.
7. Adamson, A.W., Gast, A.P., "Physical chemistry of surfaces", 6th ed., Wiley, 1967.
8. Gavtash, B., Myatt, B., O'Shea, H., Mason, F., Lewis, D., Church, T., Versteeg, H.K., Hargrave, G., Brambilla, G., "Saturated vapour pressure (SVP) measurement of ethanol/HFA binary mixtures", *Drug Delivery to the Lungs* 26, 2015.
9. Mason-Smith, N., Duke, D., Fedrizzi, M., Soria, J., Edgington-Mitchell, D., Honnery, D., "Back-Illumination Imaging of Pressurised Metered-Dose Inhaler Sprays", *7th Australian Conference on Laser Diagnostics in Fluid Mechanics and Combustion*, 2015.
10. Versteeg, H.K., Hargrave, G.K., Myatt, B., Lewis, D., Church, T., Brambilla, G., "Using Phase Doppler Anemometry and High Speed Imaging to Analyze MDI Spray Plume Dynamics", *Respiratory Drug Delivery Europe*, 2017.
11. Moon, S., Huang, W., Li, Z., Wang, J., "End-of-injection fuel dribble of multi-hole diesel injector: Comprehensive investigation of phenomenon and discussion on control strategy", *Applied Energy*, pp. 7-16, 2016.

5.2 Concluding statement

In this work, we investigated the scale of vapour distribution in ethanol-containing pMDIs. The scale at which the vapour is distributed in the liquid decreases with increasing ethanol concentration, and increases with increasing time after start of injection. Establishing this trend is necessary to model vapour/liquid inhomogeneity in thermodynamic models of pMDIs.

High magnification imaging revealed a number of sources of large droplets. These large droplets were observed to occur upstream of the atomising nozzle in propellant-only pMDIs. Additional large droplets were seen to shed from liquid pools formed on the bowl at the nozzle outlet.

Droplet sizing experiments on drug-free pMDI sprays (Myatt et al. 2015) have shown that drop size distributions in ethanol-containing pMDI sprays are narrower than those in propellant-only sprays. The large droplets in the sump of propellant-only pMDIs reported here, and the intermittent liquid accumulation and discharge observed in Chapter 4, provide a possible explanation for this reduction in droplet size distribution as ethanol is added.

The observed trend in vapour/liquid scale presented in this chapter is used to phenomenologically model flow inhomogeneity in thermodynamic modelling of pMDIs. The development and findings of this model are described in Chapter 7.

Chapter 6

A comparison of quantitative radiography and a propellant-only phenomenological model

6.1 Motivation

The radiography measurements obtained in Chapter 4 provided transverse profiles of the time-variant projected mass one nozzle diameter downstream of the nozzle exit. This projected mass can be predicted with phenomenological thermodynamic models, and the predicted value is a function of the model assumptions. One parameter of importance is the extent of in-nozzle vaporisation, which can be represented by the thermal non-equilibrium between the liquid and vapour phases. Phase change is a non-instantaneous process, and as such the system is not always in thermodynamic equilibrium. This vaporisation is important in determining the initial droplet size (Gavtash et al. 2017b), from which the drug particles precipitate in solution pMDIs. In this way, radiography measurements can provide insight into the in-nozzle behaviour of pMDIs.

6.2 Nomenclature

A - Area (m^2)

D - Diameter (m)

L - Length (m)

M - Projected mass ($\mu\text{g mm}^{-2}$)

P - Pressure (Pa)

R - Gas constant ($\text{J kg}^{-1} \text{K}^{-1}$)

T - Temperature (K)

V - Volume (m^3)

W - Axial velocity (m s^{-1})

TIM - Transverse integrated mass (kg m^{-1})

a - Amplitude parameter of Gaussian density profile (kg m^{-3})

c - Speed of sound (m s^{-1})

c_P - Mass-specific heat capacity at constant pressure ($\text{J kg}^{-1} \text{K}^{-1}$)

h - Specific enthalpy (J kg^{-1})

m - Mass (kg)

s - Specific entropy ($\text{J kg}^{-1} \text{K}^{-1}$)

v - Specific volume ($\text{m}^3 \text{kg}^{-1}$)

x - Quality

y - Coordinate perpendicular to spray axis

z - Coordinate parallel to spray axis

Greek letters

ρ - Density (kg m^{-3})

η - Thermal non-equilibrium parameter

η_{isen} - Nozzle isentropic efficiency ($\text{J kg}^{-1}/\text{J kg}^{-1}$)

σ - Standard deviation of Gaussian density profile (m)

γ - Ratio of specific heats

Subscripts

l - Liquid

v - Vapor

ml - Metastable liquid

sl - Saturated liquid

mv - Metastable vapour

sv - Saturated vapour

e - Expanded condition

t - Throat

0 - Reservoir condition

vo - Valve orifice

no - Nozzle orifice

mc - Metering chamber

ec - Expansion chamber

sat - Saturation

eq - Equilibrium

6.3 Analysis methodology

If the pMDI internal flow, and the near-nozzle spray, are treated as homogeneous two-phase mixtures, it is possible to use the one-dimensional approach that is common in gasdynamics (Liepmann and Roshko 1957). Homogeneous flows are multi-phase flows in which there is no relative velocity between phases ($W_l = W_v$). The assumption of homogeneity is reasonable for flows in which one phase is dispersed in the other at a very small scale. Recent investigations have applied homogeneous

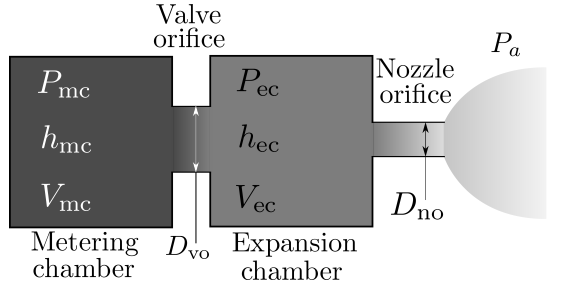


Figure 6.1: Schematic of pMDI geometry used in the thermodynamic model.

flow modelling to superheated fuels and refrigerants (Lytras et al. 2018), and assume that inertial forces dominate surface forces; that is, that the Weber number is high. Although the real flow is inhomogeneous, the analytical simplicity of the homogeneous flow assumption is the reason for its use here.

For a one-dimensional homogeneous flow model, an equation of state and/or thermodynamic property tables are used in place of the ideal gas equation of state, and a non-equilibrium model is used to describe the relationship between phases. This non-equilibrium model governs the change in quality x , which is the mass fraction of vapour in the vapour-liquid mixture, during depressurisation and acceleration from the expansion chamber to the near-nozzle region, where radiography measurements were obtained in Chapter 4.

Following the traditional approach (Clark 1991; Dunbar 1996; Ju, Shrimpton, and Hearn 2010; Gavtash et al. 2017b), for this model the pMDI is treated as two chambers; the metering chamber and expansion chamber. These are connected by a valve orifice, and the flow leaves the expansion chamber through the spray nozzle orifice. In this approach, the mixture in each chamber is treated as spatially homogeneous in temperature and quality, meaning that its thermodynamic state can be described with a pair of state variables (Callen 1960). This geometry is shown schematically in Figure 6.1.

A number of assumptions are required to develop this phenomenological model. The assumptions used are:

1. One-dimensional variable-area flow
2. The two-phase fluid is homogeneous (no relative velocity between phases) and spatially homogeneous in each chamber
3. Adiabatic flow
4. Quasi-steady flow ($\frac{\partial}{\partial t} \ll W \frac{\partial}{\partial z}$)
5. Conditions in each chamber can be represented by stagnation conditions
6. No gravitational effects
7. Propellant-only flow

Treating the flow in this way reduces the system of partial differential equations to a system of ordinary differential equations. The system of equations for the time derivatives of the propellant-only thermodynamic model is given in Appendix A. Pressure-enthalpy state variables are used to represent the two-phase mixture in each chamber.

These assumptions introduce many approximations; the real flow field is three-dimensional, non-axisymmetric, turbulent, inhomogeneous and non-adiabatic. As a method for investigating the significance of the projected mass distributions obtained from radiography, the approach provides a starting point for more exhaustive analyses.

To estimate the near-nozzle flow properties, two steps are required: a flow model to determine the expansion from stagnation conditions to the nozzle exit, and an expansion from the nozzle exit to atmospheric pressure in the near-nozzle region. These are discussed in turn.

Homogeneous flow models

To complete this system of equations, models are required for the predicted mass flow rate. In this work, only homogeneous flow models are considered. The flow

models considered are the homogeneous direct evaluation (HDE) model of Travis, Koch, and Breitung (2012), which incorporates the homogeneous equilibrium model (HEM), and the homogeneous frozen model (HFM). These are described below for isentropic flows. Non-isentropic flows are accounted for with isentropic efficiencies, which are described later in the methodology section.

Homogeneous direct evaluation

The homogeneous direct evaluation (Travis, Koch, and Breitung 2012) is a method for determining properties of homogeneous flows, accounting for thermal non-equilibrium between phases. The approach is based on the assumption that the vapour phase is at all times saturated, limiting metastability to the liquid phase. This is consistent with an energy barrier to vapour nucleation in liquid, while vapour condensation faces no such energy barrier (Skripov 1974, 1–3). The method is summarised below.

If the vapour phase is assumed to be saturated, its temperature T_v is equal to the fluid's saturation temperature at the given pressure P :

$$T_v = T_{\text{sat}}(P) \quad (6.1)$$

Thermal inhomogeneity between phases is permitted with a parameter η :

$$T_{\text{ml}} = \eta \cdot T_0 + (1 - \eta) \cdot T_{\text{sv}}(P) \quad (6.2)$$

where T_{ml} is the temperature of the metastable liquid and T_{sv} is the saturated vapour temperature. When $\eta = 0$, $T_{\text{ml}} = T_{\text{sv}}(P)$; this is the well-known homogeneous equilibrium model. At high values of η , metastability effects are significant for the liquid, and its temperature approaches that of an isentropic expansion from reservoir conditions. Phase change continues to occur even at high η values due to the condensation of vapour during depressurisation (Brennen 2005).

Having established a relationship between the pressure and the individual phase temperatures, finding the mass flux then reduces to finding conditions that satisfy

the steady one-dimensional adiabatic energy equation:

$$h_0 = (1 - x) \cdot h_{\text{ml}}(P, T_{\text{ml}}) + x \cdot h_{\text{sv}}(P) + \frac{W^2}{2} \quad (6.3)$$

where h is the specific enthalpy, and given the expansion is assumed to be isentropic:

$$s_0 = x \cdot s_{\text{sv}} + (1 - x) \cdot s_{\text{ml}} \quad (6.4)$$

where s is the specific entropy.

If the flow is critical, the velocity at the throat is equal to the two-phase speed of sound c :

$$W_t^2 = c^2 \quad (6.5)$$

$$c^2 = \left(\frac{\partial P}{\partial \rho} \right)_s \quad (6.6)$$

where ρ is the mixture density. Pressure waves propagate at low speed through homogeneous two-phase mixtures due to the large specific volume change for pressure perturbations. Details on calculating two-phase speeds of sound are given in Appendix A.

The system of equations, coupled with an equation of state, allows for the pressure and quality at the throat to be determined, providing the necessary information for the critical mass flow rate.

If the pressure downstream of the throat is sufficiently high that choking does not occur, a subsonic flow results. Calculating the properties of this subsonic two-phase flow follows the same methodology, except the exit static pressure is known.

Homogeneous frozen model

At the other extreme from the HEM, the homogeneous frozen model (HFM) assumes that the quality remains unchanged during expansion. For this model, phases are insulated from one another, and no heat or mass transfer occurs. It is most suitable for short nozzles in which phase change does not have sufficient time to occur (Wallis 1980). A similar approach to the homogeneous direct evaluation can be used. The

approach detailed here does not require the commonly-used assumptions (Fletcher 1975; Gavtash et al. 2017b) that the vapour phase obeys the ideal gas law, and that the liquid phase is incompressible.

If both liquid and vapour are assumed to be metastable, and no interphase mass transfer occurs, the downstream quality is equal to that in the reservoir. If the expansion is isentropic, the individual phase entropies remain unchanged:

$$s_{\text{ml}}(T, P) = s(T_0, x = 0) \quad (6.7)$$

$$s_{\text{mv}}(T, P) = s(T_0, x = 1) \quad (6.8)$$

$$x = x_0 \quad (6.9)$$

where s_{mv} is the specific entropy of metastable vapour.

Additionally, by the one-dimensional adiabatic energy equation:

$$h_0 = x \cdot h_{\text{mv}} + (1 - x) \cdot h_{\text{ml}} + \frac{W^2}{2} \quad (6.10)$$

Again, at choked conditions, the velocity is equal to the two-phase speed of sound:

$$W^2 = \left(\frac{\partial P}{\partial \rho} \right)_s \quad (6.11)$$

The flow conditions at the nozzle exit satisfy the conservation of entropy for each phase, and at critical conditions have a velocity equal to the two-phase speed of sound. The method for determining the two-phase speed of sound is given in Appendix A. For subcritical flows, the exit pressure is known and the determination of the exit properties is straightforward.

Near-nozzle expansion

For the model to be compared with the experimental data, which is obtained one nozzle diameter downstream of the nozzle exit, a theoretical link must be established between the flow in the nozzle, which is choked throughout much of the injection, and after expansion to atmospheric pressure. A control volume analysis is used

to relate the conditions at the nozzle exit to those after expansion to atmospheric pressure.

Gavtash et al. (2017b) argued, following Fletcher (1975), that the choked flow in the nozzle undergoes a rapid acceleration as it expands from the throat pressure to the ambient pressure. The velocity increase during this expansion can be approximated with an axial momentum balance over a diverging control volume by assuming that entrainment is negligible over the length required for the flow to expand to atmospheric pressure L_e (Gavtash et al. 2017b). Taking this approach allows the near-nozzle properties of homogeneous flows to be estimated.

The near-nozzle structure will in reality be more complicated; underexpanded jets are not one-dimensional flows, and are characterised by a series of ‘shock cells’ through which the flow expands to the ambient pressure (Edgington-Mitchell et al. 2014). The pressure across the jet cross-section may not match the ambient pressure until some diameters downstream, by which time entrainment effects may be significant. If the approximation is accepted, the time-variant transverse integrated mass measured by radiography at $z/D_{\text{no}} = 1$ can be compared with the near-nozzle transverse integrated mass predicted by phenomenological modelling.

Consider the control volume surrounding the nozzle orifice (throat) and the downstream spray shown in Figure 6.2. The control volume diverges sufficiently that the pressure on the upper and lower surfaces is equal to the ambient pressure, and there is no mass flow through the top and bottom surfaces—spray or entrained air.

By continuity:

$$\rho_t W_t A_t = \rho_e W_e A_e \quad (6.12)$$

where A_t is the cross-sectional area at the throat and A_e is that after expansion.

If the flow expands as a free jet, and the transfer of momentum to entrained air is negligible, the conservation of axial momentum becomes:

$$(P_t - P_a) \cdot A_t - (P_e - P_a) \cdot A_e = \rho_e W_e^2 A_e - \rho_t W_t^2 A_t \quad (6.13)$$

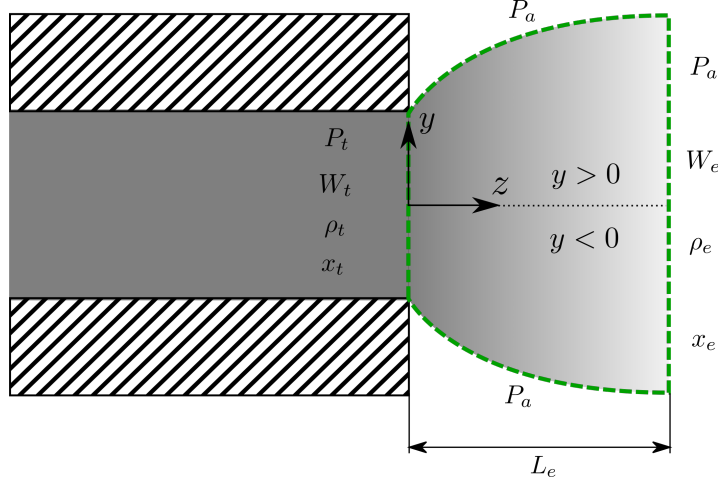


Figure 6.2: Control volume used for analysis of near-nozzle flow.

Combining the continuity and momentum equations, and assuming that $P_e = P_a$ gives (Gavtash et al. 2017b):

$$W_e = W_t + \frac{(P_t - P_a)}{\rho_t W_t} \quad (6.14)$$

The transverse integrated mass, as was determined from radiography, is the area-integrated spray density:

$$\text{TIM} = \int \rho dA \quad (6.15)$$

For the one-dimensional flow modelling used, the transverse integrated mass downstream of the throat is equal to that at the throat, divided by the velocity ratio:

$$\text{TIM}_e = \frac{\rho_t A_t W_t}{W_e} \quad (6.16)$$

If this expanded transverse integrated mass is normalised by the throat area, this is the nozzle exit density predicted with the methodology adopted in Chapters 3 and 4:

$$\frac{\text{TIM}_e}{A_t} = \rho_t \frac{W_t}{W_e} \quad (6.17)$$

In summary, the area-integrated density of the expanded state can be estimated from the throat conditions and the conservation of mass and axial momentum. This insight from the preceding analysis permits a comparison of homogeneous flow models and the experimental data reported in Chapter 4.

The spray density and area can also be obtained with the energy equation. A family of solutions are obtained for non-equilibrium conditions. For prediction of the density and area, the internal flow models are extended to the near-nozzle region. Although the area and density obtained depend on the post-nozzle phase non-equilibrium, it is important to recognise that the transverse integrated mass remains unaffected, provided that the flow is adiabatic and there is negligible entrainment.

The steady one-dimensional adiabatic energy equation is:

$$h_0 = h_e + \frac{W_e^2}{2} \quad (6.18)$$

The velocity has been determined with the control volume analysis in the previous section. The specific enthalpy of the expanded flow, h_e , is a function of the quality and the specific enthalpy of each phase:

$$h_e = h_{\text{ml}} \cdot (1 - x) + x \cdot h_v \quad (6.19)$$

For both the HDE and the HEM, $T_v = T_{\text{sat}}(P_a)$. The η parameter from Equation 6.2 is again used to determine the metastable liquid temperature, and Equations 6.18 and 6.19 can be solved to determine the quality. When the HFM is used, the quality is unchanged during expansion to atmospheric pressure.

Having obtained the quality, the density of the mixture can then be found:

$$\rho_e = \left(\frac{x}{\rho_v(P_a)} + \frac{1-x}{\rho_{\text{ml}}(T_{\text{ml}}, P_a)} \right)^{-1} \quad (6.20)$$

where ρ_v is either saturated or metastable, depending on which flow model is used. Similarly, the area is then obtained from continuity:

$$A_e = \frac{\rho_t W_t A_t}{\rho_e W_e} \quad (6.21)$$

Notably, many combinations of density and area are possible, depending on the conditions after expansion. The real flow is a spray, not a jet, and the mean spread may be greater than that predicted with the quasi one-dimensional approach. This is used to advantage in reconciling the model predictions with experimental results.

Axisymmetric projected mass

Further comparison between modelling and radiography can be made if the projected mass is used. In Chapter 4, time-variant ensemble-mean projected mass plots were shown for pMDI sprays. If the quasi one-dimensional approach used above holds, the expanded conditions downstream of the nozzle exit have a cross-sectional area that is a function of time, and a uniform density across this cross-section. Treating the flow as cylindrically axisymmetric, a projected mass M can be obtained from this density with the forward Abel transform (Dasch 1992):

$$M(y, t) = 2 \int_y^{\infty} \frac{\rho(r, t) \cdot r}{\sqrt{r^2 - y^2}} dr \quad (6.22)$$

where $\rho(r, t)$ is the radial density distribution as a function of time and y is the coordinate perpendicular to the spray axis. Different density distributions will have different projected masses, as the integral changes. Information on the Abel transform, and examples of different radial distributions and their corresponding transverse distributions, are given in Appendix D.

The assumption of axisymmetry allows the obtained plots to be compared with radiography results. The assumption of uniform density is relaxed in accounting for differences between the experimental and model results. Specifically, a radial Gaussian distribution is also considered. The expressions for projected mass as functions of TIM and a shape factor σ are derived below.

The transverse integrated mass TIM is the area-integrated density. For an axisymmetric density distribution:

$$TIM = 2\pi \cdot \int_0^{\infty} \rho(r) \cdot r dr \quad (6.23)$$

If the radial density distribution $\rho(r)$ is Gaussian:

$$\rho(r) = a \cdot \exp\left(-\left(\frac{r}{\sigma}\right)^2\right) \quad (6.24)$$

Using integration by substitution, it can be shown that:

$$a = \frac{TIM}{\pi \cdot \sigma^2} \quad (6.25)$$

and, using the Abel transform to obtain the projected mass M :

$$M(y) = \frac{\text{TIM} \cdot \exp(-(y/\sigma)^2)}{\sigma \cdot \sqrt{\pi}} \quad (6.26)$$

For a uniform density distribution with a radial extent of R from the spray axis:

$$\rho(r) = \begin{cases} \rho_0 & 0 \leq r \leq R \\ 0 & r > R \end{cases} \quad (6.27)$$

the Abel transform gives the projected mass M :

$$M(y) = \begin{cases} 2 \cdot \rho_0 \cdot \sqrt{R^2 - y^2} & 0 \leq r \leq R \\ 0 & r > R \end{cases} \quad (6.28)$$

Nozzle isentropic efficiency

Discharge coefficients are used in one-dimensional phenomenological models (Clark 1991; Gavtash et al. 2017b) to account for the discrepancy between experimentally-observed mass flow rates and those predicted by isentropic analyses. The effect of entropy generation on flow properties other than the mass flux, such as the density, pressure and velocity at the throat, are not explicitly determined with a discharge coefficient; the discharge coefficient accounts only for the product of the velocity and the density. As concentration-based flow properties are used to compare the model with experiment, a different approach is needed.

The physical phenomena that lead to reduced flow rates in real nozzles, relative to isentropic predictions, include the formation of a vena contracta at the nozzle inlet (Ward-Smith 1979) and cavitation in the nozzle (Nurick 1976). For critical flows of compressible fluids through square-edged cylindrical nozzles, several flow regimes are possible. These are shown in Figure 6.3 (adapted from Ward-Smith (1979)). For a sharp-edged orifice (as L/D approaches zero), the flow is sonic at the vena contracta, which increases in size with decreasing pressure ratio P/P_0 (Deckker and Chang 1965). When a vena contracta occurs at the nozzle inlet and the nozzle is

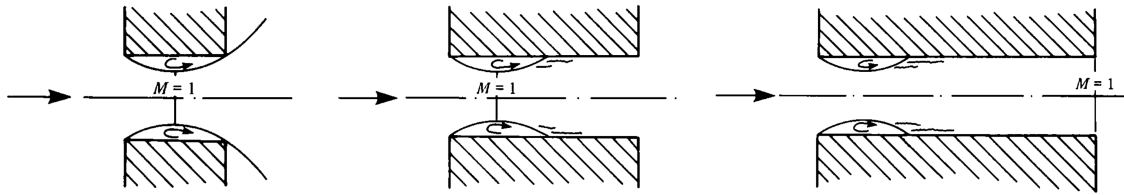


Figure 6.3: Basic flow patterns for square-edged cylindrical nozzles as the choked condition is reached: (left) marginally reattached flow, (middle) fully reattached flow with vena contracta choking, and (right) fully reattached flow with outlet (Fanno) choking (adapted from Ward-Smith (1979)).

long enough for the flow to reattach, choking occurs at the vena contracta. Intuition suggests that the vena contracta may behave like a converging-diverging nozzle; this is consistent with the in-nozzle schlieren results of Weir, York, and Morrison (1956), who observed a series of oblique shocks downstream of the vena contracta and expansion waves at the nozzle outlet. For nozzles of greater length, the specific volume increase due to frictional pressure loss in the pipe may be sufficiently great for choking to occur at the nozzle outlet, rather than the region of smallest cross-sectional area at the vena contracta. This is Fanno choking (Shapiro 1953). In addition, the one-dimensional approach ignores velocity and density gradients across the nozzle, which affect the predicted area-integrated mass flow rate. This discussion is intended to highlight the complexity of flows through square-edged orifices, and the inadequacy of discharge coefficients in describing all of the above processes.

Here, an isentropic efficiency is used to reduce the mass flow rate. This is done under the assumption that Fanno choking occurs, and vena contracta choking does not. Although this approach is also simple, it is consistent with the one-dimensional adiabatic modelling approach, and allows flow properties other than the mass flow rate to be determined.

The isentropic efficiency of a nozzle is defined as the ratio of the specific kinetic energy during an adiabatic expansion to that of a reversible adiabatic expansion to the same final pressure (Shapiro 1953, 98–100):

$$\eta_{\text{isen}} = \frac{h_0 - h(P)}{h_0 - h(P, s_0)} \quad (6.29)$$

For a clearer understanding of the characteristics of non-isentropic choked flows, a brief overview of choked flows of calorically-perfect gases is given.

For calorically-perfect gases, the enthalpy change can be expressed with total temperatures (Cohen, Rogers, and Saravanamuttoo 1996):

$$\eta_{\text{isen}} = \frac{T_0 - T(P)}{T_0 - T(P, s_0)} \quad (6.30)$$

For choked flows of calorically-perfect gases, the effect of entropy is to increase the specific volume and reduce the pressure at the throat. The specific kinetic energy at the throat is unaffected, because the solution of the one-dimensional adiabatic energy equation (Equation 6.18) and the critical flow condition:

$$W^2 = \gamma \cdot R \cdot T \quad (6.31)$$

is, for a calorically-perfect gas, independent of the entropy. In this equation, γ is the ratio of specific heats and R is the gas constant. For unchoked flows, the throat pressure is fixed, and entropy generation reduces the throat velocity and increases the specific volume. For both choked and unchoked calorically-perfect gas flows, the mass flux decreases with decreasing isentropic efficiency.

For flows that are not calorically-perfect gases, such as two-phase systems, the enthalpy is not solely a function of the temperature. The speed of sound is a function of both the enthalpy and the entropy; consequently, the increase in entropy changes both the quality, if the flow is not frozen, and the speed of sound. As a numerical approach to the problem, a root-finding algorithm is used to determine the throat pressure that satisfies:

$$h_0 = h + \frac{W^2}{2} \quad (6.32)$$

$$W = c \quad (6.33)$$

and:

$$h = h_0 - \eta_{\text{isen}} \cdot (h_0 - h(P, s_0)) \quad (6.34)$$

The non-isentropic choked flows have lower throat pressures, higher qualities and, in general, different velocities than isentropic choked flows from the same reservoir

conditions. For frozen flows, the quality remains unchanged, however other flow properties change in the same manner. For subcritical flow, the specific enthalpy at the throat can be directly determined from the reservoir conditions, exit pressure, and the nozzle isentropic efficiency.

Implementation

The system of equations described above was developed as a Python program. These were numerically integrated using the LSODA scheme from the ODEPACK numerical integration package (Hindmarsh 1983). Dynamic adjustment of both the integration scheme and time step size is achieved by monitoring the error between the integration scheme and a higher-order integration scheme, similar to the Runge-Kutta-Fehlberg method (Moin 2010). As time step monitoring was achieved within the program, the effect of time step on the solution was not investigated.

The model required a large number of thermophysical fluid properties, including partial derivatives. Modern approaches for thermodynamic property estimation use Helmholtz energy-explicit multiparameter equations of state (Bell et al. 2014), which allow determination of these properties to high accuracy. Fluid property programs that use these equations of state include the proprietary REFPROP (Lemmon, Huber, and McLinden 2002) and open-source CoolProp (Bell et al. 2014). For this program, CoolProp was used to determine all thermophysical properties.

Thermophysical properties were also required for metastable fluids. These can be determined by integrating the equation of state from the saturation line. Using the specific enthalpy of metastable liquid as an example:

$$h_{\text{ml}}(T, P) = h_{\text{sl}}(T) + \int_{P_{\text{sat}}}^P \left(\frac{\partial h}{\partial P} \right)_T dP \quad (6.35)$$

where the derivative follows the equation of state in the saturation region. Metastable fluid properties were determined by approximating the integral with a second-order Taylor series expansion from the saturation line. Again, using the specific enthalpy

as an example:

$$h_{\text{ml}}(T, P) = h_{\text{sl}}(T) + \Delta P \cdot \left(\frac{\partial h}{\partial P} \right)_T + \frac{(\Delta P)^2}{2} \cdot \left(\frac{\partial^2 h}{\partial P^2} \right)_T + \mathcal{O}((\Delta P)^3) \quad (6.36)$$

where $\Delta P = P - P_{\text{sat}}(T)$, and the partial derivatives are evaluated at the saturation line. Parameters other than the temperature can be held constant, provided the appropriate derivatives are obtained. For arbitrary processes in which no single variable is held constant, a two-dimensional Taylor series expansion can be used. Two-dimensional Taylor series expansions were used to determine the thermodynamic properties of metastable liquid and vapour in the non-isentropic homogeneous frozen model.

For liquid temperatures closer to the critical point, or with alternative propellants, the error introduced by determining metastable properties with second-order Taylor series expansions may become significant. This is especially true if the liquid expansion crosses the spinodal and enters the unstable region, where homogeneous nucleation occurs (Callen 1960). For HFA134a and HFA227ea at typical operating conditions, the error introduced by the method adopted is small (Thorade 2014).

Initial conditions

For the cases studied here, the initial conditions and modelling parameters are summarised in Table 6.1. Note that the expansion chamber, which in reality will initially contain air and/or superheated propellant vapour from priming sprays, is modelled as initially containing saturated propellant vapour at 1 atm.

In the model, the valve orifice is assumed to be completely open at start of injection. Unpublished phase contrast image sequences of the metering chamber show that the valve opening time for the apparatus used in the radiography experiments was approximately 1 ms. For this reason, it is assumed that the valve opening rate has a small effect on both the radiography and modelling. In reality, valve opening is not instantaneous (Harang 2013), due to the finite user actuation force.

Table 6.1: Initial conditions and modelling parameters.

Variable	Value
Propellant	HFA134a
T_∞	298.15 K
V_{mc}	50 μL
V_{ec}	50 μL
P_∞	1 atm
D_{no}	300 μm
D_{vo}	600 μm
$x_{mc}(t=0)$	0
$x_{ec}(t=0)$	1
$T_{mc}(t=0)$	T_∞
$T_{ec}(t=0)$	$T_{\text{sat}}(P_\infty)$
$\eta_{\text{isen,no}}$	0.7
$\eta_{\text{isen,vo}}$	0.7

6.4 Results

The results of the thermodynamic model are compared with the experimental radiography data. For the comparison to be made, the radiography data presented in Chapter 4 was smoothed with a temporal Gaussian filter that had a standard deviation of 5 ms. This allowed a more direct comparison of transverse profiles of the projected mass, which contained high-frequency variability prior to smoothing. This variability was due to two sources: interference from the experimental apparatus; and the comparatively large confidence interval of the experimental propellant-only projected mass. No filtering was performed in the transverse direction. Temporal filtering reduced, but did not eliminate, interference from the experimental apparatus, which is the dominant contributor to measurement uncertainty. Accordingly, the uncertainty on the projected mass M is estimated at $\pm 0.5 \mu\text{g mm}^{-2}$, and the uncertainty on TIM/A_t is estimated at $\pm 20 \text{ kg m}^{-3}$.

Transverse integrated mass

Results for the transverse integrated mass per unit throat area TIM_e/A_t are shown in Figure 6.4. The values predicted depend on the flow model, and the peak values

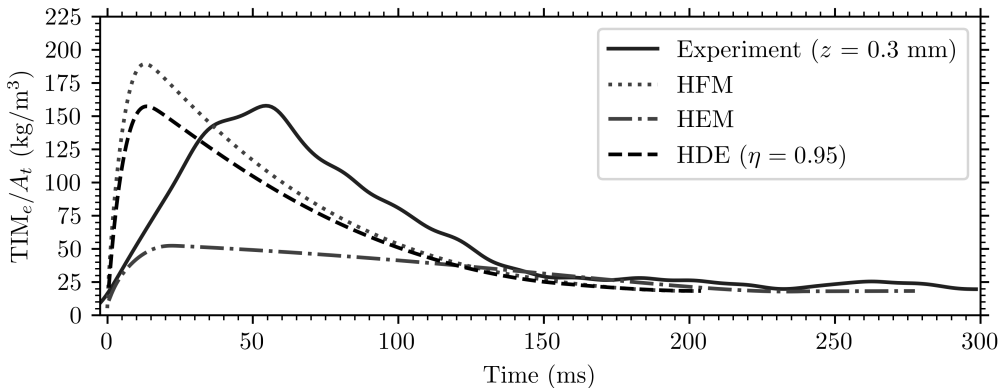


Figure 6.4: Time series of TIM_e/A_t for experiment ($z = 0.3 \text{ mm}$) and thermodynamic models.

differ by more than a factor of three, depending on which flow model is chosen. For the maximum value of TIM, HFM overpredicts the experimental result, while the HEM underpredicts it. The η parameter of the HDE is a lever between these two bounds; the model peak magnitude can be made to match that of the experiment if a value of $\eta = 0.95$ is selected. All models predict that peak TIM occurs much earlier than was observed during the experiment; this may result from a reduced flow rate at start of injection due to spatial inhomogeneity of the internal flow, which was observed in high-speed phase contrast images (Chapter 4). It is noteworthy that the transverse integrated mass to which the models converge is very similar to that observed experimentally.

Projected mass

The transverse integrated mass is a subset of the information obtainable from the radiography measurements. Further comparison can be made with the time-variant projected mass. Plots of the $y - t$ projected mass distribution are shown in Figure 6.5, assuming a uniform density across the spray cross-section for the models. To reduce the dynamic range, the colourmap is clipped to the maximum projected mass from the HDE; the transverse and temporal trends for the HFM, which are obscured by clipping in Figure 6.5, can be more clearly seen in Figure 6.6.

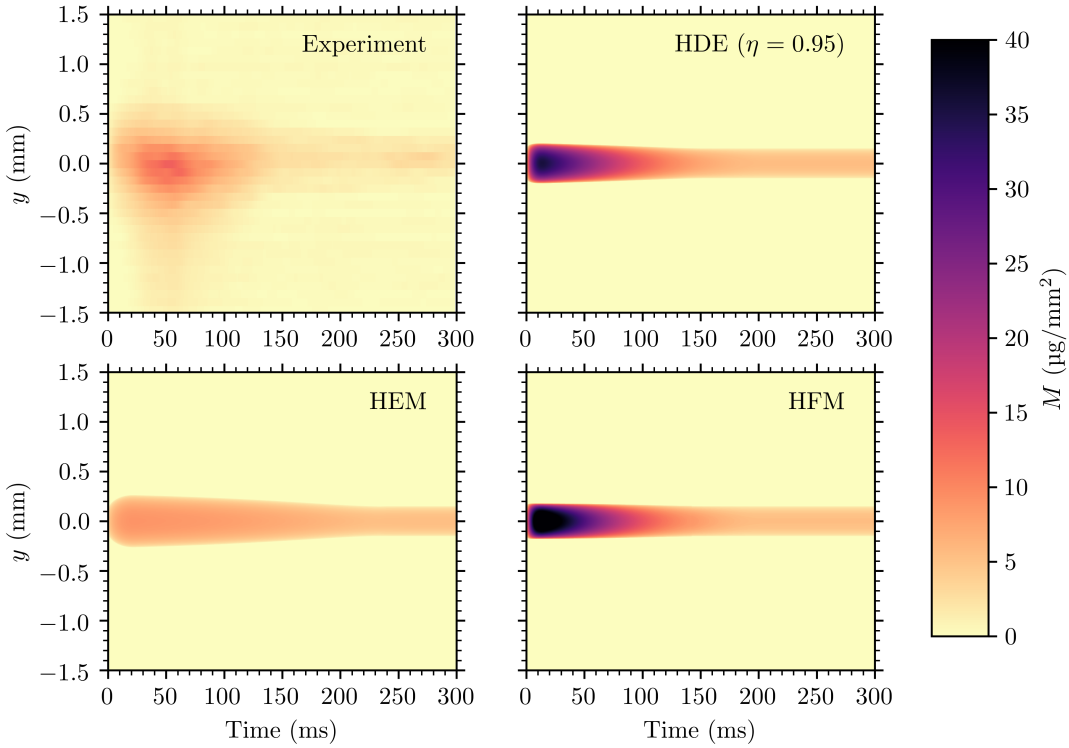


Figure 6.5: $y - t$ plots of projected mass from (left, top) experiment ($z = 0.3 \text{ mm}$), (right, top) HDE ($\eta = 0.95$), (bottom, left) HEM and (bottom, right) HFM. Dynamic range is reduced by clipping to the colour range of the HDE.

Predicted projected mass values for both non-equilibrium models differ from the experimentally-observed ensemble-mean time-average. While the peak transverse integrated mass for HDE with $\eta = 0.95$ matches that of the experiment, the projected mass distribution does not. Peak projected mass values are over $30 \mu\text{g mm}^{-2}$ for both HDE and HFM (Figure 6.6, top), while the peak HEM projected mass is similar to that of the experiment. The width of the experimental projected mass distribution is much larger than that predicted with quasi-one-dimensional modelling.

Transverse profiles of projected mass, and the centre line projected masses, are shown in Figure 6.6. All transverse profiles are obtained at the time of maximum TIM. The transverse profiles of projected mass in Figure 6.6 (bottom) show that the spray width measured experimentally is much larger than those predicted by

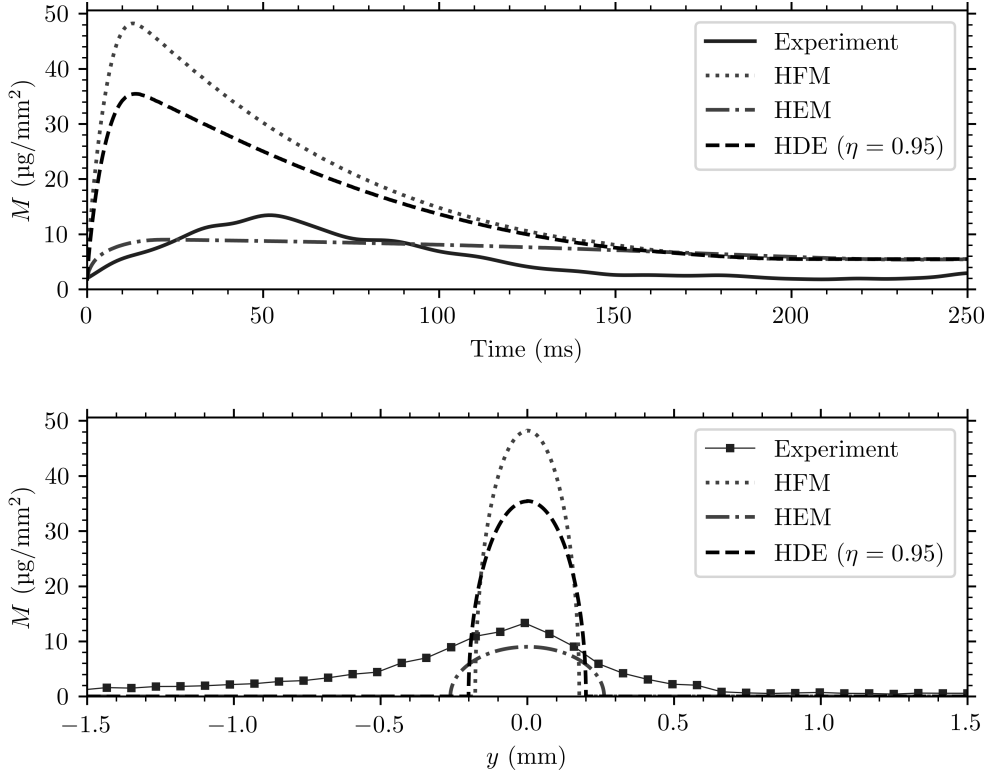


Figure 6.6: Experimental ($z = 0.3$ mm) and modelled projected mass M (top) centre line ($y = 0$ mm) time series and (bottom) transverse profiles at peak TIM.

modelling. Asymmetry of the experimental projected mass profile is apparent; the half-width half-maximum (HWHM) of the experimental data is 0.37 mm for $y < 0$, while it is 0.22 mm for $y > 0$. This profile asymmetry was also observed in the ensemble-mean time-variant optical depth (Appendix B) and radiography of the pMDI analogue (Chapter 3).

Spray asymmetry

The asymmetry in projected mass distribution can be more clearly observed if the profile is separated into two halves. If transverse integration is performed on each half of the profile to provide full-nozzle equivalent TIM values, this asymmetry in spray density can be quantified. These are shown in Figure 6.7.

For $y > 0$, the full-nozzle peak TIM_e/A_t is around 125 kg m^{-3} , while for $y < 0$ it

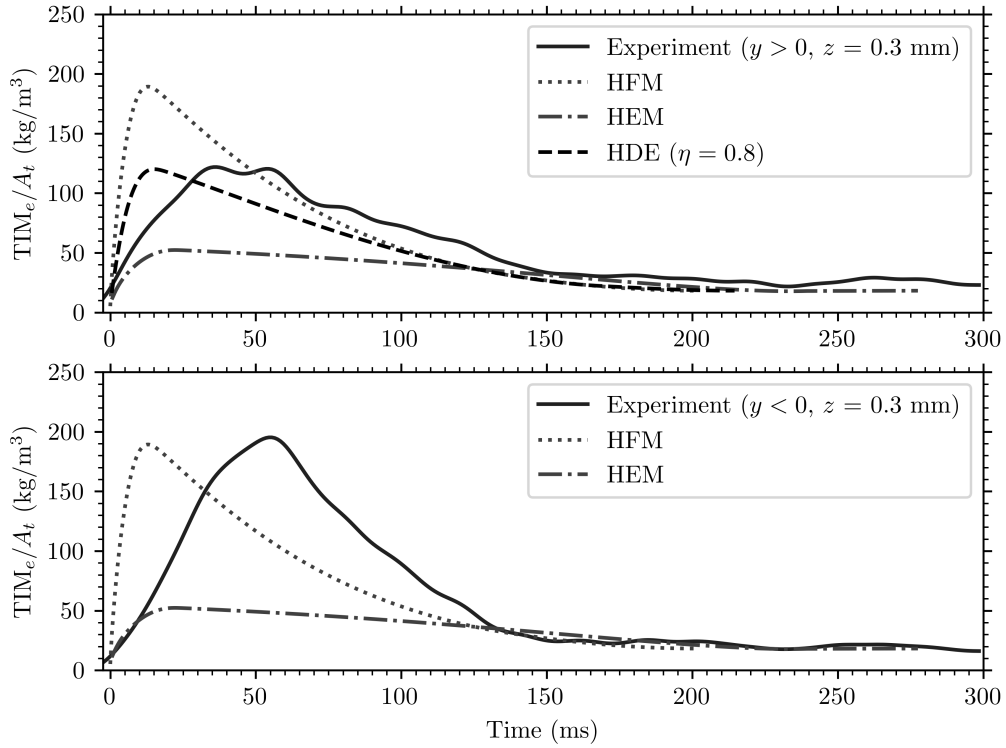


Figure 6.7: TIM_e/A_t for (top) $y > 0$ and (bottom) $y < 0$.

is approximately 200 kg m^{-3} . Reasonable agreement with the experimental profile for $y > 0$ can be obtained with the HDE if $\eta = 0.8$. Peak TIM is similar for the experimental data below the spray axis ($y < 0$) and the HFM.

Spray profiles

For the model results, many density-area combinations are consistent with a given TIM, the magnitude of which is predicted by throat conditions and the ambient pressure. Using a Gaussian profile with a time-varying width:

$$\sigma(t) = \sigma_0 \cdot \sqrt{\frac{A_e(t)}{A_t}} \quad (6.37)$$

allows the spray width to be modelled as a function of a single width parameter σ_0 , corresponding to that of subcritical flow, and the area ratio from Equation 6.21.

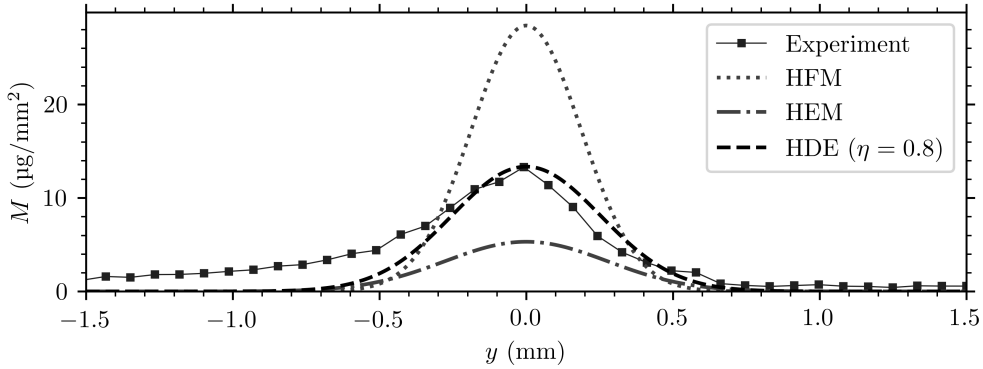


Figure 6.8: Experimental ($z = 0.3$ mm) and modelled projected mass M profiles with $\sigma_0/D_{\text{no}} = 0.75$.

Transverse profiles and time series of the projected mass with $\eta = 0.8$ and $\sigma_0/D_{\text{no}} = 0.75$ are shown in Figure 6.8. The η parameter in this case was set to 0.8 to provide a comparable TIM to the experimental data over $y > 0$. The σ_0 parameter was adjusted to find a width at which both the peak projected mass and transverse profile showed reasonable agreement with the experimental data.

For this combination of η and σ_0 , the model captures the peak M reasonably, but overpredicts M for $0.2 < y < 0.5$ as the experimental data is more strongly peaked than the modelled profile. For $y < 0$, the modelled profile deviates significantly from the experimental data.

If it is assumed that this σ_0 value is representative of the profile for $y > 0$ across the entire spray duration, a Gaussian modelled projected mass can be obtained. This is shown in Figure 6.9, and appears to capture the trends of both spray width and projected mass magnitude.

For the lower half of the spray profile, the transverse integrated mass most closely agrees with that predicted by the homogeneous frozen model. The profiles and time series in Figure 6.10 are obtained when $\sigma_0/D_{\text{no}} = 1.25$. The peak projected mass is matched by the HDE with $\eta = 0.95$ at this condition. Projected mass plots for $y < 0$ are shown in Figure 6.11. Although reasonable agreement between the

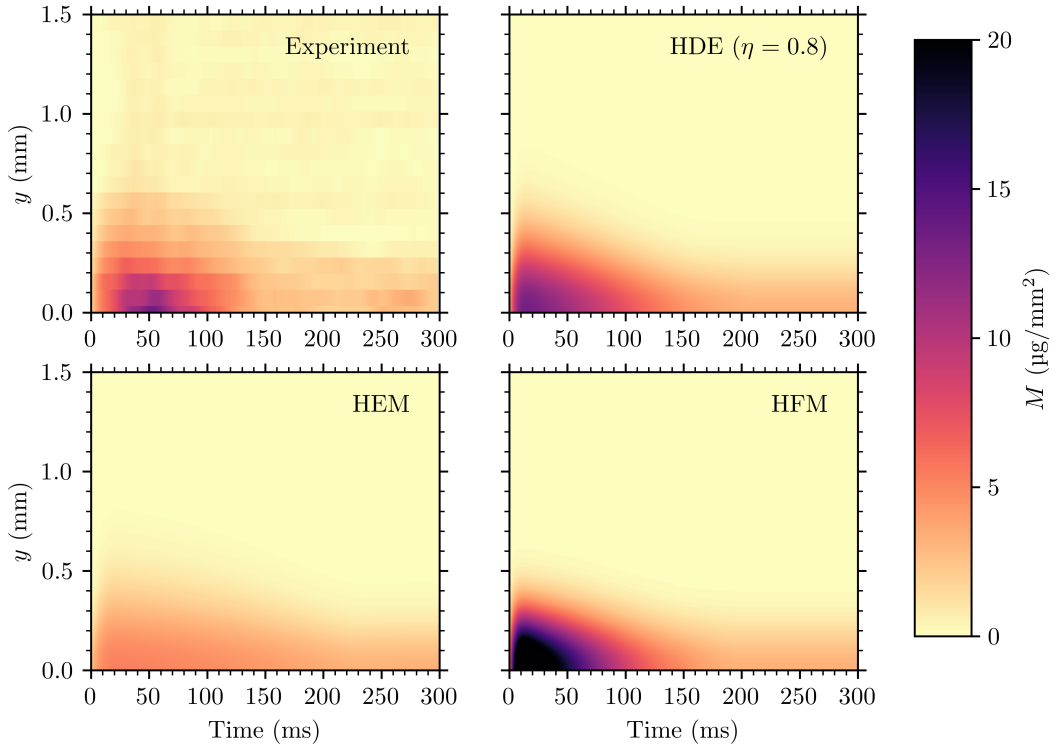


Figure 6.9: $y - t$ plots of M ($y > 0$) for (top, left) experiment ($z = 0.3 \text{ mm}$), (top, right) HDE ($\eta = 0.8$), (bottom, left) HEM and (bottom, right) HFM. For all modelled profiles, $\sigma_0/D_{\text{no}} = 0.75$. Dynamic range is reduced by clipping to the range of the experimental data.

HDE and the experimental data exist over the range $-0.5 \text{ mm} < y < 0 \text{ mm}$, the experimentally-observed off-axis projected mass at $y < -0.5 \text{ mm}$ is not present in the modelled results.

6.5 Discussion

Considering that the radiography $y - t$ plots of projected mass comprise many independent spray measurements, the agreement between model outputs, which are tuned to this experimental data with two parameters, is good. The η and σ_0 parameters are used to empirically constrain the spray width and peak projected mass, but do not otherwise constrain the predicted projected mass, which arises

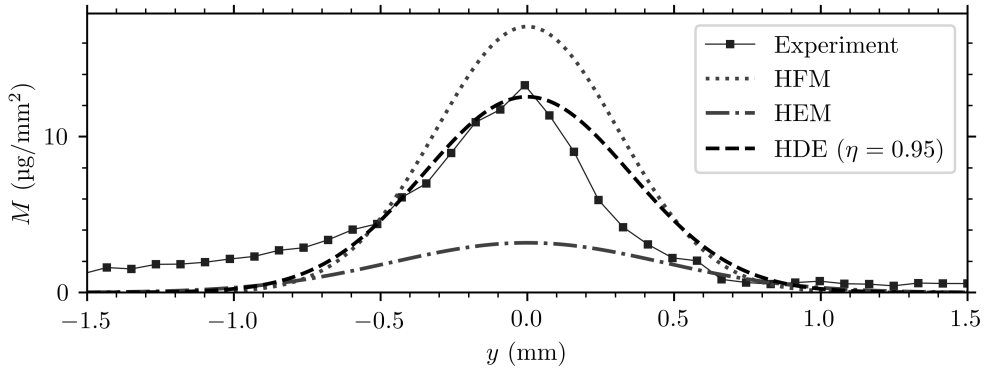


Figure 6.10: Experimental ($z = 0.3$ mm) and modelled projected mass M profiles with $\sigma_0/D_{\text{no}} = 1.25$.

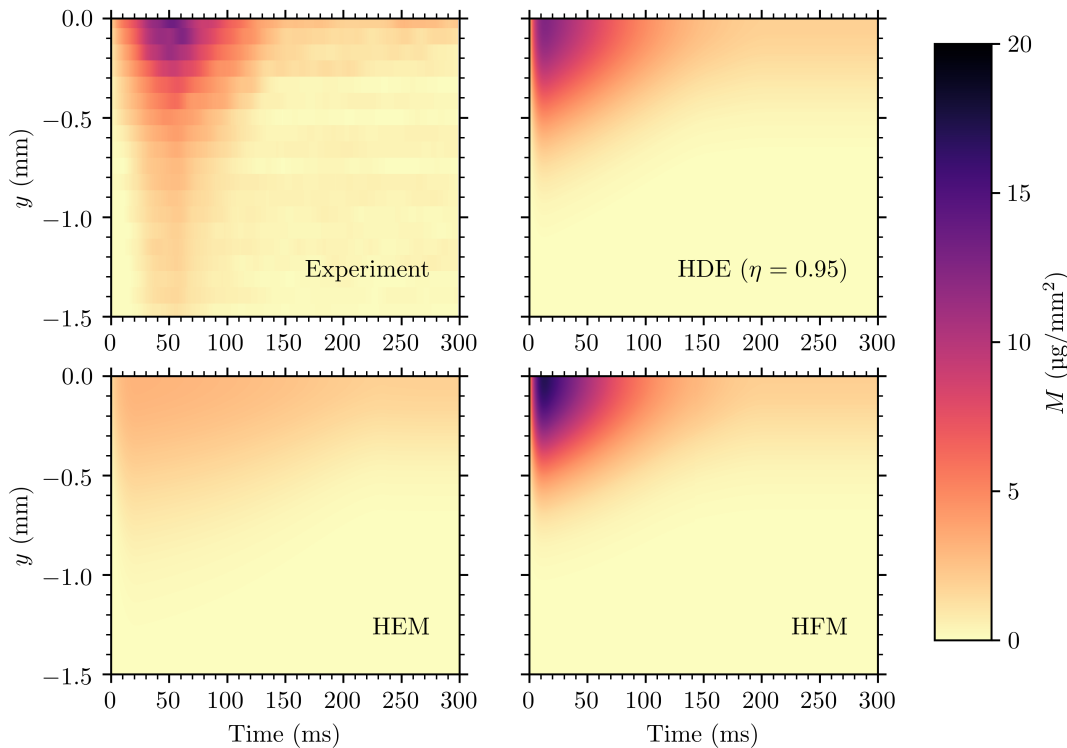


Figure 6.11: $y - t$ plots of M ($y < 0$) for (top, left) experiment ($z = 0.3$ mm), (top, right) HDE ($\eta = 0.95$), (bottom, left) HEM and (bottom, right) HFM. For all modelled profiles, $\sigma_0/D_{\text{no}} = 1.25$.

from the phenomenological model. Given this, thermodynamic modelling appears to capture some of the essential aspects of the metered flow through the pMDI.

If this model does capture these essential aspects, comparison of the experimental and numerical results suggests that thermal non-equilibrium between liquid and vapour is significant in sprays from pMDIs. This finding corroborates that of Gavtash et al. (2017b). Transverse integrated masses predicted by HEM and HFM bound that observed experimentally, and the HDE with $\eta = 0.8$ shows good agreement with the experiment for $y > 0$.

The experimental transverse profile of projected mass is dominated by asymmetry. One-dimensional modelling cannot capture this asymmetry; it is inconsistent with the assumptions used. Phase contrast imaging (Chapter 4) and back-illumination imaging (Appendix B) showed that large masses of liquid propellant intermittently pass through the nozzle (Chapter 4), and produce large liquid droplets. These have also been observed in phase doppler anemometry measurements of propellant-only pMDI sprays (Versteeg et al. 2017), and pooling on the nozzle can occur. This raises questions as to the significance of the high projected mass off the spray axis at $y < 0$.

For concentration-based spray measurements, such as radiography, slow-moving droplets have a large effect on the measurement, even though they may contribute little to the total mass flux (Edwards and Marx 1996). At an extreme, a static sample in the beam path contributes to the radiography measurement, and contributes nothing to the mass flux. The projected mass obtained from modelling assumes that all mass travels at a single axial velocity, with no spatial variation in residence time in the beam. Given the one-dimensional assumption, a conflict between the experimental measurements and modelling exists.

Concluding remarks

The assumptions used for model development are numerous and substantial. Crucial to the prediction of TIM_e/A_t is the assumption that the flow expands to atmospheric pressure within the distance from the point of choking to the point of measurement, and that entrainment is negligible. The assumption of expansion to atmospheric pressure meant that the gauge pressure on the outlet surface was zero; as a result, the estimated W_e was independent of its area (refer to Figure 6.2 and Equation 6.14). If the expansion is incomplete, TIM_e/A_t will be higher for all models, meaning that a lower η value would more closely match the experimental data. However, the large width of the experimental measurements suggests that the expansion is significant over the short axial distance from the nozzle to the measurement points. Simulation of the near-nozzle flow with two- or three-dimensional modelling would provide more information about the modelled near-nozzle structure. For the quasi-steady homogeneous flow assumed, the axisymmetric two-dimensional flow field could be predicted with the method of characteristics (Liepmann and Roshko 1957).

The homogeneous flow assumption is inconsistent with the experimental observations in Chapter 4. Given that the real flow is not homogeneous, interphase slip is likely to occur. Gavtash et al. (2017b) found that the homogeneous frozen model showed better agreement with PDA measurements of pMDI sprays than did the slip equilibrium model. A slip frozen model, or slip non-equilibrium model, may better capture the relevant physics. The high-resolution near-nozzle radiography data of Chapter 4 could be used to examine this further.

The HDE is a phenomenological model of non-equilibrium two-phase fluid flow that uses a tunable parameter. In this work, a single value of η was used per case; however, η may be a function of properties, like the upstream quality. Alternative non-equilibrium homogeneous flow models that do not require tuning parameters exist. The homogeneous relaxation model (HRM) (Downar-Zapolski et al. 1996) is one such model, and uses a quality-dependent relaxation to equilibrium. Its recent

use (Lyras et al. 2018) for simulating flows of R134a through square-edged cylindrical nozzles suggests that it may also be applicable in thermodynamic modelling of pMDIs.

Chapter 7

A non-equilibrium thermodynamic model of multicomponent pMDIs

7.1 Motivation

Radiography measurements were obtained for pMDI sprays both with and without ethanol cosolvent. A source of uncertainty for the ethanol-containing spray measurements is the unknown composition of the formulation throughout the spray event. A multicomponent thermodynamic model can provide an estimate of this composition change.

Thermodynamic models of pMDIs have been developed that allow the prediction of spray properties of cosolvent-containing pMDIs. Such models have previously been developed by Ju, Shrimpton, and Hearn (2010), who modelled the vapour and liquid as separated flows. Very recently, Gavtash et al. (2018) developed a phenomenological model of ethanol-containing pMDIs. In their approach, the vapour phase concentration of ethanol was assumed to be zero, due to its low volatility. A flexible model that allows for arbitrary formulations cannot use this overly restrictive assumption. For formulations with alternative propellants or propellant blends, cosolvents may be used with non-negligible volatilities.

This chapter details the development of a thermodynamic model that permits formulations with a range of volatilities, assists with the interpretation of radiography measurements, and provides boundary conditions for droplet and spray models.

7.2 Nomenclature

D - Diffusion coefficient ($\text{m}^2 \text{s}^{-1}$)

L - Length (m)

MW - Molar mass (kg mol^{-1})

M - Projected mass ($\mu\text{g mm}^{-2}$)

P - Pressure (Pa)

R - Gas constant ($\text{J kg}^{-1} \text{K}^{-1}$)

S - Area of liquid/vapour interface (m^2)

T - Temperature (K)

TIM - Transverse integrated mass ($\mu\text{g mm}^{-1}$)

V - Volume (m^3)

Y - Concentration

W - Velocity (m s^{-1})

a - Activity

c_P - Mass-specific heat capacity at constant pressure (J kg^{-1})

d - Diameter (m)

h - Specific enthalpy (J kg^{-1})

m - Mass (kg)

v - Specific volume ($\text{m}^3 \text{kg}^{-1}$)

w - Mass fraction

x - Quality

y - Coordinate perpendicular to spray axis (m)

y - Mole fraction

z - Coordinate parallel to spray axis (m)

Greek letters

Θ - Relaxation time (s^{-1})

Ω - Collision integral in Chapman-Enskog theory

α - Void fraction

η_{isen} - Nozzle isentropic efficiency

ρ - Density (kg m^{-3})

σ - Collision diameter in Chapman-Enskog theory (\AA)

φ - Ratio of pressures used in homogeneous relaxation model

Subscripts

sv - Saturated vapour

sl - Saturated liquid

ml - Metastable liquid

veq - Equilibrium vapour

σ - Saturation curve value

g - Gas

l - Liquid

eq - Equilibrium

0 - Reservoir conditions

7.3 Analysis methodology

The approach to modelling largely follows that described in Chapter 6. The pMDI is treated as two control volumes. The solution methodology developed is a non-equilibrium two-fluid equation set (Massoud 2005), which requires constitutive models for mass transport and interphase heat transfer. In the form presented, the equation set permits two liquids and vapours—propellant and ethanol—and a sin-

gle non-condensable gas. This allowed the expansion chamber to be filled with air at start of injection, in contrast with the model in Chapter 6. The differential equations are derived and discussed in Appendix A.

Mass flow rates

For this model, the mass flow rate is determined using a homogeneous frozen model. The homogeneous frozen model adopted here was developed with reference to Gavtash et al. (2017b) and Fletcher (1975), who assumed liquid phase incompressibility, and assumed that the vapour phase behaved as an ideal gas with constant properties. The same approach is used, except that here an isentropic efficiency is used to permit the concentration-based radiography measurements to be compared with model predictions. Extending the homogeneous equilibrium model, and/or the homogeneous direct evaluation model, to multicomponent mixtures remains an open task.

The method for determining the mass flow rate with the multicomponent non-isentropic homogeneous frozen model is described in Appendix A.

Interphase heat and mass transfer

Phase change is a non-instantaneous process; barriers to nucleation exist, and metastable states can occur (Callen 1960). Although it considers non-equilibrium states in nozzles, the model described in Chapter 6 uses equilibrium states in the metering and expansion chambers. As a result, interphase heat and mass transfers instantaneously restore the system to equilibrium.

It was thought that the internal flow visualisations of real pMDIs shown in Chapters 4 and 5 could inform the development of a model that more accurately reflects the internal processes of the pMDI. To this end, the two-fluid model used here allows thermal non-equilibrium in the metering and expansion chambers, and requires constitutive models for boiling and diffusion rates. For diffusion, the rate

terms are affected by the internal flow structure. These constitutive models are described below.

Boiling

The homogeneous relaxation model (HRM) (Downar-Zapolski et al. 1996) is a model for non-instantaneous mass transfer in two-phase flows of a single component fluid. The model relies on empirical correlations developed from experimental measurements of two-phase flashing flows obtained by Reocreux (1974), and has been used for non-equilibrium flow modelling (Lyras et al. 2018). The boiling process is modelled as a relaxation of a fluid particle's quality x towards its equilibrium quality \bar{x} with a characteristic time Θ :

$$\frac{Dx}{Dt} = -\frac{x - \bar{x}}{\Theta} \quad (7.1)$$

where it is assumed that the relaxation to equilibrium occurs at constant pressure:

$$\bar{x} = \frac{h - h_{sl}(P)}{h_{sv}(P) - h_{sl}(P)} \quad (7.2)$$

The rate constant Θ is related to the fluid and flow properties by an empirical correlation (Downar-Zapolski et al. 1996):

$$\Theta = \Theta_0 \cdot \alpha^{-0.54} \cdot \varphi^{-1.76} \quad (7.3)$$

where α is the local void fraction and φ is $\frac{P_{sat}-P}{P_{crit}-P_{sat}}$. Following Duke et al. (2013), for multicomponent formulations the bubble point pressure is used rather than the saturation pressure; the distinction is small at low values of quality. The constant term Θ_0 has been measured for water flows (Downar-Zapolski et al. 1996), but not for HFA propellants. In the absence of a value of Θ_0 for HFA propellants, the Θ_0 value obtained from flashing water flows is used. This approach has been adopted elsewhere (Lyras et al. 2018).

By the assumption of spatial homogeneity in each chamber, the material derivative in Equation 7.1 becomes a time derivative ($W(\partial x/\partial z) = 0$), and the rate of

change of quality can be expressed as:

$$\frac{dx}{dt} = (1 - x) \cdot \frac{h_{ml} - h_{sl}(P)}{h_{sv}(P) - h_{sl}(P)} \cdot \frac{1}{\Theta} \quad (7.4)$$

Treating the total mass as quasi-static, the boiling source term for vaporisation is:

$$\frac{dm_v}{dt} = m_l \cdot \frac{h_{ml} - h_{sl}(P)}{h_{sv}(P) - h_{sl}(P)} \cdot \frac{1}{\Theta} \quad (7.5)$$

The expression above is adapted to determine the boiling rate for a binary liquid. This is achieved by using the liquid phase specific enthalpy, and a latent heat of vaporisation based on the equilibrium vapour concentration:

$$\frac{dm_v}{dt} = m_l \cdot \frac{c_{p,l} \cdot (T_{ml} - T_{sat}(P, y_l))}{(h_{sv,p} - h_{sl,p}) w_{p,eqv} + (h_{sv,e} - h_{sl,e}) w_{e,eqv}} \quad (7.6)$$

where $T_{sat}(P, y_l)$ is the bubble point temperature, and $w_{i,eqv}$ is the mass fraction of component i in the vapour that is at concentration equilibrium with the liquid. These mass fractions are obtained from Dalton's law and the mixture vapour pressure.

Boiling occurs when the vapour pressure of a liquid sufficiently exceeds its pressure. In Equation 7.6, the rate of vapour generation is proportional to the superheat. To model subcooling caused by the air that fills the expansion chamber at start of injection, the superheat is converted to a pressure by approximating it with the saturation curve derivative $\frac{dP}{dT_\sigma}$:

$$T_{ml} - T_{sat}(P, y) \approx (P_{sat}(h_{ml}, y) - P) \cdot \frac{dT_\sigma}{dP} \quad (7.7)$$

The rate of change of enthalpy of the liquid phase is equal to the mass of each liquid boiled multiplied by the specific enthalpy of equilibrium vapour at the metastable liquid temperature:

$$(\dot{m}h)_{\text{flash}} = \frac{dm_{\text{flash}}}{dt} h_v(T_l) \quad (7.8)$$

This completes the description of the multicomponent boiling model.

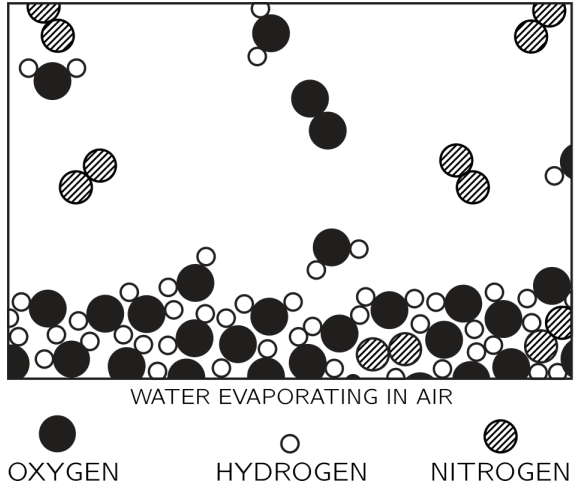


Figure 7.1: Visual representation of dynamic vapour-liquid equilibrium (adapted from Feynman, Leighton, and Sands (2011)).

Evaporation and condensation

In addition to flash boiling, phase change also occurs due to evaporation and condensation. The dynamic equilibrium of evaporation and condensation is depicted graphically in Figure 7.1 for subcooled water in contact with humid air. Clearly, the structure of the vapour/liquid interface is a determining factor of the evaporation rate.

The phenomenological model for evaporation and condensation satisfies the following criteria:

- The mass transfer rate is proportional to the liquid surface area
- The mass transfer rate is proportional to the spatial concentration gradient
- The mass transfer rate is a monotonically increasing function of the temperature

This approach models evaporation as a purely diffusive process, as per the Maxwell equation (Sazhin 2014). The mass flow rate due to this diffusion process is given by (Cussler 2009):

$$\frac{dm_{\text{evap}}}{dt} = -\rho_v D_{12} \frac{dY}{dz} S \quad (7.9)$$

where D_{12} is the binary mass diffusivity ($\text{m}^2 \text{s}^{-1}$), $\frac{dY}{dz}$ is the spatial concentration gradient (m^{-1}), S is the surface area (m^2) and ρ_v is the vapour density (kg m^{-3}).

If the liquid and vapour phases are not in equilibrium, diffusive transfers of propellant and ethanol tend to restore the system to equilibrium. If evaporation and condensation for each component is modelled as a flow of a particular species at a particular enthalpy, there are four fluxes for propellant/ethanol blends. For each flow, using Equation 7.9, the concentration varies from unity to zero. Accordingly, the evaporation rate is:

$$\frac{dm_{\text{evap}}}{dt} = \frac{\rho}{L} \cdot D_{12} \cdot S \quad (7.10)$$

with a diffusion length scale L (m).

The equilibrium density for evaporation from the liquid phase is determined from the individual phase densities of saturated vapour and the activity:

$$\rho_{vi,\text{eq,evap}} = \rho_i(T_{\text{ml}}, x = 1) \cdot a_i \quad (7.11)$$

Condensation modelling is achieved using the same approach, with an equilibrium density based on the temperature of the vapour/gas phase:

$$\rho_{vi,\text{eq,cond}} = \rho_i(T_v, x = 1) \cdot a_i \quad (7.12)$$

To complete the evaporation/condensation model, estimates are required for the diffusion coefficient and the surface area of the vapour-liquid interface. The structure of the vapour-liquid interface is a strong function of the ethanol concentration (Chapters 4 and 5), with vapour distributed at smaller scales in the liquid at higher ethanol concentrations. This is modelled phenomenologically by introducing a vapour-liquid interfacial area S that is a function of the ethanol concentration.

The vapour is modelled as comprising a number of bubbles of a characteristic size d_0 . Rather than consider diffusion in a spherical geometry, the process is simplistically treated as the diffusion into a medium between two parallel plates. Under this simplification, the appropriate length scale for diffusion is $d_0/2$, and the surface

area is $6V_v/d_0$. Accordingly, the evaporation rate becomes:

$$\frac{dm_{\text{diffusion}}}{dt} = \rho \cdot D_{12} \cdot \frac{12V_v}{d_0^2} \quad (7.13)$$

Phase contrast imaging (Chapters 4 & 5) revealed that, in the mean, the characteristic bubble diameter increases monotonically with time and decreases monotonically with increasing ethanol mole fraction:

$$d_0 = d_0(y_e, t) \quad (7.14)$$

An expression for the modelled bubble diameter that provides a qualitative account of the observed behaviour is an exponential time-dependence that decays towards a final bubble diameter, and a power law dependence on the ethanol concentration:

$$d_0(y_e, t) = (a - c) \cdot (1 - \exp(-b \cdot t) + c) \cdot (1 - y_e)^d \quad (7.15)$$

where c is the incipient bubble diameter, a is the final bubble count mean diameter for propellant-only flow, b is a time constant relating to the growth of the bubbles and d is a factor that accounts for the effect of the formulation. This relation is plotted in Figure 7.2, and was informed by bubble diameters measured in phase contrast images. For the diameters in Figure 7.2, $a = 2$ mm, $b = 10$ s⁻¹, $c = 10$ µm and $d = 6$. Preliminary attempts to automatically measure bubble diameters from multiple image sequences were not successful, consequently the relation above is developed from a small number of bubble measurements performed manually. All phase contrast imaging was performed with the same nozzle geometry and initial canister temperature; the effects of inhaler geometry and formulation temperature on internal flow structures are not known.

In addition to the surface area, the evaporation model requires diffusion coefficients D_{12} . The binary mass diffusivity of propellant and ethanol vapours can be determined with Chapman-Enskog theory (Cussler 2009):

$$D_{12} = \frac{1.86 \times 10^{-3} T^{3/2} (1/\text{MW}_1 + 1/\text{MW}_2)^{1/2}}{P \sigma_{12}^2 \Omega} \quad (7.16)$$

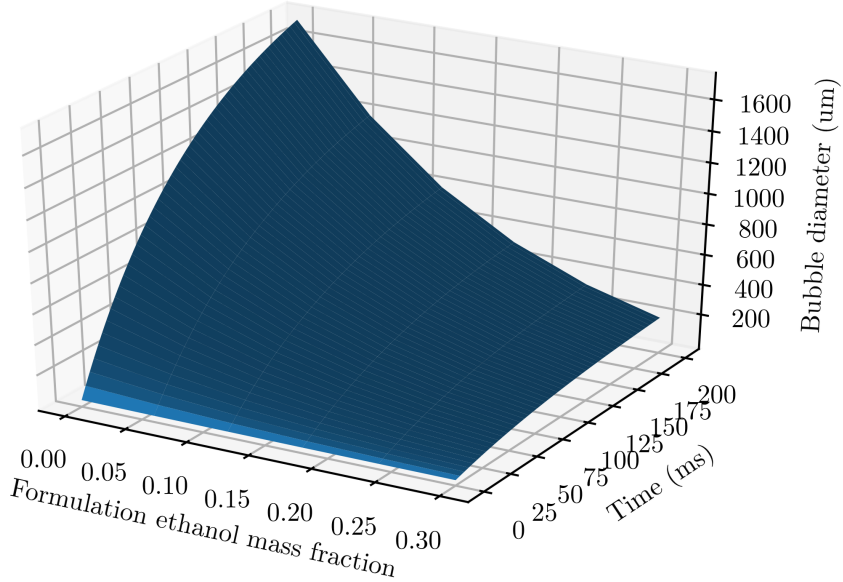


Figure 7.2: Estimated bubble diameter distribution as function of time after start of injection.

where molecular masses are given in g/mol, the pressure is given in atmospheres, and σ_{12} is the weighted sum of the collision diameters of each species (Å):

$$\sigma_{12} = \frac{1}{2} (\sigma_1 + \sigma_2) \quad (7.17)$$

The parameter Ω is a function of the temperature and the energy of interaction (Cussler 2009) ε_{12} where:

$$\varepsilon_{12} = \sqrt{\varepsilon_1 \varepsilon_2} \quad (7.18)$$

Values for the collision distance of ethanol and air were obtained from Cussler (2009). For refrigerants HFA134a and HFA227ea, these data were obtained from Huber, Laesecke, and Perkins (2003). The relevant parameters are given in Table 7.1. The Ω parameter was obtained from Cussler (2009). As the vapour phase is dominantly comprised of propellant, diffusion of propellant is modelled using its self-diffusivity, and diffusion of ethanol is modelled with the propellant-ethanol binary diffusivity.

Table 7.1: Diffusion parameters for HFA propellants, ethanol and air.

Variable	σ_{12} (Å)	ε_{12}/k_B (K)
HFA134a	4.6893	299.363
HFA227ea	5.746	289.34
Ethanol	4.530	362.6
Air	3.711	78.6

Implementation

Numerical integration was performed with ODEPACK and CoolProp, as per the methodology of Chapter 6.

The differential equations are written for two liquids and a single non-condensable gas. However, the system of equations can be written with more liquids or non-condensable gases, if a more complex formulation is to be modelled.

Propellant/ethanol mixtures show a strong positive deviation from Raoult's law (Gavtash et al. 2015). The correlation equations developed in Gavtash et al. (2015) are used to compute the mixture vapour pressure $P_v(y_e, T)$ and the activity:

$$a_p = \frac{P_v(y_e, T) - P_{v,e}(T)}{P_{v,p}(T) - P_{v,e}(T)} \quad (7.19)$$

which is used in place of liquid phase mole fraction. As the mixture is a binary liquid, $a_e = 1 - a_p$.

The vapour/gas region is treated using Dalton's law, and properties of the liquid phase have been treated using linear mixing rules. Interaction parameters, which will modify the predicted density for the mixture, have not been included (Bell and Lemmon 2016). For HFA134a and ethanol, these interaction parameters are all approximately unity; the expected error on the density is approximately 2%.

Initial conditions

For the differential equations derived in Appendix A, each chamber must start with mass of every component, although this mass can be made very small. This is because no solution exists to the system of equations if the mass of any component

Table 7.2: Initial conditions and modelling parameters.

Variable	Value
Propellant	HFA134a
T_∞	298.15 K
V_{mc}	50 μ l
V_{ec}	50 μ l
P_∞	101.325 kPa
d_{no}	300 μ m
d_{vo}	600 μ m
$\alpha_{mc}(t=0)$	0.001
$\alpha_{ec}(t=0)$	0.999
$T_{l,ec}(t=0)$	298.15 K
$\eta_{isen,vo}$	0.7
$\eta_{isen,no}$	0.7
Θ_0	3.84×10^{-7} s

(liquid or vapour/gas) is zero in any chamber. The idealised initial conditions, in which the metering chamber contains only liquid formulation and the expansion chamber contains only air, are approximated by means of a ‘starting model’. This is described below.

The metering chamber must commence with a small volume comprising propellant vapour, ethanol vapour and air. This vapour region in the metering chamber is a straightforward modification, and can be made trivially small. The approach that was taken was to set the metering chamber initial void fraction to 10^{-3} , with an initial air partial pressure of 100 Pascal. This results in the liquid initially being very slightly subcooled.

The expansion chamber must commence with a small volume of liquid propellant and ethanol, and must commence with some propellant vapour and ethanol vapour in the vapour/gas region. An initial liquid volume fraction of 10^{-3} was used for the expansion chamber, and the liquid phase composition was the same as that in the metering chamber. Varying the initial void fraction over two orders of magnitude (10^{-2} to 10^{-4}) was found to have a negligible influence on the solution. The initial conditions used are summarised in Table 7.2.

7.4 Results

Experimental and modelled results are shown for three formulations, all containing HFA134a with varying ethanol concentrations. As per the presentation in Chapter 6, the experimental data was smoothed with a Gaussian temporal filter having a standard deviation of 5 ms. The uncertainty on the projected mass M is estimated at $\pm 0.5 \mu\text{g mm}^{-2}$, and the uncertainty on TIM/A_t is estimated at $\pm 20 \text{ kg m}^{-3}$.

Sensitivity tests of the constitutive models found that the solutions obtained were not highly sensitive to changes to either the boiling rate or the diffusion rate; increasing or decreasing each of these by an order of magnitude affected peak TIM by approximately 10%. In light of this, all data are presented with the modelling parameters in Table 7.2; different results may occur if the boiling and diffusion rates were further modified.

A comparison is made between properties predicted by the model after expansion to atmospheric pressure, as per the near-nozzle expansion model presented in Chapter 6.

Transverse integrated mass

The experimental and predicted TIM time series are shown in Figure 7.3. Although they do not occur at the same time after start of injection, the peak magnitudes of experimentally-determined TIM are notably similar to their modelled counterparts. Experimental measurements of ethanol-containing formulations showed that TIM peaked at around 40 ms, while the peak value occurs at 60 ms after start of injection for the propellant-only formulation. The time difference between model and experimental peak TIM decreases with increasing ethanol concentration.

The magnitude of the TIM decreases with increasing ethanol concentration. The HFM overpredicts the projected mass obtained during experiment, as was found with the model in Chapter 6. The time of peak TIM obtained with the model presented

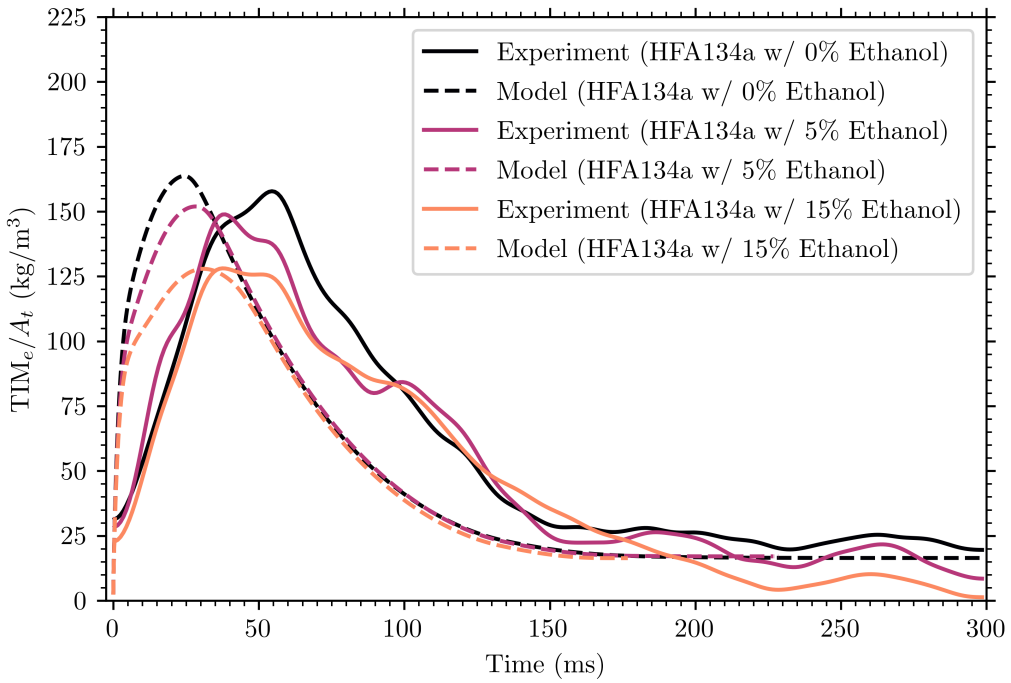


Figure 7.3: Time series of TIM_e/A_t for experiment ($z = 0.3 \text{ mm}$) and thermodynamic model.

here more closely aligns with that observed experimentally than did the propellant-only model in Chapter 6. This may be attributable to the different initial conditions in the expansion chamber, and the use of non-equilibrium states in the metering and expansion chambers in this model.

Projected mass

The projected mass profiles predicted by the quasi one-dimensional model are significantly narrower than the experimental profiles; this was also the case for all models presented in Chapter 6. In the interest of expediency, these uniform density projected mass profiles are not shown. $y - t$ plots of the projected mass obtained by assuming a Gaussian density profile, and the experimental measurements, are shown in Figure 7.4. For the modelled profiles, the spray width parameter $\sigma_0/d_{\text{no}} = 1.25$.

For both the experimental data and modelled profiles, peak M decreases with

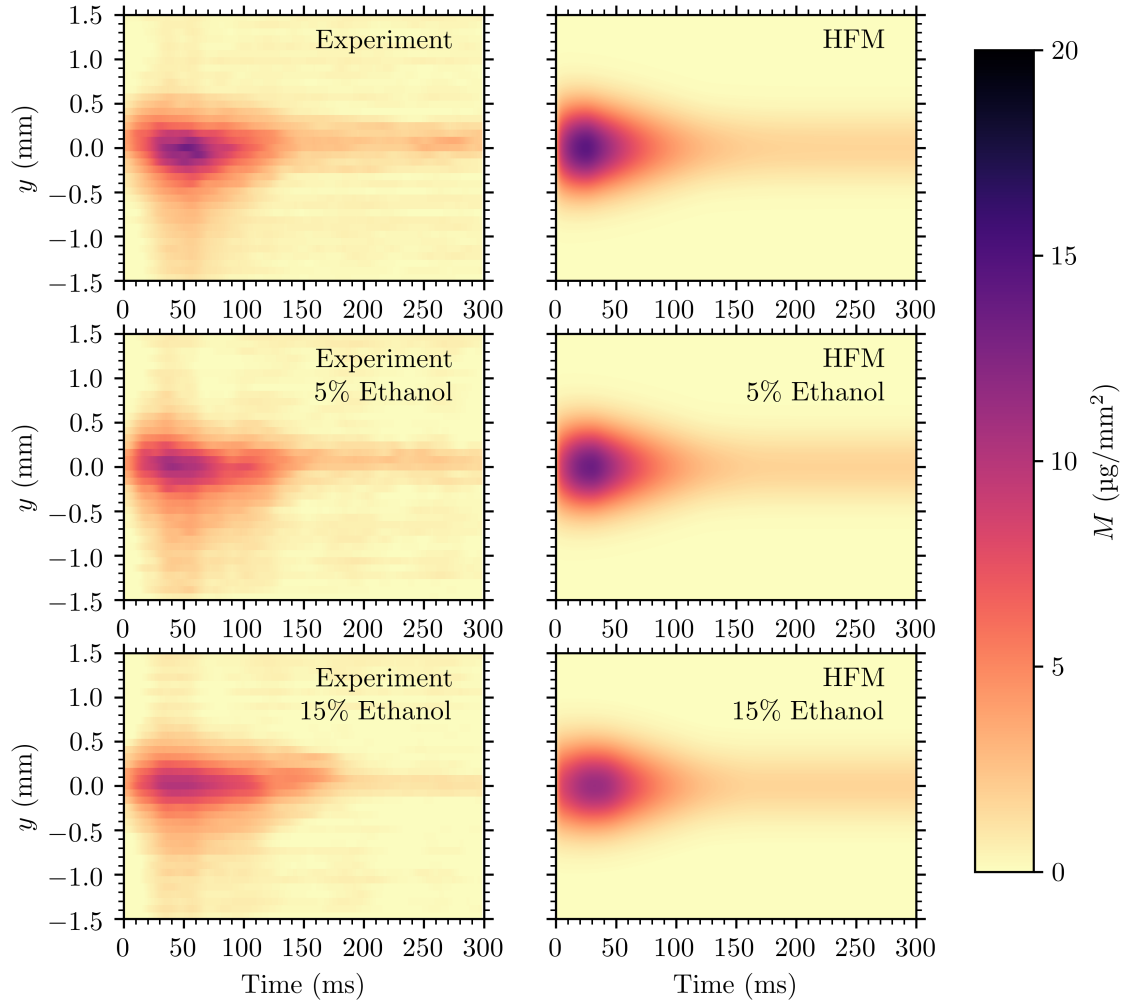


Figure 7.4: $y - t$ plots of M for (left column) experiment and (right column) HFM. Formulations are (top) HFA134a, (middle) HFA134a w/ 5% ethanol and (bottom) HFA134a w/ 15% ethanol. For all modelled profiles, $\sigma_0/d_{\text{no}} = 1.25$.

increasing ethanol concentration. The time at which peak M occurs is earlier for the model than for the experimental data. Spray widths are comparable between formulations, although appear wider in the model than in the experiment. The temporal and spatial trends of the projected mass appear to be captured reasonably by the model.

Spray profiles

For all formulations presented, the experimental projected mass profiles are asymmetric, with higher concentration of mass below the spray centre line. The spray profiles are separated about the centre line and compared with the TIM predicted from the model. These results are shown in Figure 7.5. The asymmetry is most pronounced for the propellant-only formulation, and reduces with increasing ethanol concentration.

The experimental data above the spray axis ($y > 0$) show similar time series of TIM_e/A_t for all formulations. For all experimental cases with $y > 0$, peak TIM occurs 30 ms after start of injection, whereas for $y < 0$ it occurs much later. The homogeneous frozen model overpredicts the peak TIM above the spray axis, and underpredicts TIM below the spray axis. Given the assumptions used to complete the model, the agreement appears reasonable.

Throat conditions

The properties of interest to droplet and spray modellers are the boundary conditions for their simulations, namely the conditions at the nozzle throat. Having demonstrated that the thermodynamic model results show reasonable agreement with experiment, the throat conditions predicted from the model are thought to be a reasonable set of boundary conditions for such a simulation. The conditions at the throat predicted by the model are shown in Figure 7.6. Lines are coloured according to the formulation; the legend is provided in the fourth subfigure (U_t).

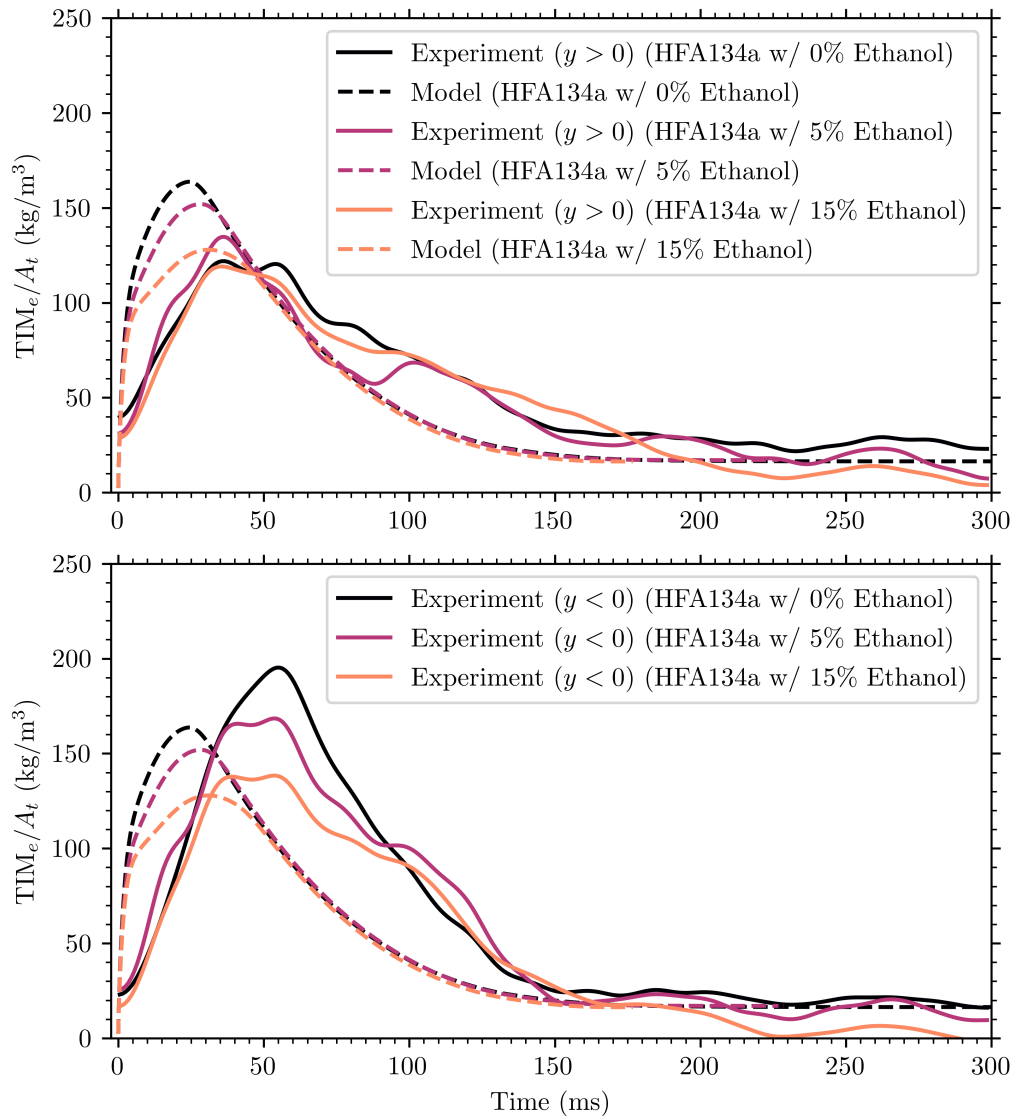


Figure 7.5: TIM_e/A_t for (top) $y > 0$ and (bottom) $y < 0$.

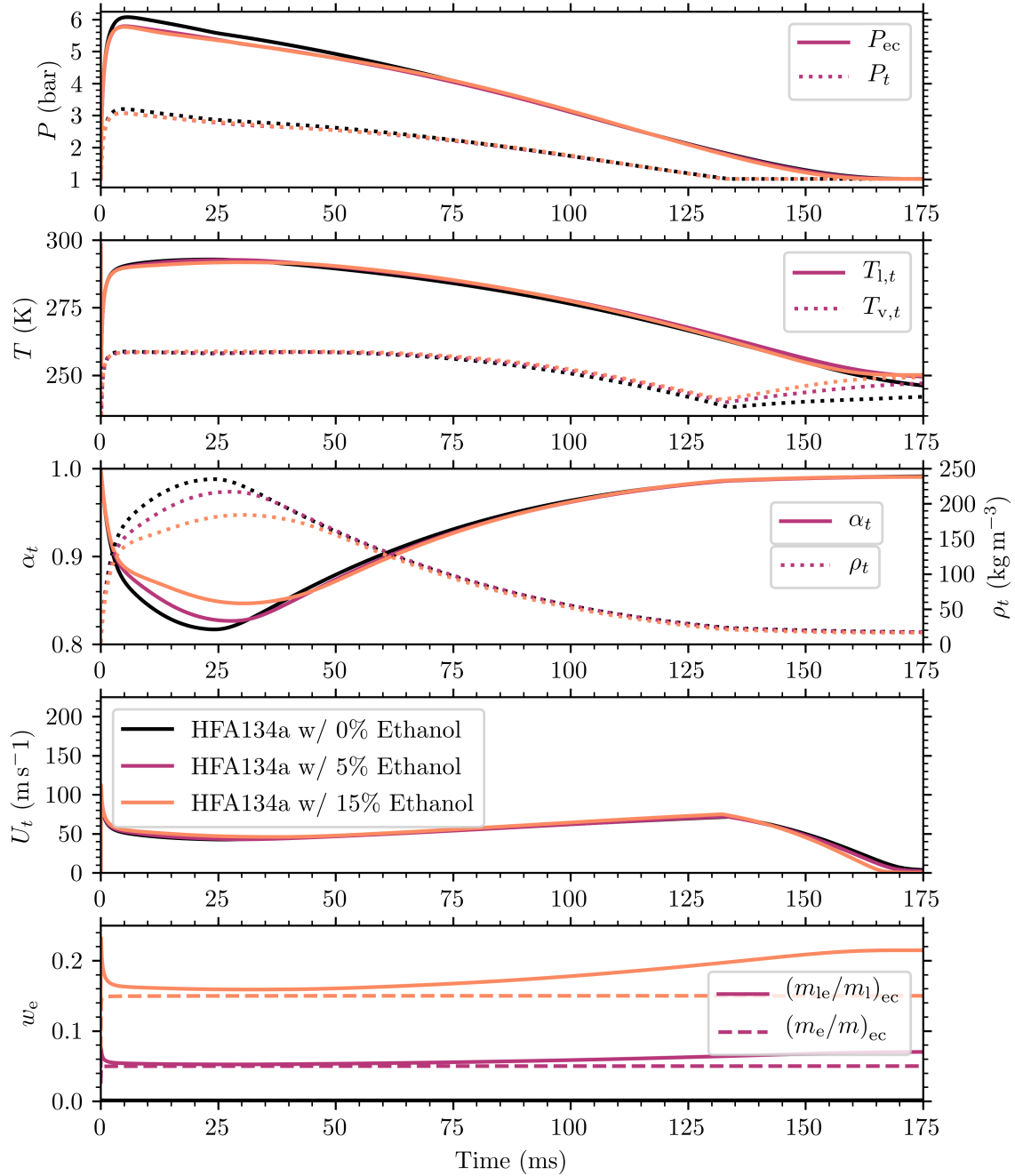


Figure 7.6: Time series of the conditions at the nozzle exit ($z = 0$). Lines are coloured by formulation as indicated in the fourth subfigure. Subfigures are, from top to bottom: expansion chamber (solid lines) and throat (dotted lines) pressures P ; expansion chamber (solid lines) and throat (dotted lines) temperatures T ; void fraction α (solid lines) and throat density ρ (dashed lines); throat velocity U_t ; and ethanol mass fraction w_e for (solid lines) liquid phase and (dashed lines) total mass.

In the first subfigure, both the expansion chamber pressure P_{ec} (solid lines) and the throat pressure P_t (dotted lines) are shown as time series for the three formulations modelled. Although the pressures predicted for these formulations differ considerably when determined with Raoult's law, the vapour pressure correlations of Gavtash et al. (2015) result in a very weak dependence of the pressure on the formulation. The spread of the data is so narrow that, at times, the individual lines cannot be discerned. The flows are choked for 130 ms, after which subcritical flows occur for an additional 30 ms.

The vapour temperature (Figure 7.6, second subfigure) is much lower than that of the liquid, showing the significant non-equilibrium effects in the model. The void fraction (third subfigure) is above 80% at all times for all formulations; if a smaller expansion chamber were used, a lower void fraction would be obtained.

The velocity at the throat (Figure 7.6, fourth subfigure) falls from an initial peak to a local minimum value of approximately 50 m s^{-1} at 25 ms after start of injection. This time corresponds to the point at which the void fraction is also at a minimum. The velocity increases until 135 ms after start of injection. At this time, the flow is no longer choked, as indicated by P_t (top axes), and the velocity decreases during a 50 ms end-of-injection subcritical flow.

The mass fractions of ethanol in the liquid phase in the expansion chamber, $(m_{le}/m_l)_{ec}$ and in the total mass in the expansion chamber, $(m_e/m)_{ec}$, are shown in Figure 7.6 (bottom). Although the ethanol concentration of the liquid phase increases, due to propellant flashing, the ethanol concentration of the total mass remains for all intents and purposes invariant throughout the injection.

7.5 Discussion

The agreement between the time series of experimental and modelled transverse integrated masses indicate that the model may capture the important phenomena of

the flow through the metered-dose inhaler. However, a large number of assumptions were required for model development, many of which are inconsistent with the known internal flow behaviour. Agreement with a single parameter is not proof of agreement of the physics. Nevertheless, if the limitations of the model are accepted, it provides some ability to answer those questions that motivated its development—namely the uncertainty of the absorption coefficient, and the effect of the internal flow structure.

Absorption coefficient uncertainty

A source of uncertainty for the absorption coefficient of ethanol-containing pMDI sprays (Chapters 3 and 4) is the composition of the liquid phase throughout the injection. This model demonstrates that, under the assumption of homogeneous flow, this composition change is negligible.

If the assumption of homogeneity is relaxed, a bias error arises in the absorption coefficient. If liquid and vapour travel at different velocities and have different ethanol mass fractions, the concentration-based ethanol mass fraction will differ from the flux-based ethanol mass fraction (Edwards and Marx 1996). Under these circumstances, the absorption coefficient required to determine the projected mass will differ from that of the formulation. If this is the case, the quantitative radiography measurements of ethanol-containing sprays, which assumed a single absorption coefficient, underpredict the projected mass. Extending the model to incorporate slip would improve the ability to estimate this potential source of error.

Constitutive models

The sensitivity of the model to the constitutive model parameters was investigated. Both Θ_0 and D were varied by a factor of two for the HFA134a formulation containing 15% ethanol by weight. Changing the boiling rate by a factor of two had very little effect on the solution. Similarly, the sensitivity of the diffusion coefficient was small; increasing D by a factor of two decreased peak TIM by approximately 6%.

The internal structures of pMDIs have little effect on the solution obtained from the phenomenological model developed here. The effects of the internal flow structure on other spray properties, such as the vapour/liquid ratio at the nozzle inlet, are not modelled in the present work. This highlights the inadequacy of simple phenomenological models in accounting for real thermofluid flows.

Concluding remarks

Further work is needed to establish the accuracy of comparing one-dimensional thermodynamic models and experimental measurements that are sampled from a stochastic process. The quasi-steady flow modelling approach taken here and by other investigators predicts values of various spray properties, which are then compared against experimentally-obtained values. The ensemble-mean is the expected value of a stochastic process only if the underlying distribution has zero skewness (Bendat and Piersol 2010). The variance of the real process was evident in high-speed phase contrast imaging (Chapter 4, laser extinction (Chapter 2) and back-illumination imaging (Appendix B). For properties such as projected mass, and droplet size, comparisons between models and ensemble-mean measurements may be in error. A detailed consideration of the higher-order statistics of experimentally-determined spray properties is needed if the models that these measurements are used to validate are to predict second-order effects (Gavtash et al. 2017a).

The thermodynamic models developed here, and in other investigations, are intended to capture the first-order phenomena in pMDIs. The high-resolution quantitative data in the near-nozzle region, and the internal flow visualisations obtained with phase contrast imaging, show that these first-order descriptions neglect a significant fraction of the phenomena that occur in pMDIs. The real flows are inhomogeneous, three-dimensional and unsteady. It may be possible to incorporate these effects into one-dimensional modelling with submodels and tunable parameters. However, it is the opinion of the author that, in light of these measurements and

visualisations, and the comparisons made in this thesis, more advanced modelling approaches are now required. Computational fluid dynamics (CFD) simulations of the internal flows of pMDIs are needed to advance the modelling of sprays from pressurised metered-dose inhalers. Given the advances in experimental measurement demonstrated in this thesis, and their exposure of the limitations of one-dimensional models, these simulations may be necessary if we are to more accurately predict the behaviour of pMDI sprays. It is remarkable and humbling that the operational processes of pMDIs, governed as they are by a rich flow physics, continue to elude our capacity to model them.

Chapter 8

Conclusions

In this thesis, an experimental campaign was undertaken to investigate pressurised metered-dose inhaler sprays with synchrotron-based x-ray techniques. The synchrotron x-ray techniques applied have not previously been used for the investigation of sprays from pMDIs, and overcome some of the limitations associated with visible-light diagnostics. The insights gained from these experiments were used to develop thermodynamic models of the flows from idealised pressurised metered-dose inhalers.

Quantitative x-ray radiography was first performed on unmetered sprays from a pMDI analogue. These experiments showed that synchrotron radiography could be used to measure pMDI spray ensemble-mean projected mass with high temporal and spatial resolutions. Ensemble-averaging of fifteen sprays and temporal binning to 0.184 ms provided a projected mass estimate with negligible shot noise and a low standard error.

The data analysis revealed that a dominant source of uncertainty associated with projected mass measurement of vaporising sprays is the absorption coefficient, to which the spray projected mass is inversely proportional. Contributors to this absorption coefficient uncertainty include the unknown phase leading to an unknown path length of ambient gas displaced by the spray. This source of uncertainty could

be minimised by measuring the projected mass as close as possible to the nozzle exit, which was used to advantage in radiography measurements of real pMDIs (Chapter 4). The absorption coefficient was also uncertain due to the unknown composition of ethanol-containing pMDI sprays.

Radiography measurements of the pMDI analogue showed that the transverse integrated mass increased linearly downstream of the nozzle exit, and could be used to predict the spray density in the near-nozzle region under a linear entrainment assumption (Chapter 3). Subsequent radiography measurements of a real pMDI (Chapter 4) showed that, at all times in the injection, the spray volume in the near-nozzle region is dominantly comprised of vapour. This quantitative mass measurement was corroborated by phase contrast visualisations, which showed that much of the region upstream of the atomising nozzle is occupied by vapour (Chapter 4).

Laser extinction measurements demonstrated that inclusion of cosolvent reduced the magnitude of optical density fluctuations in pMDI sprays (Chapter 2, Appendix B). Phase contrast images showed that the inclusion of cosolvent affected the internal flow structure of pMDIs (Chapter 4), with vapour distributed in the liquid at smaller scales with increased cosolvent concentration (Chapter 5). This change of scale is associated with a greater degree of homogeneity in the valve stem and sump, and led to a more consistent vapour/liquid ratio at the nozzle inlet. This structural effect is believed to contribute to the increased steadiness of ethanol-containing pMDI sprays (Appendix C).

High-magnification phase contrast imaging revealed that large isolated droplets are present in sprays from pMDIs (Chapter 5). These large isolated droplets were also observed in backlit spray imaging (Appendix B) and are expected to contribute to the optical density fluctuations observed in laser extinction (Chapter 2). For propellant-only sprays, large droplets and ligaments were observed in the expansion chamber, and may contribute to the unrespirable mass of suspension pMDIs. Intermittent discharge of liquid that resulted in coarse atomisation was also observed

in propellant-only flows (Chapter 4). For ethanol-containing formulations, these droplets and intermittent discharge were less prevalent. Large droplets were seen to form from liquid that pooled on the bowl at the nozzle exit (Chapter 5). Flow structural effects provide a possible explanation for the narrower droplet size distribution in ethanol-containing pMDI sprays (Myatt et al. 2015).

Thermodynamic models of pressurised metered-dose inhaler internal flows were developed. The assumptions used for these models were informed by the results of phase contrast imaging. For propellant-only flows, model outputs showed that thermal non-equilibrium may be significant, reflecting the short residence time in the nozzle of the pMDI. Under the assumption of homogeneous flow, the change in composition of ethanol-containing pMDI sprays during the spray event is entirely negligible, and it is appropriate to use the absorption coefficient of the formulation for radiography measurements. However, if slip effects are significant in sprays from pMDIs, the formulation absorption coefficient will underpredict the true projected mass.

The conditions under which suitable x-ray radiography measurements can be obtained have been established. These measurements confirm a long-held belief (Finlay 2001) that the mean nozzle exit conditions of pMDIs are dominantly vapour by volume. This is true at all times in the injection and when ethanol is included, at the concentrations studied. Vapour is generated upstream of the atomising nozzle and advects with the flow. The inclusion of cosolvent modifies the two-phase flow structure inside the valve stem and sump. This structural effect reduces spray unsteadiness, and eliminates some sources of unrespirable liquid masses in pMDI sprays.

Bibliography

- Abramovich, G.N. 1963. *The theory of turbulent jets*. The M.I.T. Press.
- Arai, Masataka. 2017. “Spray Boundary Definition and Air Entrainment”. In *Proceedings of the 19th Annual Conference on Liquid Atomization and Spray Systems - Asia*.
- Bar-Kohany, Tali, and Moti Levy. 2016. “State of the art review of flash-boiling atomization”. *Atomization and Sprays* 26 (12).
- Bell, Ian H., and Eric W Lemmon. 2016. “Automatic fitting of binary interaction parameters for multi-fluid Helmholtz-energy-explicit mixture models”. *Journal of Chemical & Engineering Data* 61 (11): 3752–3760.
- Bell, Ian H., Jorrit Wronski, Sylvain Quoilin, and Vincent Lemort. 2014. “Pure and Pseudo-pure Fluid Thermophysical Property Evaluation and the Open-Source Thermophysical Property Library CoolProp”. *Industrial & Engineering Chemistry Research* 53 (6): 2498–2508.
- Bell, John, and Steve Newman. 2007. “The rejuvenated pressurised metered dose inhaler”. *Expert opinion on drug delivery* 4 (3): 215–234.
- Bendat, Julius S, and Allan G Piersol. 1993. *Engineering applications of correlation and spectral analysis*. 2nd ed. John Wiley & Sons.
- . 2010. *Random data: analysis and measurement procedures*. 4th ed. John Wiley & Sons.

- Brennen, Christopher E. 2005. *Fundamentals of multiphase flow*. Cambridge University Press.
- Buchmann, Nicolas A, Daniel J Duke, Sayed A Shakiba, Daniel M Mitchell, Peter J Stewart, Daniela Traini, Paul M Young, David A Lewis, Julio Soria, and Damon Honnery. 2014. “A novel high-speed imaging technique to predict the macroscopic spray characteristics of solution based pressurised metered dose inhalers”. *Pharmaceutical Research* 31 (11): 2963–2974.
- Callen, Herbert B. 1960. *Thermodynamics*. John Wiley & Sons.
- Carvalho, Thiago C, Jay I Peters, and Robert O Williams III. 2011. “Influence of particle size on regional lung deposition—what evidence is there?” *International Journal of Pharmaceutics* 406 (1-2): 1–10.
- Cavallini, Alberto. 1996. “Working fluids for mechanical refrigeration—Invited paper presented at the 19th International Congress of Refrigeration, The Hague, August 1995”. *International Journal of Refrigeration* 19 (8): 485–496.
- Chigier, Norman. 1991. “Optical imaging of sprays”. *Progress in Energy and Combustion Science* 17 (3): 211–262.
- Clark, Andrew R. 1991. “Metered atomisation for respiratory drug delivery”. PhD thesis, Loughborough University of Technology.
- Cohen, H, GFC Rogers, and HIH Saravanamuttoo. 1996. *Gas Turbine Theory*. 4th ed. Longman Group.
- Crosland, Brian Michael, Matthew Ronald Johnson, and Edgar Akio Matida. 2009. “Characterization of the spray velocities from a pressurized metered-dose inhaler”. *Journal of Aerosol Medicine and Pulmonary Drug Delivery* 22 (2): 85–98.
- Cussler, Edward Lansing. 2009. *Diffusion: mass transfer in fluid systems*. Cambridge University Press.

- Dasch, Cameron J. 1992. "One-dimensional tomography: a comparison of Abel, onion-peeling, and filtered backprojection methods". *Applied Optics* 31 (8): 1146–1152.
- De Backer, Wilfried, Annick Devolder, Gianluigi Poli, Daniela Acerbi, Raffaella Monno, Christiane Herpich, Knut Sommerer, Thomas Meyer, and Fabrizia Martotti. 2010. "Lung deposition of BDP/formoterol HFA pMDI in healthy volunteers, asthmatic, and COPD patients". *Journal of Aerosol Medicine and Pulmonary Drug Delivery* 23 (3): 137–148.
- De Boer, AH, D Gjaltema, P Hagedoorn, and HW Frijlink. 2002. "Characterization of inhalation aerosols: a critical evaluation of cascade impactor analysis and laser diffraction technique". *International Journal of Pharmaceutics* 249 (1-2): 219–231.
- Deckker, BEL, and YF Chang. 1965. "An investigation of steady compressible flow through thick orifices". In *Proceedings of the Institution of Mechanical Engineers, Conference Proceedings*, 180:312–323. SAGE Publications Sage UK: London, England.
- Downar-Zapolski, P, Z Bilicki, Léon Bolle, and J Franco. 1996. "The non-equilibrium relaxation model for one-dimensional flashing liquid flow". *International Journal of Multiphase Flow* 22 (3): 473–483.
- Duke, Daniel J, David P Schmidt, Kshitij Neroorkar, Alan L Kastengren, and Christopher F Powell. 2013. "High-resolution large eddy simulations of cavitating gasoline–ethanol blends". *International Journal of Engine Research* 14 (6): 578–589.
- Duke, Daniel, Andrew Swantek, Zak Tilocco, Alan Kastengren, Kamel Fezzaa, Kshitij Neroorkar, Maryam Moulai, Christopher Powell, and David Schmidt. 2014. *X-ray imaging of cavitation in diesel injectors*. Tech. rep. SAE Technical Paper.

- Dunbar, CA. 1996. "An experimental and theoretical investigation of the spray issued from a pressurised metered-dose inhaler". PhD thesis, University of Manchester.
- Dunbar, CA, and JF Miller. 1997. "Theoretical investigation of the spray from a pressurized metered-dose inhaler". *Atomization and Sprays* 7 (4).
- Dunbar, CA, AP Watkins, and JF Miller. 1997. "An experimental investigation of the spray issued from a pMDI using laser diagnostic techniques". *Journal of Aerosol Medicine* 10 (4): 351–368.
- Edgington-Mitchell, Daniel, Kilian Oberleithner, Damon R Honnery, and Julio Soria. 2014. "Coherent structure and sound production in the helical mode of a screeching axisymmetric jet". *Journal of Fluid Mechanics* 748:822–847.
- Edwards, Christopher F, and KD Marx. 1996. "Single-point statistics of ideal sprays, Part I: Fundamental descriptions and derived quantities". *Atomization and Sprays* 6 (5): 499–536.
- Feynman, Richard P, Robert B Leighton, and Matthew Sands. 2011. *The Feynman lectures on physics, Vol. I: The new millennium edition: mainly mechanics, radiation, and heat*. Vol. 1. Basic books.
- Finlay, Warren H. 2001. *The mechanics of inhaled pharmaceutical aerosols: an introduction*. Academic Press.
- Fletcher, GE. 1975. "Factors affecting the atomization of saturated liquids". PhD thesis, Loughborough University.
- Gabrio, Brian J, Stephen W Stein, and David J Velasquez. 1999. "A new method to evaluate plume characteristics of hydrofluoroalkane and chlorofluorocarbon metered dose inhalers". *International Journal of Pharmaceutics* 186 (1): 3–12.
- Gavtash, B, B Myatt, H O'Shea, F Mason, T Church, H.K. Versteeg, G Hargrave, and G Brambilla. 2015. "Saturated vapour pressure (SVP) measurement of ethanol/HFA binary mixtures". In *Drug Delivery to the Lungs* 26.

- Gavtash, Barzin, Hendrik K Versteeg, G Hargrave, B Myatt, D Lewis, T Church, and G Brambilla. 2017a. “Transient aerodynamic atomization model to predict aerosol droplet size of pressurized metered dose inhalers (pMDI)”. *Aerosol Science and Technology* 51 (8): 998–1008.
- . 2017b. “Transient flashing propellant flow models to predict internal flow characteristics, spray velocity, and aerosol droplet size of a pMDI”. *Aerosol Science and Technology* 51 (5): 564–575.
- Gavtash, Barzin, Hendrik K Versteeg, G Hargrave, B Myatt, David Lewis, Tanya Church, and G Brambilla. 2018. “A model of transient internal flow and atomization of propellant/ethanol mixtures in pressurized metered dose inhalers (pMDI)”. *Aerosol Science and Technology* 52 (5): 494–504.
- Halls, Benjamin R, Terrence R Meyer, and Alan L Kastengren. 2015. “Quantitative measurement of binary liquid distributions using multiple-tracer x-ray fluorescence and radiography”. *Optics Express* 23 (2): 1730–1739.
- Halls, Benjamin R, Christopher D Radke, Benjamin J Reuter, Alan L Kastengren, James R Gord, and Terrence R Meyer. 2017. “High-speed, two-dimensional synchrotron white-beam x-ray radiography of spray breakup and atomization”. *Optics Express* 25 (2): 1605–1617.
- Harang, Marie. 2013. “Characterisation of Aerosols Generated by Pressurised Metered Dose Inhalers”. PhD thesis, King’s College London.
- Hindmarsh, Alan C. 1983. “ODEPACK, a systematized collection of ODE solvers”. *Scientific computing*: 55–64.
- Huber, Marcia L, Arno Laeisecke, and Richard A Perkins. 2003. “Model for the viscosity and thermal conductivity of refrigerants, including a new correlation for the viscosity of R134a”. *Industrial & Engineering Chemistry Research* 42 (13): 3163–3178.

- Ikeda, Y, N Yamada, and T Nakajima. 2000. "Multi-intensity-layer particle-image velocimetry for spray measurement". *Measurement Science and Technology* 11 (6): 617.
- Ivey, James W, David Lewis, Tanya Church, Warren H Finlay, and Reinhard Vehring. 2014. "A correlation equation for the mass median aerodynamic diameter of the aerosol emitted by solution metered dose inhalers". *International Journal of Pharmaceutics* 465 (1): 18–24.
- Jedelsky, Jan, and Miroslav Jicha. 2008. "Unsteadiness in effervescent sprays: a new evaluation method and the influence of operational conditions". *Atomization and Sprays* 18 (1).
- Jeon, Jeeyeon, Seoksu Moon, Kiyotaka Sato, and Takeshi Nagasawa. 2018. "Near-nozzle spray dynamics of 6-hole GDI injector under subcooled and superheated conditions". *Fuel* 232:308–316.
- Ju, Dehao, John Shrimpton, Moira Bowdrey, and Alex Hearn. 2012. "Effect of expansion chamber geometry on atomization and spray dispersion characters of a flashing mixture containing inerts. Part II: High speed imaging measurements". *International Journal of Pharmaceutics* 432 (1): 32–41.
- Ju, Dehao, John Shrimpton, and Alex Hearn. 2010. "The effect of reduction of propellant mass fraction on the injection profile of metered dose inhalers". *International Journal of Pharmaceutics* 391 (1): 221–229.
- Kastengren, Alan, and Christopher F Powell. 2014. "Synchrotron X-ray techniques for fluid dynamics". *Experiments in Fluids* 55 (3): 1–15.
- Kastengren, Alan, Christopher F Powell, Dohn Arms, Eric M Dufresne, Harold Gibson, and Jin Wang. 2012. "The 7BM beamline at the APS: a facility for time-resolved fluid dynamics measurements". *Journal of Synchrotron Radiation* 19 (4): 654–657.

- Kleinstreuer, Clement, Huawei Shi, and Zhe Zhang. 2007. “Computational analyses of a pressurized metered dose inhaler and a new drug-aerosol targeting methodology”. *Journal of Aerosol Medicine* 20 (3): 294–309.
- Lechner, P, C Fiorini, R Hartmann, J Kemmer, N Krause, P Leutenegger, A Longoni, H Soltau, D Stötter, R Stötter, et al. 2001. “Silicon drift detectors for high count rate X-ray spectroscopy at room temperature”. *Nuclear Instruments and Methods in Physics Research Section A: Accelerators, Spectrometers, Detectors and Associated Equipment* 458 (1-2): 281–287.
- Lee, Yohan, and Dongsoo Jung. 2012. “A brief performance comparison of R1234yf and R134a in a bench tester for automobile applications”. *Applied Thermal Engineering* 35:240–242.
- Lefebvre, Arthur H, and Vincent G McDonell. 2017. *Atomization and sprays*. CRC Press.
- Lemmon, Eric W, Marcia L Huber, and Mark O McLinden. 2002. “NIST reference fluid thermodynamic and transport properties–REFPROP”. *NIST standard reference database* 23:v7.
- Liepmann, H.W., and A. Roshko. 1957. *Elements of gasdynamics*. John Wiley & Sons.
- Linne, Mark. 2012. “Analysis of X-ray phase contrast imaging in atomizing sprays”. *Experiments in Fluids* 52 (5): 1201–1218.
- Luong, John TK. 1999. “Unsteadiness in effervescent sprays”. *Atomization and Sprays* 9 (1).
- Lyras, Konstantinos, Siaka Dembele, David P Schmidt, and Jennifer X Wen. 2018. “Numerical simulation of subcooled and superheated jets under thermodynamic non-equilibrium”. *International Journal of Multiphase Flow* 102:16–28.

- MacPhee, Andrew G, Mark W Tate, Christopher F Powell, Yong Yue, Matthew J Renzi, Alper Ercan, Suresh Narayanan, Ernest Fontes, Jochen Walther, Johannes Schaller, et al. 2002. "X-ray imaging of shock waves generated by high-pressure fuel sprays". *Science* 295 (5558): 1261–1263.
- Mannino, David M, and A Sonia Buist. 2007. "Global burden of COPD: risk factors, prevalence, and future trends". *The Lancet* 370 (9589): 765–773.
- Massoud, Mahmoud. 2005. *Engineering thermofluids: thermodynamics, fluid mechanics, and heat transfer*. Springer.
- Minor, Barbara, and Mark Spatz. 2008. "HFO-1234yf low GWP refrigerant update". In *International Refrigeration and Air Conditioning Conference*. West Lafayette, United States.
- Mitchell, Daniel, Damon Honnery, and Julio Soria. 2011. "Particle relaxation and its influence on the particle image velocimetry cross-correlation function". *Experiments in fluids* 51 (4): 933.
- Mitchell, Jolyon P, and Mark W Nagel. 2003. "Cascade impactors for the size characterization of aerosols from medical inhalers: their uses and limitations". *Journal of Aerosol Medicine* 16 (4): 341–377.
- Moin, Parviz. 2010. *Fundamentals of engineering numerical analysis*. Cambridge University Press.
- Moon, Seoksu, Weidi Huang, Zhilong Li, and Jin Wang. 2016. "End-of-injection fuel dribble of multi-hole diesel injector: Comprehensive investigation of phenomenon and discussion on control strategy". *Applied Energy* 179:7–16.
- Myatt, B, R Newton, D Lewis, T Church, G Brambilla, G Hargrave, H Versteeg, B Gavtash, and E Long. 2015. "PDA and High Speed Image Analysis of HFA/Ethanol pMDI Aerosols: New Findings". *Drug Delivery to the Lungs* 26.

- Naber, Jeffrey D, and Dennis L Siebers. 1996. "Effects of Gas Density and Vaporization on Penetration and Dispersion of Diesel Sprays". *SAE Technical Paper 960034*.
- Newman, Stephen P. 2005. "Principles of metered-dose inhaler design". *Respiratory Care* 50 (9): 1177–1190.
- Nurick, WH. 1976. "Orifice cavitation and its effect on spray mixing". *Journal of Fluids Engineering* 98 (4): 681–687.
- Pickett, Lyle M, Julien Manin, Alan Kastengren, and Christopher Powell. 2014. "Comparison of near-field structure and growth of a diesel spray using light-based optical microscopy and X-ray radiography". *SAE International Journal of Engines* 7 (2014-01-1412): 1044–1053.
- Piersol, Allan G. 1965. *Spectral analysis of nonstationary spacecraft vibration data*. Tech. rep. NASA CR-341. Los Angeles, California: Measurement Analysis Corporation.
- Raffel, Markus, Christian E Willert, Steven T Wereley, and Jürgen Kompenhans. 2013. *Particle image velocimetry: a practical guide*. Springer.
- Reocreux, Michel. 1974. "Contribution a l'étude des debits critiques en écoulement diphasique eau-vapeur". PhD thesis, L'Université Scientifique et Médicale de Grenoble.
- Reocreux, ML. 1976. *Experimental study of steam-water choked flow*. Tech. rep. CEA Centre d'Etudes Nucléaires de Saclay.
- Roland, Nicholas J, Rajiv K Bhalla, and John Earis. 2004. "The local side effects of inhaled corticosteroids: current understanding and review of the literature". *Chest* 126 (1): 213–219.
- Ruzycki, Conor A, Emadeddin Javaheri, and Warren H Finlay. 2013. "The use of computational fluid dynamics in inhaler design". *Expert Opinion on Drug Delivery* 10 (3): 307–323.

- Salzman, Gary A, and Dennis R Pyszczynski. 1988. "Oropharyngeal candidiasis in patients treated with beclomethasone dipropionate delivered by metered-dose inhaler alone and with Aerochamber". *Journal of Allergy and Clinical Immunology* 81 (2): 424–428.
- Santayana, George. 1905. *The life of reason*. Vol. 1. C. Scribner's Sons.
- Sazhin, S. S. 2014. *Droplets and sprays*. Springer.
- Shapiro, Ascher H. 1953. *The dynamics and thermodynamics of compressible fluid flow*. Vol. 1. The Ronald Press Company.
- Sharadin, Nathaniel. 2018. "Rational Coherence in Environmental Policy: Paris, Montreal, and Kigali". *Ethics, Policy & Environment*: 1–5.
- Sher, Eran, Tali Bar-Kohany, and Alexander Rashkovan. 2008. "Flash-boiling atomization". *Progress in Energy and Combustion Science* 34 (4): 417–439.
- Skripov, Vladimir Pavlovich. 1974. *Metastable liquids*. John Wiley & Sons.
- Smyth, H, AJ Hickey, G Brace, T Barbour, J Gallion, and J Grove. 2006. "Spray pattern analysis for metered dose inhalers I: orifice size, particle size, and droplet motion correlations". *Drug Development and Industrial Pharmacy* 32 (9): 1033–1041.
- Snigirev, A, I Snigireva, V Kohn, S Kuznetsov, and I Schelokov. 1995. "On the possibilities of x-ray phase contrast microimaging by coherent high-energy synchrotron radiation". *Review of Scientific Instruments* 66 (12): 5486–5492.
- Stein, Stephen W, and Paul B Myrdal. 2004. "A theoretical and experimental analysis of formulation and device parameters affecting solution MDI size distributions". *Journal of Pharmaceutical Sciences* 93 (8): 2158–2175.
- Stein, Stephen W, Poonam Sheth, P David Hodson, and Paul B Myrdal. 2014. "Advances in metered dose inhaler technology: hardware development". *AAPS PharmSciTech* 15 (2): 326–338.

- Sterne, Laurence. [1759] 1950. *The Life and Opinions of Tristram Shandy, Gentleman*. The Modern Library, Random House.
- Sun, Chunhua, Zhi Ning, Ming Lv, Kai Yan, and Juan Fu. 2016. “Acoustic performance of effervescent sprays by time–frequency method with different atomizer structures under different operating conditions”. *International Journal of Multiphase Flow* 82:35–48.
- Takagi, Shu, and Yoichiro Matsumoto. 2011. “Surfactant effects on bubble motion and bubbly flows”. *Annual Review of Fluid Mechanics* 43:615–636.
- Thiel, CG. 1996. “From Susie’s question to CFC free: an inventor’s perspective on forty years of MDI development and regulation”. In *Respiratory Drug Delivery V*, 115–123.
- Thorade, Matthis. 2014. “Entropiebasierte Bewertungskriterien für den Wärmeübergang in Kraftwerksprozessen und ihre Relevanz für praktische Anwendungen”. PhD thesis, Technische Universität Hamburg.
- Thorade, Matthis, and Ali Saadat. 2013. “Partial derivatives of thermodynamic state properties for dynamic simulation”. *Environmental earth sciences* 70 (8): 3497–3503.
- Tokumaru, PT, and PE Dimotakis. 1995. “Image correlation velocimetry”. *Experiments in Fluids* 19 (1): 1–15.
- Travis, JR, D Piccioni Koch, and W Breitung. 2012. “A homogeneous non-equilibrium two-phase critical flow model”. *International Journal of Hydrogen Energy* 37 (22): 17373–17379.
- Tukey, John W. 1977. *Exploratory data analysis*. Addison-Wesley Publishing Group.
- U.S. Pharmacopoeia. 2018. “Section 601 - Aerosols, nasal sprays, metered-dose inhalers, and dry powder inhalers”. Accessed: 19 August, 2018. http://www.pharmacopeia.cn/v29240/usp29nf24s0_c601_viewall.html.

- Versteeg, Hendrik K, Graham K Hargrave, B Myatt, DL Lewis, T Church, and G Brambilla. 2017. "Using phase Doppler anemometry & high speed imaging to analyze MDI spray plume dynamics". In *Respiratory Drug Delivery Europe*, 129–142.
- Versteeg, HK, GK Hargrave, and M Kirby. 2006. "Internal flow and near-orifice spray visualisations of a model pharmaceutical pressurised metered dose inhaler". In *Journal of Physics: Conference Series*, 45:207. 1. IOP Publishing.
- Wallis, Graham B. 1980. "Critical two-phase flow". *International Journal of Multiphase Flow* 6 (1-2): 97–112.
- Ward-Smith, AJ. 1979. "Critical flowmetering: The characteristics of cylindrical nozzles with sharp upstream edges". *International Journal of Heat and Fluid Flow* 1 (3): 123–132.
- Weir, Alexander Jr., J.L. York, and R.B. Morrison. 1956. "Two-and Three-Dimensional Flow of Air Through Square-Edged Sonic Orifices". *Transactions of the American Society of Mechanical Engineers* 78:481–488.
- Wigley, G, H Versteeg, and D Hodson. 2002. "Near-orifice PDA measurements and atomisation mechanism of a pharmaceutical pressurised metered dose inhaler". In *18th Annual Conference on Liquid Atomization & Spray Systems*. Zaragoza, Spain: Institute for Liquid Atomization & Spray Systems.
- Willmott, Philip. 2011. *An introduction to synchrotron radiation: techniques and applications*. John Wiley & Sons.
- World Health Organisation. 2018. "Burden of COPD". Accessed: 29 March, 2018.
<http://www.who.int/respiratory/copd/burden/en/>.

Appendix A

Governing equations of pMDI thermodynamic models

A.1 Two-phase speeds of sound

Propellant-only model

The approach taken to calculate the choked mass flow rate of homogeneous two-phase flows in Chapter 6 owes much to that outlined in Travis, Koch, and Breitung (2012). Their method of obtaining the two-phase speed of sound is adapted and reproduced here.

From the classical approach using the continuity and momentum equations (Shapiro 1953, 45-47), the speed of small-amplitude pressure wave propagation is:

$$c^2 = \frac{dP}{d\rho} \quad (\text{A.1})$$

with the typical thermodynamic constraint of constant entropy (Brennen 2005).

For two-phase mixtures, it is convenient to use the change in specific volume, because it is additive in mass-weighted terms:

$$v = x \cdot v_{sv} + (1 - x) \cdot v_{ml} \quad (\text{A.2})$$

By the chain rule, Equation A.1 becomes:

$$c^2 = -v^2 \left(\frac{\partial P}{\partial v} \right)_s \quad (\text{A.3})$$

Combining equations A.2 and A.3 and using the product rule:

$$c^2 = \frac{-v^2}{x \cdot \left(\frac{\partial v_{sv}}{\partial P} \right)_s + (1-x) \cdot \left(\frac{\partial v_{ml}}{\partial P} \right)_s + (v_{sv} - v_{ml}) \cdot \left(\frac{\partial x}{\partial P} \right)_s} \quad (\text{A.4})$$

Recognising that Equation A.3 also applies to each individual phase:

$$c^2 = \frac{v^2}{\frac{x}{(\rho_{sv} c_{sv})^2} + \frac{(1-x)}{(\rho_{ml} c_{ml})^2} - (v_{sv} - v_{ml}) \cdot \left(\frac{\partial x}{\partial P} \right)_s} \quad (\text{A.5})$$

The first two terms in the denominator of Equation A.5 are the volume-weighted acoustic impedances of each phase (Brennen 2005). The final term of the denominator is the specific volume change due to a change in quality during the pressure change. Using the specific entropy:

$$\left(\frac{\partial x}{\partial P} \right)_s = \left(\frac{\partial}{\partial P} \left(\frac{s - s_{ml}}{s_{sv} - s_{ml}} \right) \right)_s \quad (\text{A.6})$$

By the quotient rule (Travis, Koch, and Breitung 2012):

$$\left(\frac{\partial x}{\partial P} \right)_s = \frac{-(s_{sv} - s_{ml}) \cdot \left(\frac{\partial s_{ml}}{\partial P} \right)_s + (s - s_{ml}) \cdot \left[\left(\frac{\partial s_{sv}}{\partial P} \right)_s - \left(\frac{\partial s_{ml}}{\partial P} \right)_s \right]}{(s_{sv} - s_{ml})^2} \quad (\text{A.7})$$

For the sake of brevity, the detailed steps of obtaining $(\partial s_v / \partial P)_s$ and $(\partial s_l / \partial P)_s$ are omitted; the reader is referred to Travis, Koch, and Breitung (2012). For the homogeneous direct evaluation model used in Chapter 6, the partial derivatives of the individual phase entropies with respect to pressure are:

$$\left(\frac{\partial s_{sv}}{\partial P} \right)_s = -\frac{\beta_{sv}(T_{sv})}{\rho_{sv}} + \frac{\left(\frac{c_{p,sv}(T_{sv})}{T_{sv}} \right)}{\left(\frac{dP_\sigma(T_{sv})}{dT} \right)} \quad (\text{A.8})$$

where β is the thermal expansion coefficient, c_p is the mass-specific heat capacity at constant pressure, and $\frac{dP_\sigma}{dT}$ is the derivative along the saturation curve. The partial derivative of specific entropy for the liquid phase is given by:

$$\left(\frac{\partial s_{ml}}{\partial P} \right)_s = -\frac{\beta(T_{ml}, \rho_{ml})}{\rho_{ml}} + (1-\eta) \cdot \frac{\left(\frac{c_{p,ml}(T_{ml}, \rho_{ml})}{T_{ml}} \right)}{\left(\frac{dP_\sigma(T_{sv})}{dT} \right)} \quad (\text{A.9})$$

If the flow is isentropic:

$$s = s_0 \quad (\text{A.10})$$

and, using equations A.8 and A.9, equation A.7 can be solved. This allows equation A.5 to be solved for the two-phase speed of sound.

For the frozen model, the quality remains unchanged with pressure change:

$$\left(\frac{\partial x}{\partial P} \right)_s = 0 \quad (\text{A.11})$$

and equation A.5 can be solved directly.

If the flow is not isentropic, Equation A.10 cannot be used. In Chapter 6, an isentropic efficiency is used. The details are provided in the chapter. Although Equation A.10 can no longer be used, the isentropic efficiency provides an additional equation, and the methodology is otherwise unchanged.

Multicomponent frozen model

The assumptions used for this flow rate model are:

- Homogeneous flow ($W_l = W_v$)
- No gravitational effects
- Frozen flow (no heat or mass transfer between phases)
- Adiabatic flow
- Vapour phase is a calorically-perfect gas
- Liquid phase is incompressible

The one-dimensional adiabatic energy equation for a homogeneous frozen two-phase flow can be written as:

$$x \cdot h_{v,0} + (1 - x) \cdot h_{l,0} = x \cdot h_v(P) + (1 - x) \cdot h_l(P) + \frac{W^2}{2} \quad (\text{A.12})$$

Introducing an isentropic efficiency for the vapour phase:

$$\eta_{\text{isen},v} = \frac{h_{v,0} - h_v(P)}{h_{v,0} - h_v(P, s_{v,0})} \quad (\text{A.13})$$

and the liquid phase:

$$\eta_{\text{isen},l} = \frac{h_{l,0} - h_l(P)}{h_{l,0} - h_l(P, s_{l,0})} \quad (\text{A.14})$$

allows the energy balance to be written as:

$$\frac{W^2}{2} = x \cdot \eta_{\text{isen},v} \cdot (h_{v,0} - h_v(P, s_{v,0})) + (1 - x) \cdot \eta_{\text{isen},l} \cdot (h_{l,0} - h_l(P, s_{l,0})) \quad (\text{A.15})$$

Given the flow is frozen, there is no heat transfer between phases, and all work transfer goes into kinetic energy. Under these circumstances, there are no source terms in the enthalpy change of each phase. As a result, the first law:

$$dh = Tds + vdP \quad (\text{A.16})$$

can be used for each phase. Noting that the liquid phase is incompressible, the isentropic enthalpy change can be found:

$$h_{l,0} - h_l(P, s_{l,0}) = v_l \cdot (P_0 - P) \quad (\text{A.17})$$

where P_0 is the reservoir pressure. This is a restatement of the incompressible Bernoulli equation. For the vapour phase, treating it as isentropic:

$$h_{v,0} - h_v(P, s_{v,0}) = \int_P^{P_0} v_v dP \quad (\text{A.18})$$

where, for an ideal gas undergoing a reversible adiabatic expansion:

$$P \cdot v^\gamma = \text{const.} \quad (\text{A.19})$$

This becomes:

$$h_{v,0} - h_v(P, s_{v,0}) = P_0^{1/\gamma} \cdot v_{v,0} \cdot \left(P_0^{(\gamma-1)/\gamma} - P^{(\gamma-1)/\gamma} \right) \cdot \frac{\gamma}{\gamma - 1} \quad (\text{A.20})$$

Substitution of Equations A.20 and A.17 into Equation A.15 gives:

$$\frac{W^2}{2} = (1 - x) \cdot \eta_{\text{isen},l} \cdot v_l \cdot (P_0 - P) + x \cdot \eta_{\text{isen},v} \cdot P_0^{1/\gamma} \cdot v_{v,0} \cdot \left(P_0^{(\gamma-1)/\gamma} - P^{(\gamma-1)/\gamma} \right) \cdot \frac{\gamma}{\gamma - 1} \quad (\text{A.21})$$

For subcritical flow, the throat velocity can be obtained as a function of the reservoir conditions and the ambient pressure P . All other thermodynamic properties can be obtained, as the state at the throat is fully specified.

For critical flow, the additional constraint is that the velocity is equal to the two-phase speed of sound:

$$c^2 = \left(\frac{\partial P}{\partial \rho} \right)_s \quad (\text{A.22})$$

By the chain rule:

$$\left(\frac{\partial P}{\partial \rho} \right)_s = -v^2 \cdot \left(\frac{\partial P}{\partial v} \right)_s \quad (\text{A.23})$$

As the specific volume is additive in mass fractions:

$$v = x \cdot v_v + (1 - x) \cdot v_l \quad (\text{A.24})$$

and the flow is frozen:

$$\left(\frac{\partial x}{\partial P} \right)_s = 0 \quad (\text{A.25})$$

this becomes:

$$\left(\frac{\partial P}{\partial \rho} \right)_s = \frac{-v^2}{x \cdot \left(\frac{\partial v_v}{\partial P} \right)_s + (1 - x) \cdot \left(\frac{\partial v_l}{\partial P} \right)_s} \quad (\text{A.26})$$

As the liquid phase is incompressible:

$$\left(\frac{\partial v_l}{\partial P} \right)_s = 0 \quad (\text{A.27})$$

and noting that the speed of sound equation applies to each individual phase:

$$-v_v^2 \cdot \left(\frac{\partial P}{\partial v_v} \right)_s = c_v^2 \quad (\text{A.28})$$

this becomes:

$$\left(\frac{\partial P}{\partial \rho} \right)_s = c_v^2 \cdot \frac{v^2}{x \cdot v_v^2} \quad (\text{A.29})$$

where c_v is the speed of sound of the vapour phase. Assuming that the vapour is an ideal gas:

$$c_v^2 = \gamma \cdot P \cdot v_v \quad (\text{A.30})$$

Accordingly, the two-phase speed of sound for a homogeneous frozen mixture comprised of ideal gas and incompressible liquid can be written:

$$\left(\frac{\partial P}{\partial \rho} \right)_s = \gamma \cdot P \cdot \frac{(x \cdot v_v + (1-x) \cdot v_l)^2}{x \cdot v_v} \quad (\text{A.31})$$

We now have both the conservation of energy and the two-phase speed of sound. For critical flows with fixed quality, incompressible liquid and constant thermodynamic properties ($\gamma = \text{const.}$) the remaining unknowns are the throat pressure P and the specific volume of vapour at the throat, v_v .

Again, using the ideal gas equation of state with constant properties:

$$v_v = \frac{R \cdot T}{P} \quad (\text{A.32})$$

The temperature change for the vapour phase can be found from the enthalpy change of the vapour phase, noting that for an ideal gas $(\frac{\partial h}{\partial P})_T = 0$:

$$\eta_{\text{isen},v} \cdot (h_{v,0} - h_v(P, s_{v,0})) = c_{P,v} \cdot (T_0 - T) \quad (\text{A.33})$$

As a result, the specific volume can be found:

$$v_v = \frac{R \cdot \left(T_0 - \frac{\eta_{\text{isen},v}}{c_{P,v}} \cdot (h_{v,0} - h_v(P, s_{v,0})) \right)}{P} \quad (\text{A.34})$$

which, noting the enthalpy change during an isentropic expansion becomes:

$$v_v = \frac{R \cdot \left(T_0 - \frac{\eta_{\text{isen},v}}{c_p} \cdot P_0^{1/\gamma} \cdot v_{v,0} \cdot \left(P_0^{(\gamma-1)/\gamma} - P^{(\gamma-1)/\gamma} \right) \cdot \frac{\gamma}{\gamma-1} \right)}{P} \quad (\text{A.35})$$

The vapour specific volume has been expressed as a function of the reservoir conditions, isentropic efficiency and pressure at the throat. The only remaining unknown in equating A.31 and A.21 is the pressure at the throat. A root-finding method is used in the present work to determine the critical throat pressure, and thereby determine the mass flow rate and all other properties at the throat.

A.2 Differential equations of thermodynamic models

For a flow transient such as the discharge through the pMDI, the system can be represented in the form of an initial value problem:

$$\frac{d\mathbf{S}}{dt} = f(\mathbf{S}, t) \quad (\text{A.36})$$

If all system parameters are either constants (such as valve orifice diameter, chamber volume) or functions of the current state (density, temperature), this reduces to:

$$\frac{d\mathbf{S}}{dt} = f(\mathbf{S}) \quad (\text{A.37})$$

Propellant-only thermodynamic model

The differential equations for the propellant-only model of pMDIs in Chapter 6 are presented here.

If it is assumed that, in each chamber, the mixture is homogeneous in both composition and temperature, and that gravitational effects are negligible, the state of the two-phase mixture can be described with a single pair of pressure-enthalpy state variables.

The rates of change of these state variables are obtained from conservation laws described below.

Conservation of enthalpy ($\frac{dH}{dt} = \frac{dU}{dt} + \frac{dPV}{dt}$):

$$m \frac{dh}{dt} + h \frac{dm}{dt} = \sum_{i=1}^N (\dot{mh})_i + V \frac{dP}{dt} \quad (\text{A.38})$$

where $\sum_{i=1}^N (\dot{mh})_i = \frac{dU}{dt} + P \frac{dV}{dt}$ (Massoud 2005).

Conservation of volume ($\frac{dV}{dt} = 0$):

$$m \left[\left(\frac{\partial v}{\partial P} \right)_h \frac{dP}{dt} + \left(\frac{\partial v}{\partial h} \right)_P \frac{dh}{dt} \right] + v \frac{dm}{dt} = 0 \quad (\text{A.39})$$

Rearranging and writing in matrix form:

$$\begin{bmatrix} -V & m \\ m \left(\frac{\partial v}{\partial P} \right)_h & m \left(\frac{\partial v}{\partial h} \right)_P \end{bmatrix} \frac{d}{dt} \begin{bmatrix} P \\ h \end{bmatrix} = \begin{bmatrix} \sum_{i=1}^N (\dot{m}h)_i - h \frac{dm}{dt} \\ -v \frac{dm}{dt} \end{bmatrix} \quad (\text{A.40})$$

Mass flow rates are determined from the flow models described in Chapter 6. Provided these mass flow rates, the time derivatives $\frac{dP}{dt}$ and $\frac{dh}{dt}$ can be determined by linear algebra once the relevant thermophysical properties and derivatives are known.

In the saturation region, the Clapeyron equation gives (Callen 1960):

$$\left(\frac{\partial v}{\partial h} \right)_P = \frac{1}{T} \frac{dT_\sigma}{dP} \quad (\text{A.41})$$

where $\frac{dT_\sigma}{dP}$ is the derivative of temperature with respect to pressure along the saturation curve.

The partial derivative of specific volume with respect to pressure can be obtained, from the product rule (Thorade and Saadat 2013):

$$\left(\frac{\partial v}{\partial P} \right)_h = \left(\frac{\partial (v_{\text{sl}} + x(v_{\text{sv}} - v_{\text{sl}}))}{\partial P} \right)_h = \frac{dv_{\text{sl}}}{dP} + x \left(\frac{d(v_{\text{sv}} - v_{\text{sl}})}{dP} \right) + (v_{\text{sv}} - v_{\text{sl}}) \left(\frac{\partial x}{\partial P} \right)_h \quad (\text{A.42})$$

where x is the quality (kg kg^{-1}). Defining the quality x by the specific enthalpy:

$$x = \frac{h - h_{\text{sl}}}{h_{\text{sv}} - h_{\text{sl}}} \quad (\text{A.43})$$

allows the partial derivative of quality with respect to pressure to be obtained:

$$\left(\frac{\partial x}{\partial P} \right)_h = \left(\frac{\partial}{\partial P} \left(\frac{h - h_{\text{sl}}}{h_{\text{sv}} - h_{\text{sl}}} \right) \right)_h \quad (\text{A.44})$$

Using the quotient rule, Equation A.44 can be rearranged (Thorade and Saadat 2013) to give:

$$\left(\frac{\partial x}{\partial P} \right)_h = \frac{1}{h_{\text{sl}} - h_{\text{sv}}} \left(x \frac{dh_{\text{sv}}}{dP} + (1 - x) \frac{dh_{\text{sl}}}{dP} \right) \quad (\text{A.45})$$

Combining these gives an expression for the partial derivative of specific volume with respect to pressure at constant enthalpy:

$$\left(\frac{\partial v}{\partial P} \right)_h = \frac{dv_{\text{sl}}}{dP} + x \left(\frac{dv_{\text{sv}}}{dP} - \frac{dv_{\text{sl}}}{dP} \right) - \frac{1}{T} \frac{dT_\sigma}{dP} \left(x \frac{dh_{\text{sv}}}{dP} + (1 - x) \frac{dh_{\text{sl}}}{dP} \right) \quad (\text{A.46})$$

Multicomponent thermodynamic model

A number of conservation rules are applied to generate a macroscopic thermodynamic model of the system, along with a number of assumptions to make the model physically sound. These can be written as follows:

- Enthalpy is a conserved quantity and can be transferred into and out of vessels and between phases
- Mass is a conserved quantity and can be transferred into and out of vessels and between phases
- The sum of the liquid phase volume and the vapour phase volume in a chamber is equal to the volume of that chamber (in other words, volume is a conserved quantity)
- All components in the liquid phase are in thermal equilibrium with each other
- All vapours and gases in the gas region are in thermal equilibrium with each other
- The sum of the partial pressures of the gases and vapours is equal to the pressure inside the vessel (Dalton's law applies)

These conservation laws and equilibria give rise to the conservation equations for the system. These are derived below for a two-fluid model comprising a propellant, ethanol, and a non-condensable gas.

Conservation of liquid phase enthalpy:

$$dH = dU + PdV + VdP \quad (\text{A.47})$$

$$m_{lp} \frac{dh_{lp}}{dt} + m_{le} \frac{dh_{le}}{dt} - V_l \frac{dP}{dt} = \frac{dQ_l}{dt} + \sum_{i=1}^N (\dot{m}_l h)_i - h_{lp} \frac{dm_{lp}}{dt} - h_{le} \frac{dm_{le}}{dt} \quad (\text{A.48})$$

where m_{lp} is the mass of liquid propellant, h_{lp} is the specific enthalpy of the liquid propellant, V_l is the liquid phase volume, Q_l is any heat added or removed from

the liquid phase, $(\dot{m}_l h)_i$ is the enthalpy transfer to/from the liquid phase associated with the mass transfer of process i .

Conservation of gaseous phase enthalpy:

$$m_{vp} \frac{dh_{vp}}{dt} + m_{ve} \frac{dh_{ve}}{dt} + m_g \frac{dh_g}{dt} - V_g \frac{dP}{dt} = \frac{dQ_v}{dt} + \sum_{i=1}^N (\dot{m}_v h)_i - h_{vp} \frac{dm_{vp}}{dt} - h_{ve} \frac{dm_{ve}}{dt} - h_g \frac{dm_g}{dt} \quad (A.49)$$

Liquid phase thermal equilibrium ($\frac{dT_{lp}}{dt} = \frac{dT_{le}}{dt}$):

$$\left(\frac{\partial T_{lp}}{\partial h_{lp}} \right)_P \frac{dh_{lp}}{dt} + \left(\frac{\partial T_{lp}}{\partial P} \right)_{h_{lp}} \frac{dP}{dt} - \left(\frac{\partial T_{le}}{\partial h_{le}} \right)_P \frac{dh_{le}}{dt} - \left(\frac{\partial T_{le}}{\partial P} \right)_{h_{le}} \frac{dP}{dt} = 0 \quad (A.50)$$

Gas phase thermal equilibrium ($\frac{dT_{vp}}{dt} = \frac{dT_{ve}}{dt}; \frac{dT_{vp}}{dt} = \frac{dT_g}{dt}$):

$$\left(\frac{\partial T_{vp}}{\partial h_{vp}} \right)_{P_{vp}} \frac{dh_{vp}}{dt} + \left(\frac{\partial T_{vp}}{\partial P_{vp}} \right)_{h_{vp}} \frac{dP_{vp}}{dt} - \left(\frac{\partial T_{ve}}{\partial h_{ve}} \right)_{P_{ve}} \frac{dh_{ve}}{dt} - \left(\frac{\partial T_{ve}}{\partial P_{ve}} \right)_{h_{ve}} \frac{dP_{ve}}{dt} = 0 \quad (A.51)$$

$$\left(\frac{\partial T_{vp}}{\partial h_{vp}} \right)_{P_{vp}} \frac{dh_{vp}}{dt} + \left(\frac{\partial T_{vp}}{\partial P_{vp}} \right)_{h_{vp}} \frac{dP_{vp}}{dt} - \left(\frac{\partial T_g}{\partial h_g} \right)_{P_g} \frac{dh_g}{dt} - \left(\frac{\partial T_g}{\partial P_g} \right)_{h_g} \frac{dP_g}{dt} = 0 \quad (A.52)$$

Pressure equilibrium (the rate of change of the vessel pressure is equal to the sum of the rates of change of each gas phase partial pressure):

$$\frac{dP}{dt} - \frac{dP_{vp}}{dt} - \frac{dP_{ve}}{dt} - \frac{dP_g}{dt} = 0 \quad (A.53)$$

Conservation of volume (the rate of change of the liquid volume is equal to the rate of change of each vapour/gas component's volume): $\frac{dV_l}{dt} = -\frac{dV_g}{dt}$:

$$m_{lp} \left[\left(\frac{\partial v_{lp}}{\partial h_{lp}} \right)_P \frac{dh_{lp}}{dt} + \left(\frac{\partial v_{lp}}{\partial P} \right)_{h_{lp}} \frac{dP}{dt} \right] + m_{le} \left[\left(\frac{\partial v_{le}}{\partial h_{le}} \right)_P \frac{dh_{le}}{dt} + \left(\frac{\partial v_{le}}{\partial P} \right)_{h_{le}} \frac{dP}{dt} \right] + \\ m_{vp} \left[\left(\frac{\partial v_{vp}}{\partial h_{vp}} \right)_{P_{vp}} \frac{dh_{vp}}{dt} + \left(\frac{\partial v_{vp}}{\partial P_{vp}} \right)_{h_{vp}} \frac{dP_{vp}}{dt} \right] = -v_l \left(\frac{dm_{lp}}{dt} + \frac{dm_{le}}{dt} \right) - v_{vp} \frac{dm_{vp}}{dt} \quad (A.54)$$

$$m_{lp} \left[\left(\frac{\partial v_{lp}}{\partial h_{lp}} \right)_P \frac{dh_{lp}}{dt} + \left(\frac{\partial v_{lp}}{\partial P} \right)_{h_{lp}} \frac{dP}{dt} \right] + m_{le} \left[\left(\frac{\partial v_{le}}{\partial h_{le}} \right)_P \frac{dh_{le}}{dt} + \left(\frac{\partial v_{le}}{\partial P} \right)_{h_{le}} \frac{dP}{dt} \right] + \\ m_{ve} \left[\left(\frac{\partial v_{ve}}{\partial h_{ve}} \right)_{P_{ve}} \frac{dh_{ve}}{dt} + \left(\frac{\partial v_{ve}}{\partial P_{ve}} \right)_{h_{ve}} \frac{dP_{ve}}{dt} \right] = -v_l \left(\frac{dm_{lp}}{dt} + \frac{dm_{le}}{dt} \right) - v_{ve} \frac{dm_{ve}}{dt} \quad (A.55)$$

$$\begin{aligned}
 m_{lp} \left[\left(\frac{\partial v_{lp}}{\partial h_{lp}} \right)_P \frac{dh_{lp}}{dt} + \left(\frac{\partial v_{lp}}{\partial P} \right)_{h_{lp}} \frac{dP}{dt} \right] + m_{le} \left[\left(\frac{\partial v_{le}}{\partial h_{le}} \right)_P \frac{dh_{le}}{dt} + \left(\frac{\partial v_{le}}{\partial P} \right)_{h_{le}} \frac{dP}{dt} \right] + \\
 m_g \left[\left(\frac{\partial v_g}{\partial h_g} \right)_{P_g} \frac{dh_g}{dt} + \left(\frac{\partial v_g}{\partial P_g} \right)_{h_g} \frac{dP_g}{dt} \right] = -v_l \left(\frac{dm_{lp}}{dt} + \frac{dm_{le}}{dt} \right) - v_g \frac{dm_g}{dt}
 \end{aligned} \tag{A.56}$$

Writing these in matrix form,

$$\begin{bmatrix}
 -V_l & 0 & 0 & 0 & m_{lp} & m_{le} & 0 & 0 & 0 \\
 -V_g & 0 & 0 & 0 & 0 & 0 & m_{vp} & m_{ve} & m_g \\
 \frac{\partial T_{lp}}{\partial P} - \frac{\partial T_{le}}{\partial P} & 0 & 0 & 0 & \frac{\partial T_{lp}}{\partial h_{lp}} & -\frac{\partial T_{le}}{\partial h_{le}} & 0 & 0 & 0 \\
 0 & \frac{\partial T_{vp}}{\partial P_{vp}} & -\frac{\partial T_{ve}}{\partial P_{ve}} & 0 & 0 & 0 & \frac{\partial T_{vp}}{\partial h_{vp}} & -\frac{\partial T_{ve}}{\partial h_{ve}} & 0 \\
 0 & \frac{\partial T_{vp}}{\partial P_{vp}} & 0 & -\frac{\partial T_g}{\partial P_g} & 0 & 0 & \frac{\partial T_{vp}}{\partial h_{vp}} & 0 & -\frac{\partial T_g}{\partial P_g} \\
 1 & -1 & -1 & -1 & 0 & 0 & 0 & 0 & 0 \\
 m_{lp} \frac{\partial v_{lp}}{\partial P} + m_{le} \frac{\partial v_{le}}{\partial P} & m_{vp} \frac{\partial v_{vp}}{\partial P_{vp}} & 0 & 0 & m_{lp} \frac{\partial v_{lp}}{\partial h_{lp}} & m_{le} \frac{\partial v_{le}}{\partial h_{le}} & m_{vp} \frac{\partial v_{vp}}{\partial h_{vp}} & 0 & 0 \\
 m_{lp} \frac{\partial v_{lp}}{\partial P} + m_{le} \frac{\partial v_{le}}{\partial P} & 0 & m_{ve} \frac{\partial v_{ve}}{\partial P_{ve}} & 0 & m_{lp} \frac{\partial v_{lp}}{\partial h_{lp}} & m_{le} \frac{\partial v_{le}}{\partial h_{le}} & 0 & m_{ve} \frac{\partial v_{ve}}{\partial h_{ve}} & 0 \\
 m_{lp} \frac{\partial v_{lp}}{\partial P} + m_{le} \frac{\partial v_{le}}{\partial P} & 0 & 0 & m_g \frac{\partial v_g}{\partial P_g} & m_{lp} \frac{\partial v_{lp}}{\partial h_{lp}} & m_{le} \frac{\partial v_{le}}{\partial h_{le}} & 0 & 0 & m_g \frac{\partial v_g}{\partial h_g}
 \end{bmatrix} \\
 \frac{d}{dt} \begin{bmatrix} P \\ P_{vp} \\ P_{ve} \\ P_g \\ h_{lp} \\ h_{le} \\ h_{vp} \\ h_{ve} \\ h_g \end{bmatrix} = \begin{bmatrix} \frac{dQ_l}{dt} + \sum_{i=1}^N (\dot{m}_l h)_i - h_{lp} \frac{dm_{lp}}{dt} - h_{le} \frac{dm_{le}}{dt} \\ \frac{dQ_v}{dt} + \sum_{i=1}^N (\dot{m}_v h)_i - h_{vp} \frac{dm_{vp}}{dt} - h_{ve} \frac{dm_{ve}}{dt} - h_g \frac{dm_g}{dt} \\ 0 \\ 0 \\ 0 \\ 0 \\ -v_l \left(\frac{dm_{lp}}{dt} + \frac{dm_{le}}{dt} \right) - v_{vp} \frac{dm_{vp}}{dt} \\ -v_l \left(\frac{dm_{lp}}{dt} + \frac{dm_{le}}{dt} \right) - v_{ve} \frac{dm_{ve}}{dt} \\ -v_l \left(\frac{dm_{lp}}{dt} + \frac{dm_{le}}{dt} \right) - v_g \frac{dm_g}{dt} \end{bmatrix} \tag{A.57}$$

As this is of the form $\mathbf{Ax} = \mathbf{B}$, the rate terms \mathbf{x} can be found by $\mathbf{x} = \mathbf{A}^{-1}\mathbf{B}$.

Appendix B

Back-illumination imaging of pressurised metered-dose inhaler sprays

B.1 Introductory statement

This paper was prepared for the *7th Australian Conference on Laser Diagnostics in Fluid Mechanics & Combustion* and describes the use of back-illumination imaging for the measurement of pMDI sprays.

Back-illumination imaging is an established technique (Chigier 1991) for spray studies. The produced data can display trends in spray behaviour (Arai 2017), and, in the dilute spray region, the transmission can be used to measure the optical depth. Multiple scatter effects mean that the optical depth is not a direct mass measurement; nevertheless it is indicative of spray density.

In this paper, back-illumination imaging was performed with propellant-only and ethanol-containing sprays from metered-dose inhalers. The image sequences obtained were used to develop ensemble-mean time-variant profiles of the optical depth. This was an extension of the laser extinction method used in Chapter 2 with

metered sprays, rather than the electronic metering inhaler.

Ensemble-mean optical depth profiles showed that the spray was asymmetric about the spray axis. Peak spray widths were greater for sprays with HFA134a propellant than HFA227ea. RMS values of the optical depth were greater for propellant-only sprays than for those containing ethanol. Although not presented in the paper, it can be observed qualitatively that coefficients of variation σ/μ are also greater for the propellant-only sprays, meaning that the higher RMS optical depth for propellant-only sprays is not a result of a higher mean optical depth. These findings are consistent with an increase in spray steadiness promoted by the internal flow-structural effect observed in Chapter 4.

Back-Illumination Imaging of Pressurised Metered-Dose Inhaler Sprays

N. Mason-Smith¹, D. Duke², M. Fedrizzi¹, J. Soria^{1,3}, D. Edgington-Mitchell¹ & D. Honnery¹

¹Department of Mechanical and Aerospace Engineering
 Monash University, Clayton, Victoria, Australia

²Energy Systems Division
 Argonne National Laboratory, Illinois, USA

³Department of Aeronautical Engineering
 King Abdulaziz University, Jeddah, Kingdom of Saudi Arabia

Abstract

Sprays in the near-nozzle region of a pMDI are imaged with high spatial resolution back-illumination imaging to aid interpretation of laser extinction signals. Spray density varies continuously throughout the spray event, and between events, for all formulations studied. Spray widths increase until approximately 50 ms after the start of injection, after which the spray narrows until the metering chamber is depleted. Fluctuations in optical depth are reduced by the inclusion of ethanol, which reduces fluctuations in spray spread. In addition to many small droplets, visualisations show dense droplet clusters and large droplets.

Introduction

Pressurised metered-dose inhalers (pMDI) are used for the delivery of drugs for the treatment of asthma and other respiratory diseases. The spray developed is the result of a high vapour pressure propellant forcing a metered dose of drug-containing solution through an atomising nozzle. Cosolvents such as ethanol are commonly included to aid with drug solubility. Drug particle sizes are related to the initial droplet sizes, from which the propellant and cosolvent evaporate, by the drug concentration [16]. Typical pMDIs have small 50 μL metering chambers that isolate a volume of formulation from the canister. After actuation, the formulation flows from the metering chamber through an expansion chamber and discharges from an atomising nozzle. The pressure and temperature in the metering chamber decrease during injection [13], and injection ends when the metering chamber is depleted of formulation. Spray durations are on the order of 100 ms.

Many of the sprayed droplets have high velocities and large aerodynamic diameters, and as such are poor flow tracers that do not follow the user's comparatively slow inhalation. This results in a substantial deposition of drug in the mouth [4]. Prior studies have extensively characterised mean velocity and spreading characteristics of pMDI sprays [3, 5, 14], and there have also been observations of large fluctuations in cone angle and spray density, visualised in the near-nozzle region [5, 17] and downstream [12]. These large fluctuations in cone angle and spray density are expected to affect drug deposition *in vivo*, particularly if the droplets ejected during these events are poor tracers.

Line-of-sight optical techniques yield information on the path-integrated spray density, and with adequate temporal resolution can provide information on fluctuations in nozzle discharge. The non-dimensional optical depth τ [15], also known as the optical density [2] is related to the transmission $T = \left(\frac{I}{I_0}\right)$ by

the Beer-Lambert law:

$$\tau = -\ln\left(\frac{I}{I_0}\right) \quad (1)$$

where I is the detected flux and I_0 is the incident flux in the absence of spray.

Extinction of a laser sheet oriented through the centreline of a spray downstream of the mouthpiece of a pMDI analogue [14] showed axially-conveying fluctuations in transmission, and these were interpreted as indicative of spray unsteadiness. These fluctuations in transmission were found to be reduced by the inclusion of ethanol in the formulation, which was interpreted as indicating a higher level of unsteadiness in propellant-only sprays. However, this interpretation is based on limited information, as fluctuations in optical depth may have several sources. Full-field back-illumination imaging is a technique that can complement laser extinction and assist with signal interpretation. In this paper, we investigate the near-nozzle region of sprays from metered-dose inhalers with high spatial resolution back-illumination imaging. The obtained dataset is a complementary measure of near-nozzle spray structure, and assists the interpretation of line and point measurements of pMDI sprays. Due to the difficulty of obtaining full-field images with adequate temporal resolution, high sample-rate laser extinction remains an attractive technique for study of the time-variant spray density.

Experimental Methodology

Spray Apparatus

A linear solenoid-driven pMDI actuator was developed [1] and was used to generate sprays from metered-dose inhalers [14]. A Bespak inhaler body was used with the mouthpiece removed to allow imaging of the near-nozzle region (Figure 1). The nozzle exit is recessed in a bowl and located 3mm upstream of the coordinate system (Figure 1). Metered canisters containing propellants HFA 134a and HFA 227, with and without ethanol, were used to generate drug-free sprays. Canister metering valves were 50 μL . Inhaler body and canister dimensions are given in Table 1; the reader is referred to [9] for the significance of each dimension. Formulations used are shown in Table 2, specifying weight fractions of each constituent.

Back-Illumination Imaging

A back-illumination imaging setup was used to visualise the spray in the near-nozzle region. Illumination was provided by a strobed Phlatlight CBT-120 LED. Short pulse durations and low duty cycles allowed a current several times higher than the safe continuous rating to be used [20]. This greatly increased the lu-

Dimension	Size (mm)
Nozzle orifice diameter (d_{no})	0.3
Nozzle orifice length (l_{no})	0.6
Valve stem diameter, inner ($d_{vs,i}$)	2.0
Valve stem diameter, outer ($d_{vs,o}$)	3.2
Valve stem length (l_{vs})	12
Valve orifice diameter (d_{vo})	0.6

Table 1: Canister and nozzle dimensions.

Formulation	% HFA134a	% HFA227	% EtOH
134a	100	0	0
227	0	100	0
134a-E	85	0	15
227-E	0	85	15

Table 2: Canister formulations, composition by weight of propellant (HFA134a and HFA227) and ethanol (EtOH).

minous flux during imaging. A guide to safe operation of these LEDs for high-speed imaging is given in [18]. To minimise the light pulse duration, imaging was performed without a diffuser to maximise the luminous flux. However, the LED pulse duration of 100 ns is inadequate to image the fastest droplets without motion blur.

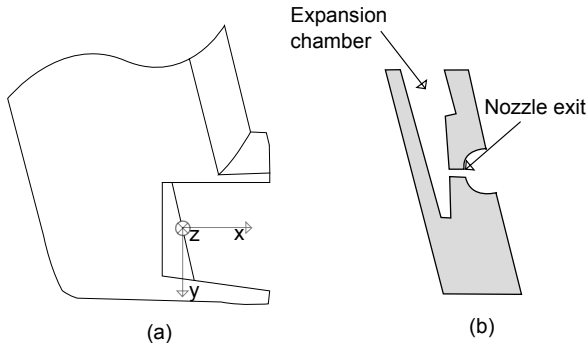


Figure 1: Schematic of (a) Bespak inhaler body with mouthpiece removed, allowing visualisation of the near-nozzle region; and (b) nozzle internal geometry.

A PCO Dimax was used to acquire image sequences of ≥ 40 spray events for each formulation. High magnification was achieved with a Nikon 105mm lens, a bellows and a 25mm macro tube. Image acquisition parameters are given in Table 3. The camera's double-shutter function was used, and the recorded image pairs can be used for "shadowgraph PIV" [7, 19]. Two-point radiometric calibration was used to correct for inhomogeneous back-illumination and the sensor's (albeit very low) fixed pattern noise [10]. Results are presented in regions where the reference intensity was sufficient to measure transmission with a minimum of 10-bit radiometric resolution. A BeagleBone Black programmable pulse generator [8] was used to trigger the experiment.

Results and Discussion

To characterise the mean spray structure, transverse profiles of optical depth were obtained by ensemble averaging. The temporal evolution of ensemble-average (≥ 40 spray events) radial profiles of optical depth at $x = 2$ mm are presented in Figure 2. Spray half-widths, defined by the half-width half-maximum (HWHM) of optical depth, are shown as isolines on the tempo-

Parameter	Value
Frame rate (image pairs/s)	500
Interpulse time (μs)	4
Light pulse duration (ns)	100
Magnification (pixels/mm)	307
Magnification factor	3.4
Radiometric resolution (bits/pixel)	12

Table 3: Back-illumination imaging parameters.

ral evolution plot.

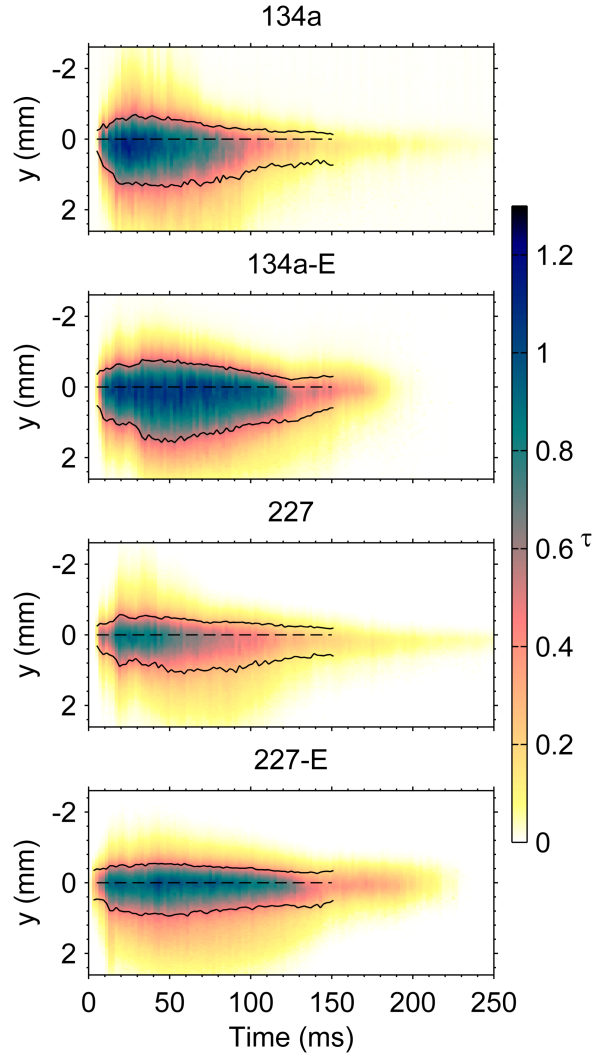


Figure 2: Temporal evolution of ensemble average transverse profile at $x = 2$ mm. Spray axes (black dashed lines) and spray half-widths (black solid lines) are overlaid.

Spray transience is observable—optical depth peaks around 25–50 ms after start of injection for all formulations, after which it decays. Discharge profiles differ for propellant-only and ethanol-containing formulations. A long time is required for the optical depth to reach zero on the centreline for propellant-only formulations, suggesting there is a long discharge. Ethanol-containing formulations cease more rapidly, though have a sustained period of high and nominally constant centreline optical depth. All formulations have high radial gradients of optical depth at $x = 2$ mm, exceeding 1 mm^{-1} . Axial gradients are

lower, on the order of 0.1 mm^{-1} . Profiles are also visibly asymmetric about the centreline, with a greater optical depth through the spray event located below the spray axis.

The observed asymmetry of the spray profiles in Figure 2 is investigated by measuring spray widths, providing a local measure of the extent of the spray. Spray half-widths are plotted in Figure 3. Half-widths are antisymmetric about the spray axis, and the spray is widest below the spray axis. With reference to the nozzle internal geometry (Figure 1), the wider spray occurs below the nozzle orifice. Formulation is also seen to affect the spray width, as HFA134a sprays are wider in the mean than those propelled by HFA227.

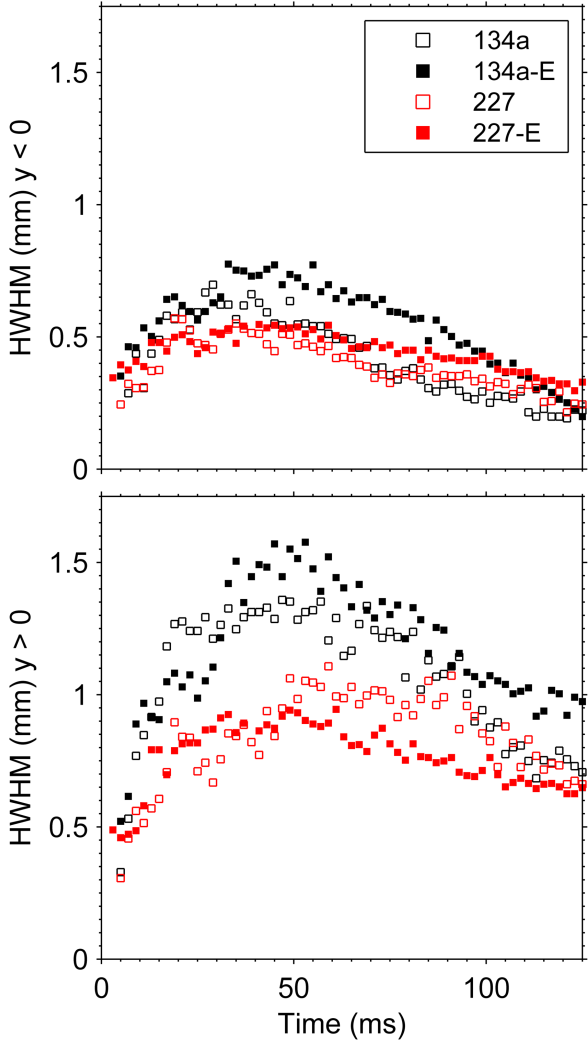


Figure 3: Ensemble-average spray half-widths at $x = 2 \text{ mm}$, above and below the spray axis.

Importantly, the transverse profiles also depict spray discharge characteristics that may be misinterpreted with a point measurement. Ethanol-containing formulations have a period of almost constant optical depth along the spray axis for 25–100 ms after the start of injection. Taken in isolation, this would suggest the presence of a steady state, however the spray width varies continuously over this period and narrows after it peaks at around 50 ms (Figure 3). For the formulations and metering volume studied, pMDI sprays exhibit no steady-state.

In addition to a transient spray density that results from metered discharge, pMDI sprays exhibit a high degree of interspray vari-

ability. This is illustrated with the time evolution of a profile ensemble RMS, shown in Figure 4. RMS profiles are generated at $x = 2 \text{ mm}$ from ≥ 40 spray events. Spatial binning of 1 nozzle diameter in x was used to increase the number of samples used to calculate the RMS, however as the samples are not independent there remains a large uncertainty on the resulting plot.

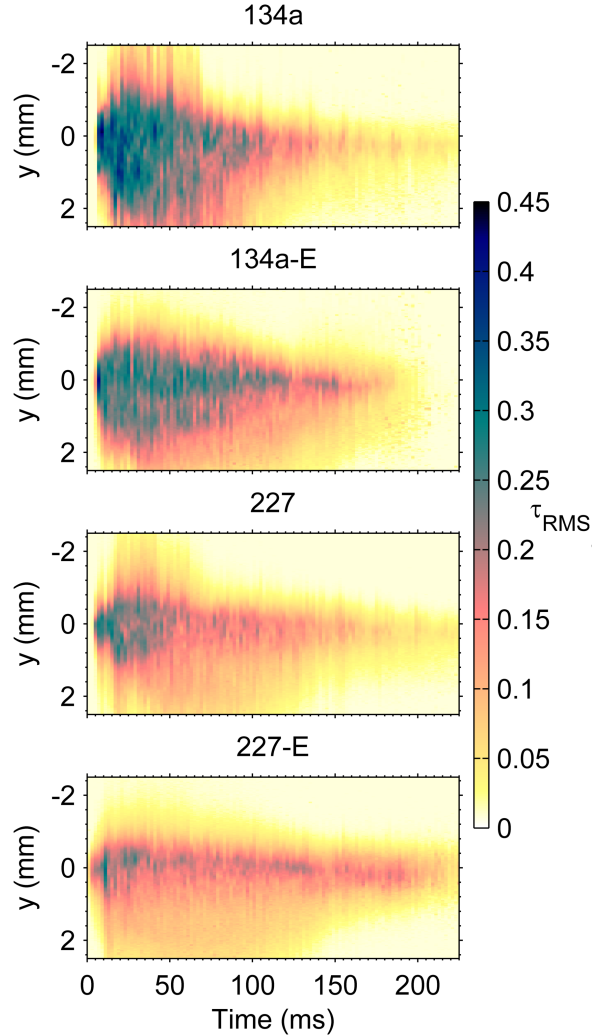


Figure 4: Temporal evolution of transverse profile RMS at $x = 2 \text{ mm}$.

Fluctuations in optical depth are highest for 134a-propelled sprays. For both propellants, fluctuations in optical depth are reduced by the inclusion of ethanol. The lowest magnitude of fluctuations was seen with 227-E, which represents the lowest vapour pressure formulation studied [14].

Instantaneous images are presented to illustrate the sources of fluctuations. Instantaneous images of 134a sprays 50 ms after start of injection are shown in Figure 5. Though imaged at the same time after start of injection, the spray structures vary considerably. In the top image, the spray appears concentrated on the centreline. Some droplet clusters are seen, and there is very little spray visualised above the spray axis. In the lower image, a large number of droplets are present above and below the spray axis, and their trajectory relative to the spray axis indicates a significant increase in the instantaneous cone angle. The overall spray density is also substantially increased. This large variability in spray density may be related to a two-phase flow

instability driven by propellant boiling in the nozzle. The spray appears finely atomised for both images.

Propellant-only sprays of HFA227 at this same time are shown in Figure 6. The spray is finely atomised in the upper image, and has a low optical density as is expected from the mean profiles (Figure 2). The lower image shows a ‘shedding’ event in which a mass of liquid emerges from the nozzle as large droplets. These droplets are unlikely to trace the user’s breath and would be expected to substantially contribute to deposition of drug in the mouth.

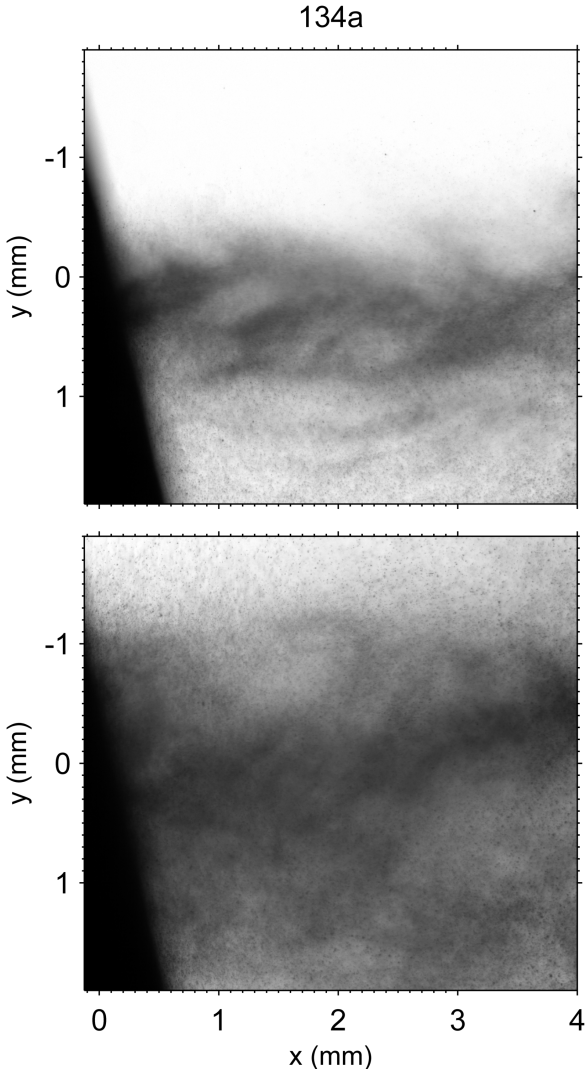


Figure 5: Instantaneous back-illumination spray images of near-nozzle region for independent 134a spray events, both imaged 50 ms after start of injection.

Instantaneous image sets show that the inclusion of ethanol alters spray morphology for both propellants, and spreading rate fluctuations are reduced. For 134a-E, RMS optical depth is high, and these fluctuations are the product of a local variability in structure that convects through the spray region. The 134a-E sprays are wider in the mean than 134a (Figure 3), and instantaneous images (Figure 7, top) show that this increased width is consistent. Substantial groups of droplet clusters are present in the sprays, and there is spray present both above and below the spray axis. 227-E sprays similarly did not fluctuate substantially in spread. As per the propellant-only case, 227-E spray

images showed the presence of many large droplets that would be unlikely to be respirable.

Unsteadiness as measured in the framework of Edwards and Marx [6] is highest at the periphery of two-phase effervescent sprays [11]. Centreline optical depths vary substantially less relative to the mean than the optical depths at the spray periphery. Laser line extinction measurements intended to characterise spray unsteadiness for pMDIs are likely to obtain a stronger signal in regions at the periphery of pMDI sprays, rather than along the spray axis [14].

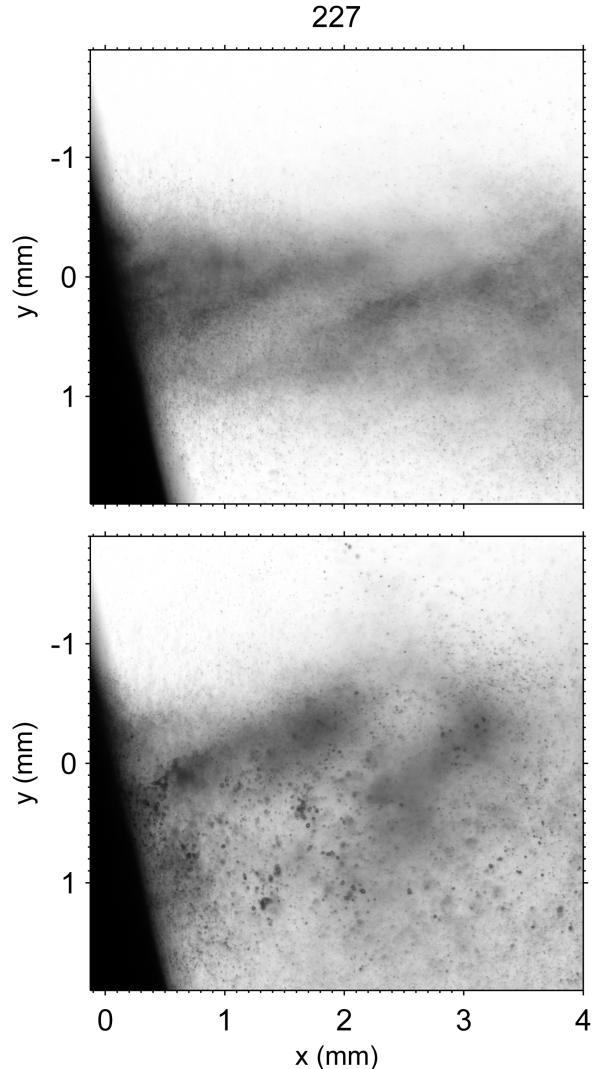


Figure 6: Instantaneous back-illumination spray images of near-nozzle region for independent 227 spray events, both imaged 50 ms after start of injection.

Conclusions

Back-illuminated images of sprays from pMDIs were collected in the near-nozzle region. Spray density was observed to vary throughout the injection, which is entirely transient. Sprays are asymmetric about the spray axis in the near-nozzle region. Fluctuations in optical depth are highest for 134a-propelled sprays, and for both propellants the fluctuations are reduced by the inclusion of ethanol. Propellant-only sprays exhibit large fluctuations in cone angle, whereas ethanol-containing sprays exhibit large fluctuations in local spray density with less substantial

fluctuations in spread. Formulations with propellant 227 discharged substantial masses of liquid as large droplets.

Acknowledgements

The authors gratefully acknowledge the support given to the project by the Australian Research Council.

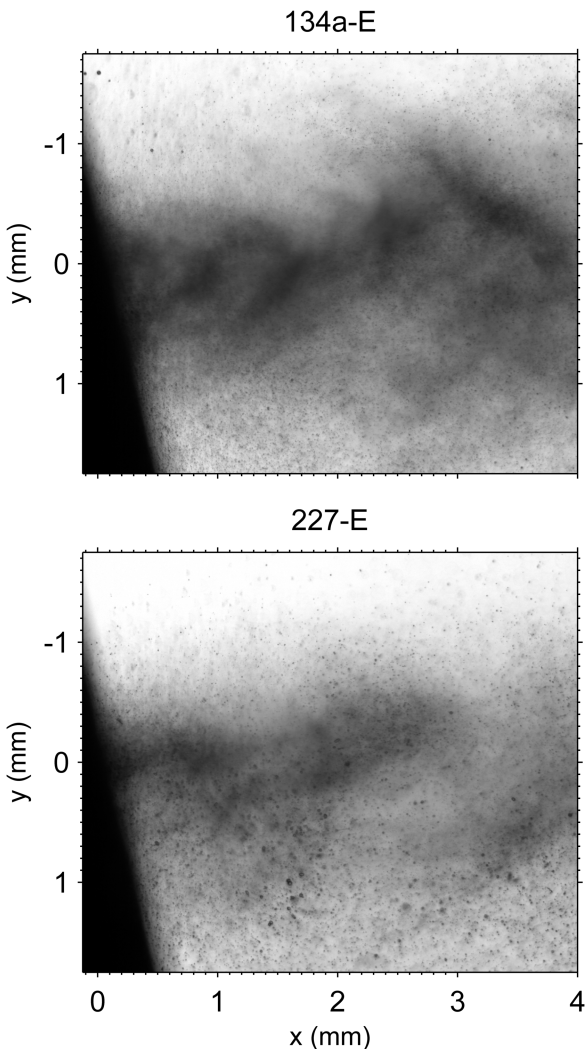


Figure 7: Instantaneous back-illumination spray images of near-nozzle region for (top) 134a-E and (bottom) 227-E sprays, both imaged 50 ms after start of injection.

References

- [1] N. A. Buchmann, D. J. Duke, S. A. Shakiba, D. M. Mitchell, P. J. Stewart, D. Traini, P. M. Young, D. A. Lewis, J. Soria, and D. Honnery, “A novel high-speed imaging technique to predict the macroscopic spray characteristics of solution based pressurised metered dose inhalers,” *Pharmaceutical research*, vol. 31, no. 11, pp. 2963–2974, 2014.
- [2] N. Chigier, “Optical imaging of sprays,” *Progress in Energy and Combustion Science*, vol. 17, no. 3, pp. 211–262, 1991.
- [3] B. M. Crosland, M. R. Johnson, and E. A. Matida, “Characterization of the spray velocities from a pressurized metered-dose inhaler,” *Journal of aerosol medicine and pulmonary drug delivery*, vol. 22, no. 2, pp. 85–98, 2009.
- [4] R. Dhand, “Aerosol plumes: Slow and steady wins the race,” *Journal of Aerosol Medicine*, vol. 18, no. 3, pp. 261–263, 2005.
- [5] C. Dunbar, A. Watkins, and J. Miller, “An experimental investigation of the spray issued from a pMDI using laser diagnostic techniques,” *Journal of aerosol medicine*, vol. 10, no. 4, pp. 351–368, 1997.
- [6] C. F. Edwards and K. Marx, “Multipoint statistical structure of the ideal spray, part II: Evaluating steadiness using the interparticle time distribution,” *Atomization and Sprays*, vol. 5, no. 4&5, 1995.
- [7] J. Estevadeordal and L. Goss, “PIV with LED: Particle shadow velocimetry (PSV),” in *43rd AIAA aerospace sciences meeting and exhibit, meeting papers*, 2005, pp. 12 355–12 364.
- [8] M. Fedrizzi and J. Soria, “Application of a single-board computer as a low-cost pulse generator,” *Measurement Science and Technology*, vol. 26, no. 9, p. 095302, 2015.
- [9] J. W. Ivey, R. Vehring, and W. H. Finlay, “Understanding pressurized metered dose inhaler performance,” *Expert opinion on drug delivery*, pp. 1–16, 2014.
- [10] B. Jähne, *Digital image processing*, 6th ed. Springer, 2005.
- [11] J. Jedelsky and M. Jicha, “Unsteadiness in effervescent sprays: A new evaluation method and the influence of operational conditions,” *Atomization and Sprays*, vol. 18, no. 1, 2008.
- [12] D. Ju, J. Shrimpton, M. Bowdrey, and A. Hearn, “Effect of expansion chamber geometry on atomization and spray dispersion characters of a flashing mixture containing inerts. part II: High speed imaging measurements,” *International journal of pharmaceutics*, vol. 432, no. 1, pp. 32–41, 2012.
- [13] D. Ju, J. Shrimpton, and A. Hearn, “The effect of reduction of propellant mass fraction on the injection profile of metered dose inhalers,” *International journal of pharmaceutics*, vol. 391, no. 1, pp. 221–229, 2010.
- [14] N. Mason-Smith, D. Edginton-Mitchell, D. Honnery, D. Duke, and J. Soria, “Pressurised metered-dose inhaler spray structure,” in *Proceedings of Turbulence and Shear Flow Phenomena 9*, Melbourne, Australia, 30 June - 3 July 2015.
- [15] L. M. Pickett, J. Manin, A. Kastengren, and C. Powell, “Comparison of near-field structure and growth of a diesel spray using light-based optical microscopy and X-ray radiography,” *SAE International Journal of Engines*, vol. 7, no. 2014-01-1412, pp. 1044–1053, 2014.
- [16] S. W. Stein and P. B. Myrdal, “A theoretical and experimental analysis of formulation and device parameters affecting solution MDI size distributions,” *Journal of pharmaceutical sciences*, vol. 93, no. 8, pp. 2158–2175, 2004.
- [17] H. Versteeg, G. Hargrave, and M. Kirby, “Internal flow and near-orifice spray visualisations of a model phar-

- maceutical pressurised metered dose inhaler,” in *Journal of Physics: Conference Series*, IOP Publishing, vol. 45, 2006, p. 207.
- [18] C. Willert, B. Stasicki, J. Klinner, and S. Moessner, “Pulsed operation of high-power light emitting diodes for imaging flow velocimetry,” *Measurement Science and Technology*, vol. 21, no. 7, p. 075 402, 2010.
 - [19] C. Willert, S. Freitag, and C. Hassa, “High speed imaging of fuel spray using a low-cost illumination source,” in *22nd European Conference on Liquid Atomization and Spray Systems (ILASS 2008), Como Lake, Italy, September*, 2008, pp. 8–10.
 - [20] C. E. Willert, D. M. Mitchell, and J. Soria, “An assessment of high-power light-emitting diodes for high frame rate schlieren imaging,” *Experiments in fluids*, vol. 53, no. 2, pp. 413–421, 2012.

Appendix C

Acoustic unsteadiness of sprays from pressurised metered-dose inhalers

C.1 Introductory statement

This paper was prepared for the *20th Australasian Fluid Mechanics Conference* and documents a technique for the measurement of acoustic unsteadiness of transient sprays.

Unsteadiness is a feature of some twin-fluid atomisers in particular modes of operation, and is defined by the fluctuation of the gas/liquid ratio at the nozzle exit. Unsteadiness can also be defined anywhere else in the spray, and in such regions can reflect, for example, particle clustering.

An acoustic unsteadiness technique for sprays was proposed by Sun et al. (2016). The technique was applicable for statistically-stationary processes. For sprays with start-up transients followed by a steady state and end-of-injection transient, the method is suitable with the relevant statistics obtained from a sufficiently long single spray record. As demonstrated in our other works on metered-dose inhalers, the

spray is a transient process with no apparent steady state. In this work, it was demonstrated that the acoustic unsteadiness for a spray from the pMDI could be determined from time-variant statistics of an ensemble of spray records.

The method was applied to sprays of HFA134a with and without 15% ethanol by weight. The acoustic unsteadiness was highest for the propellant-only formulation. Low-pass filtering of the acoustic energy reduced the unsteadinesses at different rates, suggesting the unsteadiness occurs on different timescales for each formulation. For the ethanol-containing formulation, for instance, the passage of individual bubbles results in a fluctuation of the gas/liquid ratio at the nozzle exit. This fluctuation, however, occurs on a very short timescale. Additional information about the multiphase flow structure may be obtainable from spectra of the unsteadinesses.

Acoustic unsteadiness of sprays from pressurised metered-dose inhalers

N. Mason-Smith¹, D.J. Duke², J.S. Harkess¹, D. Edgington-Mitchell¹ and D.R. Honnery¹

¹Laboratory for Turbulence Research in Aerospace and Combustion
 Department of Mechanical and Aerospace Engineering
 Monash University, Melbourne, VIC, 3800, Australia

²Energy Systems Division, Argonne National Laboratory
 Lemont, Illinois, 60439, USA

Abstract

A technique has been developed for the measurement of acoustic unsteadiness of sprays from pressurised metered-dose inhalers. An ensemble ($n \geq 126$) of acoustic measurements of sprays were obtained for two formulations with and without ethanol. Acoustic signals were analysed using the Hilbert-Huang Transform to obtain their amplitude envelopes, allowing the instantaneous energy to be determined. Ensemble statistics of each formulation's instantaneous energies allowed the determination of time-variant unsteadiness. The performance of the technique is demonstrated using two formulations with different steadiness characteristics; internal flow pattern phase contrast visualisations are presented that show the flow pattern varies by formulation. Unsteadinesses are presented for both formulations and is approximately 50% higher for the propellant-only formulation in the first 100 ms of injection. Variation of the unsteadiness with low-pass filtering of the acoustic energy demonstrates that the unsteadinesses are more separable when short-duration fluctuations are removed.

Introduction

Unsteadiness affects the performance of twin-fluid atomisers (Jedelsky and Jicha 2008). The unsteadiness is closely related to the flow pattern at the nozzle exit orifice. Flows that exhibit temporal inhomogeneity of the flow in the nozzle exit orifice tend to be unsteady. Pressurised metered-dose inhalers (pMDI) are flash atomisers in which a drug-containing formulation is discharged from a nozzle. The discharge from the nozzle is predominantly vapour (Mason-Smith et al. 2016) and the liquid phase is often multicomponent, as cosolvents are added to the propellant.

Measuring unsteadiness has been accomplished in several ways. Frameworks exist that directly measure the unsteadiness (Edwards and Marx 1995). The framework developed by Jedelsky and Jicha (2008) uses pressure fluctuation measurements in the mixing chamber to estimate the fluctuation of the gas-liquid ratio at the nozzle; this is termed the ‘two-phase flow unsteadiness’. Recent work (Sun et al. 2016) has shown that fluctuations of acoustic energy, which can be described as the ‘acoustic unsteadiness’, provide an indication of the flow unsteadiness. In this paper we extend the acoustic unsteadiness method of Sun et al. (2016) for use as a diagnostic for pMDIs. Two formulations are studied that exhibit highly different internal flow patterns, and their acoustic unsteadinesses are measured using the method outlined in this paper.

Methodology

A linear solenoid-driven rig was used to remotely actuate pMDI canisters. Phase contrast imaging was performed at the 7-ID beamline of the Advanced Photon Source at Argonne National Laboratory. Details of phase contrast imaging for fluid mechanics studied are given in Kastengren and Powell (2014).

Formulation	p_v (bar)	ρ_l (kg/m ³)
HFA134a	6.65	1208
HFA134a/Ethanol	5.95	1119

Table 1: Vapour pressures p_v and saturated liquid densities ρ_l of formulations studied.

Acoustic measurements were obtained in the Laboratory for Turbulence Research and Combustion (LTRAC). Lab temperature was monitored and was 22.4–23.9°C. A GRAS 46BE preamplified freefield microphone was connected to a National Instruments 16-bit analog-to-digital converter and was sampled at 250 kS/s. No antialiasing filter was used. The microphone was placed 23 mm from the nozzle exit orifice in the horizontal plane at an angle of 135° to the spray axis.

Two formulations were used and are tabulated in Table 1. Vapour pressures were estimated using the data provided in Gavtash et al. (2015). These two formulations had comparable vapour pressures and densities, but exhibited very different internal flow patterns. Phase contrast images of the internal flow structure in the expansion chamber and nozzle of the pMDI are shown in Figure 1. The propellant-only formulation contains large nonspherical bubbles with characteristic lengths almost equal to the expansion chamber diameter. In the parlance of multiphase flow patterns, this can be designated a slug/annular flow (Brennen 2005). By contrast, the ethanol-containing formulation is a bubbly flow with much smaller spherical bubbles on the order of 250 μm. Unsteadiness is highest for slug-type flows, as exhibited by the propellant-only formulation; bubbly flows with small bubbles relative to the size of the nozzle are most stable. Optical extinction measurements of these same formulations found a lower coefficient of variation for the ethanol-containing formulation, indicating a steadier spray process (Mason-Smith et al. 2015a). Similarly, the coefficient of variation of the optical extinction of HFA227ea sprays from a pMDI analogue were substantially reduced by the inclusion of ethanol (Mason-Smith et al. 2015b). The formulations listed in Table 1 are used as test cases for the acoustic unsteadiness technique.

Acoustic Analysis

Acoustic unsteadiness is the coefficient of variation (σ/μ) of the acoustic energy E (Sun et al. 2016). For continuous sprays, the mean and standard deviation of the acoustic energy can be obtained from a single spray record. As the pMDI spray is transient, we obtain these statistics from an ensemble of spray records and define the time-variant unsteadiness $U(t)$:

$$U(t) = \frac{\langle E^2(t) - \langle E(t) \rangle^2 \rangle^{1/2}}{\langle E(t) \rangle} \quad (1)$$

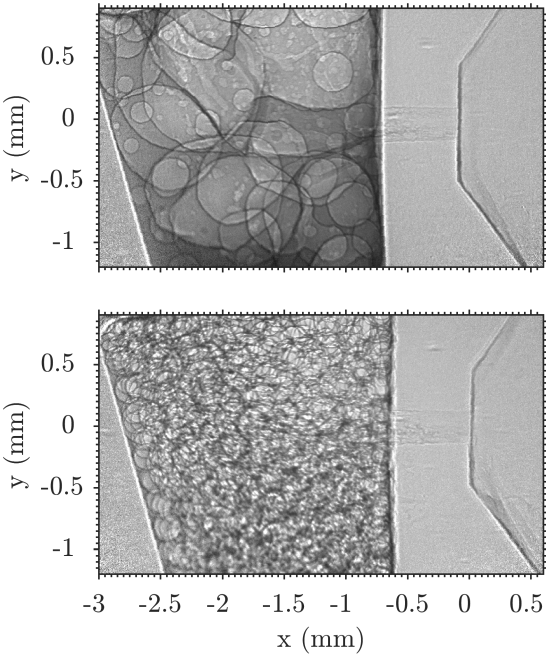


Figure 1: Phase contrast images for sump and nozzle flow 50 ms after start of injection of (top) HFA134a and (bottom) HFA134a/Ethanol.

The energy of the signal at time t is obtained by squaring the signal's instantaneous amplitude $a(t)$:

$$E(t) = a^2(t) \quad (2)$$

Defining the time-variant amplitude $a(t)$ of a non-stationary signal requires a non-stationary analysis technique. The Hilbert Huang transform (HHT) is a well-established method for analysis of non-stationary and nonlinear time series (Huang et al. 1998). A brief overview of the method is given.

The signal is decomposed into intrinsic mode functions (IMF) using the empirical mode decomposition (EMD) outlined in Huang et al. (1998). An analytic representation of each IMF is obtained by taking its Hilbert transform:

$$Y_i(t) = \frac{1}{\pi} P \int_{-\infty}^{\infty} \frac{X_i(t')}{t - t'} dt' \quad (3)$$

where X_i is the i_{th} IMF and P is the Cauchy principal value. The instantaneous amplitude a of the IMF is obtained trigonometrically:

$$a_i(t) = [X_i^2(t) + Y_i^2(t)]^{1/2} \quad (4)$$

The instantaneous amplitude of the signal is then obtained by summing the amplitudes of the modes:

$$a(t) = \sum_{i=1}^N a_i(t) \quad (5)$$

With an ensemble of instantaneous amplitudes, the unsteadiness can be evaluated.

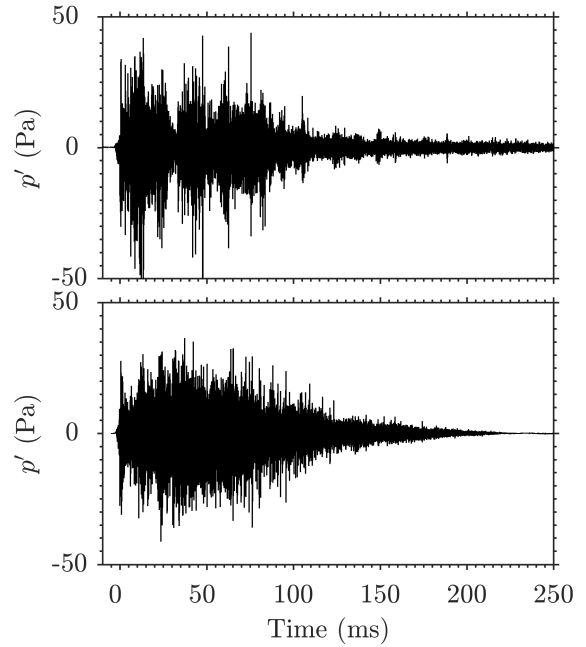


Figure 2: Acoustic signals from sprays of (top) HFA134a and (bottom) HFA134a/Ethanol.

Results and Discussion

Sample signals of the acoustic pressure fluctuation p' for each formulation are shown in Figure 2. Injections are approximately 100-200 ms in duration. For the propellant-only formulation, sound of relatively constant low amplitude is generated from 125-250 ms, and is related to the discharge of vaporous propellant from the expansion chamber. The ethanol-containing formulation has a more rapid end-of-injection event, with a continual decline in the amplitude from 50 ms until it is no longer discernible at 225 ms. Both formulations show spikes in the acoustic amplitude, likely to be associated with the passage of bubbles from the nozzle exit orifice. The propellant-only signal shows a local minimum around 30 ms. Collection of an ensemble of spray records enables the determination of which of these variations in amplitude are stochastic and which are repeatable.

Determination of the unsteadiness requires an accurate estimation of the variance of the acoustic energy, and may provide erroneous estimates in the presence of noise. The presented measurements have very high signal-to-noise ratios, demonstrated by the absence of discernible pressure fluctuations before the start of injection. The RMS amplitude of the noise is approximately 0.15 Pa, which corresponds to a peak signal-to-noise ratio of 10^5 .

Signals were decomposed into IMFs with the EMD and their amplitude envelopes reconstructed with the first two IMFs. This reconstruction acted as a high-pass filter with a cutoff of approximately 20 kHz; as the frequency in each mode varies as a function of time, some energy associated with frequencies above the cutoff may be contained in the third mode. An example of the agreement between the amplitude envelope and the raw signal is shown in Figure 3.

Statistics of the acoustic energy were calculated for each formulation at full temporal resolution. The resulting mean, RMS and unsteadiness are binned to 1 ms increments and are shown in Figure 4. The mean acoustic energy plot shows that the local minimum at 30 ms of the pressure fluctuation for the propellant-only formulation (Figure 2, top) is repeatable across the ensem-

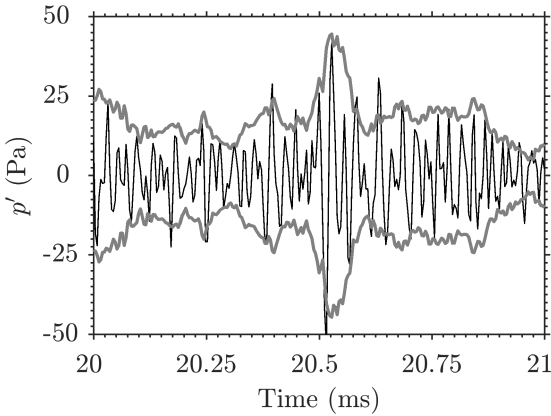


Figure 3: Short time segment of HFA134a spray acoustic signal and signal envelope $\pm a(t)$ (shown in gray).

ble. A local minimum of the droplet velocity for pure propellant pMDI sprays occurs around this same time (Myatt et al. 2015), and phase contrast videos show that this corresponds to the time required to evacuate air from the expansion chamber. Importantly, this demonstrates that the time-variant unsteadiness method separates repeatable and random fluctuations of the acoustic amplitude, which would be aggregated in a quasi-steady state implementation of the Sun et al. (2016) method. For the ethanol-containing formulation, mean acoustic energy rises until a maximum at approximately 30-35 ms and exhibits a gradual decay. The propellant-only formulation amplitude decays after a local maximum at approximately 50 ms.

RMS acoustic energy and unsteadiness are presented in Figure 4 (middle and bottom, respectively). The RMS acoustic energy traces are similar in shape to the mean acoustic energy. This results in a near-constant value of the acoustic unsteadiness. For both formulations the unsteadiness values are high, the propellant-only spray having an unsteadiness of around 1.2 during the first 100 ms of the injection. The ethanol-containing formulation has a lower unsteadiness, remaining almost invariant at 0.8 throughout this same time period.

Short-time variability of the acoustic energy prompted Sun et al. (2016) to low-pass filter the unsteadiness measurement by integrating the acoustic energy over a time T^* , noting that its selection was important to the measurement. For their study, the integration time was chosen to be 30 ms, with little explanation given for its selection. One interpretation is that time integration acts as a low-pass filter on the acoustic energy and enables separation of flow regimes above a selected time scale. Bubbly flows are unsteady on very short time scales associated with the passage of individual bubbles, and the accompanying fluctuation of the gas-liquid ratio at the nozzle exit orifice. These same flows will however be steadier at longer timescales—as will all flows, given the known effect of low-pass filtering on variance (Bendat and Piersol 1986). For a continuous spray process, the time scales of the unsteadiness could be obtained with spectra of the mean-subtracted acoustic amplitude. For transient spray processes, obtaining a time scale of the unsteadiness is not so straightforward. Investigating the effect of low-pass filtering the unsteadiness is one approach to indicate time scales associated with the fluctuations. To this end, we investigate the sensitivity of U to low-pass filtering.

The sensitivity of the unsteadiness measurement to low-pass filtering of the acoustic energy by binning is illustrated in Figure 5. The plot shows the ensemble unsteadiness time-averaged over the interval 25-75 ms as a function of bin width, to a max-

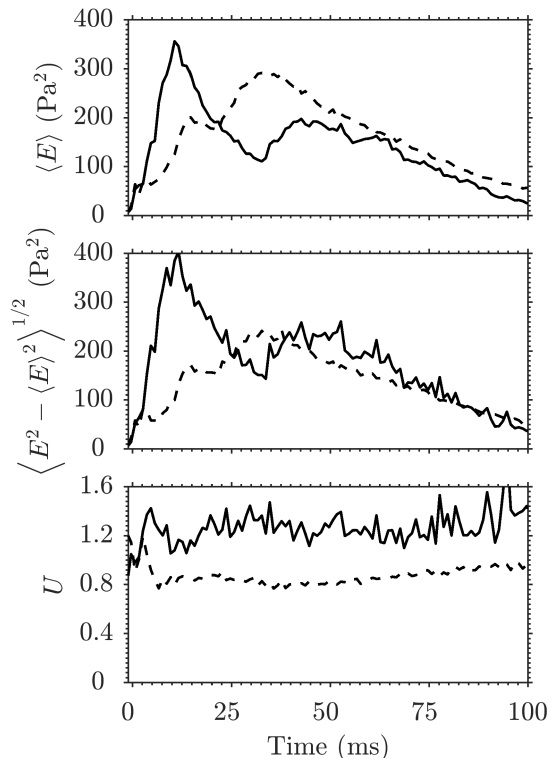


Figure 4: Ensemble (top) mean, (middle) RMS and (bottom) unsteadiness of E with (solid line) HFA134a and (dashed line) HFA134a/Ethanol formulations.

imum width of 2 ms. \bar{U} is seen to be almost invariant at small bin widths below approximately 30 μs . Logarithmic axes are used to show that the RMS energy and the unsteadiness decay at a constant amplitude ratio (dB) per octave above 30 μs bin widths. Over this range, the unsteadiness decays with an amplitude ratio of 1.18 per octave for the propellant-only case and 1.3 for the ethanol-containing formulation. At larger bin widths, the formulations become more separable as the ratio of their unsteadinesses increases. The difference in decay rates of unsteadinesses suggests that more energy is concentrated on shorter timescales for the ethanol-containing formulation, consistent with the bubbly flow regime depicted in Figure 1. If the random fluctuations for the ethanol-containing case are associated with the passage of individual bubbles, low-pass filtering these fluctuations will provide an unsteadiness indicative of longer-period fluctuations—such as those from the passage of large liquid slugs in the propellant-only formulation.

Conclusions

A method is developed for the measurement of acoustic unsteadiness of sprays from pressurised metered-dose inhalers. The method is able to separate random and repeatable fluctuations of the amplitude of the signal. Unsteadiness is near-constant for each formulation during the first 100 ms of injection and was approximately 50% higher for the propellant-only formulation. The measured unsteadiness is sensitive to low-pass filtering of the acoustic energy, and decays more rapidly with filter width for the bubbly flow case than for the slug-annular flow case.

Acknowledgements

The authors gratefully acknowledge the support given to the project by the Australian Research Council. The authors wish to thank Dr. Chris Powell and Dr. Katarzyna Matusik, Energy

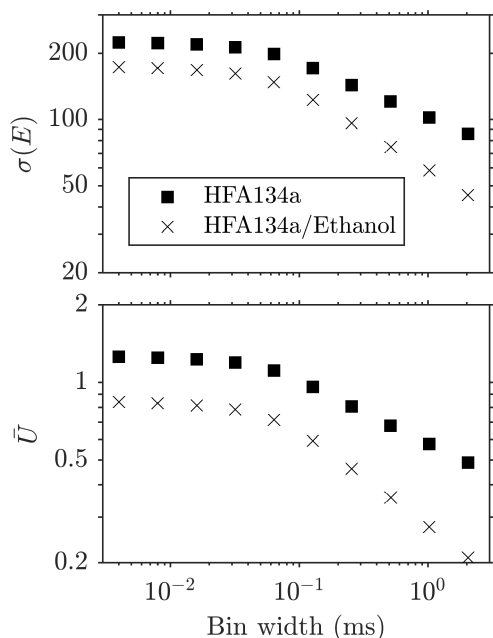


Figure 5: Effect of filter width on \bar{U} averaged over the interval 25–75 ms.

Systems Division, Argonne National Laboratory, and Dr. Alan Kastengren, Dr. Jin Wang and Dr. Don Walko, X-Ray Science Division, Argonne National Laboratory. This research was performed at the 7-ID beamline of the Advanced Photon Source at Argonne National Laboratory. Use of the APS is supported by the U.S. Department of Energy (DOE) under Contract No. DE-AC02-06CH11357.

References

- Bendat, Julius S, and Allan G Piersol. 1986. *Random data: analysis and measurement procedures*. John Wiley & Sons.
- Brennen, Christopher E. 2005. *Fundamentals of multiphase flow*. Cambridge University Press.
- Edwards, Christopher F, and KD Marx. 1995. “Multipoint statistical structure of the ideal spray, Part II: Evaluating steadiness using the interparticle time distribution”. *Atomization and Sprays* 5 (4&5).
- Gavtash, B, et al. 2015. “Saturated vapour pressure (SVP) measurement of ethanol/HFA binary mixtures”. In *Drug Delivery to the Lungs* 26.
- Huang, Norden E, et al. 1998. “The empirical mode decomposition and the Hilbert spectrum for nonlinear and non-stationary time series analysis”. *Proceedings of the Royal Society of London A: Mathematical, Physical and Engineering Sciences* 454 (1971): 903–995.
- Jedelsky, Jan, and Miroslav Jicha. 2008. “Unsteadiness in effervescent sprays: a new evaluation method and the influence of operational conditions”. *Atomization and Sprays* 18 (1).
- Kastengren, Alan, and Christopher F Powell. 2014. “Synchrotron X-ray techniques for fluid dynamics”. *Experiments in Fluids* 55 (3): 1–15.
- Mason-Smith, Nicholas, et al. 2015a. “Back-illumination imaging of pressurised metered-dose inhaler sprays”. In *Australian Conference on Laser Diagnostics in Fluid Mechanics and Combustion (Damon Honnery and Daniel Edgington-Mitchell 09 December 2015 to 11 December 2015)*, 45–50. Monash University Publishing.
- Mason-Smith, Nicholas, et al. 2016. “Insights into Spray Development from Metered-Dose Inhalers Through Quantitative X-ray Radiography”. *Pharmaceutical Research* 33 (5): 1249–1258.
- Mason-Smith, Nicholas, et al. 2015b. “Pressurised metered-dose inhaler spray structure”. In *Proceedings of Turbulence and Shear Flow Phenomena 9*. Melbourne, Australia.
- Myatt, B, et al. 2015. “PDA and High Speed Image Analysis of HFA/Ethanol pMDI Aerosols: New Findings”. *Drug Delivery to the Lungs* 26.
- Sun, Chunhua, et al. 2016. “Acoustic performance of effervescent sprays by time-frequency method with different atomizer structures under different operating conditions”. *International Journal of Multiphase Flow* 82:35–48.

Appendix D

Temporally and Spatially Resolved x-ray Fluorescence Measurements of *in-situ* Drug Concentration in Metered-Dose Inhaler Sprays

D.1 Introductory statement

Previous chapters concerned the measurement of spray projected mass and optical density in pMDI sprays. As the drug is of pharmacological importance, rather than the spray mass, it is important to measure the drug concentration directly.

Typical measurements of drug distribution in pMDI sprays are performed with cascade impactors. These have poor temporal and spatial resolutions; the entire spray is integrated into a single measurement. There are trends in drug distribution that are not captured in these measurements.

Optical diagnostics have high spatial and temporal resolutions, but cannot discriminate the drug from other spray components. Laser-based diagnostics can measure the droplet distribution with high resolution, but do not provide a measurement

of drug concentration. Quantitative x-ray radiography provides a measurement of the projected mass, of which the drug is a very small component (typically 0.1% by mass). The mass distribution of these sprays is proportional to the drug distribution if and only if the drug is well-mixed within the spray. If the drug is not well-mixed, its distribution will differ from that of the mass.

In this Appendix, x-ray fluorescence spectroscopy is used to directly measure the time-variant ensemble-mean drug concentration of sprays from a pMDI analogue. Raster-scanning of the beam allowed the spatial distribution of the drug to be determined. The drug concentration was determined from *k*-shell fluorescence of bromine in the drug. Laser extinction was also performed to measure the spray optical density, which was compared with the drug distribution.

The work is presented in the form of a journal article published in *Pharmaceutical Research*¹. This article is reprinted by permission from Springer: *Pharmaceutical Research*, “Temporally and Spatially Resolved x-ray Fluorescence Measurements of in-situ Drug Concentration in Metered-Dose Inhaler Sprays”, Duke, Daniel J., Alan L. Kastengren, Nicholas Mason-Smith *et al.* © 2016.

¹*Pharmaceutical Research* ranked at 66/255 in JCR Impact Factor rankings in Pharmacology & Pharmacy in 2015, placing it in Q2.

Temporally and Spatially Resolved x-ray Fluorescence Measurements of in-situ Drug Concentration in Metered-Dose Inhaler Sprays

Daniel J. Duke¹ • Alan L. Kastengren² • Nicholas Mason-Smith³ • Yang Chen⁴ • Paul M. Young⁴ • Daniela Traini⁴ • David Lewis⁵ • Daniel Edgington-Mitchell³ • Damon Honnery³

Received: 16 July 2015 / Accepted: 5 November 2015
© Springer Science+Business Media New York (outside the USA) 2015

ABSTRACT

Purpose Drug concentration measurements in MDI sprays are typically performed using particle filtration or laser scattering. These techniques are ineffective in proximity to the nozzle, making it difficult to determine how factors such as nozzle design will affect the precipitation of co-solvent droplets in solution-based MDIs, and the final particle distribution.

Methods In optical measurements, scattering from the constituents is difficult to separate. We present a novel technique to directly measure drug distribution. A focused x-ray beam was used to stimulate x-ray fluorescence from the bromine in a solution containing 85% HFA, 15% ethanol co-solvent, and 1 $\mu\text{g} / \mu\text{L}$ IPBr.

Results Instantaneous concentration measurements were obtained with 1 ms temporal resolution and 5 μm spatial resolution, providing information in a region that is inaccessible to many other diagnostics. The drug remains homogeneously mixed over time, but was found to be higher at the centerline than at the periphery. This may have implications for oropharyngeal deposition *in vivo*.

Conclusions Measurements in the dynamic, turbulent region of MDIs allow us to understand the physical links between formulation, inspiration, and geometry on final particle size and distribution. This will ultimately lead to a better understanding of how MDI design can be improved to enhance respirable fraction.

KEY WORDS fluorescence · pressurized metered dose inhaler · synchrotron radiation · x-ray

ABBREVIATIONS

FWHM	Full width at half maximum
HFA	Hydrofluoroalkane
IPBr	Ipratropium bromide
MDI	Metered dose inhaler
XFS	X-ray fluorescence spectroscopy

INTRODUCTION

Pressurized metered-dose inhalers (MDIs) are the predominant method of drug delivery to the lungs, and have been in use for many decades (1,2). However, MDI applications are limited by the inconsistency of the delivered dose and the respiratory fraction received by the patient (3–5). Dosing inconsistency is primarily a result of the requirement that the patient operate the device correctly and provide a suitable inspiration flow. These factors have greater influence with more acute respiratory diseases (6). The result of this is variability in respiratory fraction ranging from 40% of the metered dose to potentially as low as 10% (4,7). This is generally understood to be due to the non-ideal spreading angle of the spray (leading to oropharyngeal deposition) and non-ideal particle size (which leads to non-ideal settling times and impaction in the upper bronchial-tracheal region of the lungs) (8).

✉ Daniel J. Duke
dduke@anl.gov

¹ Energy Systems Division, Argonne National Laboratory, Lemont, Illinois, USA

² X-ray Science Division, Argonne National Laboratory, Lemont, Illinois, USA

³ Laboratory for Turbulence Research in Aerospace & Combustion, Department of Mechanical & Aerospace Engineering, Monash University, Melbourne, Victoria, Australia

⁴ Respiratory Technology, Woolcock Institute of Medical Research, University of Sydney, Sydney, New South Wales, Australia

⁵ Chiesi Limited, Chippenham, UK

The lack of quantitative, predictive physical models linking nozzle design, formulation chemistry, operating conditions and the final particle size and spray distribution are a major barrier to the development of more reliable and efficient MDIs. A thorough understanding of these links requires comprehensive knowledge of how the spray is initially formed, with regard to the fluid flow inside and outside the nozzle and how suspended or soluble drugs are transported inside the resulting spray. Most of the important physical processes, such as flash-evaporation, cavitation and precipitation, occur either inside or within centimeters of the MDI nozzle (3,9,10). In the following, we refer to this as the ‘near-field’ region of the spray.

The primary non-intrusive diagnostic suited to studying the near-field region of MDI sprays is high-speed imaging. Back-lit and front-lit photography are commonly used (11,12), however these techniques are limited to measuring the velocity and displacement of the outer boundary of the entire propellant plume (9,13,14). Schlieren and shadowgraph imaging techniques are capable of visualizing density gradients inside the spray, but cannot distinguish the drug distribution from the overall propellant and co-solvent distribution (9). Ultimately, it is the distribution of the active drug which is most important in understanding precipitation and oropharyngeal deposition, and this is difficult to obtain with imaging techniques.

To this end, many diagnostic tools are available for the analysis of drug distribution. These include intrusive ex-valve particle filtration devices such as the Andersen cascade impactor (15), and Next Generation impactor (16). Mass spectrometry, scanning electron microscopy and electron force microscopy are also used to study deposition on barriers (17,18). These are supplemented by non-intrusive laser-based diagnostics such as phase-doppler velocimetry (19,20), laser-sheet patterning (21) and laser diffraction particle sizing devices (21,22). All these techniques are generally restricted to use in the dilute region far downstream of the nozzle; intrusive sampling methods cannot determine the *in-situ* distribution of the drug very close to the nozzle without altering the fluid flow. Laser-based techniques are ineffective in the near-field since the number density of the scattering particles is too high, resulting in multiple scattering events which degrade signal quality, even if the total optical density is modest. Furthermore, it is difficult to ascertain the actual concentration of the drug present in any particles or droplets detected using these methods.

The ideal diagnostic for this problem is one which will work effectively in regions of high optical density, is non-intrusive, can distinguish the active drug from the other constituents, and is well resolved in space and time in order to capture small transient features. Synchrotron radiation techniques are well suited to this problem. Synchrotron x-rays have high penetrating power, high flux, tunable energy range, and are well-collimated (23). The properties of small static samples can be

studied using a variety of techniques, such as phase-contrast imaging, x-ray scattering, absorption radiography, and fluorescence spectroscopy (24). In recent years, focused x-ray beams have been effectively used to non-intrusively probe dense fluid flows and sprays, including cavitating flows (25–28).

X-ray fluorescence spectroscopy (XFS) techniques are of particular interest for MDI applications, since any element in the drug can be tracked, provided that it has a suitable fluorescence wavelength (24). Argon fluorescence has previously been used to study turbulent mixing in gas jets (29,30), and a similar process maybe applied to MDI sprays. The measurement is similar in principle to laser-induced fluorescence (31); however, the very short wavelengths of x-rays result in the emission of x-ray photons from the ionization of core-shell electrons. Therefore, the emission can easily penetrate the sample to reach the detector, and the measurement is independent of temperature, pressure, and valence state. XFS can track any element that has a unique emission line with sufficient yield and an acceptable absorption edge in a suitable energy range for the detector. For practical purposes, this includes elements from sulfur (atomic number 16) and up, since lighter elements have low fluorescence energies which are absorbed by the surrounding environment. This naturally excludes most organic compounds and propellants.

In this paper, we present a novel diagnostic technique for the measurement of drug concentration in a MDI spray using x-ray fluorescence. The measurement is non-intrusive, and provides a quantity which is directly proportional to the total amount of active drug integrated along the path of the x-ray beam where it interacts with the spray. The data have millisecond time resolution and 5 μm spatial resolution. We take advantage of the fluorescence properties of bromine to directly track the concentration of ipratropium bromide (IPBr) in ethanol co-solvent, with sprays driven by both HFA 134a and HFA 227 propellants.

The technique is not restricted to IPBr; other drugs can be targeted in the same manner if they contain atoms with suitable fluorescence energy (32,33), or are tagged with a suitable inert tracer. In Table I we list several candidate drugs that contain naturally suitable fluorescent species.

METHOD

The experiments were performed at the 7-BM beamline of the Advanced Photon Source at Argonne National Laboratory (25). A side-cutaway view of the experiment is shown in Fig. 1. The MDI is fired inside a spray chamber which is continuously purged with nitrogen, simulating inspiration. The inlet flow passage is designed to closely match the geometry of the flow passage in the original inhaler body. In order to obtain accurate control over the spray duration and

Table I Several Candidate Drugs for X-Ray Fluorescence Spectroscopy without a Tracer, In Order of Increasing X-Ray Emission Energy (Decreasing Wavelength, and Increasing Ease of Detection)

Name	Description	Fluorescence Line (Approx. Mean Energy) (32,33)	Formula
Salbutamol sulphate	β_2 agonist	S K_α (2.3 keV) & K_β (2.4 keV)	<chem>C26H44N2O10S</chem>
Methacoholine chloride	Cholinergic (Bronchial provocation test)	Cl K_α (2.6 keV) & K_β (2.8 keV)	<chem>C8H18ClNO2</chem>
Sodium chloride	Hypertonic solution for nebulization	Cl K_α (2.6 keV) & K_β (2.8 keV)	$\text{Na}^+ \text{Cl}^-$
Beclomethasone	Inhaled steroid	Cl K_α (2.6 keV) & K_β (2.8 keV)	<chem>C28H37ClO7</chem>
Ciprofloxacin HCl	Common antibiotic	Cl K_α (2.6 keV) & K_β (2.8 keV)	<chem>C17H18FN3O3.HCl.H2O</chem>
Pentetate zinc trisodium	Radioisotope decontaminant for nebulization	Zn K_α (8.6 keV)	<chem>Na3ZnC14H18N3O10</chem>
Tiotropium bromide	Anticholinergic	Br K_α (11.9 keV)	<chem>C20H30BrNO3</chem>
Ipratropium bromide	Anticholinergic used in this study	Br K_α (11.9 keV)	<chem>C20H30BrNO3</chem>

timing, the standard metering valve has been removed from the canister, and the formulation is supplied to a micro-dispensing solenoid valve, which is electronically controlled in sync with the data acquisition system. A stock MDI nozzle with nominal diameter $D = 300 \mu\text{m}$ is removed from the inhaler body and mounted on an aluminum tube connected to the outflow side of the solenoid valve. The stem is connected to the solenoid via a 0.8 mm diameter, 16.5 mm long connecting pipe. The total volume making up the space between the nozzle and solenoid valve exit is 38 μL , comparable to typical commercial expansion chamber volumes of around 10–30 μL .

The chamber is sealed with a thin polyimide film which contains the spray and acts as an x-ray window. The plastic walls of the mouthpiece are similarly replaced with polyimide windows mounted on a plastic frame. This maintains the shape of the original mouthpiece whilst allowing the x-ray

beam (indicated by the red line) to travel through the nozzle with minimum absorption, and allowing the fluorescent emission (blue lines) to more easily escape the mouthpiece.

A plan view of the experiment setup is shown in Fig. 2, which highlights the key features of the beamline. A double multilayer monochromator (not shown) is used to generate an x-ray beam of mean energy 15 keV, with a bandpass of 1.0% FWHM. A pair of x-ray mirrors are used to focus the beam to a $5 \times 6 \mu\text{m}$ spot, with the focal point located at the center of the mouthpiece. The beam passes through an intensity monitor (I_0 , Fig. 2), which is used to normalize out any fluctuations in the incoming intensity. The beam traverses the spray, and is collected by a PiN diode (I_1 , Fig. 2), which records the overall transmission of x-rays through the sample. Fluorescence x-rays are emitted isotropically where the beam interacts with the spray, and some fraction of those are collected by a silicon drift diode placed at right angles to the beam. This is a spectral

Fig. 1 Side cutaway view of spray chamber, showing the MDI nozzle inside the mouthpiece, the airflow passage, and the connection of the unmetered canister to the nozzle. The red line represents the x-ray beam, and the blue lines represent omnidirectional x-ray fluorescence emitted from a line source where the beam intersects the spray.

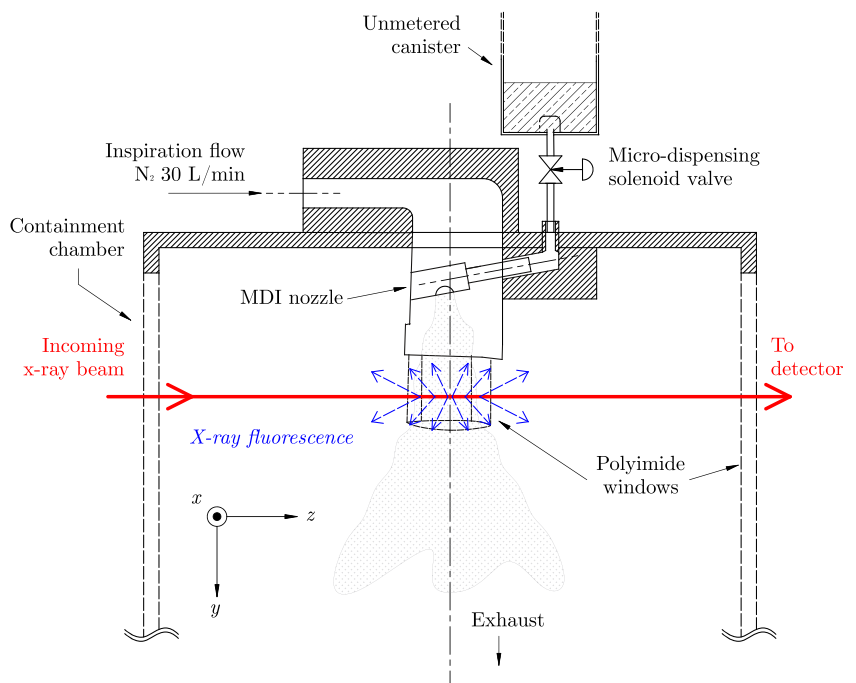
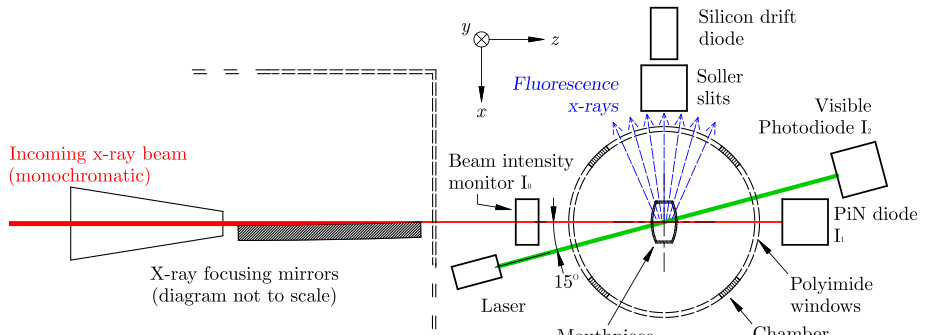


Fig. 2 Plan view of experiment. The red line represents the x-ray beam, the green line represents the 532 nm laser beam, and the blue lines represent omnidirectional x-ray fluorescence emitted from a line source where the beam intersects the spray.



detector which is capable of discriminating both the photon energy and count rate of incoming x-rays. A set of Soller slits act as a collimator, to cut down the amount of unwanted elastically scattered x-rays seen by the detector.

Simultaneously, a 532 nm laser beam is passed through the same point in the spray, offset by 15°. The laser beam has a focus spot size two orders of magnitude larger than the x-ray beam. This is collected by a photodiode, giving a nominal indication of the optical density of the plume, defined as (34);

$$\text{OD}(x,y,t) = -\log_{10}\left(\frac{I_2(x,y,t)}{I_2(x,y,0)}\right), \quad (1)$$

where I_2 is the intensity measured by the photodiode (see Fig. 2). The x-ray and laser beams are fixed; the spray chamber is translated horizontally and vertically to choose the measurement location. The origin of the measurement plane is located at the tip of the mouthpiece ($y = 0$), at the centerline ($x = 0$). The z axis is aligned with the x-ray beam. In these experiments, we pass the beam across the minor axis of the mouthpiece, and scan in x across the major axis.

A complete description of the principles of x-ray fluorescence is outside the scope of this paper and may be found elsewhere (35). Here, we provide a brief explanation of how the drug concentration was calculated. Bromine has a K-shell electron binding energy of 13.474 keV, which is excited by the 15 keV incident x-ray beam (32). When a K-shell electron is removed, a higher-shell electron will fill the hole. Most often, this results in the emission of a fluorescence x-ray photon. When the hole is filled by an L-shell electron, the emitted photon is denoted K_α . The less frequent M to K-shell transition emits a K_β photon. For Br, the K_α photon energy is 11.9 keV. This is far away enough from the incident beam energy that the detector can differentiate them from any elastic and Compton scattering.

The number of detector events corresponding to Br K_α photons can be directly related to the mass concentration of the target drug integrated along the path of the x-ray beam. Assuming weak absorption in the sample, the beam intensity remains relatively constant throughout the penetration depth (which is confirmed to be the case for these measurements).

The rate of fluorescence emission dI_f is proportional to the amount of beam absorbed in the target dI_{abs} , and this is in turn proportional to the local density of the drug ρ_{drug} in a differential pathlength dz ;

$$dI_f = \omega dI_{\text{abs}} = \omega I_0 \mu dM_{\text{drug}} = \omega I_0 \mu \rho_{\text{drug}} dz. \quad (2)$$

Here, ω is the fluorescence efficiency of the target species; this is calculated from empirical tables (36). I_0 is the incident x-ray flux, and μ is the mass attenuation coefficient of the target species (see Table II).

Following from the above, the projected density of drug M_{drug} (mass per unit area) is proportional to the count rate $I_{\text{Br } K\alpha}$ of Br K_α photons at the detector;

$$M_{\text{drug}} = \int \rho_{\text{drug}} dz = \frac{\psi I_{\text{Br } K\alpha}}{I_0 \tau f_{\text{det}} f_{\text{att}}}. \quad (3)$$

The coefficient ψ is a lumped calibration constant which accounts for all fixed quantities that determine the ratio of projected density to the number of events recorded at the detector. This includes the solid angle subtended by the detector, the mass attenuation coefficient, and fluorescence efficiency. Other variable factors are τ , the amount of fluorescence signal trapped by the medium between the measurement region and the detector, f_{det} , the correction function for the detector dead time (ie. the fraction of the time that the detector is ready to detect an

Table II Experimental Parameters and Calibration Values

Name	Value
Incident x-ray flux (I_0)	6×10^{11} photons/s
Sampling interval (Δt)	1 ms
X-ray beam spot size	$5 \times 6 \mu\text{m}$
IPBr Molar mass (M)	412.37 g/mol
IPBr mass attenuation coefficient (μ)	4.57 g/cm ²
Fluorescence efficiency for Br K_α (ω)	0.516 [36]
Lumped calibration constant (ψ)	1.57×10^5 g/mm ²
Approximate fluorescence calibration ($M_{\text{drug}}/I_{\text{Br } K\alpha}$)	371 ng/mm ² (HFA 134a)
	393 ng/mm ² (HFA 227)

incoming photon) (37), and f_{att} , the correction function for attenuation of the incident beam in the sample, which can vary depending on measurement location. In the present study, absorption in the sample is very small such that $f_{\text{att}} \approx 1$, and the other functions can be considered constant.

Normally, a known sample of the target species is placed in the beam and used as a calibration standard. However, in this paper we use a calibration obtained from first principles. As such, the assumptions introduced in the analysis will introduce some error. We therefore note that the projected density measurements presented in this proof-of-concept study are in approximate units.

Experiments were carried out at several measurement locations in two different formulations containing 85% HFA 134a or HFA 227 propellant, 15% ethanol co-solvent, and 1 $\mu\text{g} / \mu\text{L}$ IPBr. Under all test conditions an inspiration flow of 30 L/min was used. In order to increase canister lifetime, a relatively short injection of 30 ms was used. A time-history of the drug concentration integrated along the x-ray beam path was computed for each sample point as the average of at least 200 sprays, in order to determine the mean behavior of the spray and obtain an acceptable total count rate.

RESULTS AND DISCUSSION

In Fig. 3, we show the time-history of both IPBr projected density (red markers) against the optical density of the entire plume (blue line) for a single measurement location on the nozzle centerline, 5 mm downstream of the mouthpiece, with HFA 134a propellant. The 30 ms spray event begins at $t = 0$, and ends at $t = 30$ ms as indicated by the vertical dashed line.

It should be noted that the 30 ms duration of injection and total event duration of approximately 100 ms is relatively short compared to a typical MDI, in which the spray event may last from 200 to 300 ms. This short injection duration was chosen in order to extend the lifetime of the canisters under

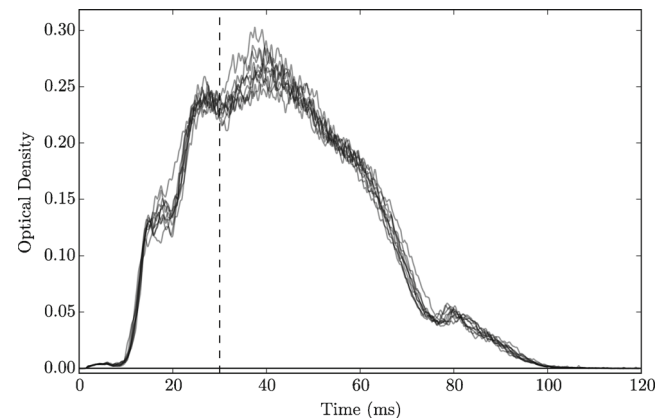


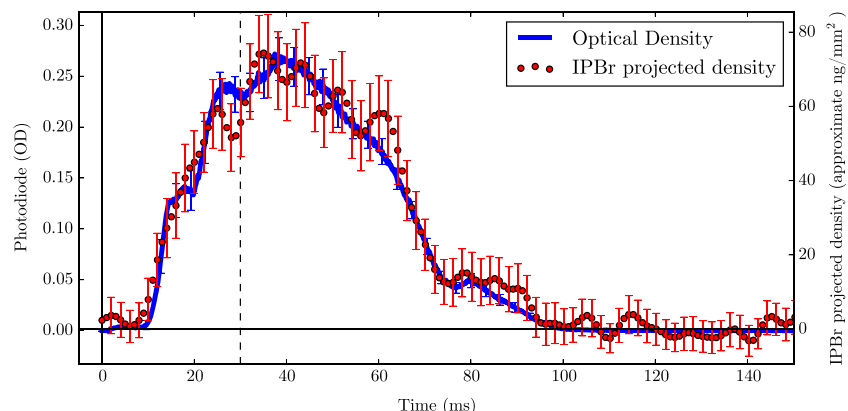
Fig. 4 Several samples of optical density measurements (from photodiode) for 30 ms injection at $x=0$, $y=5$ mm for HFA 134a propellant.

repeated testing conditions. The 30 ms injection duration was selected as the minimum injection duration at which the gross structure (9) and optical density of the spray reached the same maximum value as seen in longer injection events.

The error bars in Fig. 3 represent the standard deviation about the mean of 200 spray events. In order to improve the signal to noise ratio, a 5 ms moving average window has been applied to the IPBr projected density. The error bar in the region of zero concentration provides some indication of the uncertainty of the measurement; $\pm 5 \text{ ng/mm}^2$, which is mostly due to photon shot noise. The increase in the error bar at the peak regions ($\pm 10 \text{ ng/mm}^2$) provides some indication of the variation between spray events .

We can see that the drug concentration tracks the optical density closely, indicating that the drug concentration in the plume remains relatively constant throughout the injection duration. This indicates that the fluid is indeed well-mixed, as is expected for a solution-based formulation. We note that the rise and fall of the spray density is marked by several local peaks and troughs which appear to correspond to unsteady events in the spray; these are captured reasonably well by both the optical density and fluorescence measurements. Owing to the short injection duration, the spray never reaches a steady

Fig. 3 30ms injection at $x=0$, $y=5$ mm for HFA 134a propellant. The optical density (blue line, left vertical axis) is compared to the drug concentration (red markers, right vertical axis).



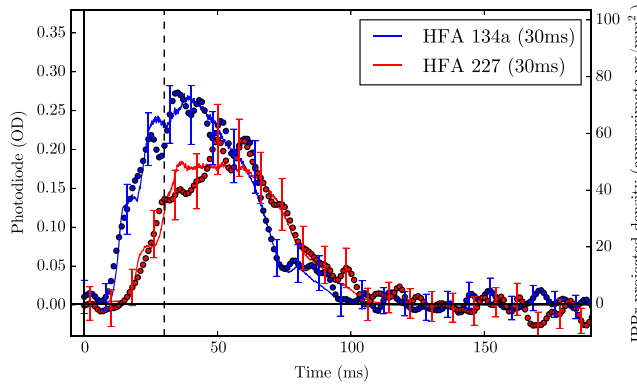


Fig. 5 30ms injection at $x=0$, $y=5$ mm for two propellants. The markers represent the XFS data, and the lines represent the optical density.

state. However, the unsteadiness of the spray is very repeatable from shot to shot, since the data shown here are the average of 200 injection events. In Fig. 4, several measurements of optical density are shown at $x=0$, $y=5$ mm for the HFA 134a propellant. It can be seen that the temporal unsteadiness of the spray is quite repeatable between events.

The quantities obtained by XFS are path-length integrated along the beam, and are thus given in units of mass per area rather than mass per volume. In order to check whether these quantities are reasonable, we can estimate what the projected density values should be by making some thermodynamic approximations; this provides an indication of whether the measurement is at the correct order of magnitude. Given the known concentration of IPBr in the solution ($1 \mu\text{g} / \mu\text{L}$) and assuming a homogeneous distribution of IPBr in a fully vaporized spray at

equilibrium thermodynamic conditions, we would expect the local density to be on the order of 3 to 6 ng/mm^3 . We base this density value on tabulated properties for the propellants and co-solvent (38). If the concentration of IPBr is within this range, then the measured peak values of approximately 80 ng/mm^2 correspond to integration path lengths of approximately 13 to 26 mm (dividing the measured value of projected density by the expected fluid density). This corresponds well to the geometry of the inhaler mouthpiece and the expected spreading angle of the plume (ie. the path length through which the beam intersects the spray), which tells us that the XFS measured quantities are at the correct order of magnitude.

In Fig. 5, we compare measurements on the nozzle centerline, 5 mm downstream of the mouthpiece, for formulations containing both HFA 134a and HFA 227 propellants. We note that the expansion of HFA 227 from the metering volume is delayed. We also note that both the optical density and drug concentration have a lower maximum value, suggesting a lower spray density. However, it is not presently possible to determine whether these changes are due to the variations in propellant properties (such as vapor pressure) or due to changes in the spray structure. The experiment operates on a fixed duration of injection where the flow is throttled by a valve, rather than a metered volume that is allowed to expand at an arbitrary rate. This will be a matter for further study.

Translating the nozzle vertically, we develop axial profiles demonstrating how the drug distribution at the nozzle centerline changes with increasing distance from the mouthpiece. Two-dimensional maps for both propellants are shown in Fig. 6, with the horizontal axes being time and axial distance

Fig. 6 Axial scans along centerline ($x=0$).

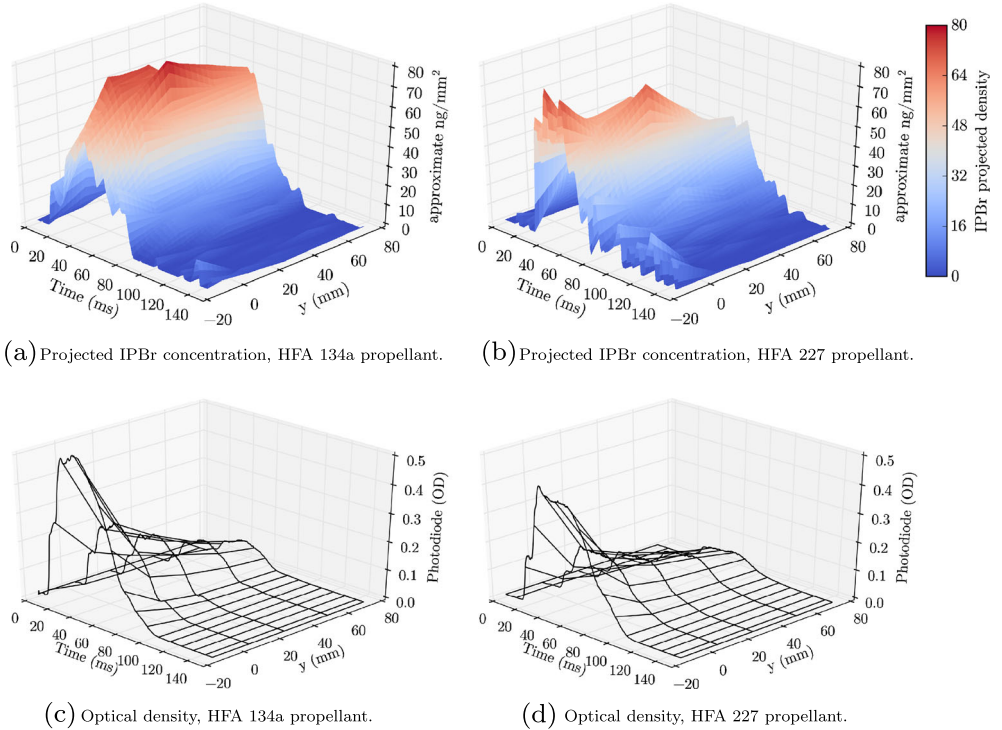
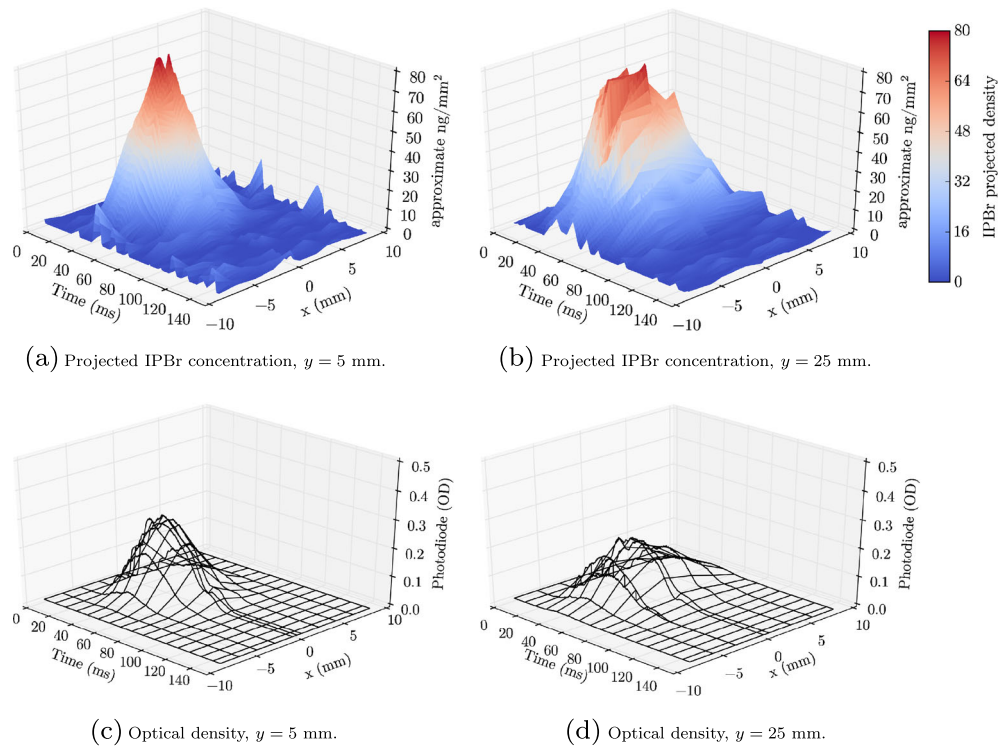


Fig. 7 Radial scans across the spray for HFA 134a propellant.



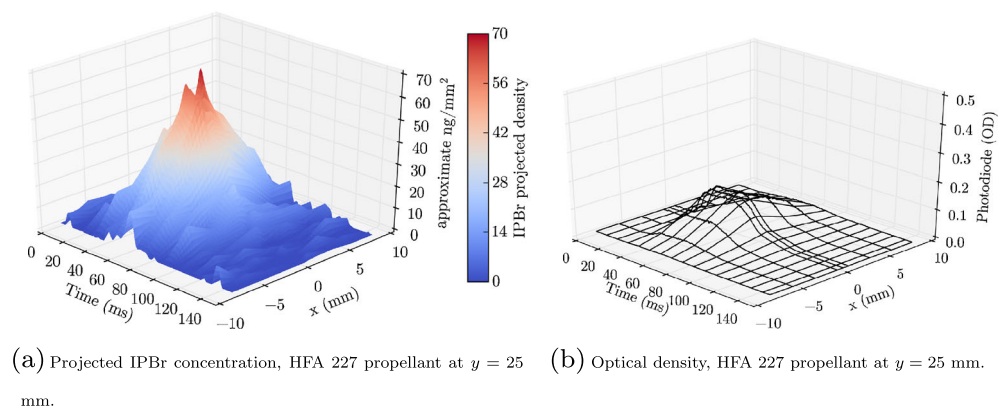
y from the mouthpiece, and the vertical axes being the projected density of the drug (a,b) and the optical density of the plume (c,d). The y axis spans negative values (inside the mouthpiece) and up to 70 mm downstream. We note that the optical density of the plume decays with increasing distance as the plume spreads, but the peak drug concentration remains relatively constant. The reduction in optical density is expected, since the plume is both spreading and becoming more dilute as inspired air is entrained and the co-solvent and propellant evaporate. However, the constant drug concentration measurement indicates that the drug distribution is being conserved within the plume; the plume is spreading in space, but once the measurement is integrated along the path of the x-ray beam, the total is approximately the same. This is exactly the result we would expect for a fully developed jet of a conserved scalar, such as the drug mass (9). The lower values for

$y < 0$ can be explained by the trapping of fluorescence photons inside the mouthpiece, which varies according to the amount of accumulated deposition on the windows.

Similarly, we can scan the nozzle across the beam and develop a radial profile showing the width of the spray and projected density of the drug. Two radial scans at $y = 5$ mm and $y = 25$ mm are shown in Fig. 7 for the HFA 134a propellant. A profile at $y = 25$ mm is also shown in Fig. 8 for HFA 227 propellant. In these figures, the horizontal axes represent time and the transverse position x relative to the centerline of the mouthpiece. Again, we note that the optical density decreases with increasing y , but the drug concentration remains relatively constant.

Figures 7 and 8 show that the radial distributions have steep gradients, while the optical density profiles have Gaussian profiles. We can see this more clearly in Fig. 9, which shows the radial profiles of both x-ray fluorescence (drug

Fig. 8 Radial scan across the spray for HFA 227 propellant.



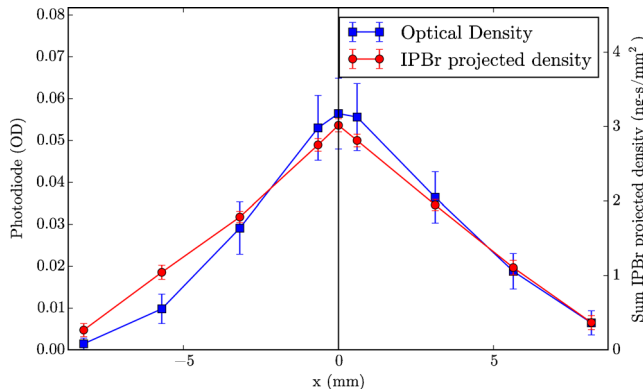


Fig. 9 Transverse line-of-sight integrated profiles of time-integrated drug concentration (red) compared to time-average optical density (blue) for a HFA 227 spray at $y=25$ mm from the nozzle. The error bars represent two standard deviations about the time-averaged value.

concentration) and optical density integrated over the entire duration of the spray event. The radial profile shows a sharp peak for the x-ray fluorescence data, and a more Gaussian peak for the optical density.

Both measurements shown in Fig. 9 are line-of-sight integrated. This means that a small change in the measured quantity can reveal a large local change in the three-dimensional density field. In practice, the small change in the peaks that we see in Fig. 9 actually represents quite a substantial change in the local density field near the centerline of the spray. As such, the concentration of drug in the spray could be quite different from what we might intuitively expect.

To understand how an axisymmetric density field appears when projected onto a plane, we consider the inverse Abel transforms (39) of several sample profiles in Fig. 10. The purpose of Fig. 10 is to show that linear, Gaussian and elliptic line-of-sight integrals (solid lines) actually represent very different local density distributions. The linear profile (Fig. 10a) has a very high density peak at its center, the Gaussian (Fig. 10b) is

proportional to its own density distribution, and the elliptic profile (Fig. 10c) is the projection of a flat density field.

We note that the x-ray fluorescence and optical density profiles in Fig. 9 have a similar shape to Fig. 10a and b respectively. From this observation, we hypothesize that the spray (as indicated by optical density) has an approximately Gaussian distribution of density like Fig. 10b, while the drug concentration is higher at the center and less at the periphery, similar to Fig. 10a. This suggests that the drug is not evenly distributed across the spray. This is important, as the concentration of the drug at the edges of the plume is a key factor in determining oropharyngeal deposition.

CONCLUSIONS

In this paper, we have demonstrated a novel method of directly measuring the *in-situ* distribution of an active drug in an MDI spray using x-ray fluorescence. The technique is non-intrusive, temporally and spatially resolved, and provides a direct quantitative measurement of the line-of-sight projected density of the drug, independent of the propellant and co-solvent. The measurement is unaffected by local temperature gradients. The high penetrating power of x-rays allows us to measure inside the mouthpiece and probe dense regions of the spray close to the nozzle, a region which is inaccessible to many other diagnostics.

Proof of concept measurements using short-duration (30 ms) spray events reveal that the time-history of the drug distribution and overall spray density never reaches a steady state. Both HFA 134a and HFA 227 propellant sprays have line-of-sight drug concentration measurements that approximately match those we would expect if the spray were fully evaporated. The plume diameters necessary to explain the measured concentrations correspond to the dimensions of

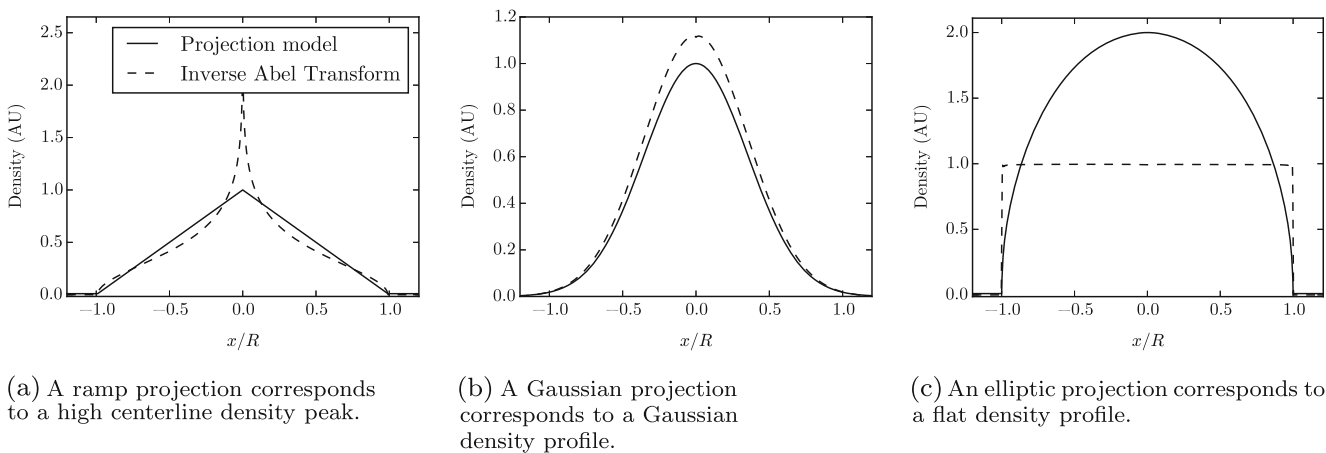


Fig. 10 Examples of several typical projected density profiles (solid lines), and their corresponding radial density distributions computed by the inverse Abel transform (dashed lines).

the mouthpiece. Axial profiles reveal that the drug distribution is conserved as the spray spreads, which is intuitive. However, radial distributions reveal that the drug distribution is more concentrated at the centerline when compared to the overall density of the plume. More work remains to be done to investigate this matter, but this may be an important factor in determining oropharyngeal deposition.

This technique is very useful in its ability to isolate drug concentration from other factors such as temperature, pressure, and the state of the propellant. However, the major limitation of the method in its presented form is the use of bromine as a tracer species. It should be noted though that the technique is not limited exclusively to brominated drugs such as IPBr. The technique is generally extensible to any drug which falls into one of two categories; it either has a naturally occurring unique element with suitable properties that can be employed as a natural tracer (see Table 1), or the drug can be chemically altered to provide an inert surrogate (ie. Mn, Fe, Ni, Cu, Zn, etc.) which may alter the drug's pharmacokinetics but will not affect precipitation or solubility properties. This could be achieved via Br - Cl substitution, doping the solution or suspension with water-soluble metal salts (sulfates or nitrates of zinc and copper) or commonly available hydrocarbon-soluble Br or Fe-based compounds, many of which also dissolve well in common co-solvents such as ethanol. We note that the fluorescence from lighter elements will be more strongly absorbed in the ambient gas. With improvements to the design of the experiment, this challenge is surmountable.

Although the measurements presented here are projected into two dimensions, in principle measurements can be combined from just a few viewing angles to obtain a tomographic representation of the three-dimensional distribution (27). Furthermore, since the drug mass is conserved, the fluorescence signal can also be used as a passive scalar. In combination with laser extinction this could provide a quantitative indication of the rate of vaporisation and precipitation; quantities which are difficult to measure with visible-light optical techniques alone.

In future work, the technique will be extended to investigate the effects of inspiration flow on near-field entrainment, and on the effects of varying formulation, nozzle and sump geometry on the drug distribution. Understanding the physical mechanisms by which these factors affect the distribution of the drug in the early formation region of the spray may explain some of the important factors which control dosing repeatability and respirable fraction.

ACKNOWLEDGMENTS AND DISCLOSURES

The authors thank Dr. Christopher Powell and Dr. Andrew Swantek from the Energy Systems Division at Argonne

National Laboratory for their assistance. The authors acknowledge funding support from the Australian Research Council. This research was performed at the 7-BM beam line of the Advanced Photon Source at Argonne National Laboratory. Use of the APS is supported by the U.S. Department of Energy (DOE) under Contract No. DE-AC02-06CH11357.

The submitted manuscript has been created by UChicago Argonne, LLC, Operator of Argonne National Laboratory ("Argonne"). Argonne, a U.S. Department of Energy Office of Science laboratory, is operated under Contract No. DE-AC02-06CH11357. The U.S. Government retains for itself, and others acting on its behalf, a paid-up nonexclusive, irrevocable worldwide license in said article to reproduce, prepare derivative works, distribute copies to the public, and perform publicly and display publicly, by or on behalf of the Government.

REFERENCES

1. Prokopovich P. Inhaler devices - fundamentals, design and drug delivery. Woodhead Publishing; 2013.
2. Dalby R, Suman J. Inhalation therapy: technological milestones in asthma treatment. *Adv Drug Deliv Rev.* 2003;55(7):779–91.
3. Rubin BK, Fink JB. Optimizing aerosol delivery by pressurized metered-dose inhalers. *Respir Care.* 2005;50(9):1191–200.
4. Preedy EC, Prokopovich P. History of inhaler devices. In: Prokopovich P, editor. *Inhaler devices - fundamentals, design and drug delivery.* Cambridge: Woodhead Publishing; 2013. p. 13.
5. Dhand R. Aerosol plumes: slow and steady wins the race. *J Aerosol Med.* 2005;18(3):261–3.
6. Crompton GK. The adult Patient's difficulties with inhalers. *Lung.* 1990;168(1):658–62.
7. Dhand R. Ventilator graphics and respiratory mechanics in the patient with obstructive lung disease. *Respir Care.* 2005;50(2):246–61.
8. Finlay WH. The Mechanics of inhaled pharmaceutical aerosols: an introduction. Academic Press; 2001.
9. Buchmann NA, Duke DJ, Shakiba SA, Mitchell DM, Stewart PJ, Traini D, et al. A novel high-speed imaging technique to predict the macroscopic spray characteristics of solution based pressurised metered dose inhalers. *Pharm Res.* 2014;31(11):2963–74.
10. Shemirani FM, Church TK, Lewis DA, Finlay WH, Vehring R. Onset of flash atomization in a propellant microjet. *ASME J Fluids Eng.* 2015;137(9):091101–9.
11. Dhand R, Malik SK, Balakrishnan M, Verma SR. High speed photographic analysis of aerosols produced by metered dose inhalers. *J Pharm Pharmacol.* 1988;40:429–30.
12. Dunbar CA. Atomization mechanisms of the pressurized metered dose inhaler. Part Sci Technol. 1997;15(3–4):253–71.
13. Duke D, Honnery D, Soria J. A comparison of subpixel edge detection and correlation algorithms for the measurement of sprays. *Int J Spray Comb Dyn.* 2011;3(2):93–110.
14. Duke D, Honnery D, Soria J. The growth of instabilities in annular liquid sheets. *Exp Thermal Fluid Sci.* 2015;68:89–99.
15. Tzou TZ. Aerodynamic particle size of metered-dose inhalers determined by the quartz crystal microbalance and the Andersen cascade impactor. *Int J Pharm.* 1999;186:71–9.

16. Marple VA, Roberts DL, Romay FJ, Miller NC, Truman KG, Van Oort M, et al. Next generation pharmaceutical impactor (A new impactor for pharmaceutical inhaler testing). Part I: design. *J Aerosol Med*. 2003;16:283–99.
17. Lewis DA, Young PM, Buttini F, Church T, Colombo P, Forbes B, et al. Towards the bioequivalence of pressurised metered dose inhalers 1: design and characterisation of aerodynamically equivalent beclomethasone dipropionate inhalers with and without glycerol as a non-volatile excipient. *Eur J Pharm Biopharm*. 2014;86(1):31–7.
18. Traini D, Young PM, Rogueda P, Price R. In vitro investigation of drug particulates interactions and aerosol performance of pressurised metered dose inhalers. *Pharm Res*. 2006;24(1):125–35.
19. Clark AR. MDIs: physics of aerosol formation. *J Aerosol Med*. 1996;9(S1):19–26.
20. Liu X, Doub WH, Guo C. Evaluation of metered dose inhaler spray velocities using Phase Doppler Anemometry (PDA). *Int J Pharm*. 2012;423:235–9.
21. Smyth H, Brace G, Barbour T, Gallion J, Grove J, Hickey AJ. Spray pattern analysis for metered dose inhalers: effect of actuator design. *Pharm Res*. 2006;23(7):1591–6.
22. Haynes A, Shaik MS, Krarup H, Singh M. Evaluation of the Malvern spraytec (R) with inhalation cell for the measurement of particle size distribution from metered dose inhalers. *J Pharm Sci*. 2004;93(2):349–63.
23. Als-Nielsen J, McMorrow D. Elements of modern X-Ray physics. New York: Wiley; 2001.
24. Sinha SK. Application of synchrotron radiation techniques to nanoscience. *Radiat Phys Chem*. 2004;70(4–5):633–40.
25. Kastengren A, Powell CF. Synchrotron X-ray techniques for fluid dynamics. *Exp Fluids*. 2014;55(3):1686.
26. Kastengren A, Powell CF, Arms D, Dufresne EM, Gibson H, Wang J. The 7BM beamline at the APS: a facility for time-resolved fluid dynamics measurements. *J Synchrotron Radiat*. 2012;19(4):654–7.
27. Kastengren AL, Tilocco F, Duke D, Powell C, Zhang X, Moon S. Time-resolved X-Ray radiography of sprays from engine combustion network spray a diesel injectors. *Atomization Sprays*. 2014;24(3):251–72.
28. Duke D, Kastengren AL, Tilocco F, Swantek AB, Powell C. X-ray radiography measurements of cavitating nozzle flow. *Atomization Sprays*. 2013;23(9):841–60.
29. Kastengren A, Powell CF, Dufresne EM, Walko DA. Application of X-ray fluorescence to turbulent mixing. *J Synchrotron Radiat*. 2011; 811–815.
30. Radke CD, Patrick McManamen J, Kastengren AL, Halls BR, Meyer TR. Quantitative time-averaged gas and liquid distributions using x-ray fluorescence and radiography in atomizing sprays. *Opt Lett*. 2015;40(9):2029–4.
31. Seitzman JM, Hanson RK. Planar fluorescence imaging in gases. In: Taylor AMKP, editor. Instrumentation for flows with combustion. Academic Press; 1993. p. 405–466.
32. Bearden JA. X-Ray wavelengths. *Rev Mod Phys*. 1967;39:78–124.
33. Krause MO, Oliver JH. Natural widths of atomic K and L Levels, Ka x-ray lines and several KLL auger lines. *J Phys Chem Ref Data*. 1979;329.
34. McNaught AD, Wilkinson A. IUPAC compendium of chemical terminology. 2nd ed. Oxford: Blackwell Scientific Publications; 1997. Available from: <http://goldbook.iupac.org/A00028.html>.
35. Miller MC. X-Ray Fluorescence. In: Smith K, Reilly E, editors. Passive Nondestructive Assay Manual - PANDA. Los Alamos National Laboratory; 1991. p. 313–335.
36. Hubbell JH, Trehan PN, Singh N, Chand B, Mehta D, Garg ML, et al. A review, bibliography, and tabulation of K, L, and higher atomic shell X-Ray fluorescence yields. *J Phys Chem Ref Data*. 1994;23(2):339–64.
37. Walko DA, Arms DA, Miceli A, Kastengren AL. Empirical dead-time corrections for energy-resolving detectors at synchrotron sources. *Nucl Inst Methods Phys Res, A*. 2011;649(1):81–3.
38. Lemmon EW, McLinden MO, Friend DG. Thermophysical properties of fluid systems. In: Linstrom PJ, Mallard WG, editors. NIST Chemistry WebBook, NIST Standard Reference Database Number 69. Gaithersburg: National Institute of Standards and Technology; 1998. p. 20899. Available from: <http://webbook.nist.gov>.
39. Dasch CJ. One-dimensional tomography - a comparison of Abel, onion-peeling, and filtered backprojection methods. *Appl Opt*. 1992;31(8):1146–52.

D.2 Concluding statement

In this Appendix, x-ray fluorescence spectroscopy was used to directly measure the drug concentration of pMDI sprays. The technique is capable of capturing spatio-temporal trends in the ensemble-mean drug distribution.

Axial scans showed that the projected drug concentration along the spray axis remains largely invariant with downstream distance. Time-variant transverse profiles of optical density and drug concentration indicate that the drug is well-mixed in the formulation temporally, but not spatially. The drug concentration is sharply peaked, while the optical density more closely resembles a Gaussian distribution. A comparison of the drug distribution with basic radial and transverse profiles indicated that the spray has a high centre line drug concentration. More work is required to determine the significance of the high centre line drug concentration.

These measurements demonstrate the capacity of x-ray fluorescence spectroscopy for the measurement of drug concentration in pMDI sprays. Measurements can be made in the near-nozzle region where laser diagnostics suffer due to high optical density and multiple scatter, and further downstream.